Direct sampling method in inverse electromagnetic scattering problem

Sangwoo Kang

université PARIS-SACLAY

NNT : 2019SACLS417

Thèse de doctorat

UNIVERSITÉ PARIS SUD
Comprendre le monde, construire l'avenir

Direct sampling method in inverse electromagnetic scattering problem

Thèse de doctorat de l'Université Paris-Saclay
préparée à l'Université Paris-Sud

École doctorale n°575 Electrical, Optical, Bio - physics and Engineering (EOBE)
Spécialité de doctorat: Génie électrique

Thèse présentée et soutenue à Gif-sur-Yvette, le 14 novembre 2019, par

Sangwoo Kang

Composition du Jury :

Houssem Haddar Directeur de recherche, INRIA	Président
Amélie Litman Maître de Conférences, Université de Marseille	Rapporteur
Matteo Pastorino Professeur, Université de Gênes	Rapporteur
Dominique Lesselier Directeur de recherche, CNRS	Examinateur
Mikyoung Lim Professeur, KAIST	Examinatrice
Marc Lambert Chargé de recherche, CNRS	Directeur de thèse

Acknowledgements

Most of all, I would like to express my sincere gratitude to thesis director Dr. Marc Lambert, Chargé de recherche, Centre National de la Recherche Scientifique (CNRS), for his excellent advice during my thesis. When I came to France three years ago, I worried about the situation because the topic of the thesis suddenly changed due to the security issue. He cared about the situation carefully, and I could release my stress and worries. Also, his expertise and insights lead me to the electromagnetic area even though I have studied the mathematical theories and their applications in my master's degree. Thanks to him, my physical insight and research view can broaden widely. It was lucky that I have studied under his supervision for thee years.

I also wish to express my appreciation to co-supervisor Prof. Won-Kwang Park, associate professor in the Department of Information Security, Cryptology, and Mathematics, Kookmin university. About ten years ago, I had decided to continue studying in an applied mathematics area after I took his class of analysis. Besides, I could have a chance to continue my studies in France thanks to his suggestion. My Ph.D. can be finished well thanks to his kind supervision and creative approaches.

I want to extend my gratitude to Dr. Amélie Litman and Prof. Matteo Pastorino for serving as the referees, and Dr. Dominique Lesselier, Dr. Houssem Haddar, and Prof. Mikyoung Lim as the jury members. Especially I want to express my gratitude once again to Dr. Dominique Lesselier for his kind support for three years. Even though I am not his Ph.D. student, he provided many advice and related papers about my research. Not only that, he helped and cared about my private life.

For three years, I enjoyed working in a research environment with many friendly people, Dr. Zicheng Liu, Dr. Hidayet Zaimaga, Dr. Xiang Liu, and Ran Peipei. They all are enthusiastic and kind people. I thank them a lot of their help and excellent relationships with me.

Finally, I'm deeply grateful to my wife, Yoomin. Thanks to her supports, I could focus only on my works for three years. My great appreciation goes to my families also.

Contents

List of Figures

List of Tables

Résumé en français

Contexte général L'objectif de la résolution d'un problème de diffraction électromagnétique inverse est de déterminer les caractéristiques d'inhomogénéités inconnues telles que leurs emplacements, formes ou propriétés matérielles (par exemple, la permittivité, la perméabilité) à partir de données diffractées collectées pour divers de champs électromagnétiques entrants. La résolution de problèmes de diffraction inverse est considérée comme un sujet de recherche intéressant pour les scientifiques et les ingénieurs, car le domaine d'utilisation s'étend à de nombreux domaines très liés à la vie humaine. Nous prenons quelques exemples, tels que l'évaluation non destructive (NDE) pour identifier les défauts (ex. vides internes, objets ou fissures) à l'intérieur d'un pont ou d'un mur, l'imagerie biomédicale pour le diagnostic et la détection des accidents cérébrovasculaires et du cancer du sein, le radar de pénétration de sol (GPR), l'ouverture synthétique radar (SAR) et l'imagerie sismique. Nous nous référons à certains articles tels (Yaman, Yakhno et Potthast 2013 ; Chandra et al. 2015) pour plus d'investigations des applications de tels problèmes. Par conséquent, résoudre les problèmes de diffraction inverse pose de grands défis afin de développer toujours plus de nouveaux outils et techniques. Malheureusement, il est difficile de les résoudre en raison du caractère mal posé et de la non-linéarité.

Au cours des dernières décennies, diverses techniques d'inversion ont été développées pour résoudre des problèmes de diffraction inverse en surmontant l'inhérent caractère mal-posé et cette non-linéarité. Elles peuvent être classées en méthodes quantitatives et qualitatives en fonction de leur objectif. Le but des méthodes quantitatives est de reconstruire la distribution de paramètres de matériaux tels que la permittivité, la perméabilité, etc. L'objectif des méthodes qualitatives est de fournir des informations sur le support des inhomogénéités, c'est-à-dire des formes, des emplacements et, dans le cas d'objets multiples, également leur nombre.

Premièrement, l'approche générale pour résoudre les problèmes de diffraction inverse dans les méthodes quantitatives est basée sur un schéma d'itération de type Newton, c'est-à-dire l'obtention de la solution minimisant une norme discrète (généralement norme L^2) entre problèmes de diffraction directe et adjointe (fonction coût). Par exemple, la valeur du contraste χ est estimée en résolvant une équation intégrale non-linéaire à chaque étape d'une méthode itérative de Born distordue et la densité de courant induite J est en sus estimée en résolvant des équations intégrales de type source à chaque étape d'une méthode d'inversion de contraste de source. Nous pouvons aussi faire référence à une méthode d'ensembles de niveaux, à des techniques de reconstruction sous contrainte de parcimonie, etc. Mais pour une application réussie de tels schémas itératifs, il faut tenir compte des points suivants :

(i) des coûts de calcul importants, en particulier une évaluation complexe du gradient (par exemple, dérivée de Fréchet ou dérivée de domaine) est nécessaire à chaque pas d'itération,

(ii) le problème de non-convergence et de minima locaux se pose, puisque la fonction coût n'est pas convexe,

(iii) une régularisation en tant que sélection de termes de régularisation appropriés qui dépendent de

manière significative du problème en question est requise,

(iv) des a priori sur les inhomogénéités inconnues sont nécessaires pour garantir la convergence.

Deuxièmement, les méthodes qualitatives, connues sous le nom de techniques d'inversion non itérative ou en une étape, évitent de traiter le problème dans sa non-linéarité entière et considèrent un modèle mathématique simplifié avec un coût de calcul inférieur. De plus, aucune information a priori sur les inhomogénéités inconnues n'est requise. En raison de ces avantages, diverses techniques ont été étudiées et appliquées avec succès à de nombreux problèmes de diffraction inverse. Par exemple, afin de fournir une image des inhomogénéités à partir de données diffractées, la classification multiple des signaux (acronyme anglais MUSIC) caractérise le rang d'un opérateur auto-adjoint et le sous-espace de bruit est orthogonal à ce rang ; la méthode d'échantillonnage linéaire (LSM) consiste quant à elle à résoudre approximativement l'équation intégrale de champ en chaque point de recherche dans la région d'intérêt ; les techniques de type migration (par exemple, migration de Kirchhoff, migration de sous-espace, migration en retournement en temps) consistent à rétro-propager les champs incidents et/ou observés complexes conjugués dans le milieu d'enfouissement. De telles techniques nécessitent un nombre suffisamment grand de directions d'incidence et d'observation pour pouvoir visualiser correctement les inhomogénéités. Malheureusement, la configuration à pleine ouverture est impossible dans diverses applications réelles telles que GPR (Catapano, Soldovieri et Crocco 2011), SAR (T. Zhang et Xia 2015) et l'imagerie sismique (Xue et al. 2015). Par conséquent, il est naturel de développer une méthode qualitative alternative qui soit efficace avec un petit nombre de directions d'incidence ou d'observation.

Objet de la thèse La méthode d'échantillonnage direct (DSM) est considérée dans divers problèmes de diffraction électromagnétique inverse 2D et 3D dans cette thèse. Contrairement aux méthodes non itératives existantes (telles que MUSIC, LSM et techniques de migration), la DSM n'a besoin que de quelques champs d'incidence pour visualiser les inhomogénéités. De plus, elle est assez rapide car ne nécessite aucune opération supplémentaire, telle qu'une décomposition en valeurs singulières ou une projection, et elle est très tolérante au bruit. La fonction indicatrice de la DSM à chaque point de recherche est définie par le produit intérieur L^2 du champ diffracté (ou diagramme de champ lointain) et de la fonction de test liée aux récepteurs. Plus précisément, la combinaison de la structure du champ diffracte dispersé et de l'identité de Kirchhoff-Helmholtz implique que la fonction indicatrice peut être représentée par la partie imaginaire de la fonction de Green de l'équation de Helmholtz dans le cas scalaire et de la fonction de Green dyadique des équations en régime harmonique de Maxwell dans le cas vectoriel. Ainsi, les inhomogénéités peuvent être reconstruites via la carte rue duite par la de DSM.

Depuis le développement de la DSM par (Ito, Jin et J. Zou 2012), sa faisabilité et sa robustesse pour l'imagerie d'inhomogénéités ont été validées dans divers problèmes de diffraction. Par exemple, le problème de mesure en champ lointain (Li et Z. Zou 2013), le cas électromagnétique tridimensionnel (Ito, Jin et J. Zou 2013), l'imagerie de fissures (W.-K. Park 2018b), le problème électrique transverse (W.-K. Park 2019b). Nous nous référons également à (Chow, Ito et J. Zou 2014), (Chow, Ito, K. Liu et al. 2015) et à (Bektas et Ozdemir 2016) pour les applications de la DSM à la tomographie par impédance électrique, à la tomographie optique par diffusion et à l'imagerie radar mono-statique, respectivement. Mais les limites de DSM ne peuvent pas être expliquées par les résultats de tels travaux aussi avancés. Par exemple :

(i) la plus petite inhomogénéité est difficile à identifier s'il existe plusieurs inhomogénéités de tailles différentes dans la région d'intérêt, un phénomène similaire étant observé en présence de défauts de même taille mais de permittivités différentes,

(ii) l'imagerie via la DSM avec des données mono-statiques fournit une localisation erronée de l'inhomogénéité,

(iii) la DSM multi-fréquence n'est pas efficace pour l'imagerie de petites inhomogénéités multiples,

(iv) les performances d'imagerie ne changent pas significativement par rapport au nombre total de directions d'incidence,

(v) les inhomogénéités ne peuvent pas être visualisées par la DSM dans le cas 3D (champ diffracté vectoriel) si la polarisation de la fonction de test incorrecte est utilisée.

Pour expliquer les raisons de ces limitations, nous analysons la structure de la DSM en utilisant la formule asymptotique de champ diffracté (ou diagramme de champ lointain) dans l'hypothèse de faible volume des inhomogénéités.

Problème direct de diffraction électromagnétique et sa formule asymptotique (§ 2) Dans le chapitre 2, nous présentons les résultats bien connus et/ou déjà dérivés du problème de diffraction électromagnétique directe dans diverses configurations 2D (cas de champ scalaire en mode TM) et 3D (cas de champ vectoriel). Pour la fréquence considérée f_0, nous supposons que les données électromagnétiques diffractées générées par chaque source dipolaire $\mathbf{y}_l \in \Gamma_{\text{inc}},\ l = 1, 2, \cdots, L$ sont collectées par les récepteurs $\mathbf{x}_n \in \Gamma_{\text{obs}},\ n = 1, 2, \cdots, N$, où Γ_{obs} and Γ_{inc} sont simplement des surfaces connectées (ou courbes) dans $\mathbb{R}^d, d = 2, 3$. De manière analogue, les diagrammes de champ lointain électromagnétique sont mesurés avec les directions d'observation $\hat{\mathbf{x}}_n \in \mathbb{S}^d,\ n = 1, 2, \cdots, N$ pour chaque direction d'incidence $\hat{\mathbf{d}}_l \in \mathbb{S}^1$ en cas scalaire 2D et chaque direction de la source $\hat{\mathbf{y}}_l \in \mathbb{S}^2,\ l = 1, 2, \cdots, L$ dans le cas vectoriel 3D. Nous supposons également qu'il existe un nombre fini d'inhomogénéités dans la région d'intérêt supposée homogène et isotrope (ROI) Ω avec la permittivité de fond ε_0, la perméabilité μ_0 et le nombre d'onde k_0. Ici, chaque inhomogénéité est notée $\tau_m = \mathbf{r}_m + \alpha_m \mathbf{D}_m \in \mathbb{R}^d,\ d = 2, 3$. $\mathbf{r}_m$ est le centre, α_m est la taille et $\mathbf{D}_m$ caractérise la forme de τ_m. Notons τ la collection de τ_m, c'est-à-dire, $\tau = \bigcup_m \tau_m$. Sous l'hypothèse de faibles volumes de toutes les inhomogénéités afin de négliger leurs interactions, nous introduisons les formules asymptotiques du champ diffracté et du diagramme de champ lointain dans les configurations 2D et 3D, formules qui jouent un rôle clé dans notre analyse de structure.

Imagerie 2D d'inhomogénéités diélectriques avec données complètes et à champ proche (§ 3) Tout d'abord, nous étudions la DSM dans une configuration à vue complète. Grâce à notre analyse, il peut être montré que pour chaque point de recherche $\mathbf{z} \in \Omega$ et champ d'incidence fixé $\hat{\mathbf{d}}$, la DSM possède la formule de représentation suivante :

$$\mathcal{I}_{\text{DSM}}(\mathbf{z}, \hat{\mathbf{d}}; k_0) \propto \sum_{m=1}^{M} \alpha_m^2 (\varepsilon_m - \varepsilon_0) |\mathbf{D}_m| \mathrm{e}^{\mathrm{i}k_0 \hat{\mathbf{d}} \cdot \mathbf{r}_m} \mathrm{J}_0(k_0 |\mathbf{z} - \mathbf{r}_m|),$$

où J_0 est la fonction de Bessel de première espèce et d'ordre zéro. Ensuite, il apparaît que les performances de la fonction d'indicateur DSM en matière d'imagerie dépendent fortement de la permittivité, de la taille et du nombre des inhomogénéités. Si l'une de celles-ci a une permittivité et/ou une taille

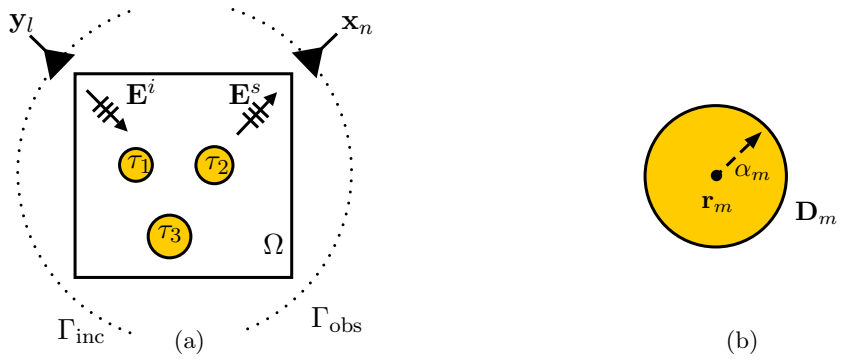

FIGURE 1 : Configuration du problème de diffraction pour $M = 3$ (à gauche) et sketch des inhomogénéités circulaires τ_m (à droite).

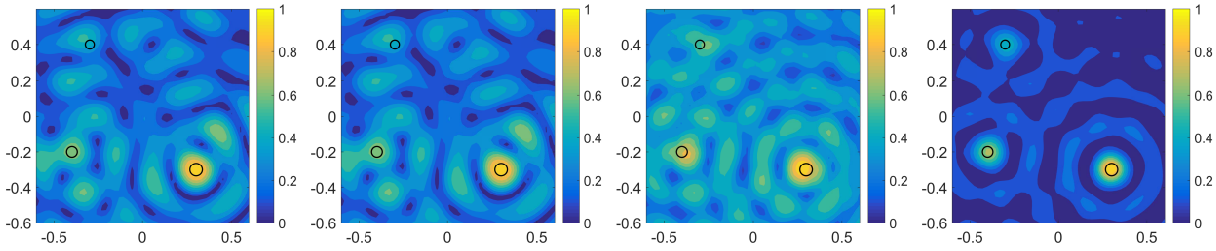

(a) DSM with $L = 1$ (b) DSMA with $L = 1$ (c) DSM with $L = 36$ (d) DSMA with $L = 36$

FIGURE 2 : Imagerie d'inhomogénéités diélectriques de différentes tailles en configuration vue complète.

significativement plus grande que les autres, elle peut être la seule à être identifiée, les autres restantes n'étant pas ou seulement partiellement vues. Malheureusement, la limitation ne peut pas être surmontée via la DSM, même avec un grand nombre de directions d'incidence, en raison de sa définition pour plusieurs directions incidentes. Pour remédier à cet inconvénient, nous suggérons une fonction indicatrice alternative de la DSM (DSMA) en donnant un poids exponentiel lié à chaque champ d'incidence. En suivant un chemin similaire dans la dérivation de l'analyse de structure de la DSM, la DSMA est caractérisée par la formule de représentation suivante :

$$\mathcal{I}_{\text{DSMA}}(\mathbf{z}; k_0) \propto \sum_{m=1}^{M} \alpha_m^2 (\varepsilon_m - \varepsilon_0) |\mathbf{D}_m| \mathrm{J}_0(k_0 |\mathbf{z} - \mathbf{r}_m|)^2.$$

A partir des propriétés d'oscillation de $\mathrm{J}_0(k_0|\mathbf{z}-\mathbf{r}_m|)^2$ et $\mathrm{J}_0(k_0|\mathbf{z}-\mathbf{r}_m|)$, nous vérifions que la DSMA est une version améliorée de la DSM si plusieurs incidences. Il est à noter que DSM et DSMA ont les mêmes performances d'imagerie dans le cas d'une direction d'incidence unique. Nos résultats théoriques sont validés via diverses simulations numériques avec des données synthétiques et expérimentales. La Figure 2 montre les simulations numériques permettant d'imager les petites inhomogénéités diélectriques de différentes tailles, ce qui est l'une de ces simulations. Il est à noter qu'un phénomène similaire sera observé dans différents cas de permittivité. De plus, nous validons la relation forte qui existe entre la DSM et la migration de Kirchhoff par l'analyse de structure.

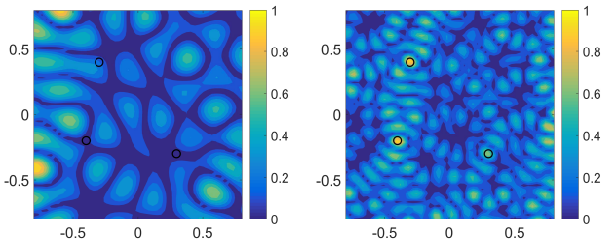

(a) DSM (b) Modified DSM

FIGURE 3 : Imagerie d'inhomogénéités diélectriques avec des données mono-statiques en configuration à pleine ouverture.

Imagerie 2D des inhomogénéités diélectriques en configuration restreinte avec des données de champ lointain (§ 4)

- **Méthode d'échantillonnage directe en configuration mono-statique (§ 4.1)** Dans diverses applications du monde réel telles que le radar à pénétration de sol, le radar à synthèse d'ouverture et l'imagerie sismique, une configuration à pleine ouverture n'est pas possible. En d'autres termes, le mouvement d'un seul émetteur-récepteur ou les plages restreintes d'incidence et d'observation doivent être pris en compte dans de telles applications. Par conséquent, l'analyse de structure et l'amélioration de la DSM dans des configurations mono-statiques et à ouverture limitée sont considérées ici.

  Dans la première partie, nous proposons la fonction indicatrice de la DSM en données mono-statiques. Cependant, le résultat de la DSM explique mal la localisation des inhomogénéités, ce qui se comprend par l'analyse de la fonction indicatrice à l'aide de la formule asymptotique du diagramme de champ lointain qui conduit à :

$$\mathcal{I}_{\mathrm{DSM}}^{\mathrm{mono}}(\mathbf{z}; k_0) \propto \sum_{m=1}^{M} \alpha_m^2(\varepsilon_m - \varepsilon_0)|\mathbf{D}_m|\mathrm{J}_0(k_0|2\mathbf{r}_m - \mathbf{z}|).$$

  c'ci montre que la raison pour laquelle la fonction indicatrice a atteint sa valeur maximale à l'emplacement déplacé $\mathbf{z} = 2\mathbf{r}_m$ conduit à une fonction indicatrice modifiée en adoptant une nouvelle fonction de test fournissant la formule de représentation suivante :

$$\mathcal{I}_{\mathrm{MDSM}}^{\mathrm{mono}}(\mathbf{z}; k_0) \propto \sum_{m=1}^{M} \alpha_m^2(\varepsilon_m - \varepsilon_0)|\mathbf{D}_m|\mathrm{J}_0(2k_0|\mathbf{r}_m - \mathbf{z}|).$$

  Le résultat signifie que notre proposition peut gérer le problème de localisation imprécise de la DSM dans la configuration mono-statique. En contraste, la DSM traditionnelle dans la configuration multi-statique est proportionnelle à $|\mathrm{J}_0(k_0|\mathbf{r}_m - \mathbf{z}|)|$. Les propriétés d'oscillation de $\mathrm{J}_0(k_0|\mathbf{r}_m - \mathbf{z}|)$ par rapport à celles de $\mathrm{J}_0(2k_0|\mathbf{r}_m - \mathbf{z}|)$ conduisent à ce que le résultat de la DSM modifiée en configuration mono-statique contient plus d'artefacts que celui de la DSM en configuration multi-statique en raison du manque d'information. Un résultat typique est proposé en Figure 3.

- **Méthode d'échantillonnage direct en configuration à ouverture limitée (§ 4.2)** Ensuite, nous étendons notre approche au problème à ouverture limitée et validons sa structure mathématique en suivant un chemin similaire à celui utilisé dans le cas d'une ouverture totale. La fonction indicatrice de la DSM a la formule de représentation suivante :

$$\mathcal{I}^{\infty}_{\mathrm{DSM}}(\mathbf{z};\hat{\mathbf{d}},k_0) \propto \sum_{m=1}^{M} \alpha_m^2 |\mathbf{D}_m| \left(\frac{\varepsilon_m-\varepsilon_0}{\sqrt{\varepsilon_0\mu_0}}\right) \mathrm{e}^{\mathrm{i}k_0\hat{\mathbf{d}}\cdot\mathbf{r}_m} \left\{ \mathrm{J}_0(k_0|\mathbf{r}_m-\mathbf{z}|) + \Lambda_S^{\theta_1,\theta_N}(k_0,|\mathbf{r}_m-\mathbf{z}|) \right\}.$$

Ici, θ_1 et θ_N sont respectivement l'angle minimal et maximal des directions d'observation. En comparaison avec le cas de la vue complète, le terme perturbatif $\Lambda_S^{\theta_1,\theta_N}(k_0,|\mathbf{r}_m-\mathbf{z}|)$ est apparu. Sur la base de ce résultat, nous établissons la condition nécessaire d'une gamme de directions d'observation (par exemple $\theta_N-\theta_1 \geq \pi$ pour visualiser correctement les inhomogénéités. De même, la DSMA, qui est proposée dans le cas de la vue complète, est également appliquée et analysée pour améliorer les performances de l'imagerie en utilisant plusieurs champs d'incidence comme dans ce qui suit :

$$\mathcal{I}^{\infty}_{\mathrm{DSMA}}(\mathbf{z};k_0) \propto \sum_{m=1}^{M} \alpha_m^2 |\mathbf{D}_m| \left(\frac{\varepsilon_m-\varepsilon_0}{\sqrt{\varepsilon_0\mu_0}}\right) \big[\mathrm{J}_0(k_0|\mathbf{r}_m-\mathbf{z}|)^2 + \mathrm{J}_0(k_0|\mathbf{r}_m-\mathbf{z}|)^2 + \Lambda_S^{\theta_1,\theta_N}(k_0,|\mathbf{r}_m-\mathbf{z}|)\Lambda_S^{\vartheta_1,\vartheta_L}(k_0,|\mathbf{r}_m-\mathbf{z}|)\big],$$

où $[\vartheta_1,\vartheta_L]$ est la plage de directions d'incidence Cela montre qu'il faut encore faire appel à des observations et/ou incidences à grandes ouvertures pour imager correctement les inhomogénéités, même si le résultat de la méthode DSMA présente moins d'oscillations. Les résultats théoriques sont également vérifiés par diverses simulations numériques. Certains de ceux-ci sont présentés vus dans la Figure 4.

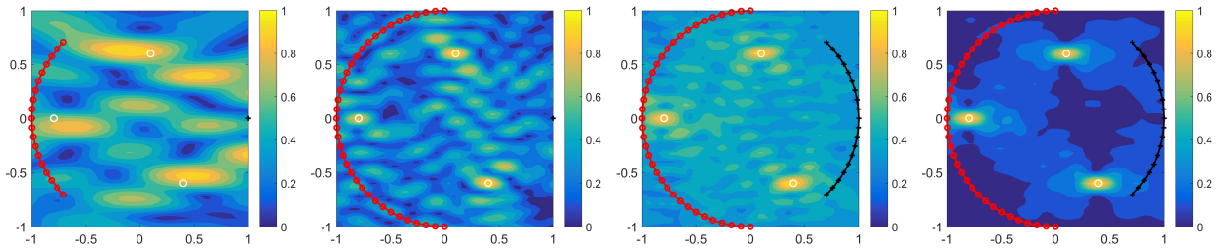

(a) DSM and DSMA (b) DSM and DSMA (c) DSM (d) DSMA

FIGURE 4 : Imagerie d'inhomogénéités diélectriques où la ligne rouge et la ligne noire indiquent l'étendue des directions d'observation et d'incidence.

Amélioration de la précision de l'imagerie 2D en utilisant plusieurs fréquences (§ 5) Nous appliquons également l'approche multi-réquence, qui est l'une des techniques populaires d'amélioration de l'efficacité de l'imagerie, à la DSM dans les problèmes d'ouverture limitée. Contrairement à plusieurs investigations (ESTATICO et al. 2015 ; JOH et W.-K. PARK 2014), la DSM multi-fréquence (MDSM) est

efficace pour l'imagerie d'une petite inhomogénéité mais ne l'est pas pour celle de plusieurs petites inhomogénéités. Pour expliquer la raison de manière théorique, la structure mathématique de la fonction indicatrice multi-fréquence a été établie comme suit :

$$\mathcal{I}^{\infty}_{\mathrm{MDSM}}(\mathbf{z};\hat{\mathbf{d}}) \propto \sum_{m=1}^{M} \alpha_m^2(\varepsilon_m-\varepsilon_0)|\mathbf{D}_m|\Bigg[\frac{1}{k_P-k_1}\Big\{\mathcal{C}_1^{k_1,k_P}(|\mathbf{r}_m|,|\mathbf{r}_m-\mathbf{z}|)+\mathcal{C}_2^{k_1,k_P}(|\mathbf{r}_m|,|\mathbf{r}_m-\mathbf{z}|)\Big\} + \Lambda_M^2(k_1,k_P,\theta_1,\theta_N,|\mathbf{r}_m|,|\mathbf{r}_m-\mathbf{z}|)\Bigg],$$

où k_1 et k_P sont les nombres d'onde correspondants aux fréquences minimale et maximale des fréquences considérées $\{f_1, f_2, \cdots, f_P\}$. Ici, $\mathcal{C}_1^{k_1,k_P}(|\mathbf{r}_m|,|\mathbf{r}_m-\mathbf{z}|)$ et $\mathcal{C}_2^{k_1,k_P}(|\mathbf{r}_m|,|\mathbf{r}_m-\mathbf{z}|)$ contribuent à reconstruire les supports des inhomogénéités. Notre analyse de structure vérifie qu'ils ont les comportements de fonctions hypergéométriques au centre des inhomogénéités. C'est ce qui explique le fait que la DSM multi-fréquence n'est pas efficace pour l'imagerie de plusieurs petites inhomogénéités. Pour surmonter cette limitation, nous suggérons une version multi-fréquence de la DSMA (MDSMA) en donnant des poids par rapport à chaque fréquence et à la direction d'incidence Nous avons la formule de représentation suivante :

$$\mathcal{I}^{\infty}_{\mathrm{MDSMA}}(\mathbf{z}) \propto \sum_{m=1}^{M} \alpha_m^2\left(\frac{\varepsilon_m-\varepsilon_0}{\sqrt{\varepsilon_m\varepsilon_0}}\right)\Bigg\{\frac{1}{k_P-k_1}\Bigg[\mathcal{H}(k_P,|\mathbf{r}_m-\mathbf{z}|)-\mathcal{H}(k_1,|\mathbf{r}_m-\mathbf{z}|) + \int_{k_1}^{k_P}\mathrm{J}_1(k|\mathbf{r}_m-\mathbf{z}|)\mathrm{d}k\Bigg] + \Lambda_M^3(k_1,k_P,\theta_1,\theta_N,\vartheta_1,\vartheta_L,|\mathbf{r}_m-\mathbf{z}|)\Bigg\},$$

où $\mathcal{H}(k,|\mathbf{r}_m-\mathbf{z}|) := k\left[\mathrm{J}_0(k|\mathbf{r}_m-\mathbf{z}|)^2+\mathrm{J}_1(k|\mathbf{r}_m-\mathbf{z}|)^2\right]$. En raison de la propriété de $\mathcal{H}(k,|\mathbf{r}_m-\mathbf{z}|)$, les pics MDSMA à tous les centres des inhomogénéités si leurs caractéristiques physiques (emplacement, forme, taille, etc.) et permittivité) sont les mêmes. Selon la Figure 5, nos résultats théoriques peuvent être validés. D'autres simulations numériques peuvent être trouvées dans le corps de cette thèse.

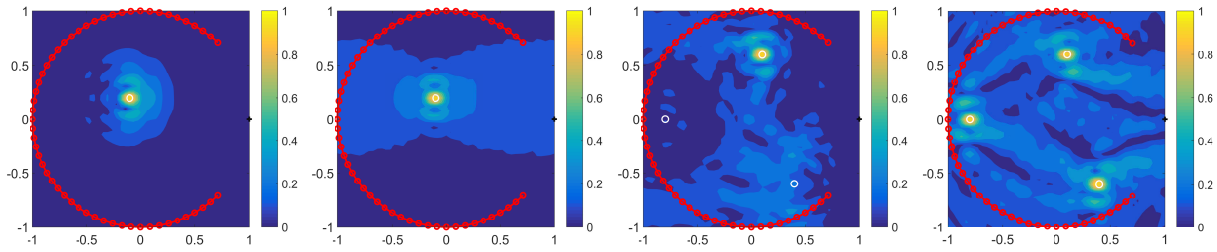

(a) MDSM (b) MDSMA (c) MDSM (d) MDSMA

FIGURE 5 : Imagerie d'inhomogénéités diélectriques où la ligne rouge et la ligne noire indiquent la couverture des directions d'observation et d'incidence ((a) et (b) pour une seule cible et (c) et (d) pour plusieurs cibles).

Imagerie 3D d'inhomogeneities diélectriques (§ 6) Enfin, nous étendons notre approche au problème de la diffraction électromagnétique inverse 3D. La différence principale entre DSM 2D et 3D réside dans

le choix de la polarisation de la fonction de test. Cependant, le résultat dans (Ito, Jin et J. Zou 2013) n'est pas suffisant pour expliquer l'effet du choix de cette fonction de test sur l'imagerie de la cible, bien que leurs auteurs aient recommandé de la choisir avec le même sens de polarisation que celui du dipôle incident (par exemple $\hat{\mathbf{q}} = \hat{\mathbf{p}}^t$). Ainsi, l'analyse complète de la structure de la fonction indicatrice de la DSM pour le cas vectoriel 3D est présentée grâce à la formule asymptotique du champ vectoriel diffracté comme suit :

$$\mathcal{I}_{\mathrm{DSM3D}}(\mathbf{z};\mathbf{y},\hat{\mathbf{q}}) \propto \sum_{m=1}^{M} A_m \left[C_1 \left(\mathrm{j}_0(k_0|\mathbf{r}_m-\mathbf{z}|) - \frac{\mathrm{j}_1(k_0|\mathbf{r}_m-\mathbf{z}|)}{k_0|\mathbf{r}_m-\mathbf{z}|} \right) + C_2 \frac{\mathrm{j}_2(k_0|\mathbf{r}_m-\mathbf{z}|)}{|\mathbf{r}_m-\mathbf{z}|^2} \right],$$

où j_s est une fonction de Bessel sphérique d'ordre entier s. Sur la base des formes explicites de C_1 et C_2 dans l'analyse de structure, nous vérifions théoriquement la validation du choix de la polarisation de test proposée dans ces travaux. En outre, nous suggérons une autre méthode pour la choisir, telle que l'optimisation de l'amplitude de la rétro-propagation à chaque point d'échantillonnage, conformément à l'idée du travail pionnier (X. Chen et Zhong 2008) conduisant à un algorithme MUSIC amélioré. Nous étendons également notre idée à la configuration en champ lointain et la fonction indicatrice correspondante de la DSM est proposée. Grâce à la formule de Funk-Hecke, la fonction indicatrice peut être analysée comme suit :

$$\mathcal{I}^{\infty}_{\mathrm{DSM3D}}(\mathbf{z};\hat{\mathbf{y}},\hat{\mathbf{q}}) \propto \left| \sum_{m=1}^{M} A_m \mathrm{e}^{\mathrm{i}k_0\mathbf{r}_m\cdot\hat{\mathbf{y}}} \left[\frac{8\pi}{3} \left(\left(\Delta(\hat{\mathbf{y}})\hat{\mathbf{p}}^t\right)\cdot\hat{\mathbf{q}} \right) \mathrm{j}_0(k_0|\mathbf{r}_m-\mathbf{z}|) + (C_1+C_2)\,\mathrm{j}_2(k_0|\mathbf{r}_m-\mathbf{z}|) \right] \right|,$$

où $\hat{\mathbf{y}}$ est la direction de la source. Notre résultat théorique et notre proposition peuvent être vérifiées sur la Figure 6, qui est l'un des résultats parmi les diverses simulations numériques du corps de cette thèse.

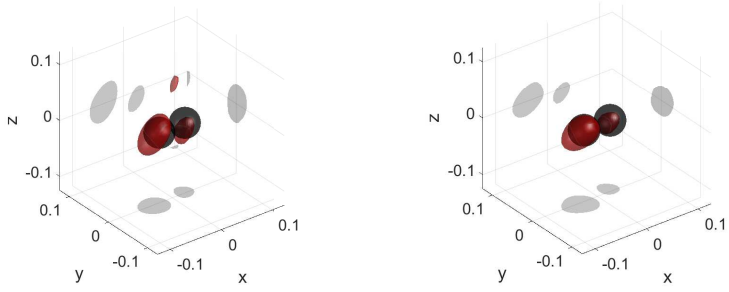

(a) $\mathcal{I}^{\infty}_{\mathrm{DSM3D}}(\mathbf{z};\mathbf{y},\hat{\mathbf{q}})$, where $\hat{\mathbf{q}} = \hat{\mathbf{p}}^t$ (b) $\mathcal{I}^{\infty}_{\mathrm{DSM3D}}(\mathbf{z};\mathbf{y},\hat{\mathbf{q}})$, where $\hat{\mathbf{q}} = \hat{\mathbf{q}}_{\max}$

Figure 6 : Imagerie d'inhomogénéités diélectriques avec une isosurface $\rho = 0.8$

Conclusions et perspectives (§ 7) Dans cette thèse, la méthode d'échantillonnage direct (DSM) a été étudiée dans divers problèmes de diffraction électromagnétique inverse 2D et 3D. Contrairement à de nombreuses méthodes qualitatives existantes, la DSM n'a besoin que de quelques (un ou deux) champs incidents pour une application réussie d'imagerie des inhomogénéités à partir de champs diffractés. De par plusieurs études, il est également bien connu que la DSM est une méthode rapide et efficace de type non-itératif pour résoudre les problèmes de diffraction inverse. Malheureusement, les applications les

plus avancées de la DSM restent heuristiques. L'objectif principal du travail était donc de déterminer la structure mathématique de la fonction indicatrice de la DSM afin de vérifier la raison théorique des phénomènes observés et de concevoir une nouvelle méthode efficace non-itérative pour l'imagerie des inhomogénéités (appelée DSMA dans ce travail). Les résultats théoriques ont été validés par diverses simulations numériques avec des données synthétiques et expérimentales.

Même si cette thèse traite de cas variés, la poursuite des études constitue un défi intéressant. Améliorer les performances d'imagerie avec des données mono-statiques utilisant plusieurs fréquences, améliorer les performances d'imagerie en adoptant des pondérations différentes pour chaque fréquence introduite dans (Joh et W.-K. Park 2014), imager les inhomogénéités enfouies par DSM, développer d'une version 3D de la DSMA, vérifier la relation entre une technique de type migration et la DSM 3D et imager 3D des inhomogénéités dans des configurations restreintes, etc.

Liste de mes publications (§ B) La liste des publications en lien avec ces travaux se trouve en appendice.

1

Introduction

Contents

1.1 General context

The purpose of solving an inverse electromagnetic scattering problem is to determine the characteristics of unknown inhomogeneities such as their locations, shapes, or material properties (e.g. permittivity, permeability) from collected scattered data from incoming electromagnetic fields. We refer to Figure 1.1 for a sketch of scattering problems in the presence of four inhomogeneities in the homogeneous medium ($\mathbb{R}^d, d = 2, 3$). The inhomogeneities $\tau_m, m = 1, \cdots, 4$ are located in the domain Ω, which is a region of interest. The incoming electromagnetic field is generated at the transmitter denoted by $\mathbf{y}$. The fields scattered from each incoming field are measured by an array of receivers $\mathbf{x}_n, n = 1, 2, \cdots, N$.

Solving inverse scattering problems has been regarded as an attractive research topic to scientists and engineers because the utilization area has been expanded in many different fields that are highly related to nowadays human life. We take some examples such as nondestructive evaluation (NDE) to identify defects (e.g. internal voids, objects or cracks) inside a bridge or wall (Caorsi, Massa, Pastorino, and Donelli 2004; Ploix et al. 2011; Völker and Shokouhi 2015), biomedical imaging for diagnosing brain stroke (Scapaticci et al. 2012; Ireland, Bialkowski, and Abbosh 2013; Tournier et al. 2017) and breast cancer detection (Fear et al. 2002; Rubæk et al. 2007; Irishina, Moscoso, and Dorn 2009; Haynes, Stang, and Moghaddam 2012), Ground Penetrating Radar (GPR) (Catapano, Soldovieri, and Crocco 2011; X. Liu, Serhir, and Lambert 2018; Torrione et al. 2014), Synthetic-Aperture Radar (SAR) (L. Zhang et al. 2010; Çetin et al. 2014; T. Zhang and Xia 2015), and seismic imaging (Tilmann, Ni, and INDEPTH III Seismic Team 2003; Y. Chen et al. 2015; Xue et al. 2015). We refer to some review articles (Yaman, Yakhno, and Potthast 2013; Chandra et al. 2015) for more investigations in the applications of such

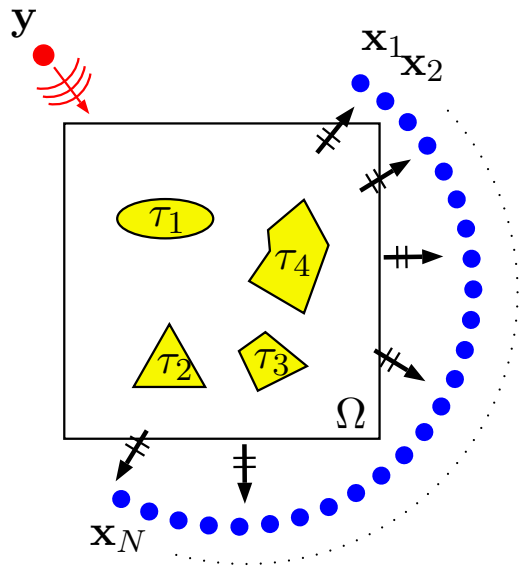

Figure 1.1: Sketch of scattering problems with 4 inhomogeneities in a homogeneous embedding medium

problems. Hence, solving inverse scattering problems poses great challenges to modern scientists for developing novel tools and techniques. Unfortunately, it is difficult to solve them due to ill-posedness and nonlinearity (refer to Appendix A.1 for more on those).

1.2 Inversion techniques

Over the past several decades, various inversion techniques have been developed to solve diverse inverse scattering problems by overcoming the inherent ill-posedness and non-linearity. They can be classified as quantitative and qualitative methods depending on their purpose. The aim of quantitative methods is to recover the distribution of material parameters such as permittivity, permeability, and so on. On the other hand, the aim of qualitative methods is to provide information about the support of the inhomogeneities, i.e. shapes, locations and in case of multiple objects also their numbers.

First, the general approach for solving inverse scattering problems in quantitative methods is based on a iteration scheme, i.e., obtaining the solution which minimizes a discrete norm (generally, L^2-norm) between direct and adjoint scattering problem (cost functional): find u to minimize

$$\mathcal{E}(u) = \frac{1}{2}||\mathcal{F}u - \mathcal{M}||^2_{L^2}, \tag{1.1}$$

where $\mathcal{F}$ denotes the forward operator and $\mathcal{M}$ contains measurements data. For instance, the value of contrast χ is estimated by solving a nonlinear integral equation at each step of a distorted Born iterative method (Chew and Wang 1990; Remis and P. V. d. Berg 2000), and the induced current density J is additionally estimated by solving source-type integral equations at each step of a contrast source inversion method (P.M. Van Den Berg and Kleinman 1997; P. v. d. Berg, Broekhoven, and Abubakar 1999). We also refer to a level-set method (Dorn and Lesselier 2006; Dorn and Lesselier 2009), joint sparse recovery techniques (Zaimaga, Fraysse, and Lambert 2017; Yoo et al. 2017) and others (Caorsi, Massa, and Pastorino 2000; Nounouh et al. 2014; Voznyuk, Litman, and Tortel 2015;

Rubæk et al. 2007; X. Chen 2018). Unfortunately, for a successful application of such iteration schemes, one must consider the following matters:

1. large computation costs as in particular complex evaluation of the gradient (e.g. Fréchet or domain derivative) is required for each iteration step,
2. non-convergence and local minima issue, since (1.1) is not convex,
3. regularization as selection of appropriate regularization terms that are significantly dependent on the problem at hand is required,
4. prior information as estimation of *a priori* information of unknown inhomogeneities is needed to guarantee the convergence.

Second, the qualitative methods, which are known as non-iterative or one-step inversion techniques, avoid dealing with the problem in its full non-linearity and consider a simplified mathematical model with a lower computational cost (Bevacqua and Palmeri 2019). Furthermore, any *a priori* information of unknown inhomogeneities is not needed to apply. Because of such advantages, various techniques have been investigated and applied successfully to many inverse scattering problems. We introduce below some known techniques to discuss the pros and cons to give the motivation of current thesis.

MUSIC (MUltiple SIgnal Classification) The MUSIC algorithm is a well-known non-iterative technique for solving inverse scattering problems. Originally, it was used in signal processing problems for estimating individual frequencies of multiple time-harmonic signals. In (Devaney 2000), MUSIC is applied to identify location the point-like scatterers. According to (Cheney 2001), the main idea of MUSIC in inverse scattering problems is characterizing the range of a self-adjoint operator and noise subspace is orthogonal to the range. This means that a vector $\mathbf{f}(\mathbf{z})$ is in the range of self-adjoint operator $\mathbb{A}$ if and only if its projection onto the noise subspace is zero, i.e.,

$$\mathbf{f}(\mathbf{z}) \in \text{Range}(\mathbb{A}) \quad \text{if and only if} \quad |\underline{\mathbf{P}}\mathbf{f}(\mathbf{z})| = 0, \tag{1.2}$$

where $\underline{\mathbf{P}}$ is a projection onto the noise subspace. Based on this, the indicator function of MUSIC is defined as

$$\mathcal{I}_{\text{MUSIC}}(\mathbf{z}) = \frac{1}{|\underline{\mathbf{P}}\mathbf{f}(\mathbf{z})|}, \quad \mathbf{z} \in \Omega, \tag{1.3}$$

where Ω denotes the region of interest. Then, $\mathcal{I}_{\text{MUSIC}}(\mathbf{z}) = +\infty$ if the search point $\mathbf{z}$ is at the center of each inhomogeneity. MUSIC is applied to various inverse scattering problems such as detection of inhomogeneities buried in a half-space (Ammari, Iakovleva, and Lesselier 2005), 3D electromagnetic inhomogeneities (Ammari, Iakovleva, Lesselier, and Perrusson 2007), arbitrary shaped inhomogeneity (Hou, Solna, and Zhao 2006), internal corrosion (Ammari, H. Kang, et al. 2008), 3D enhanced resolution (X. Chen and Zhong 2008), crack-like defects (W.-K. Park and Lesselier 2009), eddy-current nondestructive evaluation (Henriksson, Lambert, and Lesselier 2011), radar imaging (Odendaal, Barnard, and Pistorius 1994), and virtual electrical breast biopsy (Scholz 2002). According to such investigations, it turned out that for a successful application of MUSIC, some conditions must be considered at early stage, for example, (i) total number of incident and corresponding observation directions must be large enough, and (ii) nonzero singular values to generate the projection operator $\underline{\mathbf{P}}$ must be chosen carefully. We also mention that MUSIC is not a suitable imaging technique for large volumetric inhomogeneities.

Linear sampling method (LSM) The concept of LSM was first investigated in (Colton and Kirsch 1996) for reconstructing arbitrary-shaped inhomogeneities in homogeneous and scalar wave fields. The main idea of LSM is to approximately solve the far-field integral equation for searching point $\mathbf{z} \in \Omega$:

$$(Fa_z)(\hat{\mathbf{x}}) = g_\infty(\hat{\mathbf{x}}). \tag{1.4}$$

Here, a far-field operator $F : L^2(\mathbb{S}^{d-1}) \to L^2(\mathbb{S}^{d-1})$ is defined by

$$(Fa_z)(\hat{\mathbf{x}}) := \int_{\mathbb{S}^{d-1}} u_\infty(\hat{\mathbf{x}}, \hat{\mathbf{d}}) a_z(\hat{\mathbf{d}}) dS(\hat{\mathbf{d}}), \ \hat{\mathbf{x}} \in \mathbb{S}^{d-1}, \tag{1.5}$$

where d denotes the dimension, and $g_\infty(\hat{\mathbf{x}})$ is the far-field pattern of the Green function. Recently, the feasibility and applicability of LSM have been mathematically validated in (Arens 2003). Rigorously, under proper assumptions, there exists an approximated solution $a_z^\varepsilon \in L^2(\Omega)$ of (1.4) satisfying $\lim_{\mathbf{z}\to\partial\Omega} \|a_z^\varepsilon\| = \infty$, i.e., the solution gives a characterization of the inhomogeneities. LSM is now applied to various inverse scattering problems, for example, isotropic medium problem (Cakoni, Colton, and Haddar 2002), 3D electromagnetic case (Haddar and Monk 2002; Colton, Haddar, and Monk 2002), imaging of crack with Dirichlet and mixed boundary conditions (Cakoni and Colton 2003), and limited aperture problem (Audibert and Haddar 2017). We also refer to (Aramini, Brignone, and Piana 2006) for LSM without sampling and (Audibert and Haddar 2014) for a generalized version of LSM. Throughout the results, it has been known that the LSM is an effective and stable technique. Notice that (1.4) must be solved very accurately in order to obtain a reliable result. This means that a sufficiently large number of incident and observation directions must be applied. Moreover, solving the linear integral equation (1.5) is ill-posed, so that selection of a proper regularization should be considered, refer to (Audibert and Haddar 2014; Arens and Lechleiter 2009).

Migration techniques Migration techniques (e.g., Kirchhoff, subspace, and reverse-time migration) are widely used in geophysical areas such as seismic inversion (Bleistein, Cohen, and John 2013) and ground penetrating radar (GPR) (Moran et al. 2000; X. Liu, Serhir, and Lambert 2018). Such techniques consist of back-propagating the complex conjugated incident and/or observation fields into the background medium to provide the imaging of inhomogeneities. They are applied to several interesting inverse scattering problems, for example, application of Kirchhoff migration without phase (Bardsley and Vasquez 2016) and GPR (X. Liu, Serhir, and Lambert 2018), subspace migration for imaging of cracks in full- and limited-view problem (W.-K. Park 2015), microwave imaging (W.-K. Park 2019a), and extended inhomogeneities (Ammari, Garnier, H. Kang, Lim, and Sølna 2012), reverse-time migrations for imaging of extended obstacles (J. Chen, Z. Chen, and Huang 2013a; J. Chen, Z. Chen, and Huang 2013b). We also refer to (Ammari, Garnier, H. Kang, W.-K. Park, et al. 2011) for further mathematical theory about Kirchhoff and subspace migrations. Similarly with MUSIC and LSM, a sufficiently large number of incident and observation directions must be applied to guarantee a good result, refer to (W.-K. Park 2016) as an example.

As we have seen, the total number of incident and observation directions must be large enough for a successful application of the qualitative methods. Therefore, it is natural to develop an alternative qualitative method with a small number of incident or observation directions.

1.3 Object of the thesis

The direct sampling method (DSM) is considered in various 2D and 3D inverse electromagnetic scattering problems in this thesis. On the contrary to the existing non-iterative methods (e.g. MUSIC, LSM and migration techniques), the DSM only needs a few incident fields for imaging the inhomogeneities. Furthermore, it is quite fast since it does not require any additional operation such as singular value decomposition or projection, and it is highly tolerant to noise. We refer to (Ito, Jin, and J. Zou 2012; Li and Z. Zou 2013) for 2D scalar problem and (Ito, Jin, and J. Zou 2013) for 3D vectorial case for detail. Note that it is also introduced in chapter 3 (2D case) and chapter 6 (3D case), respectively.

Since the development of DSM in (Ito, Jin, and J. Zou 2012), its feasibility and robustness for imaging of inhomogeneities have been validated in various scattering problems. For instance, the far-field measurement problem (Li and Z. Zou 2013), 3D electromagnetic case (Ito, Jin, and J. Zou 2013), imaging of crack (W.-K. Park 2018b), transverse electronic problem (W.-K. Park 2019b). We also refer to (Chow, Ito, and J. Zou 2014), (Chow, Ito, K. Liu, et al. 2015) and (Bektas and Ozdemir 2016) for applications of the DSM to electrical impedance tomography, diffusive optical tomography, and mono-static radar imaging, respectively. Unfortunately, the limitations of DSM cannot be explained through the results in such advanced works. For example:

1. the smallest inhomogeneity is hard to be identified if there are multiple inhomogeneities of different sizes in the region of interest, a similar phenomenon being observed in with different permittivities,

2. the imaging via DSM with mono-static data provides a miss-location of inhomogeneity,

3. multi-frequency DSM is not effective for imaging small multiple inhomogeneities,

4. the imaging performance is not significantly relevant to the total number of incident directions,

5. the inhomogeneities cannot be visualized by DSM in 3D case (vector scattered field) if the improper polarization of test function is used.

Thanks to the asymptotic formula of scattered field within the small obstacle hypothesis, the analytic representations of the DSM indicator function are presented in 2D and 3D full-aperture configurations, 2D restricted configurations (mono-static and limited-aperture configuration) with single- and multi-frequency. According to our theoretical results, we elucidate the theoretical reason of the limitations and design an alternative indicator function of DSM (DSMA) to overcome them. The mathematical structure of DSMA is also presented along a similar path of derivations as in traditional DSM case. Then, multi-frequency DSM (MDSM) is introduced for further improvement of imaging performance. On the contrary to the several investigations (Guzina, Cakoni, and Bellis 2010; Joh, Kwon, et al. 2013; Griesmaier and Schmiedecke 2017), the MDSM is effective only for imaging a small single inhomogeneity but is not effective for several small inhomogeneities. The reason of the limitation is investigated by mathematical analysis and multi-frequency DSMA (MDSMA) is designed to handle the problem. Finally, we extend our approach to 3D inverse electromagnetic scattering problems. The analytic representation formula of the indicator function of 3D DSM is presented by establishing the relationship of spherical Bessel functions with integer orders, the polarization of the incident wave and the test

dipole, and information about inhomogeneities. Thanks to our mathematical analysis, we verify the necessary condition for the choice of polarization of the test dipole and propose method to choose the proper polarization.

1.4 Organization of the thesis

Chapter 2 The well-known results about the 2D and 3D direct electromagnetic scattering problems in the presence of small dielectric inhomogeneities in a homogeneous medium are reviewed with our notations. Especially, we introduce the asymptotic formulas of scattered field and far-field pattern which play key roles in our mathematical analysis.

Chapter 3 We introduce the concepts of traditional DSM (in 2D near-field and full-view configuration) and analyze its structure within the framework of the asymptotic hypothesis. Thanks to this analytical expression, the limitation of the DSM is exhibited and illustrated. An improved DSM (DSMA) is proposed to overcome the intrinsic limitation. Then, we show that both DSM and DSMA are closely related to a normalized version of the Kirchhoff migration.

Chapter 4 The imaging of dielectric inhomogeneities via DSM in restricted configurations is studied. First, we apply the DSM to mono-static data and verify the reason of miss-localizations of the inhomogeneities by mathematical analysis. To overcome them, a modified version of indicator function is designed and its structure is identified. Next, the DSM and DSMA in limited-aperture configuration are considered. Through mathematical analysis, we establish the relationship of imaging performance and range of observation and/or incident directions.

Chapter 5 In this chapter, the multi-frequency DSM (MDSM) and DSMA (MDSMA) are investigated. According to our analysis, the reason of the limitation of MDSM is elucidated by establishing a correlation of imaging performance with the Bessel functions, Struve functions, Legendre polynomials, generalized hypergeometric function, the range of incident and/or observation directions, and the physical property of inhomogeneities. By adopting a exponential weighted function related to each frequency, we design the indicator function of MDSMA and examine its adequacy for imaging the inhomogeneities in a limited-aperture problem.

Chapter 6 This chapter presents the structure analysis of DSM in the 3D inverse electromagnetic scattering problems by showing the relationship of imaging performance and polarization of the test dipole. Based on our analysis, we suggest a way to choose a proper polarization of the test dipole for imaging the inhomogeneities. We also extend our approach to the far-field configuration case. Moreover, the 3D version of DSMA is proposed with some numerical simulations, its mathematical analysis being verified to show up its structure.

Chapter 7 The achieved works and their perspectives are summarized in this chapter.

2

Direct electromagnetic scattering problem and its asymptotic formula

Contents

It is worth mentioning that this chapter contributes the introduction of well-known and/or already derived results just with our notations.

2.1 Problem formulations of electromagnetic scattering problem

Throughout this thesis, we assume that scattered electromagnetic data are collected at the receivers $\mathbf{x} \in \Gamma_{\text{obs}}$ and generated by a dipole source $\mathbf{y} \in \Gamma_{\text{inc}}$, where Γ_{obs} and Γ_{inc} are simply connected surfaces (or curve) in $\mathbb{R}^d, d = 2, 3$. Furthermore, there is a finite number of inhomogeneities in the homogeneous and isotropic region of interest (ROI) Ω where each inhomogeneity is denoted by

$$\tau_m = \mathbf{r}_m + \alpha_m \mathbf{D}_m \in \mathbb{R}^d, \ d = 2, 3. \tag{2.1}$$

Here, $\mathbf{r}_m$ is the center, α_m is the size, and $\mathbf{D}_m$ characterizes the shape of τ_m. Let us denote τ be the collection of τ_m, i.e., $\tau = \bigcup_m \tau_m$. We also assume that all inhomogeneities are well-separated to ignore the interaction between them, i.e., there exists a positive constant d_0 such that

$$0 < d_0 < |\mathbf{r}_m - \mathbf{r}_{m'}| \quad \text{and} \quad \tau_m \cap \tau_{m'} = \emptyset, \quad m \neq m' \tag{2.2}$$

Let ε_m and μ_m be the electric permittivity and magnetic permeability of τ_m, respectively. The ε_0 and μ_0 are analogously defined in the embedding medium. For the sake of simplicity, we assume that all inhomogeneities are non-magnetic ($\mu_m = \mu_0$) so it is characterized by its electric permittivity at

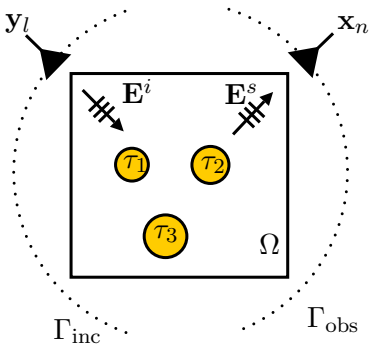

(a) Configuration

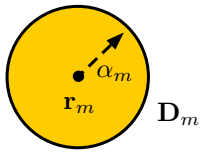

(b) Circular inhomogeneity τ_m

Figure 2.1: Configuration of the scattering problem for $M = 3$ (left) and sketch of the circular inhomogeneities τ_m (right).

angular frequency $\omega_0 = 2\pi f_0$ where f_0 is the considered frequency in Hz. Now, we can define the piece-wise constant electric permittivity ε and wavenumber k such that

$$\varepsilon(\mathbf{x}) = \begin{cases} \varepsilon_0, \text{ if } \mathbf{x} \in \mathbb{R}^d \backslash \tau, \\ \varepsilon_m, \text{ if } \mathbf{x} \in \tau, \end{cases} \quad \text{and} \quad k(\mathbf{x}) = \begin{cases} k_0 = \omega_0 \sqrt{\varepsilon_0 \mu_0}, \text{ if } \mathbf{x} \in \mathbb{R}^d \backslash \tau, \\ k_m = \omega_0 \sqrt{\varepsilon_m \mu_0}, \text{ if } \mathbf{x} \in \tau. \end{cases} \tag{2.3}$$

Then, the time-harmonic total electromagnetic fields (with $\mathrm{e}^{-\mathrm{i}\omega t}$ time convention) satisfy the following Maxwell's equations:

$$\begin{cases} \nabla \times \mathbf{E} = \mathrm{i}\omega\mu_0 \mathbf{H}, \\ \nabla \times \mathbf{H} = -\mathrm{i}\omega\varepsilon \mathbf{E} + \mathbf{J}, \\ \nu \times \mathbf{E} \text{ and } \nu \times \mathbf{H} \text{ are continuous across } \partial\tau_m, \\ \nu \cdot (\varepsilon \mathbf{E})^+ = \nu \cdot (\varepsilon \mathbf{E})^- \text{ on } \partial\tau_m, \\ \nu \cdot (\mu_0 \mathbf{H})^+ = \nu \cdot (\mu_0 \mathbf{H})^- \text{ on } \partial\tau_m, \end{cases} \tag{2.4}$$

where $\mathbf{J}$ is the point electrical current density, and ν is the outward unit normal to τ_m. Here, the scripts $+$ and $-$ indicate the limiting direction from outside τ_m and inside τ_m, respectively. Since the embedding medium is homogeneous and isotropic, we have

$$\nabla \times \nabla \times \mathbf{E} - k^2 \mathbf{E} = \mathrm{i}\omega_0 \mu_0 \mathbf{J} \tag{2.5}$$

Due to the vector identity $\nabla \times \nabla \times \mathbf{E} = \nabla(\nabla \cdot \mathbf{E}) - \nabla^2 \mathbf{E}$ and the fact that $\nabla \cdot \mathbf{E} = 0$, the electric total field satisfies the following vector Helmholtz equation:

$$\nabla^2 \mathbf{E} + k^2 \mathbf{E} = \mathrm{i}\omega_0 \mu_0 \mathbf{J}. \tag{2.6}$$

2.2 2D direct scattering problem

Generally, the electromagnetic scattering problem is a 3D problem, i.e., the scattered field is a vector. The 2D problem is a special case of 3D such as all parameters are invariant in one direction. We assume that the direction is $(0, 0, 1)$, which is the standard basis in the z-axis. Here, we focus only on 2D transverse magnetic (TM) case, i.e., $\mathbf{E}_z \neq 0$ and $\mathbf{H}_z = 0$.

Let us denote the z-component of total, incident, and scattered field as u, u^i, and u^s, respectively. We consider the following plane-wave illumination: let $u^i(\mathbf{x}, \hat{\mathbf{d}}; k_0) = \mathrm{e}^{\mathrm{i}k_0\hat{\mathbf{d}}\cdot\mathbf{x}}$ be the incident field with propagation direction $\hat{\mathbf{d}} \in \mathbb{S}^1$, where $\mathbb{S}^1$ denotes the two-dimensional unit circle. Then, TM polarized total electric field $\mathbf{E}_z(\mathbf{x}, \hat{\mathbf{d}}; k_0) = u(\mathbf{x}, \hat{\mathbf{d}}; k_0)$ satisfies the following Helmholtz equation:

$$\nabla^2 u(\mathbf{x}, \hat{\mathbf{d}}; k_0) + k^2(\mathbf{x}) u(\mathbf{x}, \hat{\mathbf{d}}; k_0) = \mathrm{i}\omega_0\mu_0 J \tag{2.7}$$

with appropriate transmission conditions on the boundary of τ_m where $J = \mathbf{J}_z$. The total field $u(\mathbf{x}, \hat{\mathbf{d}}; k_0)$ can be decomposed into incident field $u^i(\mathbf{x}, \hat{\mathbf{d}}; k_0)$ and scattered field $u^s(\mathbf{x}, \hat{\mathbf{d}}; k_0)$ such as $u(\mathbf{x}, \hat{\mathbf{d}}; k_0) = u^i(\mathbf{x}, \hat{\mathbf{d}}; k_0) + u^s(\mathbf{x}, \hat{\mathbf{d}}; k_0)$. In order to guarantee the uniqueness of solution, the scattered field satisfies Sommerfeld radiation condition

$$\lim_{|\mathbf{x}|\to\infty} \left(\frac{\partial u^s(\mathbf{x}, \hat{\mathbf{d}}; k_0)}{\partial \mathbf{x}} - \mathrm{i}k_0 u^s(\mathbf{x}, \hat{\mathbf{d}}; k_0) \right) = 0 \tag{2.8}$$

uniformly in all directions $\hat{\mathbf{x}} = \mathbf{x}/|\mathbf{x}| \in \mathbb{S}^1$. It is well known that the scattered field $u^s(\mathbf{x}, \hat{\mathbf{d}}; k_0)$ can be expressed by the following single-layer potential

$$u^s(\mathbf{x}, \hat{\mathbf{d}}; k_0) = \sum_{m=1}^{M} \int_{\tau_m} g(\mathbf{x}, \mathbf{x}') \varphi_m(\mathbf{x}', \hat{\mathbf{d}}) \mathrm{d}\mathbf{x}' \tag{2.9}$$

with unknown density $\varphi_m(\mathbf{x}', \hat{\mathbf{d}})$. Here, $g(\mathbf{x}, \mathbf{y})$ is the Green function of homogeneous Helmholtz equation such as

$$g(\mathbf{x}, \mathbf{y}) = \frac{\mathrm{i}}{4} \mathrm{H}_0^1(k_0|\mathbf{x} - \mathbf{x}'|) = \frac{\mathrm{i}}{4} \left(\mathrm{J}_0(k_0|\mathbf{x} - \mathbf{x}'|) + \mathrm{i}\mathrm{Y}_0(k_0|\mathbf{x} - \mathbf{x}'|) \right), \tag{2.10}$$

where J_0 and Y_0 are the zeroth-order Bessel and Neumann function, respectively. We refer to (Colton and Kress 1998; Ammari and H. Kang 2004; X. Chen 2018) for details. But it is not enough to analyze the structure of numerical simulations due to the unknown density $\varphi_m(\mathbf{x}', \hat{\mathbf{d}})$. Hence, we introduce the following asymptotic formula of the scattered field explained in (Ammari and H. Kang 2004), which holds under the small volume assumption of inhomogeneities to neglect their interaction.

Lemma 2.2.1 *Assume that τ_m are well separated from each other and that $\alpha_m \sqrt{\varepsilon_m/\varepsilon_0} \ll 0.5\lambda_0$, then, $u^s(\mathbf{x}, \hat{\mathbf{d}}; k_0)$ can be represented by the following asymptotic expansion:*

$$u^s(\mathbf{x}, \hat{\mathbf{d}}; k_0) = \frac{k_0^2(1+\mathrm{i})}{4\sqrt{k_0\pi}} \sum_{m=1}^{M} \alpha_m^2 \left(\frac{\varepsilon_m - \varepsilon_0}{\sqrt{\varepsilon_0\mu_0}} \right) |\mathbf{D}_m| g(\mathbf{x}, \mathbf{r}_m) \mathrm{e}^{\mathrm{i}k_0\mathbf{r}_m\cdot\hat{\mathbf{d}}} + O\left(\alpha^3\right), \tag{2.11}$$

where $|\mathbf{D}_m|$ denotes the area of $\mathbf{D}_m$ and $\alpha := \max\{\alpha_m,\ m = 1, 2\cdots, M\}$.

If the receivers or transmitters are located far from the region of interest, the directions of incidence or observation can be used for imaging. Let us denote the directions of receivers as $\hat{\mathbf{x}} = \mathbf{x}/|\mathbf{x}| \in \mathbb{S}^1$. Then, the following far-field approximation holds in $\mathbb{R}^2$:

$$g(\mathbf{x}, \hat{\mathbf{d}}) = \frac{\mathrm{e}^{\mathrm{i}(k_0\mathbf{x} + \pi/4)}}{\sqrt{8\pi k_0|\mathbf{x}|}} \mathrm{e}^{-\mathrm{i}k_0\hat{\mathbf{x}}\cdot\hat{\mathbf{d}}} + O\left(\frac{1}{\mathbf{x}^2}\right) = \frac{\mathrm{e}^{\mathrm{i}k_0\mathbf{x}}}{\sqrt{|\mathbf{x}|}} \left\{ \frac{\mathrm{e}^{\mathrm{i}\pi/4}}{\sqrt{8\pi k_0}} \mathrm{e}^{-\mathrm{i}k_0\hat{\mathbf{x}}\cdot\hat{\mathbf{d}}} \right\} + O\left(\frac{1}{\mathbf{x}^2}\right), \tag{2.12}$$

and

$$u^s(\mathbf{x}, \hat{\mathbf{d}}; k_0) = \frac{\mathrm{e}^{\mathrm{i}k_0\mathbf{x}}}{\sqrt{|\mathbf{x}|}} \left\{ u_\infty(\hat{\mathbf{x}}, \hat{\mathbf{d}}; k_0) + O\left(\frac{1}{|\mathbf{x}|}\right) \right\}, \tag{2.13}$$

uniformly into all directions $\hat{\mathbf{x}}$ and $|\mathbf{x}| \to \infty$ where the function u_∞ is called the far-field pattern of u^s. The combination with (2.9) leads to the integral representation

$$u_\infty(\hat{\mathbf{x}}, \hat{\mathbf{d}}; k_0) = \frac{\mathrm{e}^{\mathrm{i}\pi/4}}{\sqrt{8\pi k_0}} \int_\Omega \mathrm{e}^{-\mathrm{i}k_0 \hat{\mathbf{x}}\cdot\mathbf{x}'} \varphi(\mathbf{x}') \mathrm{d}\mathbf{x}', \tag{2.14}$$

and the following asymptotic formula can be derived.

Lemma 2.2.2 (Far-field hypothesis) *Assume that τ_m are well separated from each other and that $\alpha_m \sqrt{\varepsilon_m/\varepsilon_0} \ll 0.5\lambda_0$, then, $u_\infty(\hat{\mathbf{x}}, \hat{\mathbf{d}}; k_0)$ can be represented by the following asymptotic expansion:*

$$u_\infty(\hat{\mathbf{x}}, \hat{\mathbf{d}}; k_0) = \frac{k_0^2(1+\mathrm{i})}{4\sqrt{k_0\pi}} \sum_{m=1}^{M} \alpha_m^2 \left(\frac{\varepsilon_m - \varepsilon_0}{\sqrt{\varepsilon_0\mu_0}}\right) |\mathbf{D}_m| \mathrm{e}^{\mathrm{i}k_0 \mathbf{r}_m \cdot (\hat{\mathbf{d}} - \hat{\mathbf{x}})} + O\left(\alpha^3\right). \tag{2.15}$$

See again (Ammari and H. Kang 2004) for the details.

2.3 3D direct scattering problem

Let $\mathbf{E}(\mathbf{x}, \mathbf{y}; k_0)$ be the time-harmonic total electric field in the presence of set of inhomogeneities τ. Then it is the solution of Maxwell's equations (2.5):

$$\begin{cases} \nabla \times \nabla \times \mathbf{E}(\mathbf{x}, \mathbf{y}; k_0) - k^2(\mathbf{x}) \mathbf{E}(\mathbf{x}, \mathbf{y}; k_0) = \mathrm{i}\omega_0\mu_0 \mathbf{J}(\mathbf{x}, \mathbf{y}; k_0) \\ \nu \cdot (\varepsilon \mathbf{E}(\mathbf{x}, \mathbf{y}; k_0))^+ - \nu \cdot (\varepsilon \mathbf{E}(\mathbf{x}, \mathbf{y}; k_0))^- = 0 \quad \text{on } \partial\tau, \end{cases} \tag{2.16}$$

where ν is the outward unit normal to τ_m. Here, the scripts $+$ and $-$ indicate the limiting direction from outside τ_m and from inside τ_m, respectively. The total electric field can be expressed as the sum of the incident and scattered electric fields, i.e., $\mathbf{E}(\mathbf{x}, \mathbf{y}; k_0) = \mathbf{E}^i(\mathbf{x}, \mathbf{y}; k_0) + \mathbf{E}^s(\mathbf{x}, \mathbf{y}; k_0)$. Let us assume that the incoming field $\mathbf{E}^i(\mathbf{x}, \mathbf{y}; k_0)$ is generated by an electric dipole source located at $\mathbf{y} \in \Gamma_{\text{inc}}$, polarized $\hat{\mathbf{p}}^t \in \mathbb{S}^2$, and with current density $\mathbf{J}_0(\mathbf{x}, \mathbf{y}) = \hat{\mathbf{p}}^t Il\delta(\mathbf{x} - \mathbf{y})$, i.e.,

$$\mathbf{E}^i(\mathbf{x}, \mathbf{y}; k_0) = \mathrm{i}\omega\mu_0 Il \underline{\mathbf{G}}(\mathbf{x}, \mathbf{y}) \cdot \hat{\mathbf{p}}^t. \tag{2.17}$$

Here, the constant Il is the current moment and $\underline{\mathbf{G}}(\mathbf{x}, \mathbf{y})$ is the dyadic Green function of time-harmonic Maxwell equations (2.5). Namely, the latter is the solution of

$$\nabla \times \nabla \times \underline{\mathbf{G}}(\mathbf{x}, \mathbf{y}) - k_0^2 \underline{\mathbf{G}}(\mathbf{x}, \mathbf{y}) = \delta(\mathbf{x} - \mathbf{y}) \mathbf{I_3}, \tag{2.18}$$

and has the matrix form of

$$\underline{\mathbf{G}}(\mathbf{x}, \mathbf{y}) := \left(\underline{\mathbf{I}}_3 + \frac{1}{k_0^2} \nabla\nabla\right) g(\mathbf{x}, \mathbf{y}) \tag{2.19}$$

where $\underline{\mathbf{I}}_3$ is the 3×3 identity matrix and $g(\mathbf{x}, \mathbf{y})$ is the Green function of three-dimensional Helmholtz equation, i.e.,

$$g(\mathbf{x}, \mathbf{y}) = \frac{\mathrm{e}^{\mathrm{i}k_0|\mathbf{x}-\mathbf{y}|}}{4\pi|\mathbf{x} - \mathbf{y}|}. \tag{2.20}$$

in order to guarantee the uniqueness of solution, the scattered electric field satisfies following the Silver-Müller radiation condition:

$$\lim_{|\mathbf{x}|\to\infty} |\mathbf{x}| \left[\nabla \times \mathbf{E}^s(\mathbf{x}, \mathbf{y}; k_0) \times \hat{\mathbf{x}} - \mathrm{i}k_0 \mathbf{E}^s(\mathbf{x}, \mathbf{y}; k_0)\right] = 0, \tag{2.21}$$

uniformly in all directions $\hat{\mathbf{x}} = \mathbf{x}/|\mathbf{x}| \in \mathbb{S}^2$.

Lemma 2.3.1 *Assume that all inhomogeneities are dielectric and sufficiently small ($\alpha_m\sqrt{\varepsilon_m/\varepsilon_0} \ll \lambda/2$). Then the electric scattered field $\mathbf{E}^s(\mathbf{x},\mathbf{y})$ has the following asymptotic formula for a generic incident field $\mathbf{E}^i(\mathbf{r}_m,\mathbf{y};k_0)$*

$$\mathbf{E}^s(\mathbf{x},\mathbf{y};k_0) = \omega_0^2\mu_0 \sum_{m=1}^{M} \left[\alpha_m^3\,(\varepsilon_m-\varepsilon_0)\,\underline{\mathbf{G}}(\mathbf{x},\mathbf{r}_m)\cdot\underline{\mathbf{M}}\left(\frac{\varepsilon_m}{\varepsilon_0};\mathbf{D}_m\right)\mathbf{E}^i(\mathbf{r}_m,\mathbf{y};k_0)\right] + O(\alpha^4) \tag{2.22}$$

where $\alpha := \max\{\alpha_m,\ m=1,2\cdots,M\}$ and $\underline{\mathbf{M}}(\varepsilon_m/\varepsilon_0;\mathbf{D}_m)\in\mathbb{C}^{3\times3}$ is a polarization tensor related to $\mathbf{D}_m$. By combining (2.17) and (2.22) the electric scattered field $\mathbf{E}^s(\mathbf{x},\mathbf{y};k_0)$ in the case of an incident field due to a dipole with a polarization direction $\hat{\mathbf{p}}^t$ placed in $\mathbf{y}$ is given by

$$\mathbf{E}^s(\mathbf{x},\mathbf{y};k_0) = C\sum_{m=1}^{M}\left[\alpha_m^3\left(\frac{\varepsilon_m-\varepsilon_0}{\varepsilon_0}\right)\underline{\mathbf{G}}(\mathbf{x},\mathbf{r}_m)\cdot\underline{\mathbf{M}}\left(\frac{\varepsilon_m}{\varepsilon_0};\mathbf{D}_m\right)(\underline{\mathbf{G}}(\mathbf{r}_m,\mathbf{y})\cdot\hat{\mathbf{p}}^t)\right] + O(\alpha^4), \tag{2.23}$$

with $C = \mathrm{i}\omega_0\mu_0k_0^2Il$.

In (Ammari, Iakovleva, Lesselier, and Perrusson 2007; Griesmaier 2011; Ammari, Garnier, H. Kang, Lim, and Yu 2014), the explicit form of $\underline{\mathbf{M}}(\varepsilon_m/\varepsilon_0;\mathbf{D}_m)$ for various forms such as sphere, thin tube, or sheet, is provided. For the sake of simplicity, we assume that all inhomogeneities are the spheres, so $\underline{\mathbf{M}}(\varepsilon_m/\varepsilon_0;\mathbf{D}_m)$ then has the following form

$$\underline{\mathbf{M}}\left(\frac{\varepsilon_m}{\varepsilon_0};\mathbf{D}_m\right) = \frac{3\varepsilon_0}{2\varepsilon_0+\varepsilon_m}|\mathbf{D}_m|\underline{\mathbf{I}}_3, \tag{2.24}$$

and the remainder of either (2.22) or (2.23) becomes $O(\alpha^5)$ as shown in (Ammari and Volkov 2003). So the field scattered by M small spheres illuminated by a single dipole under the asymptotic hypothesis in near field is given by

$$\mathbf{E}^s(\mathbf{x},\mathbf{y};k_0) = \mathrm{i}\omega_0\mu_0k_0^2Il\sum_{m=1}^{M}\alpha_m^3\frac{3(\varepsilon_m-\varepsilon_0)}{2\varepsilon_0+\varepsilon_m}\,|\mathbf{D}_m|\,\underline{\mathbf{G}}(\mathbf{x},\mathbf{r}_m)\cdot(\underline{\mathbf{G}}(\mathbf{y},\mathbf{r}_m)\cdot\hat{\mathbf{p}}^t) + O(\alpha^5) \tag{2.25}$$

Similar to the 2D case, the following far-field approximation also holds:

$$g(\mathbf{x},\mathbf{y}) = \frac{\mathrm{e}^{\mathrm{i}k_0\mathbf{x}}}{4\pi\mathbf{x}}\mathrm{e}^{-\mathrm{i}k_0\hat{\mathbf{x}}\cdot\mathbf{y}} + O\left(\frac{1}{\mathbf{x}^2}\right) \tag{2.26}$$

and

$$\underline{\mathbf{G}}(\mathbf{x},\mathbf{y}) = \frac{\mathrm{e}^{\mathrm{i}k_0\mathbf{x}}}{4\pi\mathbf{x}}\mathrm{e}^{-\mathrm{i}k_0\hat{\mathbf{x}}\cdot\mathbf{y}}\Delta(\hat{\mathbf{x}}) + O\left(\frac{1}{\mathbf{x}^2}\right), \tag{2.27}$$

where $\Delta(\hat{\mathbf{x}}) = \underline{\mathbf{I}}_3 - \hat{\mathbf{x}}\otimes\hat{\mathbf{x}}$. Then the far-field pattern of $\underline{\mathbf{G}}(\mathbf{x},\mathbf{y})$ is given by

$$\underline{\mathbf{G}}_\infty(\hat{\mathbf{x}},\mathbf{y}) := \mathrm{e}^{-\mathrm{i}k_0\hat{\mathbf{x}}\cdot\mathbf{y}}\Delta(\hat{\mathbf{x}}). \tag{2.28}$$

Since $\Delta(\hat{\mathbf{y}})\hat{\mathbf{p}} = -\hat{\mathbf{y}}\times(\hat{\mathbf{y}}\times\hat{\mathbf{p}})$, the incident plane wave can be expressed as

$$\mathbf{E}^i_\infty(\mathbf{x},\hat{\mathbf{y}};k_0) := \mathrm{i}\omega_0\mu_0Il\mathrm{e}^{-\mathrm{i}k_0\hat{\mathbf{y}}\cdot\mathbf{x}}\Delta(\hat{\mathbf{y}})\cdot\hat{\mathbf{p}}^t = \mathrm{i}\omega_0\mu_0Il\underline{\mathbf{G}}_\infty(\mathbf{x},\hat{\mathbf{y}})\cdot\hat{\mathbf{p}}^t, \tag{2.29}$$

where $\hat{\mathbf{y}}$ is the source direction and $\hat{\mathbf{p}}^t$ is its polarization on $\mathbb{S}^2$. Hence, the total electric field $\mathbf{E}^s(\mathbf{x},\hat{\mathbf{y}})$ has the far-field pattern $\mathbf{E}_\infty(\hat{\mathbf{x}},\hat{\mathbf{y}})$ such that

$$\mathbf{E}^s(\mathbf{x},\hat{\mathbf{y}};k_0) = \frac{\mathrm{e}^{\mathrm{i}k_0\mathbf{x}}}{4\pi\mathbf{x}}\mathbf{E}_\infty(\hat{\mathbf{x}},\hat{\mathbf{y}}) + O\left(\frac{1}{\mathbf{x}^2}\right), \tag{2.30}$$

uniformly into all directions $\hat{\mathbf{x}} = \mathbf{x}/|\mathbf{x}| \in \mathbb{S}^2$ as $|\mathbf{x}| \to \infty$.

Following the same path than with the near-field formulation, $\mathbf{E}_\infty(\hat{\mathbf{x}}, \hat{\mathbf{y}}; k_0)$ has the following asymptotic formula.

Lemma 2.3.2 (Far-field hypothesis) *Assume that all inhomogeneities are dielectric and sufficiently small ($\alpha_m \sqrt{\varepsilon_m/\varepsilon_0} \ll 0.5\lambda_0$). Then $\mathbf{E}_\infty(\hat{\mathbf{x}}, \hat{\mathbf{y}}; k_0)$ has the following asymptotic formula:*

$$\mathbf{E}_\infty(\hat{\mathbf{x}}, \hat{\mathbf{y}}; k_0) = \omega_0^2 \mu_0 \sum_{m=1}^{M} \alpha_m^3 (\varepsilon_m - \varepsilon_0) \underline{\mathbf{G}}_\infty(\hat{\mathbf{x}}, \mathbf{r}_m) \cdot \underline{\mathbf{M}} \left(\frac{\varepsilon_m}{\varepsilon_0}; \mathbf{D}_m \right) \mathbf{E}_\infty^i(\mathbf{r}_m, \hat{\mathbf{y}}; k_0) + O(\alpha^4) \tag{2.31}$$

where $\alpha := \max\{\alpha_m,\ m = 1, 2 \cdots, M\}$ for a generic incident field $\mathbf{E}_\infty^i(\mathbf{r}_m, \hat{\mathbf{y}}; k_0)$. Let introduce (2.28) and (2.29) in (2.31). Then, the field scattered by M spherical inhomogeneities can be expressed as

$$\mathbf{E}_\infty(\hat{\mathbf{x}}, \hat{\mathbf{y}}; k_0) = \mathrm{i}\omega_0 \mu_0 k_0^2 Il \sum_{m=1}^{M} A_m \mathrm{e}^{-\mathrm{i}k_0(\hat{\mathbf{x}}+\hat{\mathbf{y}})\cdot \mathbf{r}_m} \Delta(\hat{\mathbf{x}}_n) \cdot \hat{\mathbf{p}}^t + O(\alpha^5), \tag{2.32}$$

for an incident plane wave of impinging direction $\hat{\mathbf{y}}$ and polarization $\hat{\mathbf{p}}^t$. Here, A_m is given in (2.25)

2.4 Conclusion

In this chapter, the direct electromagnetic scattering problem has been reviewed under the small volume assumption of the well-separated inhomogeneities to neglect interactions between them. In particular, we have introduced the asymptotic formula of scattered field with respect to near and far measurement configuration. Because it will play a key role in our analysis of behavior of DSM indicator function in each cases. The structure analysis of DSM under the various conditions will be derived using the formulas presented in this chapter and validated via the numerical simulations with the synthetic and experimental data in the next chapters.

3

2D imaging of dielectric inhomogeneities with full-view and near-field data

Contents

3.1 Introduction

In the present chapter, we analyze the structure of DSM in time-harmonic 2D inverse electromagnetic scattering problem in the TM-mode. According to (Ito, Jin, and J. Zou 2012; Li and Z. Zou 2013; Ito, Jin, and J. Zou 2013), DSM is fast and stable because it does not require any additional operation such as singular-value decomposition (subspace migration), generating a projection operator onto the noise space (MUSIC algorithm), solving ill-posed integral equations (linear sampling method) or adjoint problems (topological derivatives), and is robust with respect to the random noise. However, DSM might fail to identify an inhomogeneity that is much smaller than the others or whose permittivity is much lower. This behavior can be explained in the framework of scattering asymptotic theory of small inhomogeneities which, to our best knowledge, has not been done yet.

With the help of the expression of the scattered field obtained using the already mentioned asymptotic theory in section 2.2, the indicator function of DSM is expressed as a function of the number, the

sizes and the permittivities of the inhomogeneities and the Bessel function of order zero. Thanks to this analysis, the reasons of the limitations of the original DSM are exhibited and an improved version is proposed. Then, we show that the original DSM and its alternative version are strongly connected with a normalized version of the Kirchhoff migration, which is one of the most popular technique in geophysical imaging such as seismic inversion (Bleistein, Cohen, and John 2013) and ground penetrating radar (GPR) imaging (Moran et al. 2000; X. Liu, Serhir, and Lambert 2018), etc. The mathematical and statistical methods for multi-static imaging are described from a mathematical point of view in (Ammari. et al. 2013) (including, among others methods, Kirchhoff migration, back-propagation and MUSIC algorithms and theirs relations).

3.2 Introduction of the direct sampling method

To analyze the structure of DSM, we firstly investigate the notion of DSM in this section. According to (Ito, Jin, and J. Zou 2012), the indicator function of DSM is defined as follows.

Single impinging direction For each sampling point $\mathbf{z} \in \Omega$ and fixed impinging direction $\hat{\mathbf{d}} \in \mathbb{S}^1$, the DSM indicator function with fixed frequency (corresponding wavenumber k_0) is defined by

$$\mathcal{I}_{\mathrm{DSM}}(\mathbf{z}, \hat{\mathbf{d}}; k_0) := \frac{\left| \left\langle u^s(\mathbf{x}, \hat{\mathbf{d}}; k_0), g(\mathbf{x}, \mathbf{z}) \right\rangle_{L^2(\Gamma_{\mathrm{obs}})} \right|}{\left\| u^s(\mathbf{x}, \hat{\mathbf{d}}; k_0) \right\|_{L^2(\Gamma_{\mathrm{obs}})} \| g(\mathbf{x}, \mathbf{z}) \|_{L^2(\Gamma_{\mathrm{obs}})}}, \tag{3.1}$$

where $g(\mathbf{x}, \mathbf{z})$ is the 2D Green function of Helmholtz equation given by (2.10) and the L^2-inner product $\langle \cdot, \cdot \rangle_{L^2(\Gamma_{\mathrm{obs}})}$ is defined by (A.2).

Multiple impinging directions For incident directions $\hat{\mathbf{d}}_l \in \mathbb{S}^1,\ l = 1, 2, \cdots, L$, the indicator function is given by

$$\mathcal{I}_{\mathrm{DSM}}(\mathbf{z}; k_0) := \max \left\{ \mathcal{I}_{\mathrm{DSM}}(\mathbf{z}; \hat{\mathbf{d}}_l, k_0); l = 1, 2, \cdots, L, \mathbf{z} \in \Omega \right\}, \tag{3.2}$$

where $\mathcal{I}_{\mathrm{DSM}}(\mathbf{z}; \hat{\mathbf{d}}_l, k_0)$ is the indicator function for the incident direction $\hat{\mathbf{d}}_l$. Note that (3.2) also works if $L = 1$ and provides the same result as (3.1).

The definition (3.1) comes from the following relationships: (i) the integral representation of the scattered field (2.9) can be expressed as

$$u^s(\mathbf{x}, \hat{\mathbf{d}}; k_0) \approx \sum_{m=1}^{M} W_m(\hat{\mathbf{d}}, \mathbf{r}_m) g(\mathbf{x}, \mathbf{r}_m), \tag{3.3}$$

where $W_m(\hat{\mathbf{d}}, \mathbf{r}_m)$ denotes the weight function corresponding to τ_m, (ii) the following approximation derived in (Ito, Jin, and J. Zou 2012, (8)) holds:

$$\int_{\Gamma_{\mathrm{obs}}} g(\mathbf{x}, \mathbf{z}_1) \overline{g(\mathbf{x}, \mathbf{z}_2)} \mathrm{d}S(\mathbf{x}) \approx \frac{1}{k_0} \mathrm{Im}(g(\mathbf{z}_1, \mathbf{z}_2)). \tag{3.4}$$

The combination with (3.3) and (3.4) leads to

$$\begin{aligned}\left\langle u^s(\mathbf{x},\hat{\mathbf{d}};k_0), g(\mathbf{x},\mathbf{z})\right\rangle_{L^2(\Gamma_{\text{obs}})} &\approx \frac{1}{k_0}\sum_{m=1}^{M} W_m(\hat{\mathbf{d}},\mathbf{r}_m)\text{Im}\left(g(\mathbf{r}_m,\mathbf{z})\right)\\ &\approx \frac{\mathrm{i}}{4k_0}\sum_{m=1}^{M} W_m(\hat{\mathbf{d}},\mathbf{r}_m)\mathrm{J}_0(k_0|\mathbf{r}_m-\mathbf{z}|)\end{aligned} \tag{3.5}$$

and thanks to the Hölder's inequality, we have

$$\mathcal{I}_{\text{DSM}}(\mathbf{z},\hat{\mathbf{d}};k_0) = \frac{\left|\left\langle u^s(\mathbf{x},\hat{\mathbf{d}};k_0), g(\mathbf{x},\mathbf{z})\right\rangle_{L^2(\Gamma_{\text{obs}})}\right|}{\left\|u^s(\mathbf{x},\hat{\mathbf{d}};k_0)\right\|_{L^2(\Gamma_{\text{obs}})}\left\|g(\mathbf{x},\mathbf{z})\right\|_{L^2(\Gamma_{\text{obs}})}} = \frac{\left|\sum_{m=1}^{M} W_m(\hat{\mathbf{d}},\mathbf{r}_m)\mathrm{J}_0(k_0|\mathbf{r}_m-\mathbf{z}|)\right|}{\max\left|\sum_{m=1}^{M} W_m(\hat{\mathbf{d}},\mathbf{r}_m)\mathrm{J}_0(k_0|\mathbf{r}_m-\mathbf{z}|)\right|}. \tag{3.6}$$

Hence, if a point $\mathbf{z}$ is in the support of one of the inhomogeneities (i.e., $\mathbf{z}\approx\mathbf{r}_m\in\tau$) then $\mathcal{I}_{\text{DSM}}(\mathbf{z},\hat{\mathbf{d}};k_0)\approx 1$; otherwise, if $\mathbf{z}\notin\tau$ then $\mathcal{I}_{\text{DSM}}(\mathbf{z},\hat{\mathbf{d}};k_0)\not\approx 1$ which allows the localization $\mathbf{r}_m$ of τ_m via the map of $\mathcal{I}_{\text{DSM}}(\mathbf{z},\hat{\mathbf{d}};k_0)$. The details of such evaluations can be found in (Ito, Jin, and J. Zou 2012).

3.3 Structure analysis of the direct sampling method and alternative direct sampling method

3.3.1 Analysis of the direct sampling method in the asymptotic hypothesis

Thanks to the asymptotic formula of the scattered field introduced in Lemma 2.2.1, the following analysis can be derived under the small volume assumption of inhomogeneities.

Theorem 3.3.1 *Assume that the total number N of measurement points is sufficiently large. Then, for fixed incident direction $\hat{\mathbf{d}}$, $\mathcal{I}_{\text{DSM}}(\mathbf{x},\hat{\mathbf{d}};k_0)$ can be represented as*

$$\mathcal{I}_{\text{DSM}}(\mathbf{z},\hat{\mathbf{d}};k_0) = \frac{|\Psi_1(\mathbf{z},\hat{\mathbf{d}};k_0)|}{\max_{\mathbf{z}\in\Omega}|\Psi_1(\mathbf{z},\hat{\mathbf{d}};k_0)|},\ \textit{where}\ \Psi_1(\mathbf{z},\hat{\mathbf{d}};k_0) = \sum_{m=1}^{M}\mathcal{A}_m \mathrm{e}^{\mathrm{i}k_0\hat{\mathbf{d}}\cdot\mathbf{r}_m}\mathrm{J}_0(k_0|\mathbf{z}-\mathbf{r}_m|). \tag{3.7}$$

Here, $\mathcal{A}_m = \alpha_m^2(\varepsilon_m-\varepsilon_0)|\mathbf{D}_m|$.

Proof Combining (2.11) and (3.4) leads to

$$\begin{aligned}&\left\langle u^s(\mathbf{x},\hat{\mathbf{d}};k_0), g(\mathbf{z},\mathbf{x})\right\rangle_{L^2(\Gamma_{\text{obs}})}\\ &\quad= \sum_{n=1}^{N} u^s(\mathbf{x}_n,\hat{\mathbf{d}};k_0)\overline{g(\mathbf{z},\mathbf{x})}\\ &\quad\approx \int_{\Gamma_{\text{obs}}}\frac{k_0^2(1+\mathrm{i})}{4\sqrt{k_0\pi}}\sum_{m=1}^{M}\alpha_m^2\left(\frac{\varepsilon_m-\varepsilon_0}{\sqrt{\varepsilon_0\mu_0}}\right)|\mathbf{D}_m|\,\mathrm{e}^{\mathrm{i}k_0\hat{\mathbf{d}}\cdot\mathbf{r}_m}g(\mathbf{r}_m,\mathbf{x})\overline{g(\mathbf{z},\mathbf{x})}\mathrm{d}S(\mathbf{x})\\ &\quad= \frac{k_0^2(1+\mathrm{i})}{4\sqrt{k_0\pi}}\sum_{m=1}^{M}\alpha_m^2\left(\frac{\varepsilon_m-\varepsilon_0}{\sqrt{\varepsilon_0\mu_0}}\right)|\mathbf{D}_m|\,\mathrm{e}^{\mathrm{i}k_0\hat{\mathbf{d}}\cdot\mathbf{r}_m}\int_{\Gamma_{\text{obs}}} g(\mathbf{r}_m,\mathbf{x})\overline{g(\mathbf{z},\mathbf{x})}\mathrm{d}S(\mathbf{x})\\ &\quad\approx \frac{k_0(\mathrm{i}-1)}{16\sqrt{k_0\pi}}\sum_{m=1}^{M}\alpha_m^2\left(\frac{\varepsilon_m-\varepsilon_0}{\sqrt{\varepsilon_0\mu_0}}\right)|\mathbf{D}_m|\,\mathrm{e}^{\mathrm{i}k_0\hat{\mathbf{d}}\cdot\mathbf{r}_m}\mathrm{J}_0(k_0|\mathbf{z}-\mathbf{r}_m|).\end{aligned} \tag{3.8}$$

Applying Hölder's inequality gives

$$\left|\left\langle u^s(\mathbf{x},\hat{\mathbf{d}};k_0), g(\mathbf{z},\mathbf{x}_n)\right\rangle_{L^2(\Gamma_{\text{obs}})}\right| \leq \left\|u^s(\mathbf{x},\hat{\mathbf{d}};k_0)\right\|_{L^2(\Gamma_{\text{obs}})} \|g(\mathbf{x},\mathbf{z})\|_{L^2(\Gamma_{\text{obs}})}, \tag{3.9}$$

which implies neglecting constant $\frac{k_0(\mathrm{i}-1)}{16\sqrt{k_0\pi}}$, so (3.7) is derived. □

Remark 3.3.2 *Theorem 3.3.1 shows that the imaging performance of the DSM indicator function is highly dependent on the permittivity, size, and number of the inhomogeneities. If one of those has a permittivity and/or a size which is significantly larger than of the others, it might be the only one to be identified, the remaining others being not or only partially seen.*

Remark 3.3.3 *If the radii and permittivities of all circular inhomogeneities are the same (i.e., $\alpha_m \equiv \alpha$, $|\mathbf{D}_m| = \pi$, and $\varepsilon_m \equiv \varepsilon$ for $m = 1, 2, \cdots, M$), and knowing that $|\mathrm{e}^{\mathrm{i}k_0\hat{\mathbf{d}}\cdot\mathbf{r}_m}| = 1$ and $\alpha_m^2(\varepsilon_m - \varepsilon_0)|\mathbf{D}_m| \equiv \alpha^2(\varepsilon - \varepsilon_0)\pi$ then $\mathcal{I}_{\text{DSM}}(\mathbf{z},\hat{\mathbf{d}};k_0)$ becomes*

$$\mathcal{I}_{\text{DSM}}(\mathbf{z},\hat{\mathbf{d}};k_0) \propto \left|\sum_{m=1}^{M} \mathrm{J}_0(k_0|\mathbf{r}_m - \mathbf{z}|)\right| \tag{3.10}$$

which is the same as (3.6) derived in (Ito, Jin, and J. Zou 2012).

Remark 3.3.4 (Multiple impinging directions) *By combining (3.2) and (3.7), it is easy to see that*

$$\mathcal{I}_{\text{DSM}}(\mathbf{z};k_0) \propto \max\left\{\left|\sum_{m=1}^{M} \alpha_m^2(\varepsilon_m - \varepsilon_0)\,|\mathbf{D}_m|\,\mathrm{e}^{\mathrm{i}k_0\hat{\mathbf{d}}_l\cdot\mathbf{r}_m}\mathrm{J}_0(k_0|\mathbf{z}-\mathbf{r}_m|)\right|, l = 1,\ldots,L : \mathbf{z}\in\Omega\right\} \tag{3.11}$$

for which Remark 3.3.2 and Remark 3.3.3 are also verified.

3.3.2 Introduction and analysis of an alternative direct sampling method

Thanks to our analysis of $\mathcal{I}_{\text{DSM}}(\mathbf{z},\hat{\mathbf{d}};k_0)$ and, in particular, $\Psi_1(\mathbf{z},\hat{\mathbf{d}};k_0)$ (3.7), it can be seen that the latter (3.11) contains a factor of the form of $\mathrm{e}^{\mathrm{i}k_0\hat{\mathbf{d}}_l\cdot\mathbf{r}_m}$ which generates artifacts due to the oscillating nature of the exponential function. To reduce such a behavior, an alternative indicator function of DSM, $\mathcal{I}_{\text{DSMA}}(\mathbf{z};k_0)$, is proposed

$$\mathcal{I}_{\text{DSMA}}(\mathbf{z};k_0) := \frac{\left|\sum_{l=1}^{L} \mathrm{e}^{-\mathrm{i}k_0\hat{\mathbf{d}}_l\cdot\mathbf{z}}\left\langle u^s(\mathbf{x},\hat{\mathbf{d}}_l;k_0), g(\mathbf{x},\mathbf{z})\right\rangle_{L^2(\Gamma_{\text{obs}})}\right|}{\max\limits_{\mathbf{z}\in\Omega}\left|\sum_{l=1}^{L} \mathrm{e}^{-\mathrm{i}k_0\hat{\mathbf{d}}_l\cdot\mathbf{z}}\left\langle u^s(\mathbf{x},\hat{\mathbf{d}}_l;k_0), g(\mathbf{x},\mathbf{z})\right\rangle_{L^2(\Gamma_{\text{obs}})}\right|}. \tag{3.12}$$

Theorem 3.3.5 *Assume that the number N of measurement points and the number L of incident fields are sufficiently large. Then, $\mathcal{I}_{\text{DSMA}}(\mathbf{z};k_0)$ can be represented as*

$$\mathcal{I}_{\text{DSMA}}(\mathbf{z};k_0) = \frac{|\Psi_2(\mathbf{z};k_0)|}{\max\limits_{\mathbf{z}\in\Omega}|\Psi_2(\mathbf{z};k_0)|}, \text{ where } \Psi_2(\mathbf{z};k_0) = \sum_{m=1}^{M} \mathcal{A}_m \mathrm{J}_0(k_0|\mathbf{z}-\mathbf{r}_m|)^2. \tag{3.13}$$

Here, $\mathcal{A}_m = \alpha_m^2(\varepsilon_m - \varepsilon_0)|\mathbf{D}_m|$.

Proof Let us note that if L is sufficiently large, the following relationship holds (see (W.-K. Park 2015) and (Li and Z. Zou 2013)):

$$\sum_{l=1}^{L} \mathrm{e}^{\mathrm{i}k_0\hat{\mathbf{d}}_l\cdot\mathbf{r}_m}\overline{\mathrm{e}^{\mathrm{i}k_0\hat{\mathbf{d}}_l\cdot\mathbf{z}}} \approx \int_{\mathbb{S}^1} \mathrm{e}^{\mathrm{i}k_0\hat{\mathbf{d}}\cdot\mathbf{r}_m}\mathrm{e}^{-\mathrm{i}k_0\hat{\mathbf{d}}\cdot\mathbf{z}}\mathrm{d}S(\hat{\mathbf{d}}) = 2\pi \mathrm{J}_0(k_0|\mathbf{r}_m-\mathbf{z}|). \tag{3.14}$$

Hence, by combining (3.8) and (3.14), we obtain

$$\begin{aligned}
\Psi_2(\mathbf{z};k_0) &= \sum_{l=1}^{L} \overline{\mathrm{e}^{\mathrm{i}k_0\hat{\mathbf{d}}_l\cdot\mathbf{z}}} \left\langle u^s(\mathbf{x}_n,\hat{\mathbf{d}}_l), g(\mathbf{z},\mathbf{x}_n)\right\rangle_{L^2(\Gamma_{\mathrm{obs}})} \\
&= \sum_{l=1}^{L} \overline{\mathrm{e}^{\mathrm{i}k_0\hat{\mathbf{d}}_l\cdot\mathbf{z}}} \left(\frac{k_0(\mathrm{i}-1)}{16\sqrt{k_0\pi}} \sum_{m=1}^{M} \alpha_m^2 \left(\frac{\varepsilon_m-\varepsilon_0}{\sqrt{\varepsilon_0\mu_0}}\right) |\mathbf{D}_m|\, \mathrm{e}^{\mathrm{i}k_0\hat{\mathbf{d}}_l\cdot\mathbf{r}_m} \mathrm{J}_0(k_0|\mathbf{z}-\mathbf{r}_m|)\right) \\
&= \frac{k_0(\mathrm{i}-1)}{16\sqrt{k_0\pi}} \sum_{m=1}^{M} \alpha_m^2 \left(\frac{\varepsilon_m-\varepsilon_0}{\sqrt{\varepsilon_0\mu_0}}\right) |\mathbf{D}_m|\, \mathrm{J}_0(k_0|\mathbf{z}-\mathbf{r}_m|) \left(\sum_{l=1}^{L} \mathrm{e}^{\mathrm{i}k_0\hat{\mathbf{d}}_l\cdot\mathbf{r}_m}\overline{\mathrm{e}^{\mathrm{i}k_0\hat{\mathbf{d}}_l\cdot\mathbf{z}}}\right) \\
&\approx \frac{k_0(\mathrm{i}-1)\pi}{8\sqrt{k_0\pi}} \sum_{m=1}^{M} \alpha_m^2 \left(\frac{\varepsilon_m-\varepsilon_0}{\sqrt{\varepsilon_0\mu_0}}\right) |\mathbf{D}_m|\, \mathrm{J}_0(k_0|\mathbf{z}-\mathbf{r}_m|)^2.
\end{aligned} \tag{3.15}$$

Finally, applying Hölder's inequality, (3.13) is derived which completes the proof. □

Remark 3.3.6 *Based on the result in Theorem 3.3.5, we see that*

$$\mathcal{I}_{\mathrm{DSM}}(\mathbf{z};k_0) \propto |\mathrm{J}_0(k_0\,|\mathbf{z}-\mathbf{r}_m|)| \quad \textit{and} \quad \mathcal{I}_{\mathrm{DSMA}}(\mathbf{z};k_0) \propto \mathrm{J}_0(k_0\,|\mathbf{z}-\mathbf{r}_m|)^2. \tag{3.16}$$

One-dimensional plots of (3.16) are shown in Figure 3.1 and illustrate that $\mathcal{I}_{\mathrm{DSMA}}(\mathbf{z};k_0)$ would yield better images because its oscillations are smaller than those of $\mathcal{I}_{\mathrm{DSM}}(\mathbf{z};k_0)$. Hence, any unexpected artifact in the plot of $\mathcal{I}_{\mathrm{DSMA}}(\mathbf{z};k_0)$ is mitigated by having a sufficiently large number L of incident fields. This result explains theoretically why $\mathcal{I}_{\mathrm{DSMA}}(\mathbf{z};k_0)$ with large L offers better results than $\mathcal{I}_{\mathrm{DSM}}(\mathbf{z};k_0)$.

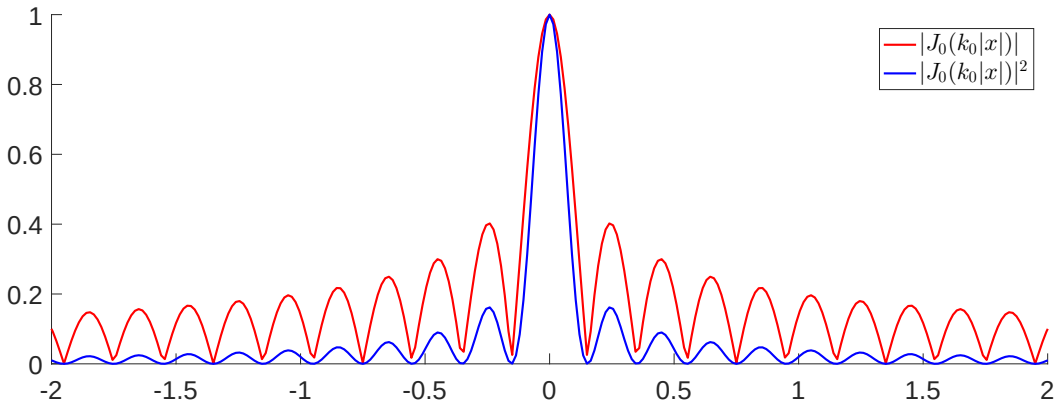

Figure 3.1: One-dimensional plots of $|\mathrm{J}_0(k_0|x|)|$ and $|\mathrm{J}_0(k_0|x|)|^2$ for $k_0 = 2\pi/0.4$.

3.4 Comparison between Kirchhoff migration and direct sampling method

In the following, the structures of Kirchhoff migration, DSM and DSMA are compared. Let us assume that the total numbers of measurement N and of incident fields L are sufficiently large and let us define the Multi-Static Response (MSR) matrix $\mathbb{K} \in \mathbb{C}^{N\times L}$ as

$$\mathbb{K} = \begin{bmatrix} u^s(\mathbf{x}_1, \hat{\mathbf{d}}_1; k_0) & u^s(\mathbf{x}_1, \hat{\mathbf{d}}_2; k_0) & \cdots & u^s(\mathbf{x}_1, \hat{\mathbf{d}}_L; k_0) \\ u^s(\mathbf{x}_2, \hat{\mathbf{d}}_1; k_0) & u^s(\mathbf{x}_2, \hat{\mathbf{d}}_2; k_0) & \cdots & u^s(\mathbf{x}_2, \hat{\mathbf{d}}_L; k_0) \\ \vdots & \vdots & \ddots & \vdots \\ u^s(\mathbf{x}_N, \hat{\mathbf{d}}_1; k_0) & u^s(\mathbf{x}_N, \hat{\mathbf{d}}_2; k_0) & \cdots & u^s(\mathbf{x}_N, \hat{\mathbf{d}}_L; k_0) \end{bmatrix}. \tag{3.17}$$

For $\mathbf{z} \in \Omega$, the indicator function of Kirchhoff migration is defined as (e.g., see (Ammari, Garnier, H. Kang, W.-K. Park, et al. 2011))

$$\mathcal{I}_{\mathrm{KM}}(\mathbf{z}; k_0) := \left|\overline{\mathbf{W}}_1(\mathbf{z})^T \mathbb{K} \overline{\mathbf{W}}_2(\mathbf{z})\right|, \tag{3.18}$$

where

$$\begin{aligned} \mathbf{W}_1(\mathbf{z}) &= \left[g(\mathbf{x}_1, \mathbf{z}), g(\mathbf{x}_2, \mathbf{z}) \cdots, g(\mathbf{x}_N, \mathbf{z})\right]^T, \\ \mathbf{W}_2(\mathbf{z}) &= \left[\mathrm{e}^{\mathrm{i}k_0 \hat{\mathbf{d}}_1 \cdot \mathbf{z}}, \mathrm{e}^{\mathrm{i}k_0 \hat{\mathbf{d}}_2 \cdot \mathbf{z}}, \cdots, \mathrm{e}^{\mathrm{i}k_0 \hat{\mathbf{d}}_L \cdot \mathbf{z}}\right]^T. \end{aligned} \tag{3.19}$$

A normalized version of (3.18) is defined as

$$\mathcal{I}_{\mathrm{NKM}}(\mathbf{z}; k_0) := \frac{\left|\overline{\mathbf{W}}_1(\mathbf{z})^T \mathbb{K} \overline{\mathbf{W}}_2(\mathbf{z})\right|}{\max\limits_{\mathbf{z}\in\Omega} \left|\overline{\mathbf{W}}_1(\mathbf{z})^T \mathbb{K} \overline{\mathbf{W}}_2(\mathbf{z})\right|} \tag{3.20}$$

and will be used for our purpose. Then, the following statement is proposed:

Theorem 3.4.1 *Suppose that the total numbers L of incident fields and N of measurement points are sufficiently large. Then, $\mathcal{I}_{\mathrm{NKM}}(\mathbf{z}; k_0)$ can be represented as*

$$\mathcal{I}_{\mathrm{NKM}}(\mathbf{z}; k_0) = \frac{|\Psi_3(\mathbf{z}; k_0)|}{\max\limits_{\mathbf{z}\in\Omega} |\Psi_3(\mathbf{z}; k_0)|}, \ \textit{where } \Psi_3(\mathbf{z}; k_0) = \sum_{m=1}^{M} \mathcal{A}_m \mathrm{J}_0(k_0 |\mathbf{z} - \mathbf{r}_m|)^2. \tag{3.21}$$

Here, $\mathcal{A}_m = \alpha_m^2(\varepsilon_m - \varepsilon_0)|\mathbf{D}_m|$.

Proof From (3.18) it can be shown that

$$\begin{aligned} \overline{\mathbf{W}}_1(\mathbf{z})^T \mathbb{K} &= \begin{bmatrix} \overline{g(\mathbf{z}, \mathbf{x}_1)} \\ \overline{g(\mathbf{z}, \mathbf{x}_2)} \\ \vdots \\ \overline{g(\mathbf{z}, \mathbf{x}_N)} \end{bmatrix}^T \begin{bmatrix} u^s(\mathbf{x}_1, \hat{\mathbf{d}}_1; k_0) & u^s(\mathbf{x}_1, \hat{\mathbf{d}}_2; k_0) & \cdots & u^s(\mathbf{x}_1, \hat{\mathbf{d}}_L; k_0) \\ u^s(\mathbf{x}_2, \hat{\mathbf{d}}_1; k_0) & u^s(\mathbf{x}_2, \hat{\mathbf{d}}_2; k_0) & \cdots & u^s(\mathbf{x}_2, \hat{\mathbf{d}}_L; k_0) \\ \vdots & \vdots & \ddots & \vdots \\ u^s(\mathbf{x}_N, \hat{\mathbf{d}}_1; k_0) & u^s(\mathbf{x}_N, \hat{\mathbf{d}}_2; k_0) & \cdots & u^s(\mathbf{x}_N, \hat{\mathbf{d}}_L; k_0) \end{bmatrix} \\ &= \left[U_1\left(\mathbf{z}, \hat{\mathbf{d}}_1\right), U_2\left(\mathbf{z}, \hat{\mathbf{d}}_2\right), \cdots, U_L\left(\mathbf{z}, \hat{\mathbf{d}}_L\right)\right] := \mathbf{U}(\mathbf{z}), \end{aligned} \tag{3.22}$$

where

$$U_l\left(\mathbf{z},\hat{\mathbf{d}}_l\right) := \sum_{n=1}^{N} \overline{g(\mathbf{z},\mathbf{x}_n)} u^s(\mathbf{x}_n,\hat{\mathbf{d}}_l), \quad l=1,\cdots,L. \tag{3.23}$$

Combining the latter with (3.8) leads to

$$U_l\left(\mathbf{z},\hat{\mathbf{d}}_l\right) \approx \frac{k_0\mu_0(\mathrm{i}-1)}{16\sqrt{k_0\pi}} \sum_{m=1}^{M} \alpha_m^2 \left(\frac{\varepsilon_m-\varepsilon_0}{\sqrt{\varepsilon_0\mu_0}}\right) |\mathbf{B}|\, \mathrm{e}^{\mathrm{i}k_0\hat{\mathbf{d}}_l\cdot\mathbf{r}_m} \mathrm{J}_0(k_0|\mathbf{z}-\mathbf{r}_m|). \tag{3.24}$$

Rewriting (3.18) with the use of (3.24) and (3.14) gives

$$\begin{aligned}
\mathcal{I}_{\mathrm{KM}}(\mathbf{z};k_0) &= \overline{\mathbf{W}}_1(\mathbf{z})^T \mathbb{K}_1 \overline{\mathbf{W}}_2(\mathbf{z}) = \mathbf{U}\left(\mathbf{z}\right) \overline{\mathbf{W}}_2(\mathbf{z}) \\
&= \left[U_1\left(\mathbf{z},\hat{\mathbf{d}}_1\right), U_2\left(\mathbf{z},\hat{\mathbf{d}}_2\right), \cdots, U_L\left(\mathbf{z},\hat{\mathbf{d}}_L\right)\right] \left[\mathrm{e}^{-\mathrm{i}k_0\hat{\mathbf{d}}_1\cdot\mathbf{z}}, \mathrm{e}^{-\mathrm{i}k_0\hat{\mathbf{d}}_2\cdot\mathbf{z}}, \cdots, \mathrm{e}^{-\mathrm{i}k_0\hat{\mathbf{d}}_L\cdot\mathbf{z}}\right]^T \\
&\approx \frac{k_0(\mathrm{i}-1)}{16\sqrt{k_0\pi}} \sum_{m=1}^{M} \alpha_m^2 \left(\frac{\varepsilon_m-\varepsilon_0}{\sqrt{\varepsilon_0\mu_0}}\right) |\mathbf{B}|\, \mathrm{J}_0(k_0|\mathbf{z}-\mathbf{r}_m|) \left(\sum_{l=1}^{L} \mathrm{e}^{\mathrm{i}k_0\hat{\mathbf{d}}_l\cdot(\mathbf{r}_m-\mathbf{z})}\right) \\
&\approx \frac{k_0(\mathrm{i}-1)\pi}{8\sqrt{k_0\pi}} \sum_{m=1}^{M} \alpha_m^2 \left(\frac{\varepsilon_m-\varepsilon_0}{\sqrt{\varepsilon_0\mu_0}}\right) |\mathbf{B}_m|\, \mathrm{J}_0(k_0\,|\mathbf{z}-\mathbf{r}_m|)^2,
\end{aligned} \tag{3.25}$$

which completes the proof. □

Remark 3.4.2 *The comparison of* (3.13) *and* (3.21) *shows that the alternative DSM and normalized Kirchhoff migration are identical when the number of incident fields becomes sufficiently large. Furthermore, for a single impinging direction, DSM can be regarded as normalized Kirchhoff migration since* $|\mathrm{e}^{\mathrm{i}k_0\hat{\mathbf{d}}\cdot\mathbf{r}_m}| = |\mathrm{e}^{\mathrm{i}k_0\hat{\mathbf{d}}\cdot(\mathbf{r}_m-\mathbf{z})}| \equiv 1$, $\mathcal{I}_{\mathrm{DSM}}(\mathbf{z};k_0)$ (3.7) *can then be rewritten as*

$$\mathcal{I}_{\mathrm{DSM}}(\mathbf{z};k_0) = \frac{\left|\overline{\mathbf{W}}_1(\mathbf{z})^T\mathbb{K}\right|}{\max\limits_{\mathbf{z}\in\Omega}\left|\overline{\mathbf{W}}_1(\mathbf{z})^T\mathbb{K}\right|} = \frac{\left|\overline{\mathbf{W}}_1(\mathbf{z})^T\mathbb{K}\overline{\mathbf{W}}_2(\mathbf{z})\right|}{\max\limits_{\mathbf{z}\in\Omega}\left|\overline{\mathbf{W}}_1(\mathbf{z})^T\mathbb{K}\overline{\mathbf{W}}_2(\mathbf{z})\right|} = \mathcal{I}_{\mathrm{NKM}}(\mathbf{z};k_0). \tag{3.26}$$

where $\mathbf{W}_1(\mathbf{z})$ *and* $\mathbf{W}_2(\mathbf{z})$ *are defined in* (3.19).

In summary the relationship between $\mathcal{I}_{\mathrm{NKM}}(\mathbf{z};k_0)$, $\mathcal{I}_{\mathrm{DSM}}(\mathbf{z};k_0)$ *and* $\mathcal{I}_{\mathrm{DSMA}}(\mathbf{z};k_0)$ *is given by*

$$\mathcal{I}_{\mathrm{NKM}}(\mathbf{z};k_0) = \begin{cases} \mathcal{I}_{\mathrm{DSM}}(\mathbf{z};k_0)\,(=\mathcal{I}_{\mathrm{DSMA}}(\mathbf{z};k_0)) & \text{when} \quad L=1 \\ \mathcal{I}_{\mathrm{DSMA}}(\mathbf{z};k_0) & \text{when} \quad L\geq 2. \end{cases} \tag{3.27}$$

3.5 Numerical experiments

In this section, some numerical experiments are provided in order to support our theoretical proposal. Throughout this section, the applied wavenumber k_0 is of the form $k_0 = 2\pi/\lambda_0$ with $\lambda_0 = 0.4\,\mathrm{m}$ (corresponding frequency $f_0 = 750\,\mathrm{MHz}$), the measurement curve Γ_{obs} is chosen as a circle with radius $7.5\lambda_0 = 3\,\mathrm{m}$ centered at the origin, and the total number of measurement points is set to $N = 36$. The search domain Ω is a square of side length $3\lambda_0 (= 1.2\,\mathrm{m})$ divided into squares ot equal side $h = 0.612\lambda_0 = 0.0245\,\mathrm{m}$.

The scattered fields $u^s(\mathbf{x}_n,\hat{\mathbf{d}}_l;k_0)$ due to planar incident waves are generated by `FEKO` (EM simulation software) and a 20dB white Gaussian random noise is added using the MATLAB function `awgn`. Furthermore, in order to compare the accuracy of the results, we adopt the Jaccard index explained in Appendix A.3.

Example 3.5.1 (Small disks with the same radius and permittivity) *First, let us consider the small dielectric disks* τ_m, $m = 1, 2, 3$ *located at* $\mathbf{r}_1 = (0.75\lambda_0, -0.75\lambda_0) = (0.3\,\mathrm{m}, -0.3\,\mathrm{m})$, $\mathbf{r}_2 = (-\lambda_0, -0.5\lambda_0) = (-0.4\,\mathrm{m}, -0.2\,\mathrm{m})$, *and* $\mathbf{r}_3 = (-0.75\lambda_0, \lambda_0) = (-0.3\,\mathrm{m}, 0.4\,\mathrm{m})$, *respectively. In this example, we consider the identification of* τ_m *with constant radius and permittivity* $\alpha_m \equiv 0.075\lambda_0 = 0.03\,\mathrm{m}$ *and* $\varepsilon_m \equiv 5\varepsilon_0$, *respectively.*

Figure 3.2 shows the map of $\mathcal{I}_{\mathrm{DSM}}(\mathbf{z}; k_0)$ for a single incident wave with $\hat{\mathbf{d}} = (-1, 0)$. As shown by the previous results (Ito, Jin, and J. Zou 2012) and the discussion in Remark 3.3.3, the locations of each inhomogeneity τ_m are identified even though the Jaccard index has not a high value. It can be explained by the fact that a lot of artifacts are present in the image and a high κ threshold is needed to better identify the location of the defect. Then the imaging performance of $\mathcal{I}_{\mathrm{DSM}}(\mathbf{z}; k_0)$ and $\mathcal{I}_{\mathrm{DSMA}}(\mathbf{z}; k_0)$ is compared as a function of the number of incident fields L (Figure 3.2 with $L = 1$, 2, 12, and 36). As stated in Remark 3.3.6 and confirmed by the comparison of the Jaccard index, $\mathcal{I}_{\mathrm{DSMA}}(\mathbf{z}; k_0)$ is an improved version of $\mathcal{I}_{\mathrm{DSM}}(\mathbf{z}; k_0)$.

Hereafter, Remark 3.4.2 is verified by comparing $\mathcal{I}_{\mathrm{DSMA}}(\mathbf{z}; k_0)$ and $\mathcal{I}_{\mathrm{NKM}}(\mathbf{z}; k_0)$ (Figure 3.3), only the maps and the corresponding Jaccard indexes for $L = 1$ and $L = 36$ incident fields being presented for brevity. As expected, the maps of $\mathcal{I}_{\mathrm{DSMA}}(\mathbf{z}; k_0)$ and $\mathcal{I}_{\mathrm{NKM}}(\mathbf{z}; k_0)$ and their corresponding Jaccard index are identical whatever the number of incidences. From now on, only the Jaccard index of $\mathcal{I}_{\mathrm{NKM}}(\mathbf{z}; k_0)$ will be provided.

Example 3.5.2 (Small disks with different radii but same permittivities) *Now, the imaging of* τ_m *with different radii but the same permittivity* $\varepsilon_m \equiv 5\varepsilon_0$ *is dealt with. The values of* α_m *are* $\alpha_1 = 0.0875\lambda_0 = 0.035\,\mathrm{m}$, $\alpha_2 = 0.075\lambda_0 = 0.03\,\mathrm{m}$, *and* $\alpha_3 = 0.0625\lambda_0 = 0.025\,\mathrm{m}$. *The locations* $\mathbf{r}_m$ *of* τ_m *are chosen as* $\mathbf{r}_1 = (0.75\lambda_0, -0.75\lambda) = (0.3\,\mathrm{m}, -0.3\,\mathrm{m})$, $\mathbf{r}_2 = (-\lambda_0, -0.5\lambda_0) = (-0.4\,\mathrm{m}, -0.2\,\mathrm{m})$, *and* $\mathbf{r}_3 = (-0.75\lambda_0, \lambda_0) = (-0.3\,\mathrm{m}, 0.4\,\mathrm{m})$.

As illustrated in Figure 3.4, when using the original DSM (Figure 3.4, left column) the location of the inhomogeneity with the largest radius (τ_1) is well identified whereas the others (τ_2 and τ_3) are not. Even when the number of sources is increased, the location of the inhomogeneity τ_3 is still difficult to be identified due to the presence of important artifacts in the image. The use of DSMA (Figure 3.4, centered column) improves the quality of the image thanks to the smoothing of the artifacts. This illustrates the statement proposed in Theorem 3.3.1 and the discussions in Remark 3.3.2 and Remark 3.3.6.

Note that some numerical experiments (not presented in the following) have been performed in the closely related case of small disks with the same radius but different permittivities and the conclusions are the same, DSMA performs better than DSM when the number of incident fields increases.

Example 3.5.3 (Large disk) *In order to verify that our proposal still behaves properly when the small obstacle hypothesis is no longer verified, we are considering the case of a large circular single inhomogeneity* τ *with radius* $\alpha \equiv 1\lambda_0 = 0.4\,\mathrm{m}$ *and permittivity* $\varepsilon = 5\varepsilon_0$. *A location is chosen as* $\mathbf{r} = (-0.75\lambda_0, -0.75\lambda_0) = (-0.3\,\mathrm{m}, -0.3\,\mathrm{m})$. *In this example, the search domain* Ω *is a square with side of* $2.5\lambda_0 (= 1\,\mathrm{m})$, *which is divided into small squares with side* $h = 0.102\lambda_0 = 0.0408\,\mathrm{m}$.

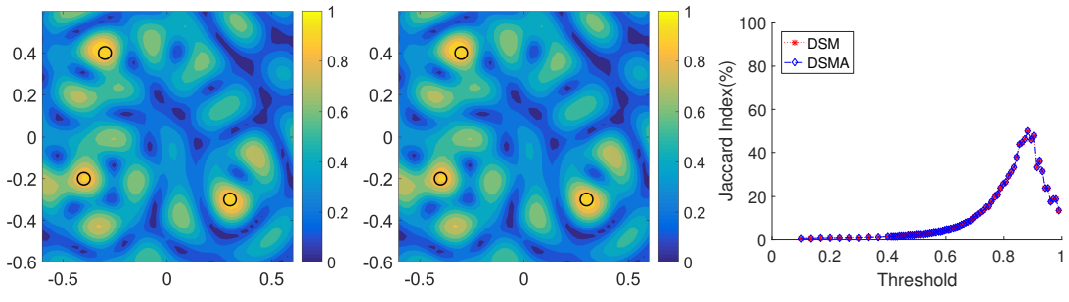

(a) DSM with $L = 1$ (b) DSMA with $L = 1$ (c) Jaccard index for $L = 1$

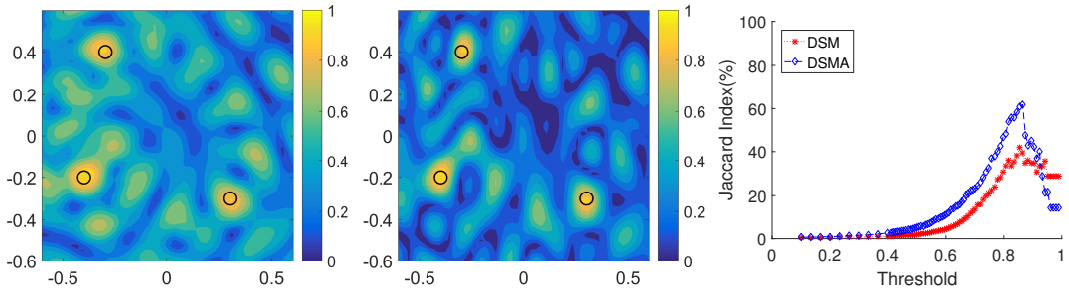

(d) DSM with $L = 2$ (e) DSMA with $L = 2$ (f) Jaccard index for $L = 2$

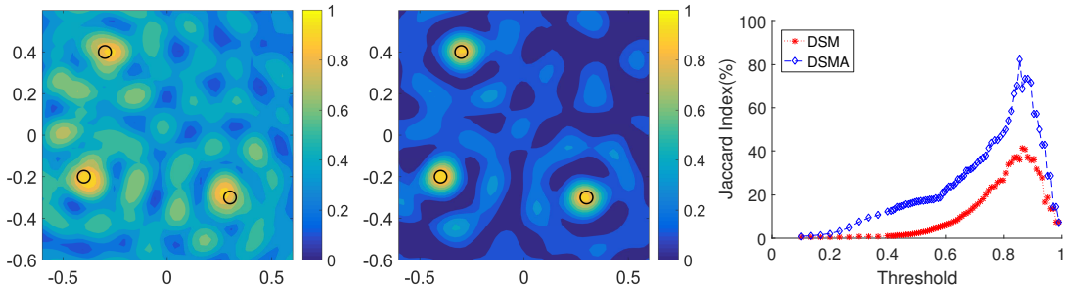

(g) DSM with $L = 12$ (h) DSMA with $L = 12$ (i) Jaccard index for $L = 12$

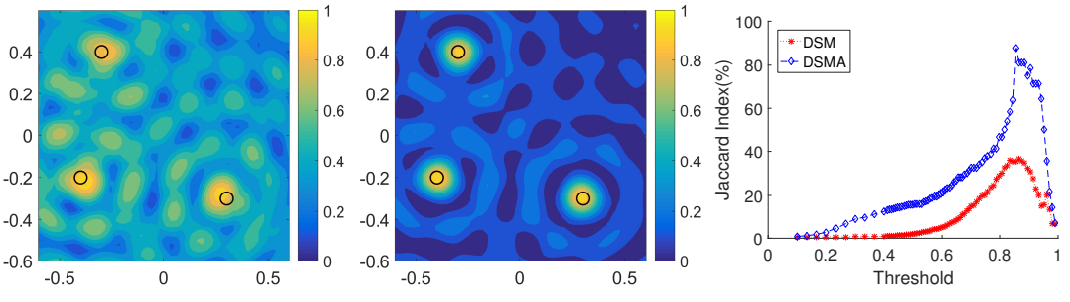

(j) DSM with $L = 36$ (k) DSMA with $L = 36$ (l) Jaccard index for $L = 36$

Figure 3.2: (Example 3.5.1) Map of $\mathcal{I}_{\text{DSM}}(\mathbf{z}; k_0)$ (left column) $\mathcal{I}_{\text{DSMA}}(\mathbf{z}; k_0)$ (center column), and Jaccard index (right column).

According to Figure 3.5, the exact location and shape of τ with a few incident waves (one or two) are difficult to be obtained via both DSM and DSMA. But, as the number of incident waves increases, the image of τ is improving with $\mathcal{I}_{\text{DSM}}(\mathbf{z}; k_0)$ and with $\mathcal{I}_{\text{DSMA}}(\mathbf{z}; ; k_0)$. From the Jaccard index it can be seen that DSMA has better performance than DSM even if we are no more within the small obstacle hypothesis.

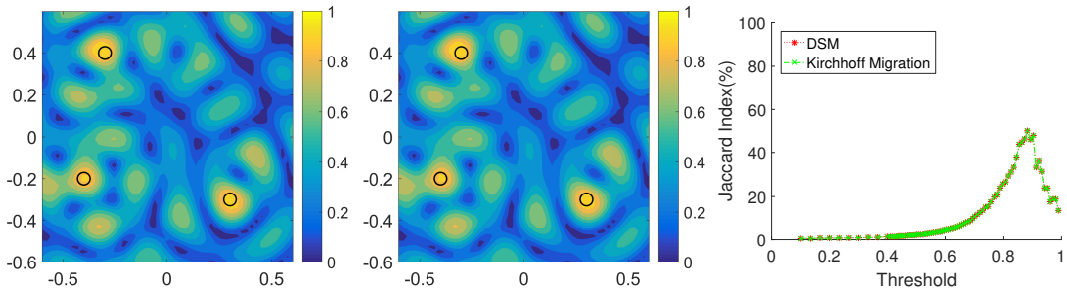

(a) DSM with $L = 1$ (b) NKM with $L = 1$ (c) Jaccard index for $L = 1$

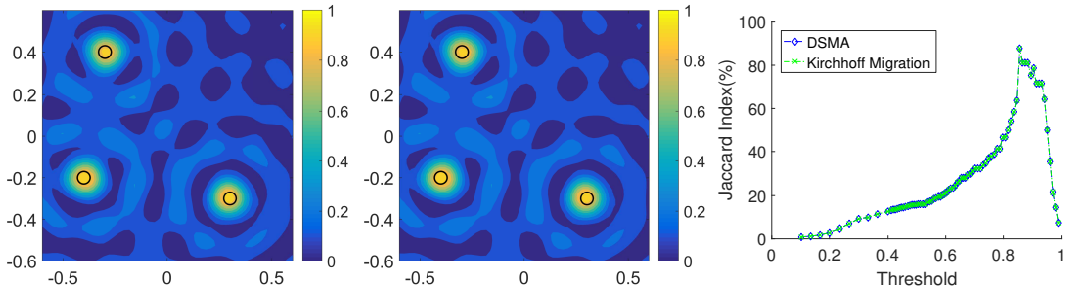

(d) DSMA with $L = 36$ (e) NKM with $L = 36$ (f) Jaccard index for $L = 36$

Figure 3.3: (Example 3.5.1) Map of $\mathcal{I}_{\mathrm{DSMA}}(\mathbf{z}; k_0)$ (first column), $\mathcal{I}_{\mathrm{NKM}}(\mathbf{z}; k_0)$ (second column), and Jaccard index (last column).

3.6 Illustration with some experimental data

In the following both approaches are applied to experimental data available at `http://www.fresnel.fr/3Ddatabase/database.php` and described in (Belkebir and Saillard 2001). In order to be as close as possible to the framework of the theoretical results, the frequency is chosen as $f_0 = 4\,\mathrm{GHz}$, which corresponds to a wavelength $\lambda_0 = 0.0749\,\mathrm{m}$. The measurement configuration is as follows, $L = 36$ sources are at a distance of $\hat{\mathbf{d}}_l \approx 9.87\lambda_0$ evenly distributed from 10° to 350° and $N = 49$ receivers are placed at $\mathbf{x}_n \approx 10.14\lambda_0$ and evenly distributed from 5° to 355°. Ω is a square area of $2\lambda_0 \times 2\lambda_0$ and has been discretized in 51×51 pixels. It is worth to note that

- due to experimental set-up limitations the full Multi-Static Response is not available;
- since the sources are located far from the center of our region of interest, they can be regarded as a plane wave approximately.

Example 3.6.1 (Two dielectric cylinders, file name is *twodielTM_8f.exp*) *The chosen target is the set of two dielectric cylinders with radius* $\alpha_m \approx \lambda/10, m = 1, 2$ *and permittivity* $\varepsilon_m = (3.0 \pm 0.3)\,\varepsilon_0$. *They are located at* $\mathbf{r}_1 \approx (-2\lambda/30, -3\lambda/10\ \mathrm{m})$ *and* $\mathbf{r}_2 \approx (0\,\mathrm{m}, 3\lambda/10\ \mathrm{m})$, *respectively.*

The results are displayed in Figure 3.6. For the case of a single source (figure 3.6, first line) neither DSM nor DSMA provides a good localization of the defect even though the two maps are almost identical. Some discrepancies can be seen between the two, thanks to the Jaccard index comparison. They are related to the fact that, as already mentioned, the incident field is approximately the same as a plane

wave, i.e., $\left|e^{ik_0\hat{\mathbf{d}}\cdot\mathbf{x}}\right| = 1$. When the number of incident fields L is increasing (figure 3.6, second and third line) the improvement provided by $\mathcal{I}_{\text{DSMA}}$ compared to $\mathcal{I}_{\text{DSM}}$ is still valid up to a threshold of $\kappa = 80\,\%$.

Example 3.6.2 (Metallic rectangle pole, file name is *rectTM_dece.exp*) *Here, we apply the algorithms to a non-circular target with metallic square shape. It has side lengths* $0.0127\,\text{m}$ *and* $0.0245\,\text{m}$ *and is located at* $\mathbf{r} \approx (0\,\text{m}, 0.04\,\text{m})$.

Figure 3.7 shows that the center of the target is identified via DSM and DSMA. The artifacts in the maps of $\mathcal{I}_{\text{DSM}}(\mathbf{z}; k_0)$ and $\mathcal{I}_{\text{DSMA}}(\mathbf{z}; k_0)$ decrease as the total number of incident fields increases and accuracy of DSMA is better than DSM. However, it seems to be almost a circle not a rectangle. In other words, the edges of the target are hard to be identified via both DSM and DSMA.

Example 3.6.3 (Metallic U-shaped pole, file name is *uTM_shaped.exp*) *Now, a complex target (metallic U-shape) with the size* $0.05\,\text{m} \times 0.08\,\text{m}$ *is considered.*

The results are presented in Figure 3.8. In this case, it is not sufficient to identify the exact shape and location of the target with the data from a single incident field. On the other hand, the target can be reconstructed by both DSM and DSMA with a lot of sources ($L = 12,\ 36$). DSMA also has a better result than DSM as stated in Remark 3.3.6.

3.7 Conclusion

In this chapter, the direct sampling method (DSM) is analyzed in the case of small obstacles thanks to the asymptotic formula of the scattered field. Some drawbacks of the classical DSM are exhibited and DSMA which improves the performance of the former in the case of multiple transmitters is proposed. Once the DSMA indicator function has been derived a strong connection between Kirchhoff migration and traditional and alternative DSM has been identified. Numerical simulations under various conditions are provided to support our theoretical results either with synthetic or with experimental data.

In the next chapter, we study the DSM in restricted configurations such as mono-static and limited-aperture configuration.

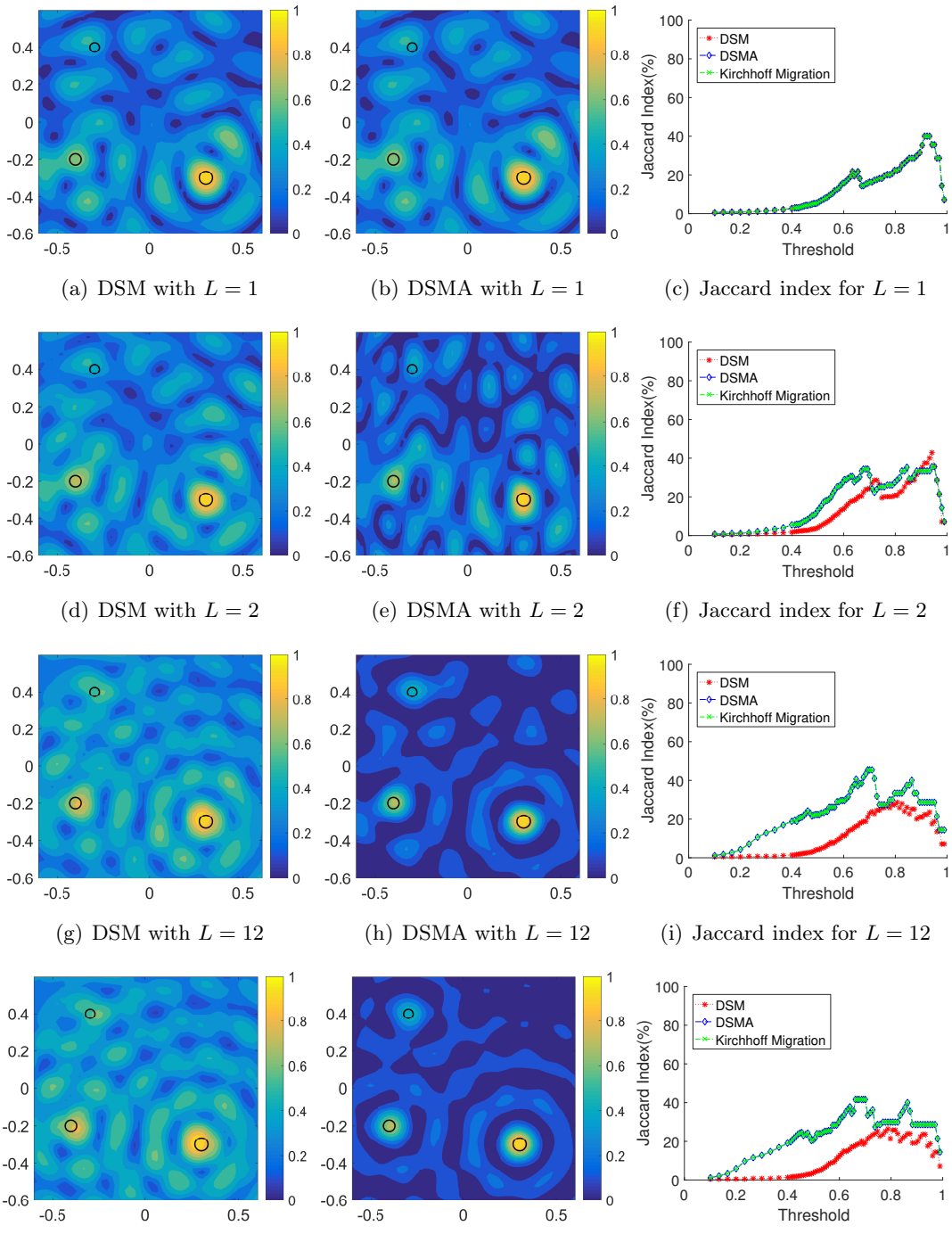

(a) DSM with $L = 1$ (b) DSMA with $L = 1$ (c) Jaccard index for $L = 1$

(d) DSM with $L = 2$ (e) DSMA with $L = 2$ (f) Jaccard index for $L = 2$

(g) DSM with $L = 12$ (h) DSMA with $L = 12$ (i) Jaccard index for $L = 12$

(j) DSM with $L = 36$ (k) DSMA with $L = 36$ (l) Jaccard index for $L = 36$

Figure 3.4: (Example 3.5.2) Map of $\mathcal{I}_{\mathrm{DSM}}(\mathbf{z}; k_0)$ (left column) $\mathcal{I}_{\mathrm{DSMA}}(\mathbf{z}; k_0)$ (center column), and Jaccard index (right column).

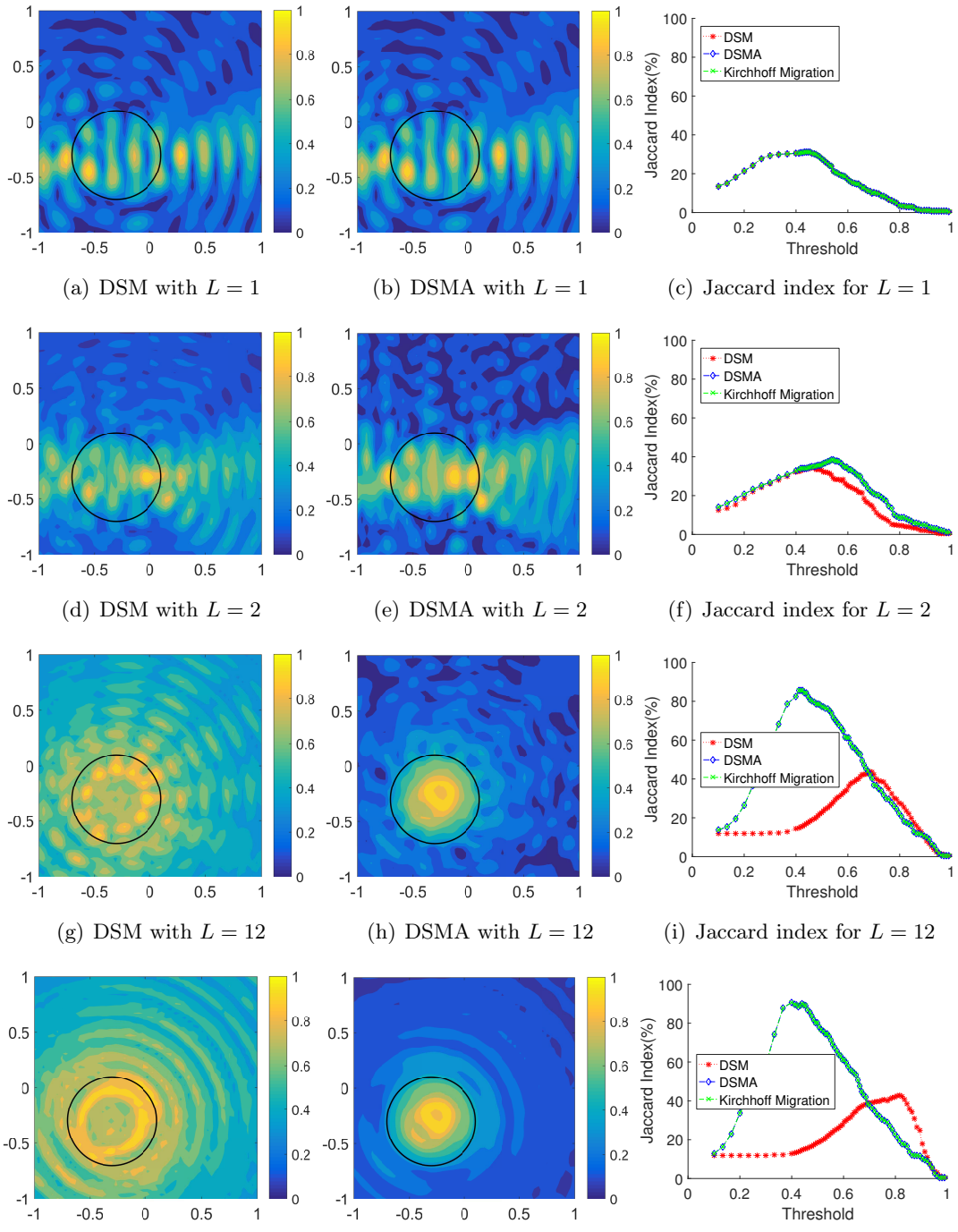

(a) DSM with $L = 1$ (b) DSMA with $L = 1$ (c) Jaccard index for $L = 1$

(d) DSM with $L = 2$ (e) DSMA with $L = 2$ (f) Jaccard index for $L = 2$

(g) DSM with $L = 12$ (h) DSMA with $L = 12$ (i) Jaccard index for $L = 12$

(j) DSM with $L = 36$ (k) DSMA with $L = 36$ (l) Jaccard index for $L = 36$

Figure 3.5: (Example 3.5.3) Map of $\mathcal{I}_{\text{DSM}}(\mathbf{z}; k_0)$ (left column) $\mathcal{I}_{\text{DSMA}}(\mathbf{z}; k_0)$ (center column), and Jaccard index (right column).

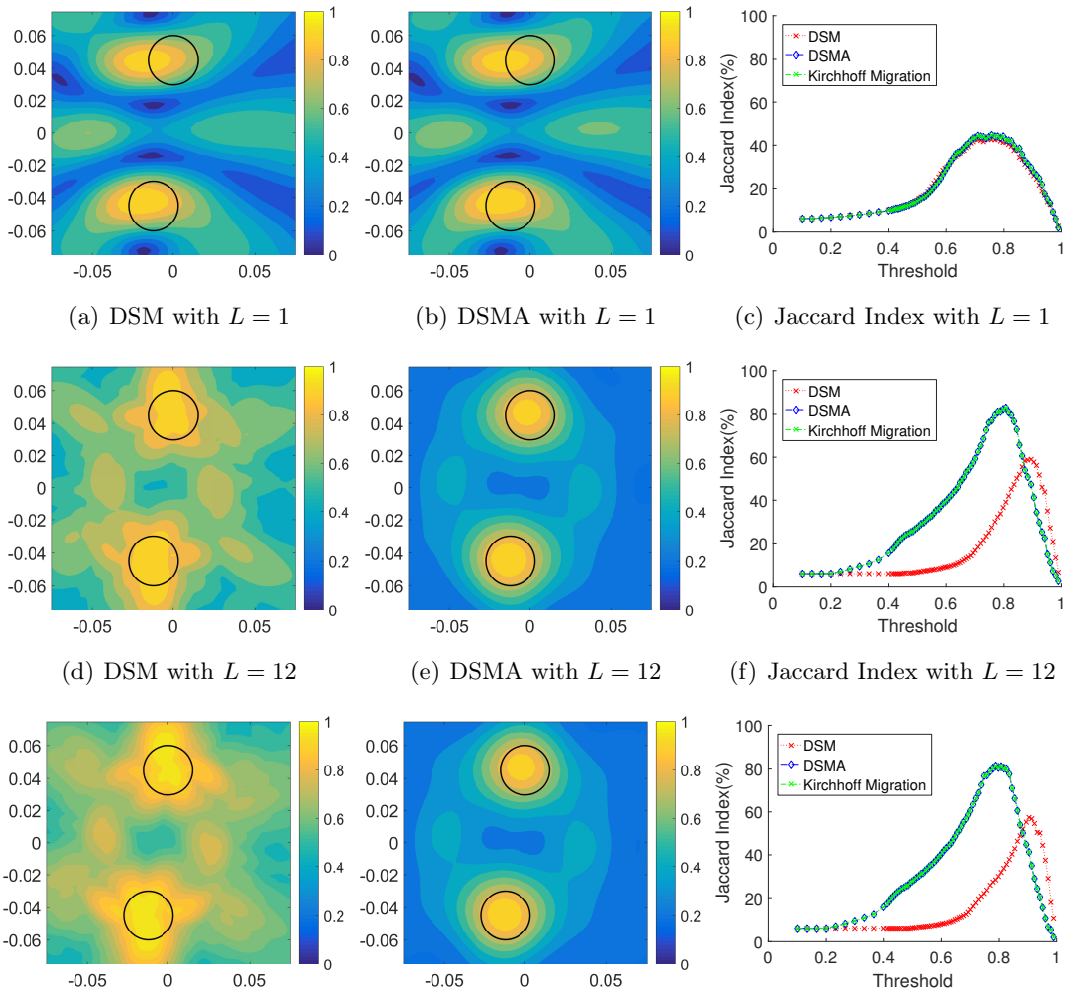

(a) DSM with $L = 1$ (b) DSMA with $L = 1$ (c) Jaccard Index with $L = 1$

(d) DSM with $L = 12$ (e) DSMA with $L = 12$ (f) Jaccard Index with $L = 12$

(g) DSM with $L = 36$ (h) DSMA with $L = 36$ (i) Jaccard Index with $L = 36$

Figure 3.6: (Example 3.6.1) Map of $\mathcal{I}_{\text{DSM}}(\mathbf{z}; k_0)$ (left column) $\mathcal{I}_{\text{DSMA}}(\mathbf{z}; k_0)$ (center column), and Jaccard index (right column) using the experimental data at 4 GHz.

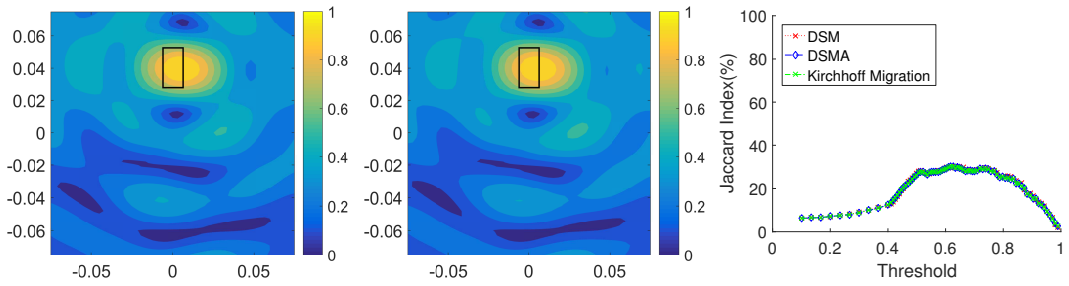

(a) DSM with $L = 1$ (b) DSMA with $L = 1$ (c) Jaccard Index with $L = 1$

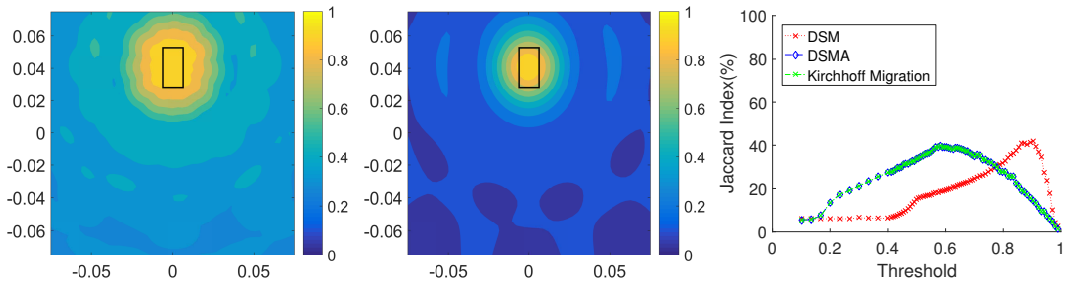

(d) DSM with $L = 12$ (e) DSMA with $L = 12$ (f) Jaccard Index with $L = 12$

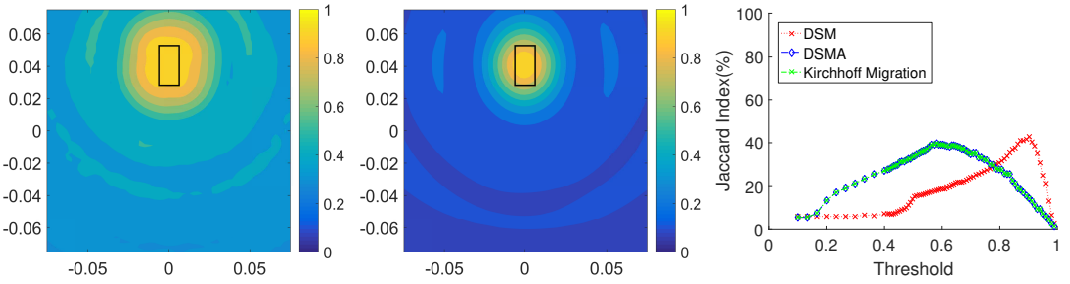

(g) DSM with $L = 36$ (h) DSMA with $L = 36$ (i) Jaccard Index with $L = 36$

Figure 3.7: (Example 3.6.2) Map of $\mathcal{I}_{\text{DSM}}(\mathbf{z}; k_0)$ (left column) $\mathcal{I}_{\text{DSMA}}(\mathbf{z}; k_0)$ (center column), and Jaccard index (right column) using the experimental data at 4 GHz.

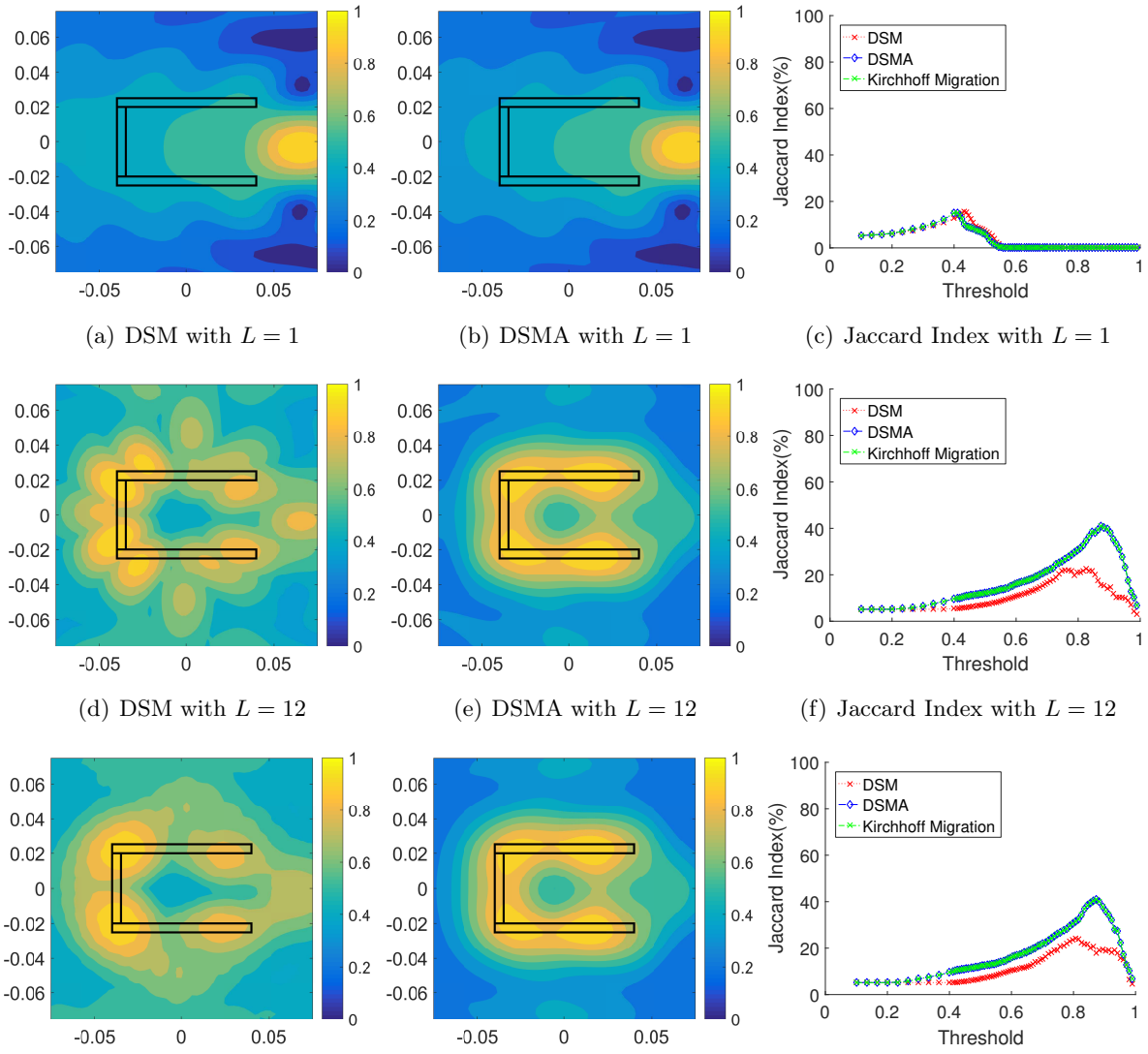

(a) DSM with $L = 1$ (b) DSMA with $L = 1$ (c) Jaccard Index with $L = 1$

(d) DSM with $L = 12$ (e) DSMA with $L = 12$ (f) Jaccard Index with $L = 12$

(g) DSM with $L = 36$ (h) DSMA with $L = 36$ (i) Jaccard Index with $L = 36$

Figure 3.8: (Example 3.6.3) Map of $\mathcal{I}_{\text{DSM}}(\mathbf{z}; k_0)$ (left column) $\mathcal{I}_{\text{DSMA}}(\mathbf{z}; k_0)$ (center column), and Jaccard index (right column) using the experimental data at 4 GHz.

4

2D imaging of dielectric inhomogeneities in restricted configuration with far-field data

Contents

4.1 Introduction

In the previous chapter, we have verified the mathematical structure of DSM and DSMA with near-field data in multi-static and full-aperture configuration. Unfortunately, in various real-world applications such as ground penetrating radar (GPR) (Catapano, Soldovieri, and Crocco 2011; X. Liu, Serhir, and Lambert 2018; Torrione et al. 2014), synthetic aperture radar (SAR) (L. Zhang et al. 2010; Çetin et al. 2014; T. Zhang and Xia 2015), and seismic imaging (Tilmann, Ni, and INDEPTH III Seismic Team 2003; Y. Chen et al. 2015; Xue et al. 2015), a full aperture set-up is not possible. In other words, the motion of a single transducer or the restricted ranges of incident and observation directions must be considered in such applications. Hence, we consider the DSM in a mono-static and limited-aperture configuration for identifying small or extended dielectric inhomogeneities in this chapter.

In the first part of this chapter, we propose the indicator function of DSM with mono-static data. Thanks to the asymptotic formula introduced in chapter 2, the mathematical structure of the indicator function of DSM and its limitation in the mono-static configuration are identified. According to our analysis, a new indicator function of the DSM is introduced and analyzed in order to improve the imaging performance of DSM in this mono-static configuration. Next, we extend our approach to limited-aperture problem and validate its mathematical structure with a similar path as in the mono-static case. We investigate the structure of DSM by establishing a relationship with a Bessel function of integer order of the first kind, the range of observation directions and properties of inhomogeneities (location, shape, size, etc.), and explain unexplored intrinsic properties of DSM. The alternative DSM (DSMA), proposed in the previous chapter, is also applied here to improve performance by using multiple incident fields. Simulation results with synthetic data corrupted by random noise and real data are exhibited for supporting theoretical results and demonstrating the effectiveness and limitations.

This chapter is organized as follows. In section 4.2, the DSM and its modified version in a mono-static configuration are designed and analyzed to explain and overcome the limitation. The study of DSM and DSMA in a limited-aperture problem is presented in section 4.3. Our theoretical results are validated with diverse numerical simulations in section 4.2.4 and 4.3.3, respectively.

4.2 Direct sampling method in mono-static configuration

According to (Li and Z. Zou 2013), for a fixed incident direction $\hat{\mathbf{d}}$, the indicator function of DSM with far-field data $\mathbb{F} = \{u_\infty(\hat{\mathbf{x}}_n, \hat{\mathbf{d}}) : \hat{\mathbf{x}}_n \in \mathbb{S}^1,\ n = 1, 2, \cdots, N\}$ is defined as

$$\mathcal{I}^\infty_{\mathrm{DSM}}(\mathbf{z}, \hat{\mathbf{d}}; k_0) := \frac{\left| \left\langle u_\infty(\hat{\mathbf{x}}_n, \hat{\mathbf{d}}; k_0), \mathrm{e}^{-\mathrm{i}k_0 \hat{\mathbf{x}}_n \cdot \mathbf{z}} \right\rangle_{L^2(\mathbb{S}^1)} \right|}{||u_\infty(\hat{\mathbf{x}}_n, \hat{\mathbf{d}})||_{L^2(\mathbb{S}^1)} ||\mathrm{e}^{-\mathrm{i}k_0 \hat{\mathbf{x}}_n \cdot \mathbf{z}}||_{L^2(\mathbb{S}^1)}}, \tag{4.1}$$

where the L^2-inner product $\langle \cdot, \cdot \rangle_{L^2(\mathbb{S}^1)}$ and $\|\cdot\|_{L^2(\mathbb{S}^1)}$ are defined by (A.2). The combination of the integral representation for far-field pattern (2.14) and of the following known lemma:

Lemma 4.2.1 (See (W.-K. Park 2015) and (Li and Z. Zou 2013)) *For sufficiently large N, $\hat{\mathbf{x}}$, $\hat{\mathbf{x}}_n \in \mathbb{S}^1$, and $\mathbf{z} \in \mathbb{R}^2$, the following relation holds:*

$$\sum_{n=1}^{N} \mathrm{e}^{\mathrm{i}k_0 \hat{\mathbf{x}}_n \cdot \mathbf{z}} \approx \int_{\mathbb{S}^1} e^{ik_0 \hat{\mathbf{x}} \cdot \mathbf{z}} \mathrm{d}S(\hat{\mathbf{x}}) = 2\pi \mathrm{J}_0(k_0 |\mathbf{z}|), \tag{4.2}$$

leads to

$$\mathcal{I}^\infty_{\mathrm{DSM}}(\mathbf{z}, \hat{\mathbf{d}}; k_0) \propto \sum_{m=1}^{M} W_m \mathrm{J}_0(k_0 |\mathbf{r}_m - \mathbf{z}|),, \tag{4.3}$$

which is the same relation as with DSM with near-field data described in (3.5). Namely, the result of $\mathcal{I}^\infty_{\mathrm{DSM}}(\mathbf{z}, \hat{\mathbf{d}}; k_0)$ has maximum amplitude if $\mathbf{z} = \mathbf{r}_m$, so the location of each inhomogeneity can be identified via $\mathcal{I}^\infty_{\mathrm{DSM}}(\mathbf{z}, \hat{\mathbf{d}}; k_0)$ even with far-field data.

Now, we design the indicator function of the direct sampling method with data measured in a mono-static configuration motivated by the fact that DSM needs only one (or a few) incident field for imaging. Let us consider the mono-static configuration in which an antenna acts as receiver and

transmitter (transducer), implying $\hat{\mathbf{d}}_n = -\hat{\mathbf{x}}_n$, and is successively set at N locations, then giving a set of measured far-field pattern data denoted by

$$\mathbb{F}_{\text{mono}} = \{u_\infty(\hat{\mathbf{x}}_n, \hat{\mathbf{d}}_n; k_0),\ n = 1, 2, \cdots, N\},\ \hat{\mathbf{d}}_n = -\hat{\mathbf{x}}_n.$$

The indicator function $\mathcal{I}^{\text{mono}}_{\text{DSM}}(\mathbf{z}; k_0)$ is directly deduced from (4.1) and defined as

$$\mathcal{I}^{\text{mono}}_{\text{DSM}}(\mathbf{z}; k_0) := \frac{\left|\left\langle u_\infty(\hat{\mathbf{x}}_n, \hat{\mathbf{d}}_n; k_0), \mathrm{e}^{-\mathrm{i}k_0\hat{\mathbf{x}}_n\cdot\mathbf{z}}\right\rangle_{L^2(\mathbb{S}^1)}\right|}{\max\limits_{\mathbf{z}\in\Omega} ||u_\infty(\hat{\mathbf{x}}_n, \hat{\mathbf{d}}_n; k_0)||_{L^2(\mathbb{S}^1)} ||\mathrm{e}^{-\mathrm{i}k_0\hat{\mathbf{x}}_n\cdot\mathbf{z}}||_{L^2(\mathbb{S}^1)}}. \tag{4.4}$$

However, as exemplified in (Bektas and Ozdemir 2016), the DSM in such a configuration failed to provide a proper localization of the defects (see also Figure 4.1). So further analysis and improvement are the main work in this section.

4.2.1 Analysis of indicator function

In (Bektas and Ozdemir 2016), a modified indicator involving a heuristic factor is proposed to solve the problem, yet no theoretical explanation is provided. In the following, we analyze the indicator function $\mathcal{I}^{\text{mono}}_{\text{DSM}}(\mathbf{z}; k_0)$ to explain the reason of such an inaccurate localization in the mono-static configuration.

Theorem 4.2.2 *Assume that the total number N of incident and observation directions is sufficiently large. Then, $\mathcal{I}^{mono}_{\text{DSM}}(\mathbf{z}; k_0)$ can be represented as:*

$$\mathcal{I}^{mono}_{\text{DSM}}(\mathbf{z}; k_0) = \frac{|\Psi_1(\mathbf{z}; k_0)|}{\max\limits_{\mathbf{z}\in\Omega} |\Psi_1(\mathbf{z}; k_0)|},\ \textit{where}\ \Psi_1(\mathbf{z}; k_0) \approx \sum_{m=1}^{M} \alpha_m^2(\varepsilon_m - \varepsilon_0)|\mathbf{D}_m|\mathrm{J}_0(k_0|2\mathbf{r}_m - \mathbf{z}|). \tag{4.5}$$

Proof Since $\hat{\mathbf{d}}_n = -\hat{\mathbf{x}}_n$, applying (2.15) and Lemma 4.2.1 to (4.4), we can evaluate

$$\begin{aligned}\left\langle u_\infty(\hat{\mathbf{x}}_n, \hat{\mathbf{d}}_n; k_0), \mathrm{e}^{-\mathrm{i}k_0\hat{\mathbf{x}}_n\cdot\mathbf{z}}\right\rangle_{L^2(\mathbb{S}^1)} &\approx \frac{k_0^2(1+\mathrm{i})}{4\sqrt{k\pi}} \sum_{m=1}^{M} \alpha_m^2 \left(\frac{\varepsilon_m - \varepsilon_0}{\sqrt{\varepsilon_0\mu_0}}\right) |\mathbf{D}_m| \left(\sum_{n=1}^{N} \mathrm{e}^{-\mathrm{i}k_0\hat{\mathbf{x}}_n\cdot(2\mathbf{r}_m - \mathbf{z})}\right) \\ &\approx \frac{k_0^2(1+\mathrm{i})\pi}{2\sqrt{k_0\pi}} \sum_{m=1}^{M} \alpha_m^2 \left(\frac{\varepsilon_m - \varepsilon_0}{\sqrt{\varepsilon_0\mu_0}}\right) |\mathbf{D}_m|\, \mathrm{J}_0(k_0|2\mathbf{r}_m - \mathbf{z}|).\end{aligned}$$

Finally, applying Hölder's inequality

$$\left|\left\langle u_\infty(\hat{\mathbf{x}}_n, \hat{\mathbf{d}}; k_0), \mathrm{e}^{-\mathrm{i}k_0\hat{\mathbf{x}}_n\cdot\mathbf{z}}\right\rangle_{L^2(\mathbb{S}^1)}\right| \le \left\|u_\infty(\hat{\mathbf{x}}_n, \hat{\mathbf{d}}; k_0)\right\|_{L^2(\mathbb{S}^1)} \left\|\mathrm{e}^{-\mathrm{i}k_0\hat{\mathbf{x}}_n\cdot\mathbf{z}}\right\|_{L^2(\mathbb{S}^1)}$$

leads to (4.5), which completes the proof. □

The structure of (4.5) explains that DSM within the mono-static configuration is no longer proportional to $|\mathrm{J}_0(k_0|\mathbf{r}_m - \mathbf{z}|)|$ but to $|\mathrm{J}_0(k_0|2\mathbf{r}_m - \mathbf{z}|)|$. This means that $\mathcal{I}^{\text{mono}}_{\text{DSM}}(\mathbf{z}; k_0)$ reaches its maximum value at shifted locations $\mathbf{z} = 2\mathbf{r}_m$. Due to this reason, a traditional application of DSM will lead to miss-localization of the inhomogeneities. Hence, further improvement is needed to overcome the limitation.

4.2.2 Modified indicator function of DSM to overcome the limitation

Thanks to (4.5), a modified indicator function of DSM $\mathcal{I}^{\text{mono}}_{\text{MDSM}}(\mathbf{z})$ can be proposed: for $\mathbf{z} \in \Omega$,

$$\mathcal{I}^{\text{mono}}_{\text{MDSM}}(\mathbf{z}; k_0) := \frac{\left| \left\langle u_\infty(\hat{\mathbf{x}}_n, \hat{\mathbf{d}}_n; k_0), \mathrm{e}^{-2\mathrm{i}k_0 \hat{\mathbf{x}}_n \cdot \mathbf{z}} \right\rangle_{L^2(\mathbb{S}^1)} \right|}{\|u_\infty(\hat{\mathbf{x}}_n, \hat{\mathbf{d}}_n; k_0)\|_{L^2(\mathbb{S}^1)} \|\mathrm{e}^{-2\mathrm{i}k_0 \hat{\mathbf{x}}_n \cdot \mathbf{z}}\|_{L^2(\mathbb{S}^1)}}. \tag{4.6}$$

Following the same path (omitted here) as for Theorem 4.2.2 leads to

Theorem 4.2.3 *Assume that the total number N of incident and observation directions is sufficiently large. Then, $\mathcal{I}^{mono}_{\text{MDSM}}(\mathbf{z}; k_0)$ can be represented as:*

$$\mathcal{I}^{mono}_{\text{MDSM}}(\mathbf{z}; k_0) = \frac{|\Psi_2(\mathbf{z}; k_0)|}{\max\limits_{\mathbf{z} \in \Omega} |\Psi_2(\mathbf{z}; k_0)|}, \text{ where } \Psi_3(\mathbf{z}; k_0) \approx \sum_{m=1}^{M} \alpha_m^2 (\varepsilon_m - \varepsilon_0) |\mathbf{D}_m| \mathrm{J}_0(2k_0 |\mathbf{r}_m - \mathbf{z}|). \tag{4.7}$$

Proof The combination of (2.15) and Lemma 4.2.1 leads to

$$\begin{aligned} \left\langle u_\infty(\hat{\mathbf{x}}_n, \hat{\mathbf{d}}_n; k_0), \mathrm{e}^{-2\mathrm{i}k_0 \hat{\mathbf{x}}_n \cdot \mathbf{z}} \right\rangle_{L^2(\mathbb{S}^1)} &\approx \frac{k_0^2 (1+\mathrm{i})}{4\sqrt{k\pi}} \sum_{m=1}^{M} \alpha_m^2 \left(\frac{\varepsilon_m - \varepsilon_0}{\sqrt{\varepsilon_0 \mu_0}} \right) |\mathbf{D}_m| \left(\sum_{n=1}^{N} \mathrm{e}^{-2\mathrm{i}k_0 \hat{\mathbf{x}}_n \cdot (\mathbf{r}_m - \mathbf{z})} \right) \\ &\approx \frac{k_0^2 (1+\mathrm{i})\pi}{2\sqrt{k\pi}} \sum_{m=1}^{M} \alpha_m^2 \left(\frac{\varepsilon_m - \varepsilon_0}{\sqrt{\varepsilon_0 \mu_0}} \right) |\mathbf{D}_m| \, \mathrm{J}_0(2k_0 |\mathbf{r}_m - \mathbf{z}|). \end{aligned}$$

Finally, the constant $\frac{k^2(\mathrm{i}-1)\pi}{2\sqrt{k\pi}}$ is eliminated by applying Hölder's inequality and the proof is completed. □

As shown in (4.7), $\mathcal{I}^{\text{mono}}_{\text{MDSM}}(\mathbf{z}; k_0)$ is proportional to $|\mathrm{J}_0(2k_0 |\mathbf{r}_m - \mathbf{z}|)|$ which, on the contrary of (4.5), has its maximum values at $\mathbf{z} = \mathbf{r}_m$, $m = 1, 2, \cdots, M$, which corresponds to the localization of the defects to be identified.

4.2.3 Comparison of the imaging performance between mono-static and multi-static data

Now, we analyze the indicator function of DSM with multi-static data to compare the imaging performance of MDSM. With the same derivations as in previous theorem, the DSM in the multi-static configuration has the following representation formula.

Theorem 4.2.4 *Assume that the total number of receiving (N) directions is sufficiently large. Then, for a fixed incident direction of propagation $\hat{\mathbf{d}} \in \mathbb{S}^1$, $\mathcal{I}^{\infty}_{\text{DSM}}(\mathbf{z}, \hat{\mathbf{d}}; k_0)$ can be represented as:*

$$\mathcal{I}^{\infty}_{\text{DSM}}(\mathbf{z}, \hat{\mathbf{d}}; k_0) = \frac{\left| \Psi_3(\mathbf{z}, \hat{\mathbf{d}}; k_0) \right|}{\max\limits_{z \in \Omega} \left| \Psi_3(\mathbf{z}, \hat{\mathbf{d}}; k_0) \right|}, \text{ where } \Psi_3(\mathbf{z}, \hat{\mathbf{d}}; k_0) \approx \sum_{m=1}^{M} \alpha_m^2 (\varepsilon_m - \varepsilon_0) |\mathbf{D}_m| \mathrm{J}_0(k_0 |\mathbf{r}_m - \mathbf{z}|). \tag{4.8}$$

Proof We apply the asymptotic formula (2.2.2) and Lemma 4.2.1 to the indicator function of DSM (4.1):

$$\begin{aligned} \left\langle u_\infty(\hat{\mathbf{x}}_n, \hat{\mathbf{d}}; k_0), \mathrm{e}^{-\mathrm{i}k_0 \hat{\mathbf{x}}_n \cdot \mathbf{z}} \right\rangle_{L^2(\mathbb{S}^1)} &\approx \frac{k_0^2 (1+\mathrm{i})}{4\sqrt{k_0\pi}} \sum_{m=1}^{M} \alpha_m^2 \left(\frac{\varepsilon_m - \varepsilon_0}{\sqrt{\varepsilon_0 \mu_0}} \right) |\mathbf{D}_m| \mathrm{e}^{\mathrm{i}k_0 \hat{\mathbf{d}} \cdot \mathbf{r}_m} \left(\sum_{n=1}^{N} \mathrm{e}^{\mathrm{i}k_0 \hat{\mathbf{x}}_n \cdot (\mathbf{z} - \mathbf{r}_m)} \right) \\ &\approx \frac{k_0^2 \pi (1+\mathrm{i})}{2\sqrt{k_0\pi}} \sum_{m=1}^{M} \alpha_m^2 \left(\frac{\varepsilon_m - \varepsilon_0}{\sqrt{\varepsilon_0 \mu_0}} \right) |\mathbf{D}_m| \mathrm{e}^{\mathrm{i}k_0 \hat{\mathbf{d}} \cdot \mathbf{r}_m} \mathrm{J}_0(k_0 |\mathbf{z} - \mathbf{r}_m|). \end{aligned} \tag{4.9}$$

Combining $\left|\mathrm{e}^{\mathrm{i}k_0\hat{\mathbf{d}}\cdot\mathbf{r}_m}\right| = 1$ and Hölder's inequality leads to the result of Theorem (4.2.4). □

Our analysis shows that the DSM with far-field data has the same efficiency and properties as the DSM using near-field data stated in Remark 3.3.3. For multiple impinging directions $(\hat{\mathbf{d}}_l,\ l = 1, 2, \cdots, L)$, the indicator function $\mathcal{I}_{\mathrm{DSM}}(\mathbf{z})$ is defined as

$$\mathcal{I}^{\infty}_{\mathrm{DSM}}(\mathbf{z}; k_0) := \max\left\{\mathcal{I}^{\infty}_{\mathrm{DSM}}(\mathbf{z}, \hat{\mathbf{d}}_l; k_0),\ l = 1, 2, \cdots, L\ ;\ \mathbf{z} \in \Omega\right\}, \tag{4.10}$$

where $\mathcal{I}^{\infty}_{\mathrm{DSM}}(\mathbf{z}, \hat{\mathbf{d}}_l; k_0)$ is the indicator function for the direction of incident field $\hat{\mathbf{d}}_l$, as defined in (4.1). So it is easy to see that

$$\mathcal{I}^{\infty}_{\mathrm{DSM}}(\mathbf{z}; k_0) \propto \max\left\{\left|\sum_{m=1}^{M} \alpha_m^2(\varepsilon_m - \varepsilon_0)\,|\mathbf{D}_m|\,\mathrm{e}^{\mathrm{i}k_0\hat{\mathbf{d}}_l\cdot\mathbf{r}_m}\mathrm{J}_0(k_0|\mathbf{z} - \mathbf{r}_m|)\right|, l = 1, \ldots, L : \mathbf{z} \in \Omega\right\}. \tag{4.11}$$

It is interesting to observe that, according to (Ito, Jin, and J. Zou 2012; Li and Z. Zou 2013; W.-K. Park 2018a; W.-K. Park 2018b), the traditional DSM in the multi-static configuration is proportional to $|\mathrm{J}_0(k_0|\mathbf{r}_m - \mathbf{z}|)|$. By comparing the oscillation property of $\mathrm{J}_0(k_0|x|)$ and $\mathrm{J}_0(2k_0|x|)$, it can be shown that $\mathcal{I}^{\mathrm{mono}}_{\mathrm{MDSM}}(\mathbf{z}; k_0)$ will contain more artifacts than $\mathcal{I}^{\infty}_{\mathrm{DSM}}(\mathbf{z}; k_0)$.

4.2.4 Numerical simulations

Numerical experiments are provided to support the results presented in Theorems 4.2.4 and 4.2.2. For the simulation, a fixed frequency $f_0 = c_0/\lambda_0 \approx 749.481\,\mathrm{MHz}$, where $c_0 = 1/\sqrt{\varepsilon_0\mu_0}$ is the speed of light and $\lambda_0 = 0.4\,\mathrm{m}$, is considered. The number of incident and observation directions is set to $N = 36$, the latter being uniformly distributed on $\mathbb{S}^1$ except stated otherwise. We set Ω as a square of side length $4\lambda_0$ uniformly discretized with 51×51 square pixels. The far-field patterns $u_\infty(\hat{\mathbf{x}}_n, \hat{\mathbf{d}}_n; k_0)$ are generated via `FEKO` (EM simulation software), where

$$\hat{\mathbf{x}}_n = \left(\cos\frac{2\pi(n-1)}{N}, \sin\frac{2\pi(n-1)}{N}\right)$$

with $N = 36$. A 20 dB white Gaussian random noise is added to unperturbed data using `MATLAB` function `awgn` included in the signal processing package.

To compare the accuracy of the results, the Jaccard index in Appendix A is used. For each example the map of the indicator function is presented in the multi-static case (4.1) using the N^2 collected data and in the mono-static case using the N collected data thanks to either (4.4) or (4.6).

Example 4.2.5 (Small disks of same radii and permittivity) *First, we consider the small dielectric disks τ_m with $\alpha_m \equiv 0.075\lambda_0$ and $\varepsilon_m \equiv 5\varepsilon_0$, $m = 1, 2, 3$. The locations $\mathbf{r}_m$ of τ_m are $\mathbf{r}_1 = (0.75\lambda_0, -0.75\lambda_0)$, $\mathbf{r}_2 = (-\lambda_0, -0.5\lambda_0)$, and $\mathbf{r}_3 = (-0.75\lambda_0, \lambda_0)$.*

According to the results in Fig. 4.1, the location of $\mathbf{r}_m \in \tau_m$ can be identified using the classical DSM indicator function $\mathcal{I}^{\infty}_{\mathrm{DSM}}(\mathbf{z}; k_0)$ (3.1) when using the multi-static data (Figure 4.1(a)) but it fails when using the mono-static ones (Figure 4.1(b)), whereas more accurate locations are retrieved via the map of $\mathcal{I}^{\mathrm{mono}}_{\mathrm{MDSM}}(\mathbf{z}; k_0)$ (Fig. 4.1(c)); however, due to the intrinsic lack of information of the mono-static configuration, only two of the three defects are properly identified. As expected in the mono-static configuration a number of artifacts are also included in the map as discussed at the end of section 4.2.1.

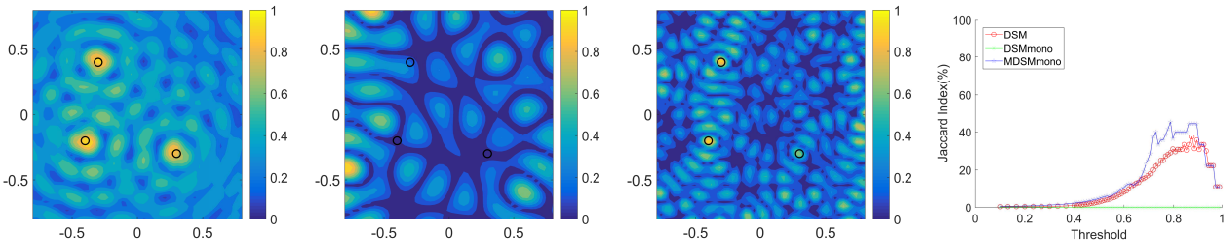

(a) $\mathcal{I}^{\infty}_{\mathrm{DSM}}(\mathbf{z};k_0)$ (b) $\mathcal{I}^{\mathrm{mono}}_{\mathrm{DSM}}(\mathbf{z};k_0)$ (c) $\mathcal{I}^{\mathrm{mono}}_{\mathrm{MDSM}}(\mathbf{z};k_0)$ (d) Jaccard index

Figure 4.1: Simulation results of Example 4.2.5

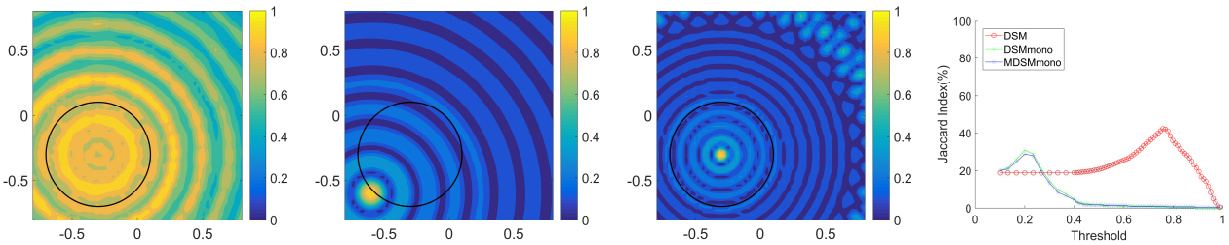

(a) $\mathcal{I}^{\infty}_{\mathrm{DSM}}(\mathbf{z};k_0)$ (b) $\mathcal{I}^{\mathrm{mono}}_{\mathrm{DSM}}(\mathbf{z};k_0)$ (c) $\mathcal{I}^{\mathrm{mono}}_{\mathrm{MDSM}}(\mathbf{z};k_0)$ (d) Jaccard index

Figure 4.2: Simulation results of Example 4.2.6

Example 4.2.6 (Large disk) *In order to verify that our approach still behaves properly when the small obstacle hypothesis is no longer verified, we are considering the identification of an extended target designed as a single disk circle τ located at $\mathbf{r} = (-0.75\lambda_0, -0.75\lambda_0)$ with radius $\alpha \equiv 1\lambda_0$ and permittivity $\varepsilon = 5\varepsilon_0$.*

Here also the shifting problem occurs in $\mathcal{I}^{\mathrm{mono}}_{\mathrm{DSM}}(\mathbf{z};k_0)$ as shown in Figure 4.2(b) whereas, when using $\mathcal{I}^{\mathrm{mono}}_{\mathrm{MDSM}}(\mathbf{z};k_0)$, a better localization of the center of the target is obtained (Figure 4.2(c)) even if none of them is able to estimate the shape and size of this target. As expected, better results are obtained when using the multi-static data (Figure 4.2(a)).

Example 4.2.7 (Limited aperture) *Motivated by the application in GPR and SAR, we apply the designed indicator function $\mathcal{I}^{mono}_{\mathrm{MDSM}}(\mathbf{z};k_0)$ when the range of incident and observation directions is limited. It is important to emphasize that due to the use of the far-field hypothesis such a configuration is not directly related to a GPR configuration, even if the influence of the limited aspect of the data is exemplified.*

The configuration is the same as for Example 4.2.5 except the range of incident and observation directions which is limited to the upper half-circle with only $N = 19$ collected far-field data. The simulation results are displayed in Figure 4.3. As for the two previous examples the results using the multi-static scattered field provide the best localizations (Figure 4.3(a)) whereas the mono-static case using the classical DSM does not provide any good results since the shifting problem still occurs (Figure 4.3(b)). As expected the mono-static modified DSM is able to localize two obstacles among the three (Figure 4.3(c)) as it was the case with full-view aperture (Figure 4.1(c)).

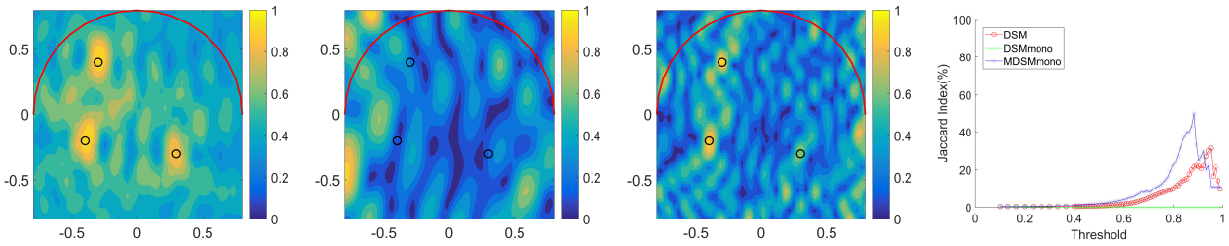

(a) Map of $\mathcal{I}_{\mathrm{DSM}}(\mathbf{z}; k_0)$ (b) Map of $\mathcal{I}^{\mathrm{mono}}_{\mathrm{DSM}}(\mathbf{z}; k_0)$ (c) Map of $\mathcal{I}^{\mathrm{mono}}_{\mathrm{MDSM}}(\mathbf{z}; k_0)$ (d) Jaccard index

Figure 4.3: Simulation results in Example 4.2.7. The red-colored solid line indicates the limited range of incident and observation directions.

4.3 Direct sampling method in limited-aperture configuration

Here, we focus on the structure analysis of DSM in limited-aperture problem as shown in Example 4.2.7. We define a finite set of observation directions $\mathbb{S}^1_{\mathrm{obs}}$ such as

$$\mathbb{S}^1_{\mathrm{obs}} := \left\{ \hat{\mathbf{x}}_n = (\cos\theta_n, \sin\theta_n) : \theta_n = \theta_1 + (\theta_N - \theta_1)\frac{n-1}{N-1},\ n = 1, 2, \cdots, N \right\} \subset \mathbb{S}^1, \tag{4.12}$$

for a fixed wavenumber k_0 and propagation direction $\hat{\mathbf{d}} \in \mathbb{S}^1$. The corresponding set of far-field pattern data $\mathbb{F}$ can also be defined by

$$\mathbb{F}_\star := \{u_\infty(\hat{\mathbf{x}}_n, \hat{\mathbf{d}}; k_0) : \hat{\mathbf{x}}_n \in \mathbb{S}^1_{\mathrm{obs}}\}. \tag{4.13}$$

Based on traditional DSM defined by (4.1), the indicator function of DSM in limited-aperture configuration can be introduced as follows: for $\mathbf{z} \in \Omega$,

$$\mathcal{I}^{\infty}_{\mathrm{DSM}}(\mathbf{z}; \hat{\mathbf{d}}, k_0) := \frac{\left| \left\langle u_\infty(\hat{\mathbf{x}}, \hat{\mathbf{d}}; k_0), \mathrm{e}^{-\mathrm{i}k_0\hat{\mathbf{x}}\cdot\mathbf{z}} \right\rangle_{L^2(\mathbb{S}^1_{\mathrm{obs}})} \right|}{\left\| u_\infty(\hat{\mathbf{x}}, \hat{\mathbf{d}}; k_0) \right\|_{L(\mathbb{S}^1_{\mathrm{obs}})} \left\| \mathrm{e}^{-\mathrm{i}k_0\hat{\mathbf{x}}\cdot\mathbf{z}} \right\|_{L^2(\mathbb{S}^1_{\mathrm{obs}})}}. \tag{4.14}$$

According to the previous work presented in Theorem 4.2.4, the result from $\mathcal{I}^{\infty}_{\mathrm{DSM}}(\mathbf{z}; \hat{\mathbf{d}}, k_0)$ should be $\mathcal{I}^{\infty}_{\mathrm{DSM}}(\mathbf{z}; \hat{\mathbf{d}}, k_0) = 1$ if $\mathbf{z} \in \tau$ while $\mathcal{I}^{\infty}_{\mathrm{DSM}} \neq 1$ if $\mathbf{z} \notin \tau$ due to the oscillation properties of the Bessel function. So the location of each inhomogeneity should be identified in the map of $\mathcal{I}^{\infty}_{\mathrm{DSM}}(\mathbf{z}; \hat{\mathbf{d}}, k_0)$, but other phenomena are observed in the limited-aperture configuration case, refer to Figure 4.7 for instance, so a new analysis and interpretation are needed to handle them.

4.3.1 Analysis of the indicator function for single and several incident fields

In this section, we derive the mathematical structure of indicator function $\mathcal{I}^{\infty}_{\mathrm{DSM}}(\mathbf{z}; \hat{\mathbf{d}}, k_0)$. Before starting, recall a useful result derived in (W.-K. Park 2015, Theorem 4.1) that demonstrates a relationship between exponential function and an infinite series of Bessel functions of integer order.

Lemma 4.3.1 *Let* $\mathbf{z} = |\mathbf{z}|\,(\cos\varphi, \sin\varphi) \in \mathbb{R}^2$ *and* $\hat{\mathbf{x}} \in \mathbb{S}^1_{\text{obs}}$. *Then, for sufficiently large* N, *the following relations holds uniformly*

$$\begin{aligned}\frac{1}{N}\sum_{n=1}^{N} \mathrm{e}^{\mathrm{i}k_0\hat{\mathbf{x}}_n\cdot\mathbf{z}} &\approx \frac{1}{\theta_N-\theta_1}\int_{\mathbb{S}^1_{\text{obs}}} \mathrm{e}^{\mathrm{i}k_0\hat{\mathbf{x}}\cdot\mathbf{z}}\mathrm{d}S(\hat{\mathbf{x}}) \\ &= \mathrm{J}_0(k_0|\mathbf{z}|) + \frac{4}{\theta_N-\theta_1}\sum_{s=1}^{\infty}\frac{\mathrm{i}^s}{s}\mathrm{J}_s(k_0|\mathbf{z}|)\cos\left(\frac{s\,(\theta_N+\theta_1-2\varphi)}{2}\right)\sin\left(\frac{s(\theta_N-\theta_1)}{2}\right).\end{aligned} \tag{4.15}$$

where J_s *denotes the Bessel function of first kind with order* s.

4.3.1.1 Single impinging direction

In the following, the mathematical structure of the DSM indicator function (Theorem 4.3.2) is derived thanks to the asymptotic formula (2.15) and a relationship (4.15).

Theorem 4.3.2 *Assume that the total number of observation directions* N *is sufficiently large. Let* $\mathbf{r}_m - \mathbf{z} = |\mathbf{r}_m - \mathbf{z}|(\cos\varphi_m, \sin\varphi_m)$. *Then, the DSM indicator function can be represented as*

$$\mathcal{I}^{\infty}_{\text{DSM}}(\mathbf{z};\hat{\mathbf{d}},k_0) \approx \frac{|\mathcal{L}_1(\mathbf{z},\hat{\mathbf{d}};k_0)|}{\max|\mathcal{L}_1(\mathbf{z},\hat{\mathbf{d}};k_0)|}, \tag{4.16}$$

where

$$\mathcal{L}_1(\mathbf{z},\hat{\mathbf{d}};k_0) := \sum_{m=1}^{M}\alpha_m^2|\mathbf{D}_m|\left(\frac{\varepsilon_m-\varepsilon_0}{\sqrt{\varepsilon_0\mu_0}}\right)\mathrm{e}^{\mathrm{i}k_0\hat{\mathbf{d}}\cdot\mathbf{r}_m}\left\{\mathrm{J}_0(k_0|\mathbf{r}_m-\mathbf{z}|) + \Lambda_S^{\theta_1,\theta_N}(k_0,|\mathbf{r}_m-\mathbf{z}|)\right\} \tag{4.17}$$

with

$$\begin{aligned}\Lambda_S^{\theta_1,\theta_N}(k_0,|\mathbf{r}_m-\mathbf{z}|) := \frac{4}{\theta_N-\theta_1}\sum_{s=1}^{\infty}\frac{\mathrm{i}^s}{s}\mathrm{J}_s(k_0|\mathbf{r}_m-\mathbf{z}|) \\ \times\cos\left(\frac{s\,(\theta_N+\theta_1-2\varphi_m)}{2}\right)\sin\left(\frac{s(\theta_N-\theta_1)}{2}\right).\end{aligned} \tag{4.18}$$

Proof Applying the asymptotic formula of far-field pattern (2.15) to the indicator function (4.14), we can evaluate

$$\begin{aligned}\left|\left\langle u_\infty(\hat{\mathbf{x}},\hat{\mathbf{d}};k_0), \mathrm{e}^{-\mathrm{i}k_0\hat{\mathbf{x}}\cdot\mathbf{z}}\right\rangle_{L^2(\mathbb{S}^1_{\text{obs}})}\right| &= \left|\sum_{m=1}^{M}\alpha_m^2|\mathbf{D}_m|\left(\frac{\varepsilon_m-\varepsilon_0}{\sqrt{\varepsilon_0\mu_0}}\right)\mathrm{e}^{\mathrm{i}k_0\hat{\mathbf{d}}\cdot\mathbf{r}_m}\sum_{n=1}^{N}\mathrm{e}^{\mathrm{i}k_0\hat{\mathbf{x}}_n\cdot(\mathbf{r}_m-\mathbf{z})}\right| \\ &\approx \left|\sum_{m=1}^{M}\alpha_m^2|\mathbf{D}_m|\left(\frac{\varepsilon_m-\varepsilon_0}{\sqrt{\varepsilon_0\mu_0}}\right)\mathrm{e}^{\mathrm{i}k_0\hat{\mathbf{d}}\cdot\mathbf{r}_m}\int_{\mathbb{S}^1_{\text{obs}}}\mathrm{e}^{\mathrm{i}k_0\hat{\mathbf{x}}\cdot(\mathbf{r}_m-\mathbf{z})}\mathrm{d}S(\hat{\mathbf{x}})\right|.\end{aligned} \tag{4.19}$$

The combination of (4.15) and (4.19) yields

$$\begin{aligned}\left|\left\langle u_\infty(\hat{\mathbf{x}},\hat{\mathbf{d}};k_0), \mathrm{e}^{-\mathrm{i}k_0\hat{\mathbf{x}}\cdot\mathbf{z}}\right\rangle_{L^2(\mathbb{S}^1_{\text{obs}})}\right| \approx \Bigg|\frac{\theta_N-\theta_1}{N}\frac{k_0^2(1+\mathrm{i})}{4\sqrt{k_0\pi}}\sum_{m=1}^{M}\alpha_m^2|\mathbf{D}_m|\left(\frac{\varepsilon_m-\varepsilon_0}{\sqrt{\varepsilon_0\mu_0}}\right)\mathrm{e}^{\mathrm{i}k_0\hat{\mathbf{d}}\cdot\mathbf{r}_m} \\ \times\left\{\mathrm{J}_0(k_0|\mathbf{r}_m-\mathbf{z}|) + \Lambda_S^{\theta_1,\theta_N}(k_0,|\mathbf{r}_m-\mathbf{z}|)\right\}\Bigg|\end{aligned} \tag{4.20}$$

where $\Lambda_S^{\theta_1,\theta_N}(k_0,|\mathbf{r}_m-\mathbf{z}|)$ is given by (4.18). Finally, applying Hölder's inequality completes the proof and leads to the final result (4.16). □

Remark 4.3.3 (Properties of indicator function)

1. *Based on the analyzed structure (4.16), the terms* $\mathrm{J}_0(k_0|\mathbf{r}_m-\mathbf{z}|)$ *and* $\Lambda_S^{\theta_1,\theta_N}(k_0,|\mathbf{r}_m-\mathbf{z}|)$ *contribute to and disturb the imaging performance, respectively, because* $\mathrm{J}_0(k_0|\mathbf{r}_m-\mathbf{z}|)=1$ *and* $\Lambda_S^{\theta_1,\theta_N}(k_0,|\mathbf{r}_m-\mathbf{z}|)=0$ *when* $\mathbf{z}=\mathbf{r}_m\in\tau_m$. *This means that it will be possible to identify the location of* τ_m *via the map of* $\mathcal{I}_{\mathrm{DSM}}^{\infty}(\mathbf{z};k_0)$. *Notice that, due to the oscillating property of the Bessel function, the map of* $\mathcal{I}_{\mathrm{DSM}}^{\infty}(\mathbf{z};k_0)$ *should contain artifacts.*

2. *It is worth mentioning that the term* $\mathrm{J}_0(k_0|\mathbf{r}_m-\mathbf{z}|)$ *is independent from the range of observation directions, but* $\Lambda_S^{\theta_1,\theta_N}(k_0,|\mathbf{r}_m-\mathbf{z}|)$ *significantly depends on the range of such directions. This means that eliminating or lowering the magnitude of the disturbing term* $\Lambda_S^{\theta_1,\theta_N}(k_0,|\mathbf{r}_m-\mathbf{z}|)$ *is important to improve the imaging accuracy.*

3. *If the range of observation directions is large, the effect of the term* $\Lambda_S^{\theta_1,\theta_N}(k_0,|\mathbf{r}_m-\mathbf{z}|)$ *becomes negligible, so that the imaging result will be good. In contrast, if the range of such directions becomes small, the term* $\Lambda_S^{\theta_1,\theta_N}(k_0,|\mathbf{r}_m-\mathbf{z}|)$ *will significantly affect the imaging performance.*

Remark 4.3.4 (Methods for improving imaging performance) *Based on the structure established in Theorem 4.3.2 and the discussion in Remark 4.3.3, further improvement is still required to improve imaging performance.*

1. *A way to improve the imaging performance of DSM in the limited-aperture configuration is to eliminate the disturbing term* $\Lambda_S^{\theta_1,\theta_N}(k_0,|\mathbf{r}_m-\mathbf{z}|)$. *An optimal solution would be to choose* θ_1 *and* θ_N *such as* $\Lambda_S^{\theta_1,\theta_N}(k_0,|\mathbf{r}_m-\mathbf{z}|)=0$. *Since* $\mathbf{z}$ *is arbitrary and* $\mathbf{r}_m$ *is unknown, we cannot handle the value of* $\mathrm{J}_s(k_0|\mathbf{r}_m-\mathbf{z}|)$ *so that the condition on the range has to be set on:*

$$\cos\left(\frac{s\,(\theta_N+\theta_1-2\varphi_m)}{2}\right)\sin\left(\frac{s(\theta_N-\theta_1)}{2}\right)=0,\quad s\in\mathbb{N}. \tag{4.21}$$

   a) *One possible selection is* $\theta_N-\theta_1=2\pi$, *i.e., full-view case. Based on Theorem 4.2.4, it turns out that*

$$\mathcal{I}_{\mathrm{DSM}}^{\infty}(\mathbf{z};\hat{\mathbf{d}},k_0)\approx\frac{|\mathcal{L}_1(\mathbf{z},\hat{\mathbf{d}};k_0)|}{\max|\mathcal{L}_1(\mathbf{z},\hat{\mathbf{d}};k_0)|}, \tag{4.22}$$

   where

$$\mathcal{L}_1(\mathbf{z},\hat{\mathbf{d}};k_0):=\sum_{m=1}^{M}\alpha_m^2|\mathbf{D}_m|\left(\frac{\varepsilon_m-\varepsilon_0}{\sqrt{\varepsilon_0\mu_0}}\right)\mathrm{e}^{\mathrm{i}k_0\hat{\mathbf{d}}\cdot\mathbf{r}_m}\mathrm{J}_0(k_0|\mathbf{r}_m-\mathbf{z}|). \tag{4.23}$$

   Therefore, since there is no disturbing term, one will obtain good imaging results.

   b) *Except the full-view case, the other way to satisfy (4.21) is to have* $\theta_N+\theta_1-2\varphi_m=\pi$ *and* $\theta_N-\theta_1=\pi$. *One possible solution is to choose* $\theta_1=\varphi_m$ *and* $\theta_N=\pi+\varphi_m$ *that satisfies (4.21). This means that one must know a priori information about* τ_m *(i.e., value of* φ_m*) for all* $m=1,2,\cdots,M$. *Based on this observation, it is possible to examine that if the range of the observation directions is wider than* π, *one can obtain an acceptable result, refer to Figure 4.5.*

2. *Notice that since*

$$\Lambda_S^{\theta_1,\theta_N}(k_0,|\mathbf{r}_m-\mathbf{z}|)=O\left(\frac{1}{(\theta_N-\theta_1)\sqrt{k_0|\mathbf{r}_m-\mathbf{z}|}}\right), \tag{4.24}$$

another way to eliminate the disturbing term $\Lambda_S^{\theta_1,\theta_N}(k_0,|\mathbf{r}_m-\mathbf{z}|)$ *is to apply sufficiently high frequency such as* $k_0\longrightarrow+\infty$. *However, this is an ideal assumption.*

4.3.1.2 Multiple impinging directions

Based on several investigations, it is obvious that application of several direction of incident field is another way of improve imaging accuracy. Now, let us introduce a finite set of incident directions $\mathbb{S}^1_{\text{inc}}$ such as

$$\mathbb{S}^1_{\text{inc}}:=\left\{\hat{\mathbf{d}}_l=(\cos\vartheta_l,\sin\vartheta_l):\vartheta_l=\vartheta_1+(\vartheta_L-\vartheta_1)\frac{l-1}{L-1},\ l=1,2,\cdots,L\right\}\subset\mathbb{S}^1. \tag{4.25}$$

On the basis of (Ito, Jin, and J. Zou 2012; Li and Z. Zou 2013), the indicator function of DSM with multiple impinging directions has been introduced by

$$\mathcal{I}_{\text{DSM}}(\mathbf{z};k_0):=\max_{\mathbf{z}\in\Omega}\left\{\mathcal{I}_{\text{DSM}}(\mathbf{z};\hat{\mathbf{d}}_1,k_0),\mathcal{I}_{\text{DSM}}(\mathbf{z};\hat{\mathbf{d}}_2,k_0),\cdots,\mathcal{I}_{\text{DSM}}(\mathbf{z};\hat{\mathbf{d}}_L,k_0)\right\}. \tag{4.26}$$

Remark 4.3.5 (Some properties) *We can observe several properties of* $\mathcal{I}^\infty_{\text{DSM}}(\mathbf{z};k_0)$ *of* (4.26) *which can be summarized as follows.*

1. *Based on the result in Theorem 4.3.2, we can observe that*

$$\mathcal{I}^\infty_{\text{DSM}}(\mathbf{z};k_0)\propto\max\left|\sum_{m=1}^M\alpha_m^2|\mathbf{D}_m|\left(\frac{\varepsilon_m-\varepsilon_0}{\sqrt{\varepsilon_0\mu_0}}\right)\mathrm{e}^{\mathrm{i}k_0\hat{\mathbf{d}}_l\cdot\mathbf{r}_m}\left\{\mathrm{J}_0(k_0|\mathbf{r}_m-\mathbf{z}|)+\Lambda_S^{\theta_1,\theta_N}(k_0,|\mathbf{r}_m-\mathbf{z}|)\right\}\right|. \tag{4.27}$$

Thus, the imaging result will be similar to the one via $\mathcal{I}^\infty_{\text{DSM}}(\mathbf{z};\hat{\mathbf{d}},k_0)$ *even with many incident fields.*

2. *Assume that the total number of observation directions is equal to one, i.e.,* $N=1$. *Then, since the following Jacobi-Anger expansion holds uniformly*

$$\mathrm{e}^{\mathrm{i}z\cos\theta}=\mathrm{J}_0(z)+2\sum_{s=1}^\infty\mathrm{i}^s\mathrm{J}_s(z)\cos(s\theta), \tag{4.28}$$

we can derive

$$\begin{aligned}&\lim_{\theta_N\to\theta_1}\Lambda_S^{\theta_1,\theta_N}(k_0,|\mathbf{r}_m-\mathbf{z}|)\\&=\lim_{\theta_N\to\theta_1}\frac{4}{\theta_N-\theta_1}\sum_{s=1}^\infty\frac{\mathrm{i}^s}{s}\mathrm{J}_s(k_0|\mathbf{r}_m-\mathbf{z}|)\cos\left(\frac{s\,(\theta_N+\theta_1-2\varphi_m)}{2}\right)\sin\left(\frac{s(\theta_N-\theta_1)}{2}\right)\\&=2\sum_{s=1}^\infty\mathrm{i}^s\mathrm{J}_s(k_0|\mathbf{r}_m-\mathbf{z}|)\cos(s\varphi_m)=\mathrm{e}^{\mathrm{i}k_0|\mathbf{r}_m-\mathbf{z}|\cos\varphi_m}-\mathrm{J}_0(k_0|\mathbf{r}_m-\mathbf{z}|).\end{aligned} \tag{4.29}$$

Thus, we arrive at

$$\mathcal{I}^\infty_{\text{DSM}}(\mathbf{z};k_0)\propto\max_{\mathbf{z}\in\Omega}\left|\sum_{m=1}^M\alpha_m^2|\mathbf{D}_m|\left(\frac{\varepsilon_m-\varepsilon_0}{\sqrt{\varepsilon_0\mu_0}}\right)\mathrm{e}^{\mathrm{i}k_0(\hat{\mathbf{d}}_l\cdot\mathbf{r}_m+|\mathbf{r}_m-\mathbf{z}|\cos\varphi_m)}\right|. \tag{4.30}$$

The relation indicates that in the case of a single observation direction, we have

$$\mathcal{I}^{\infty}_{\mathrm{DSM}}(\mathbf{z}; k_0) = 1 \quad \textit{for all} \quad \mathbf{z} \in \Omega. \tag{4.31}$$

and it will be impossible to identify the location of τ_m via $\mathcal{I}^{\infty}_{\mathrm{DSM}}(\mathbf{z}; k_0)$.

4.3.2 Alternative indicator function of DSM to improve imaging performance

Based on Remark 4.3.5, the accuracy of the indicator function $\mathcal{I}^{\infty}_{\mathrm{DSM}}(\mathbf{z}; k_0)$ is not significantly increased even though the total number of incident directions is getting large. Therefore, we must consider an alternative method for a further improvement. For the multiple incident directions within the full aperture case (S. Kang, Lambert, and W.-K. Park 2018b; W.-K. Park 2018b), it has been shown that an alternative indicator function (DSMA) defined by (4.32) yields a better imaging result than the traditional DSM given by (4.26).

$$\mathcal{I}^{\infty}_{\mathrm{DSMA}}(\mathbf{z}, k_0) := \frac{\left| \left\langle \left\langle u_{\infty}(\hat{\mathbf{x}}, \hat{\mathbf{d}}; k_0), \mathrm{e}^{-\mathrm{i}k_0 \hat{\mathbf{x}}_n \cdot \mathbf{z}} \right\rangle_{L^2(\mathbb{S}^1_{\mathrm{obs}})}, \mathrm{e}^{\mathrm{i}k_0 \hat{\mathbf{d}} \cdot \mathbf{z}} \right\rangle_{L^2(\mathbb{S}^1_{\mathrm{inc}})} \right|}{\max \left| \left\langle \left\langle u_{\infty}(\hat{\mathbf{x}}, \hat{\mathbf{d}}; k_0), \mathrm{e}^{-\mathrm{i}k_0 \hat{\mathbf{x}}_n \cdot \mathbf{z}} \right\rangle_{L^2(\mathbb{S}^1_{\mathrm{obs}})}, \mathrm{e}^{\mathrm{i}k_0 \hat{\mathbf{d}} \cdot \mathbf{z}} \right\rangle_{L^2(\mathbb{S}^1_{\mathrm{inc}})} \right|}, \tag{4.32}$$

where the inner product $\langle \cdot, \cdot \rangle_{L^2(\mathbb{S}^1_{\mathrm{obs}})}$ and norm $|| \cdot ||_{L^2(\mathbb{S}^1_{\mathrm{obs}})}$ are defined with (A.2).

Fortunately, $\mathcal{I}^{\infty}_{\mathrm{DSMA}}(\mathbf{z}, k_0)$ is still an improved version of $\mathcal{I}^{\infty}_{\mathrm{DSM}}(\mathbf{z}; k_0)$ of (4.26) in the limited aperture configuration. The theorem is as follows.

Theorem 4.3.6 *Assume that the total number of observation directions N and incident directions L is sufficiently large. Then, the indicator function $\mathcal{I}_{\mathrm{DSMA}}(\mathbf{z}, k_0)$ can be represented as*

$$\mathcal{I}^{\infty}_{\mathrm{DSMA}}(\mathbf{z}; k_0) = \frac{|\mathcal{L}_2(\mathbf{z}; k_0)|}{\max |\mathcal{L}_2(\mathbf{z}; k_0)|}, \tag{4.33}$$

where

$$\begin{aligned} \mathcal{L}_2(\mathbf{z}; k_0) := \sum_{m=1}^{M} \alpha_m^2 |\mathbf{D}_m| \left(\frac{\varepsilon_m - \varepsilon_0}{\sqrt{\varepsilon_0 \mu_0}} \right) [\mathrm{J}_0(k_0 |\mathbf{r}_m - \mathbf{z}|)^2 + \left(\Lambda_S^{\theta_1, \theta_N}(k_0, |\mathbf{r}_m - \mathbf{z}|) + \Lambda_S^{\vartheta_1, \vartheta_L}(k_0, |\mathbf{r}_m - \mathbf{z}|) \right) \\ \times \mathrm{J}_0(k_0 |\mathbf{r}_m - \mathbf{z}|) + \Lambda_S^{\theta_1, \theta_N}(k_0, |\mathbf{r}_m - \mathbf{z}|) \Lambda_S^{\vartheta_1, \vartheta_L}(k_0, |\mathbf{r}_m - \mathbf{z}|)]. \end{aligned} \tag{4.34}$$

Here, $\Lambda_S^{\alpha, \beta}(k_0, |\mathbf{r}_m - \mathbf{z}|)$ is given by (4.18).

Proof By combining (4.20) and (4.32),

$$\begin{aligned} &\left| \left\langle \left\langle u_{\infty}(\hat{\mathbf{x}}, \hat{\mathbf{d}}; k_0), \mathrm{e}^{-\mathrm{i}k_0 \hat{\mathbf{x}} \cdot \mathbf{z}} \right\rangle_{L^2(\mathbb{S}^1_{\mathrm{obs}})}, \mathrm{e}^{-\mathrm{i}k_0 \hat{\mathbf{d}} \cdot \mathbf{z}} \right\rangle_{L^2(\mathbb{S}^1_{\mathrm{inc}})} \right| \\ &\quad = \left| \frac{k_0^2 (1 + \mathrm{i})}{4 \sqrt{k_0 \pi}} \sum_{m=1}^{M} \mathcal{A}_m \left(\int_{\mathbb{S}^1_{\mathrm{inc}}} \mathrm{e}^{\mathrm{i}k_0 \hat{\mathbf{d}} \cdot (\mathbf{r}_m - \mathbf{z})} \mathrm{d}S(\hat{\mathbf{d}}) \right) (\theta_N - \theta_1) \left\{ \mathrm{J}_0(k_0 |\mathbf{r}_m - \mathbf{z}|) + \Lambda_S^{\theta} \right\} \right|, \end{aligned} \tag{4.35}$$

where $A_m := \alpha_m^2 |\mathbf{D}_m| \left(\frac{\varepsilon_m - \varepsilon_0}{\sqrt{\varepsilon_0 \mu_0}}\right)$ and $\Lambda_S^{\theta_1,\theta_N}(k_0, |\mathbf{r}_m - \mathbf{z}|)$ is given by (4.18). The Lemma 4.3.1 yields

$$\left| \left\langle \left\langle u_\infty(\hat{\mathbf{x}}, \hat{\mathbf{d}}; k_0), \mathrm{e}^{-\mathrm{i}k_0 \hat{\mathbf{x}}\cdot\mathbf{z}} \right\rangle_{L^2(\mathbb{S}^1_{\mathrm{obs}})}, \mathrm{e}^{-\mathrm{i}k_0 \hat{\mathbf{d}}\cdot\mathbf{z}} \right\rangle_{L^2(\mathbb{S}^1_{\mathrm{inc}})} \right| = \left| (\vartheta_L - \vartheta_1)(\theta_N - \theta_1) \frac{k_0^2(1+\mathrm{i})}{4\sqrt{k_0 \pi}} \sum_{m=1}^{M} \mathcal{A}_m \right.$$
$$\left. \times \left\{ \mathrm{J}_0(k_0|\mathbf{r}_m - \mathbf{z}|) + \Lambda_S^{\vartheta_1,\vartheta_L}(k_0, |\mathbf{r}_m - \mathbf{z}|) \right\} \left\{ \mathrm{J}_0(k_0|\mathbf{r}_m - \mathbf{z}|) + \Lambda_S^{\theta_1,\theta_N}(k_0, |\mathbf{r}_m - \mathbf{z}|) \right\} \right|. \quad (4.36)$$

Then, applying Hölder inequality leads to (4.33), which completes the proof. □

Remark 4.3.7 (Properties of indicator function) *On the basis of the identified structure (4.33), we can examine some properties of DSMA.*

1. *Similar to the properties of $\mathcal{I}^\infty_{\mathrm{DSM}}(\mathbf{z}, \hat{\mathbf{d}}; k_0)$ stated in Remark 4.3.3, $\mathrm{J}_0(k_0|\mathbf{r}_m - \mathbf{z}|)^2$ contributes to, and $\Lambda_S^{\theta_1,\theta_N}(k, |\mathbf{r}_m - \mathbf{z}|)$ and $\Lambda_S^{\vartheta_1,\vartheta_L}(k, |\mathbf{r}_m - \mathbf{z}|)$ disturb the retrieval of the location of τ_m via $\mathcal{I}^\infty_{\mathrm{DSMA}}(\mathbf{z}; k_0)$. The map of $\mathcal{I}^\infty_{\mathrm{DSMA}}(\mathbf{z}; k_0)$ will have peaks at the center of τ_m due to the properties of $\mathrm{J}_0(k_0|\mathbf{r}_m - \mathbf{z}|)^2$, which means that the location of each inhomogeneity can be identified by the map of $\mathcal{I}^\infty_{\mathrm{DSMA}}(\mathbf{z}; k_0)$.*

2. *It is worth noticing that the contributing term $\mathrm{J}_0(k_0|\mathbf{r}_m - \mathbf{z}|)^2$ is independent upon the range of incident and/or observation directions like in the case of DSM. So it is sufficient to compare contributing terms of $\mathcal{I}^\infty_{\mathrm{DSMA}}(\mathbf{z}; k_0)$ and $\mathcal{I}^\infty_{\mathrm{DSM}}(\mathbf{z}; k_0)$ to compare their imaging performance:*

$$\mathcal{I}^\infty_{\mathrm{DSMA}}(\mathbf{x}; k_0) \propto |\mathrm{J}_0(k_0|\mathbf{r}_m - \mathbf{z}|)^2| \quad \textit{and} \quad \mathcal{I}^\infty_{\mathrm{DSM}}(\mathbf{x}; k_0) \propto |\mathrm{J}_0(k_0|\mathbf{r}_m - \mathbf{z}|)| \quad (4.37)$$

Note that $|\mathrm{J}_0(k_0|\mathbf{z}|)|^2$ has many less oscillations than $|\mathrm{J}_0(k_0|\mathbf{z}|)|$ (see Figure 4.4 for illustration). This means that $\mathcal{I}^\infty_{\mathrm{DSMA}}(\mathbf{z}; k_0)$ is an improved version of $\mathcal{I}^\infty_{\mathrm{DSM}}(\mathbf{z}; k_0)$, which is the same result as in chapter 3 (full-aperture case).

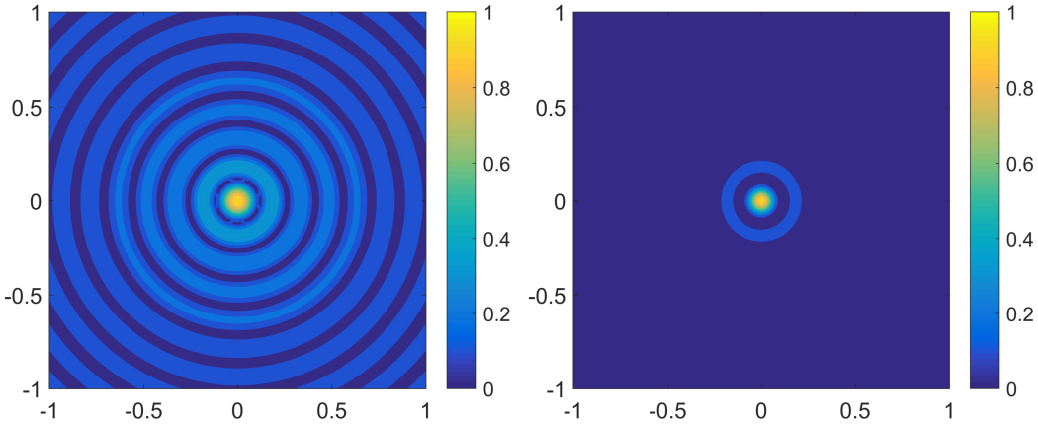

(a) $|\mathrm{J}_0(k_0|\mathbf{z}|)|$ (b) $|\mathrm{J}_0(k_0|\mathbf{z}|)^2|$

Figure 4.4: Two-dimensional plots of $|\mathrm{J}_0(k_0|\mathbf{z}|)|$ and $|\mathrm{J}_0(k_0|\mathbf{z}|)^2|$ using $f_0 = 1\,\mathrm{GHz}$

Remark 4.3.8 (Improving imaging performance) *Since the disturbing terms* $\Lambda_S^{\theta_1,\theta_N}(k,|\mathbf{r}_m-\mathbf{z}|)$ *and* $\Lambda_S^{\vartheta_1,\vartheta_L}(k,|\mathbf{r}_m-\mathbf{z}|)$ *are significantly depending on the range of incident and/or observation directions, we have to choose the ranges* $[\theta_1,\theta_N]$ *and* $[\vartheta_1,\vartheta_L]$ *satisfying* $\Lambda_S^{\theta_1,\theta_N}(k,|\mathbf{r}_m-\mathbf{z}|)=0$ *and* $\Lambda_S^{\vartheta_1,\vartheta_L}(k,|\mathbf{r}_m-\mathbf{z}|)=0$*, respectively. In other words, we must find a condition of incident and observation directions to satisfy*

$$\cos\left(\frac{s\,(\vartheta_N+\vartheta_1-2\varphi_m)}{2}\right)\sin\left(\frac{s(\vartheta_L-\vartheta_1)}{2}\right)=0, \tag{4.38}$$

and

$$\cos\left(\frac{t\,(\theta_N+\theta_1-2\varphi_m)}{2}\right)\sin\left(\frac{t(\theta_N-\theta_1)}{2}\right)=0, \tag{4.39}$$

respectively for integers s *and* t*. Similar to the Remark 4.3.4, we can say that (i) full-aperture of observation* ($\theta_N-\theta_1=2\pi$) *and incident* ($\vartheta_L-\vartheta_1=2\pi$) *and (ii) the ranges of observation and incident directions wider than* π *will provide a good imaging performance of DSMA.*

4.3.3 Numerical simulations

We validate our theoretical results via various numerical simulations with synthetic and experimental data. To compare the imaging efficiency, the Jaccard index A.3 is again adopted here. Note that the red line and black line indicate the $\mathbf{x}_n$ and $-\hat{\mathbf{d}}_l$, respectively.

Synthetic data A fixed frequency $f_0=c_0/\lambda_0=1\,\text{GHz}$ is considered where $c_0=1/\sqrt{\varepsilon_0\mu_0}$ is the speed of light and $\lambda_0\approx 0.3\,\text{m}$. The far-field patterns are measured at N observation directions uniformly distributed on $\mathbb{S}^1_{\text{obs}}$ for each of the L incident directions $\hat{\mathbf{d}}\in\mathbb{S}^1_{\text{inc}}$, here, $\mathbb{S}^1_{\text{obs}}$ and $\mathbb{S}^1_{\text{inc}}$ are the simply connected subsets of $\mathbb{S}^1$.

The range and number of observation directions are defined by $[\theta_1,\theta_N]$ and N, respectively, the angle between two adjacent directions being as $\Delta\theta=(\theta_N-\theta_1)/(N-1)$. The various acquisition configurations are shown in Table 4.1. The cases for the incident directions are given by Table 4.2 analogously, where $[\vartheta_1,\vartheta_L]$ and L are the range and number of incident directions, respectively.

Cases	θ_1	θ_N	N	Description
Case A1	180°	180°	1	Single receiver direction
Case A2	135°	225°	19	Narrow, limited observation directions
Case A3	90°	270°	37	Semi-circular range, limited observation directions
Case A4	45°	315°	55	Wide, limited observation directions

Table 4.1: Values of θ_1, θ_N, and N used to obtained the synthetic data

The region of interest Ω is a square of side length $20\lambda_0/3=2\,\text{m}$ uniformly discretized in 51×51 pixels. The far-field patterns $u_\infty(\hat{\mathbf{x}}_n,\hat{\mathbf{d}}_l;k_0),\ n=1,2,\cdots,N,\ l=1,2,\cdots,L$ are generated by `FEKO` (EM simulation software) as previously and a 20 dB white Gaussian random noise is added using the `MATLAB` function `awgn` included in signal processing package.

Example 4.3.9 (Small dielectric disk) *First, a single small dielectric disk with radius* $\alpha\equiv 0.1\lambda_0=0.03\,\text{m}$ *and permittivity* $\varepsilon\equiv 5\varepsilon_0$ *is considered. It is located at* $\mathbf{r}=(-0.3333\lambda_0,0.6667\lambda_0)=(-0.1\,\text{m},0.2\,\text{m})$

Cases	ϑ_1	ϑ_L	L	Description
Case B1	180°	180°	1	Single incident direction
Case B2	135°	225°	19	Narrow, limited incident directions
Case B3	90°	270°	37	Semi-circular range, limited incident directions
Case B4	45°	315°	55	Wide, limited incident directions

Table 4.2: Values of ϑ_1, ϑ_L, and L used to obtained the synthetic data

All the results obtained from the combination of the configurations presented in Tables 4.1 and 4.2 are gathered in Figure 4.5 for DSM and in Figure 4.6 for DSMA. According to Remark 4.3.5, DSM is unable to identify the inhomogeneities when using only one receiver whatever the number of sources as shown in Figure 4.5 (first line). The targets τ_m, $m = 1, 2, 3$ cannot be identified if the observation range is too narrow ($\theta_1 - \theta_N < 2\pi$) as exemplified in case A1 and A2 (first and second rows, respectively) via DSM with single-frequency even though incident directions are increased. On the other hand, imaging efficiencies are improved when the total number of incident directions is increased via the maps of $\mathcal{I}_{\text{DSMA}}(\mathbf{z}; k_0)$, see cases A1 and A2 in Figure 4.6. In cases A3, A4, and A5 which verify $\pi \leq \theta_N - \theta_1 \leq 2\pi$, the targets τ_m can be identified via the maps of $\mathcal{I}^{\infty}_{\text{DSM}}(\mathbf{z}; k_0)$ and $\mathcal{I}^{\infty}_{\text{DSMA}}(\mathbf{z}; k_0)$. According to the Jaccard index (bottom row), it can be shown, as expected, that the larger the range of observation directions, the better the results.

Example 4.3.10 (Small three dielectric disks with same size and permittivity) *The small dielectric disks τ_m with $\alpha_m \equiv 0.1\lambda_0 = 0.03\,\text{m}$ and $\varepsilon_m \equiv 5\varepsilon_0$, $m = 1, 2, 3$ are considered. Their locations of τ_m are $\mathbf{r}_1 = (-8\lambda_0/3, 0) = (-0.8\,\text{m}, 0)$, $\mathbf{r}_2 = (4\lambda_0/3, -2\lambda_0) = (0.4\,\text{m}, -0.6\,\text{m})$, and $\mathbf{r}_3 = (\lambda_0/3, 2\lambda_0) = (0.1\,\text{m}, 0.6\,\text{m})$.*

Figure 4.7 and 4.8 display the results with respect to cases of ranges of incident and observation directions in Tables 4.1 and 4.2. Even though more oscillations are observed in both maps of $\mathcal{I}^{\infty}_{\text{DSM}}(\mathbf{z}; k_0)$ and $\mathcal{I}^{\infty}_{\text{DSMA}}(\mathbf{z}; k_0)$ because of the interaction between inhomogeneities, the results are almost similar to those of Example 4.3.9 (single target case).

Example 4.3.11 (Large dielectric disk) *In order to verify that our proposal still behaves properly when the small obstacle hypothesis is no longer verified, we are considering the case of a large circular single inhomogeneity of location $\mathbf{r} = (-\lambda_0, -\lambda_0)$ and radius $\alpha_m \equiv \lambda_0$, respectively, the dielectric permittivity being given by $\varepsilon \equiv 5\varepsilon_0$.*

As shown in Figure 4.9, in contrast with results of Example 4.3.10, we cannot identify exact shape and location from the map of $\mathcal{I}^{\infty}_{\text{DSM}}(\mathbf{z}, \hat{\mathbf{d}}; k_0)$ even with broad (i.e., $\theta_N - \theta_1 \geq \pi$) ranges of observation directions but with the narrow range of incident directions. On the contrary, by using the indicator function of DSMA instead of DSM, the location of the inhomogeneity can be identified even with a narrow range of observation directions when the range of incident directions is increased.

Experimental data In the following, the efficiency of the DSM algorithm and of our theoretical developments are verified using the Fresnel experimental data (Belkebir and Saillard 2001). The cases

of two dielectric disks, square, and metallic U-shaped target are considered using the 4 GHz results, which corresponds to the following wavelength $\lambda_0 \approx 0.075\,\mathrm{m}$. The region of interest $\Omega := [1\lambda_0]$ is a square of side length $2\lambda_0 \approx 0.15\,\mathrm{m}$ uniformly discretized with 51×51 pixels. It is worth to note that

- due to experimental set-up limitations the full-view problem is not available. More specifically, the maximum range or observation directions is $\theta_1 = 60°$ and $\theta_N = 300°$ for $N = 49$.
- the scattered field has been measured within the near-field configuration but the antennas are located far from the region of interest. Hence, it can be approximated by the far-field pattern.
- the cases depend on the range of observation direction for limited-ranged of incident direction are unavailable since the locations of observation direction are changed for each incident direction. Therefore, the DSM is only applied since it has same performance as DSMA as is already stated in Remark 3.4.2.

We refer (Belkebir and Saillard 2001) for additional details about the experimental set-up and various cases shown in Table 4.3 will be used.

Cases	θ_1	θ_N	N	Description
Case 1	150°	210°	12	Narrow, limited-aperture problem
Case 2	135°	225°	18	Narrow, limited-aperture problem
Case 3	120°	240°	24	Not narrow, limited-aperture problem
Case 4	90°	270°	36	Semi-circular range, limited-aperture problem
Case 5	60°	300°	54	Wide, limited-aperture problem but maximum range

Table 4.3: Values of θ_1 and θ_N, and N for numerical simulations with experimental data

Example 4.3.12 (Small two dielectric disks with same size and permittivity) *The radius and dielectric permittivity being* $0.015\,\mathrm{m}$ *and* $\varepsilon \propto 3\varepsilon_0$*, where* ε_0 *is the background permittivity, respectively. The locations of the targets are* $(-0.012\,\mathrm{m}, -0.045\,\mathrm{m})$ *and* $(0\,\mathrm{m}, 0.045\,\mathrm{m})$.

According to Figure 4.11 and as expected, the results are similar with those obtained in Example 4.3.10 so the same conclusions can be drawn, the imaging performance of the DSM increases with respect to the range of the acquisition angle, which verifies again our theoretical results and the related remarks (Remarks 4.3.4 and 4.3.8).

Example 4.3.13 (Small metallic square) *Now, we consider a metallic and quadrangular target which is non-circular. It is located at* $\mathbf{r} \approx (0\,\mathrm{m}, 0.04\,\mathrm{m})$ *and has side lengths* $0.0127\,\mathrm{m}$ *and* $0.0245\,\mathrm{m}$.

The results are displayed in Figure 4.12. They show that the accuracy of the localization of the target via DSM is getting better as the range of observation directions is wider. But the maps of DSM have a maximum value at the right side of target, which is the direction of the incident field, even with a wide range of observation directions. Therefore, it is essential to use a wider range of incident directions to achieve a better accuracy of imaging.

Example 4.3.14 (Metallic U-shape) *More complex U-shaped metal is considered here. Its size is* $0.05\,\mathrm{m} \times 0.08\,\mathrm{m}$ *with thickness* $0.005\,\mathrm{m}$.

Figure 4.13 shows that we cannot reconstruct the shape and location of the target using a single incident direction even with a wide range of observation directions. As already shown in Example 3.6.3, more incident directions are necessary to get a proper reconstruction.

4.4 Conclusions

In this chapter, we considered the direct sampling method in restricted configurations (mono-static and limited-aperture configurations). Thanks to the use of the asymptotic expansion formula of far-field pattern in the presence of small inhomogeneities and the far-field hypothesis, the mathematical structures of the indicator function of the traditional DSM and its improved versions (MDSM in the mono-static case and DSMA in limited-aperture case) are established. Especially, the reason for which it fails to image the targets is clearly identified in the mono-static configuration and MDSM is proposed to overcome the miss-localization. In the limited-aperture problem, we explored that DSM and DSMA are related to infinite series of Bessel functions of integer orders, range of observation and incident directions, and physical information of targets (e.g., location, shape, size, and dielectric permittivity), and the relation between accuracy of algorithms and the measurement set-up is also verified. Various numerical simulations with synthetic and experimental data are presented to support our theoretical results.

Nevertheless, some improvements are still required to improve imaging performance with restricted ranges of observation and incident directions. So the multi-frequency approach of DSM in the limited aperture scattering problem will be treated to that effect in the next chapter.

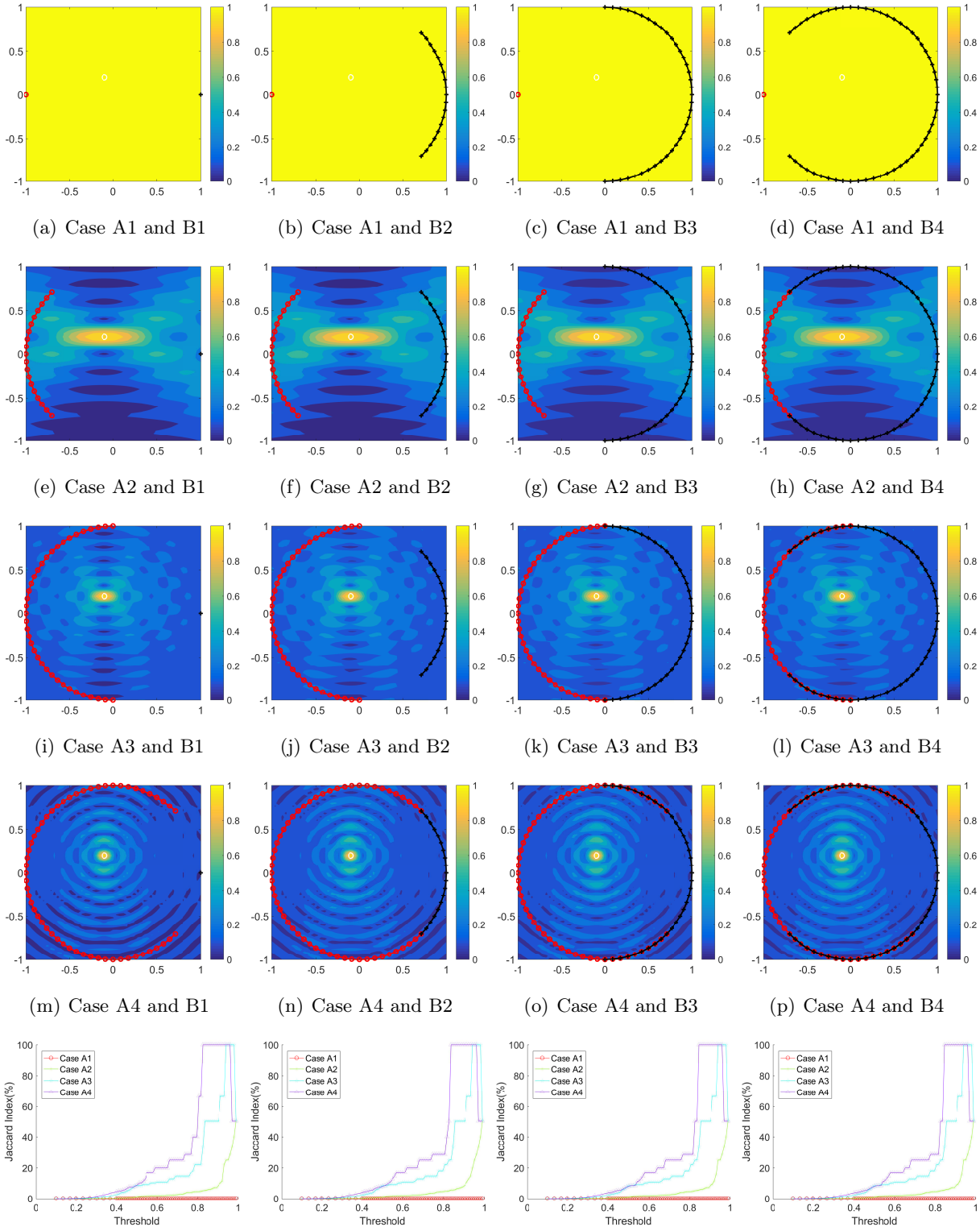

(a) Case A1 and B1 (b) Case A1 and B2 (c) Case A1 and B3 (d) Case A1 and B4

(e) Case A2 and B1 (f) Case A2 and B2 (g) Case A2 and B3 (h) Case A2 and B4

(i) Case A3 and B1 (j) Case A3 and B2 (k) Case A3 and B3 (l) Case A3 and B4

(m) Case A4 and B1 (n) Case A4 and B2 (o) Case A4 and B3 (p) Case A4 and B4

(q) Jaccard index (B1 case) (r) Jaccard index (B2 case) (s) Jaccard index (B3 case) (t) Jaccard index (B4 case)

Figure 4.5: (Example 4.3.9) Maps of $\mathcal{I}^{\infty}_{\mathrm{DSM}}(\mathbf{z}; k_0)$ and Jaccard index

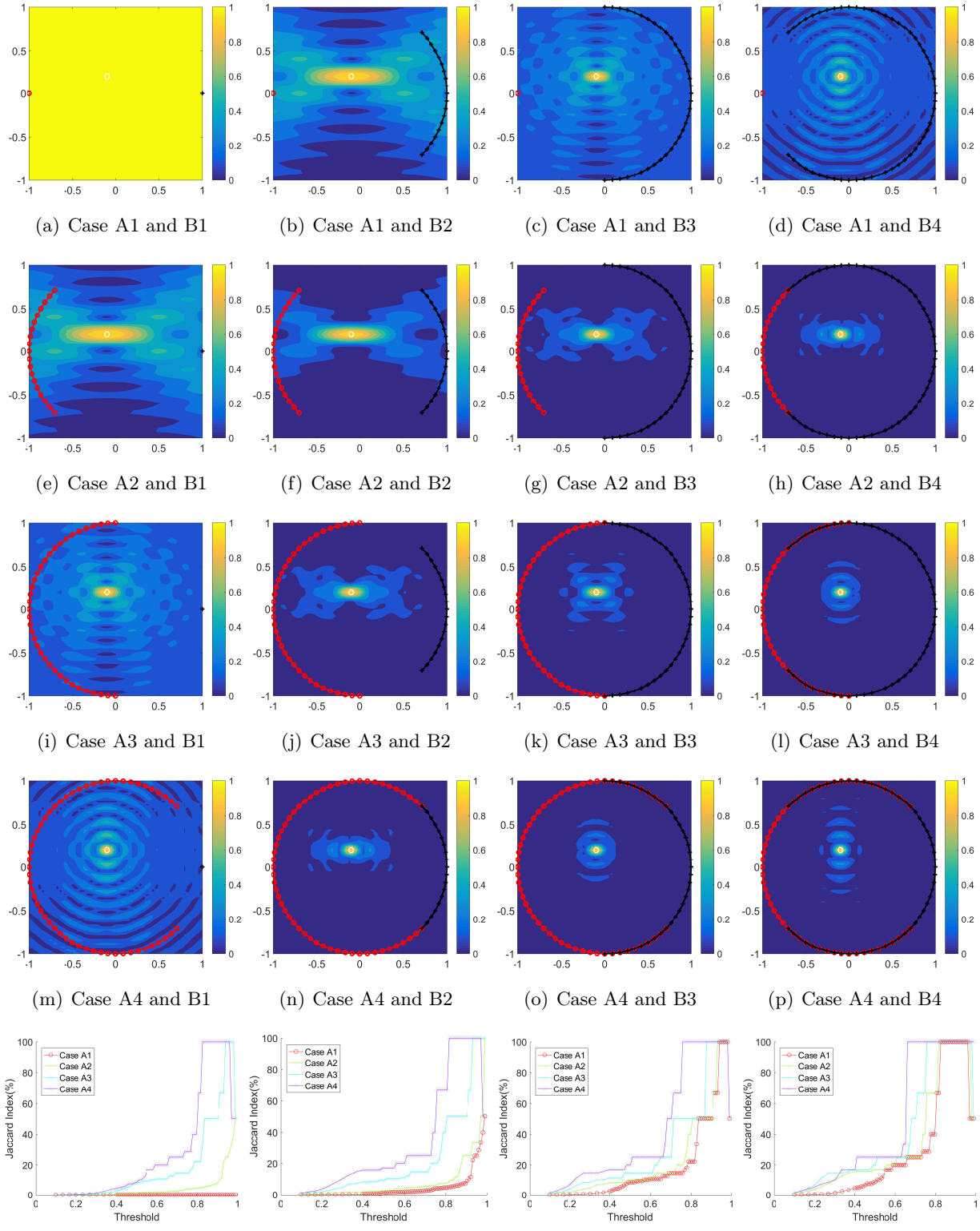

(a) Case A1 and B1 (b) Case A1 and B2 (c) Case A1 and B3 (d) Case A1 and B4

(e) Case A2 and B1 (f) Case A2 and B2 (g) Case A2 and B3 (h) Case A2 and B4

(i) Case A3 and B1 (j) Case A3 and B2 (k) Case A3 and B3 (l) Case A3 and B4

(m) Case A4 and B1 (n) Case A4 and B2 (o) Case A4 and B3 (p) Case A4 and B4

(q) Jaccard index (B1 case) (r) Jaccard index (B2 case) (s) Jaccard index (B3 case) (t) Jaccard index (B4 case)

Figure 4.6: (Example 4.3.9) Maps of $\mathcal{I}^{\infty}_{\mathrm{DSMA}}(\mathbf{z}; k_0)$ and Jaccard index

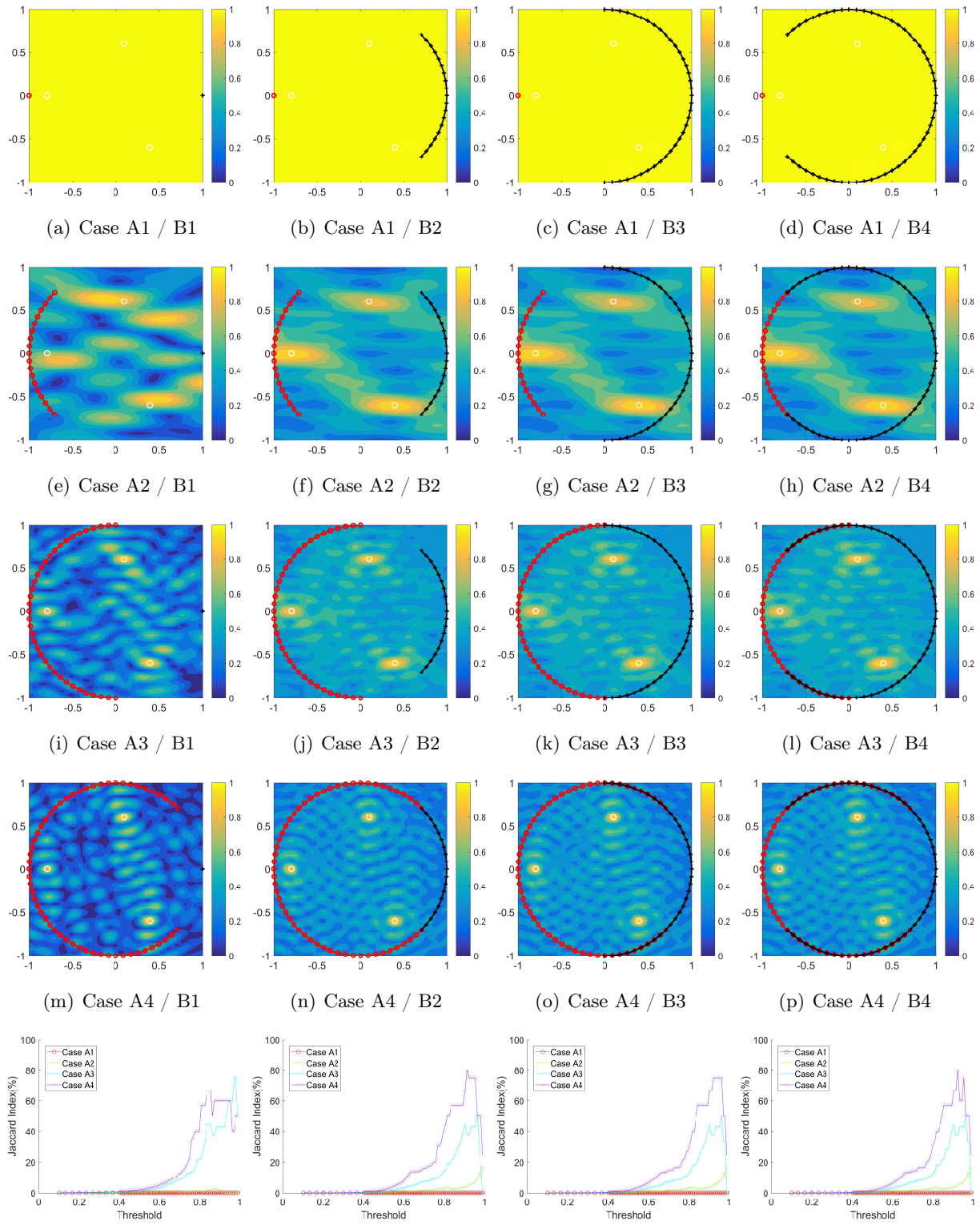

(a) Case A1 / B1 (b) Case A1 / B2 (c) Case A1 / B3 (d) Case A1 / B4

(e) Case A2 / B1 (f) Case A2 / B2 (g) Case A2 / B3 (h) Case A2 / B4

(i) Case A3 / B1 (j) Case A3 / B2 (k) Case A3 / B3 (l) Case A3 / B4

(m) Case A4 / B1 (n) Case A4 / B2 (o) Case A4 / B3 (p) Case A4 / B4

(q) Jaccard index (B1 case) (r) Jaccard index (B2 case) (s) Jaccard index (B3 case) (t) Jaccard index (B4 case)

Figure 4.7: (Example 4.3.10) Maps of $\mathcal{I}^{\infty}_{\mathrm{DSM}}(\mathbf{z}; k_0)$ and Jaccard index

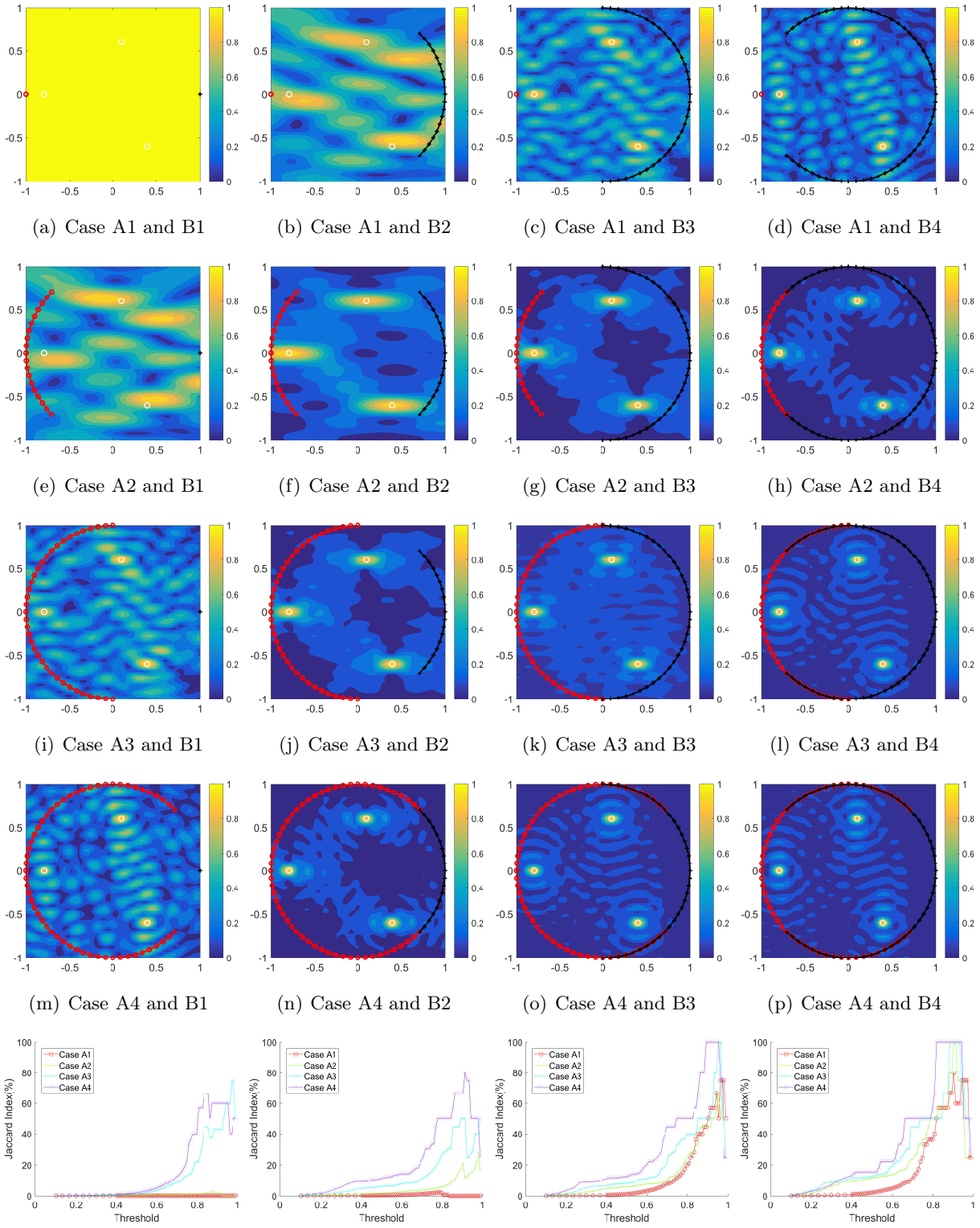

(a) Case A1 and B1 (b) Case A1 and B2 (c) Case A1 and B3 (d) Case A1 and B4

(e) Case A2 and B1 (f) Case A2 and B2 (g) Case A2 and B3 (h) Case A2 and B4

(i) Case A3 and B1 (j) Case A3 and B2 (k) Case A3 and B3 (l) Case A3 and B4

(m) Case A4 and B1 (n) Case A4 and B2 (o) Case A4 and B3 (p) Case A4 and B4

(q) Jaccard index (B1 case) (r) Jaccard index (B2 case) (s) Jaccard index (B3 case) (t) Jaccard index (B4 case)

Figure 4.8: (Example 4.3.10) Maps of $\mathcal{I}^{\infty}_{\mathrm{DSMA}}(\mathbf{z}; k_0)$ and Jaccard index

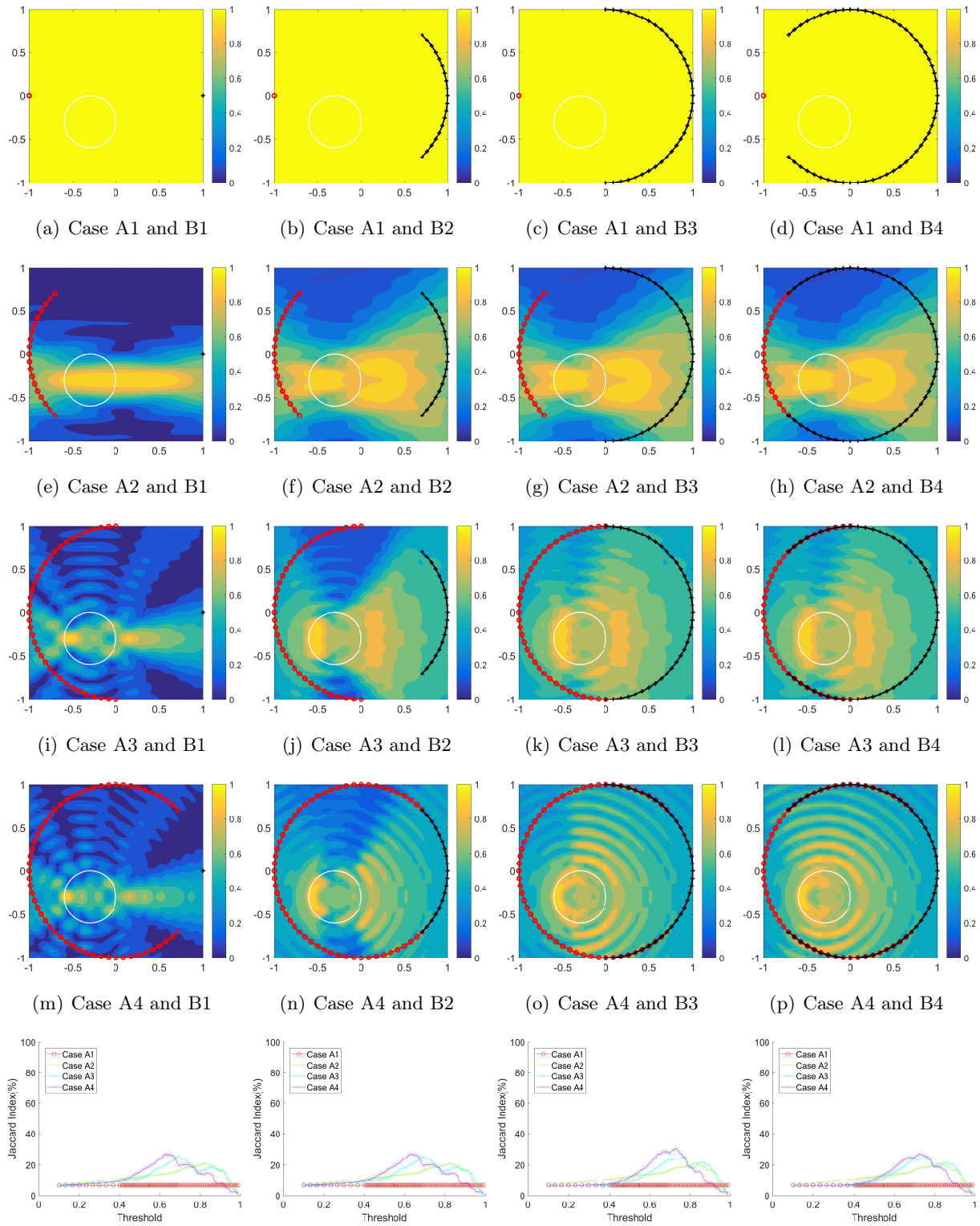

(a) Case A1 and B1 (b) Case A1 and B2 (c) Case A1 and B3 (d) Case A1 and B4

(e) Case A2 and B1 (f) Case A2 and B2 (g) Case A2 and B3 (h) Case A2 and B4

(i) Case A3 and B1 (j) Case A3 and B2 (k) Case A3 and B3 (l) Case A3 and B4

(m) Case A4 and B1 (n) Case A4 and B2 (o) Case A4 and B3 (p) Case A4 and B4

(q) Jaccard index when B1 case (r) Jaccard index when B1 case (s) Jaccard index when B1 case (t) Jaccard index when B1 case

Figure 4.9: (Example 4.3.10) Maps of $\mathcal{I}^{\infty}_{\mathrm{DSM}}(\mathbf{z}; k_0)$ and Jaccard index

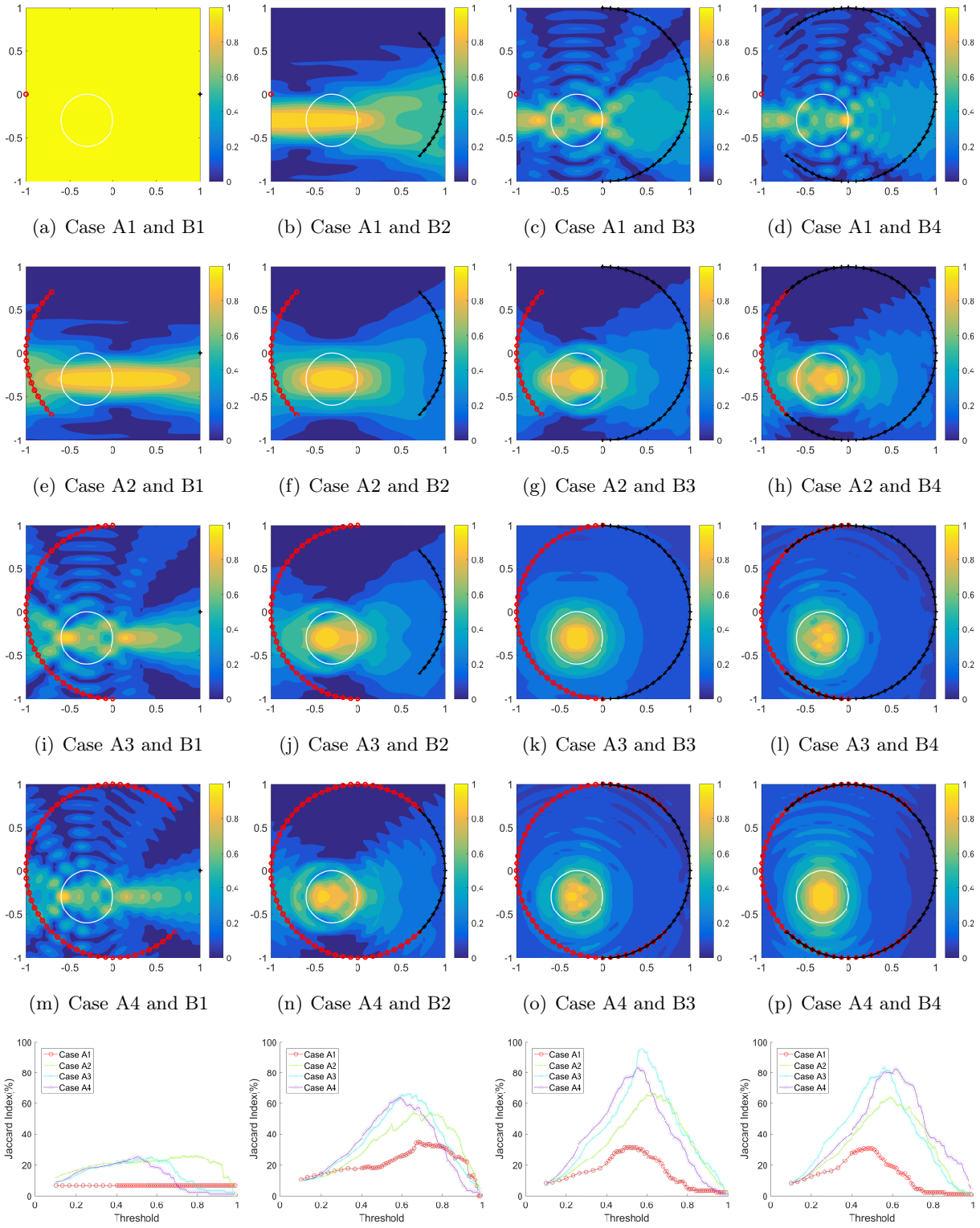

(a) Case A1 and B1 (b) Case A1 and B2 (c) Case A1 and B3 (d) Case A1 and B4

(e) Case A2 and B1 (f) Case A2 and B2 (g) Case A2 and B3 (h) Case A2 and B4

(i) Case A3 and B1 (j) Case A3 and B2 (k) Case A3 and B3 (l) Case A3 and B4

(m) Case A4 and B1 (n) Case A4 and B2 (o) Case A4 and B3 (p) Case A4 and B4

(q) Jaccard index when B1 case (r) Jaccard index when B1 case (s) Jaccard index when B1 case (t) Jaccard index when B1 case

Figure 4.10: (Example 4.3.11) Maps of $\mathcal{I}^{\infty}_{\mathrm{DSMA}}(\mathbf{z}; k_0)$ and Jaccard index

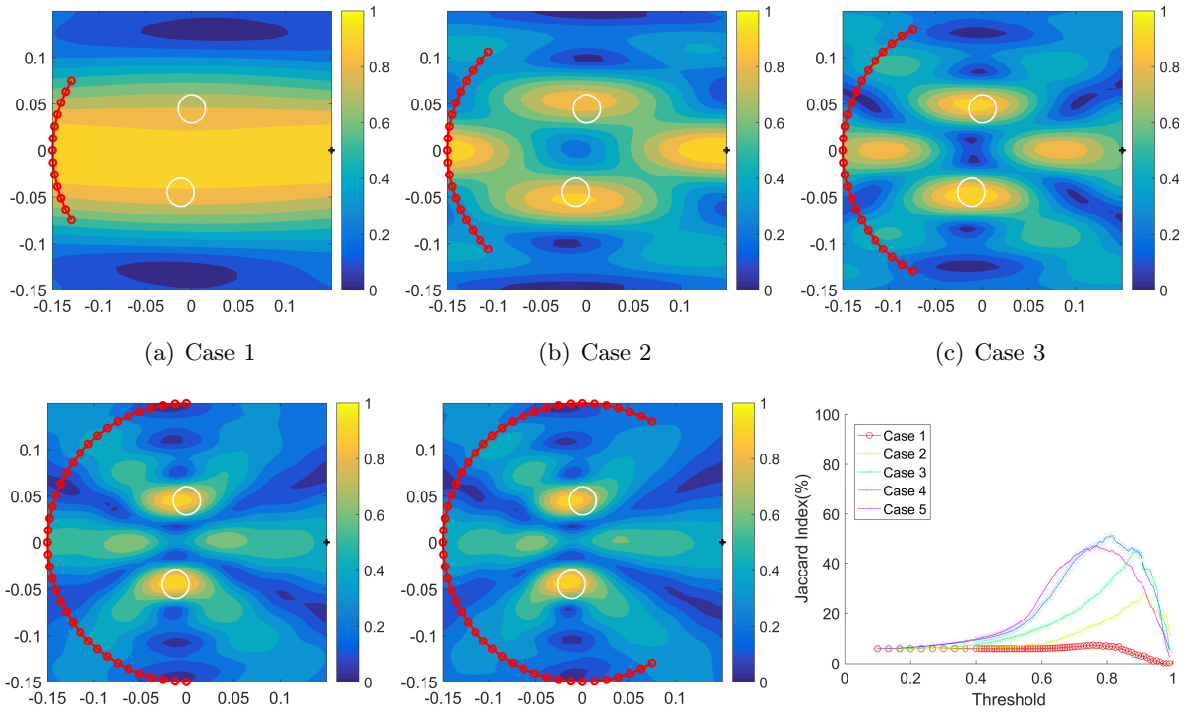

(a) Case 1 (b) Case 2 (c) Case 3

(d) Case 4 (e) Case 5 (f) Jaccard Index

Figure 4.11: (Example 4.3.12) Maps of $\mathcal{I}^{\infty}_{\mathrm{DSM}}(\mathbf{z}, \hat{\mathbf{d}}; k_0)$ and Jaccard index

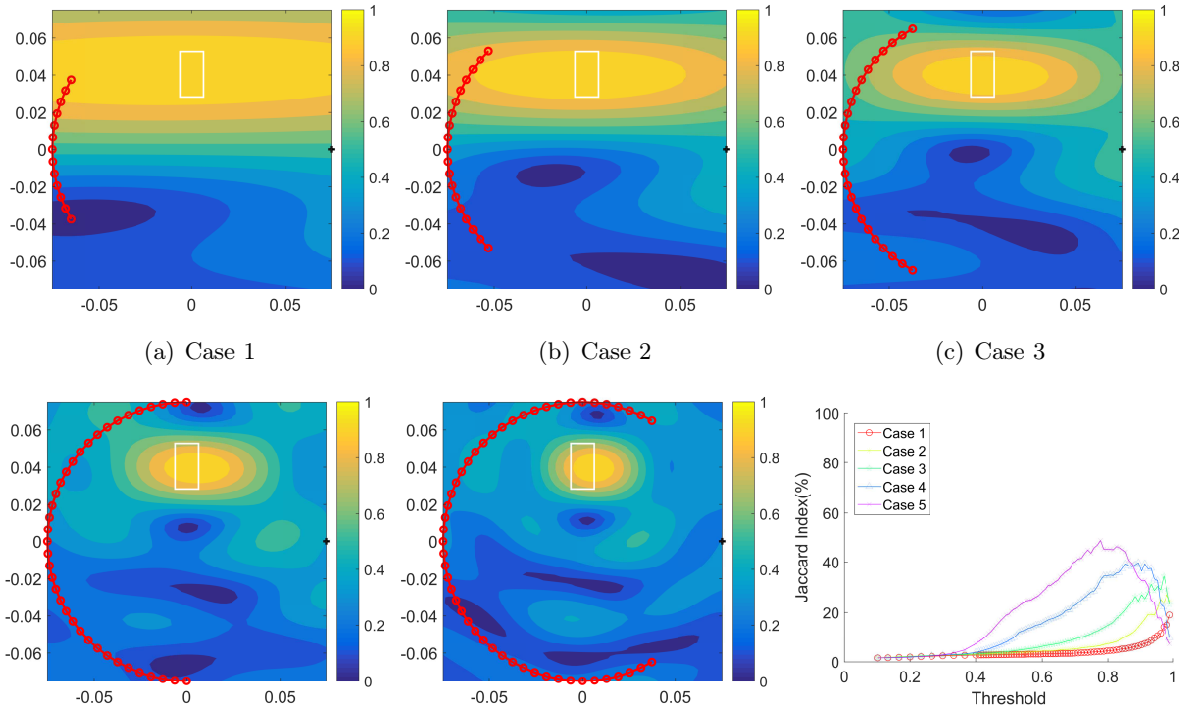

(a) Case 1 (b) Case 2 (c) Case 3

(d) Case 4 (e) Case 5 (f) Jaccard Index

Figure 4.12: (Example 4.3.13) Maps of $\mathcal{I}^{\infty}_{\mathrm{DSM}}(\mathbf{z}, \hat{\mathbf{d}}; k_0)$ and Jaccard index

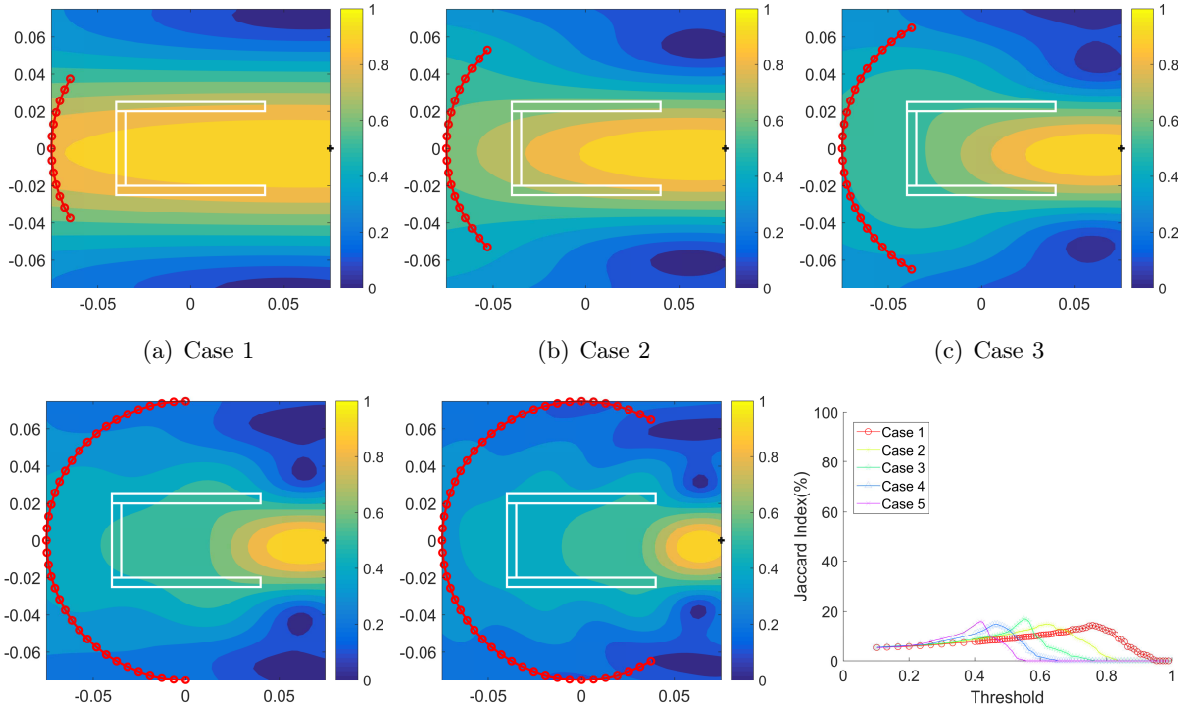

(a) Case 1 (b) Case 2 (c) Case 3

(d) Case 4 (e) Case 5 (f) Jaccard Index

Figure 4.13: (Example 4.3.14) Maps of $\mathcal{I}^{\infty}_{\mathrm{DSM}}(\mathbf{z}, \hat{\mathbf{d}}; k_0)$ and Jaccard index

5

Improvement of 2D imaging accuracy using multiple frequencies

Contents

5.1 Introduction

In this chapter, we apply the multi-frequency approach, which is one of the popular techniques to improve the imaging efficiency, to DSM. In (W.-K. Park 2018b) (TM-mode) and (W.-K. Park 2019b) (TE-mode), the author has validated that multi-frequency of DSM is an improved version of DSM with a fixed frequency in full-view configuration. So we focus only onto the multi-frequency of DSM in a limited-aperture scattering problem.

From the mathematical analysis of DSM and DSMA with fixed frequency presented in chapter 4, we have verified the relation between accuracy of algorithms and the measurement set-up. However, another approach is needed to improve the imaging performance when the ranges of observation and incident directions are narrow (e.g., $\theta_N - \theta_1 < \pi$ and $\vartheta_L - \vartheta_1 < \pi$). Hence, multi-frequency indicator function of DSM is introduced for further improvement. Contrarily to the several investigations (Estatico et al. 2015; Joh and W.-K. Park 2014), multi-frequency DSM is effective only for imaging a small single inhomogeneity but is not effective for several small inhomogeneities. To explain the reason theoretically, we derive below the mathematical structure of the multi-frequency indicator function by establishing a relationship with Bessel functions, Struve functions, Legendre polynomials, generalized

hypergeometric function, the range of incident and observation directions, and physical characteristics of targets. We then examine undiscovered properties of multi-frequency DSM, design an alternative indicator function based on an exponential weight with respect to each frequency for further improvement, and analyze its mathematical structure. Same as for the single-frequency case in section 4.3, the multi-frequency indicator functions are compared via numerical simulations with synthetic and experimental data.

The multi-frequency versions of DSM and DSMA are proposed and analyzed based on asymptotic formula of scattered field in the sections 5.2.1 and 5.2.2, respectively. Various numerical simulations are presented in section 5.3 to validate our theoretical results. Conclusions follow in section 5.4.

5.2 Multi-frequency indicator function

Let us consider the multi-frequency DSM for obtaining better results. Based on several investigations (W.-K. Park 2018b; Guzina, Cakoni, and Bellis 2010; Joh, Kwon, et al. 2013; Griesmaier and Schmiedecke 2017; W.-K. Park 2019b), we introduce an indicator function operated at several frequencies $f_p,\ p = 1, 2, \cdots, P$, as follows

$$\mathcal{I}^{\infty}_{\mathrm{MDSM}}(\mathbf{z}; \hat{\mathbf{d}}) := \left| \frac{1}{P} \sum_{p=1}^{P} \frac{\langle u_\infty(\hat{\mathbf{x}}_n, \hat{\mathbf{d}}; k_p), \mathrm{e}^{-\mathrm{i}k_p \hat{\mathbf{x}}_n \cdot \mathbf{z}} \rangle_{L^2(\mathbb{S}^1_{\mathrm{obs}})}}{||u_\infty(\hat{\mathbf{x}}_n, \hat{\mathbf{d}}; k_p)||_{L^2(\mathbb{S}^1_{\mathrm{obs}})} ||\mathrm{e}^{-\mathrm{i}k_p \hat{\mathbf{x}}_n \cdot \mathbf{z}}||_{L^2(\mathbb{S}^1_{\mathrm{obs}})}} \right|, \tag{5.1}$$

where $u_\infty(\hat{\mathbf{x}}, \hat{\mathbf{d}}; k_p) \in \mathbb{F}_p$ denotes the far-field pattern defined in (2.13) with wavenumber k_p, $p = 1, 2, \cdots, P$ with $k_1 < k_2 < \cdots, k_P$, and $\mathbb{F}_p$ is the set of measurement data such that

$$\mathbb{F}_p := \left\{ u_\infty(\hat{\mathbf{x}}_n, \hat{\mathbf{d}}; k_p) : p = 1, 2, \cdots, P,\ \hat{\mathbf{x}}_n \in \mathbb{S}^1_{\mathrm{obs}} \right\}. \tag{5.2}$$

5.2.1 Analysis of the indicator function for single and several incident fields

Single impinging direction For the sake of simplicity, let us consider the imaging of a single inhomogeneity with radius α, permittivity ε, and location $\mathbf{r}$. The result is dealt with in Theorem 5.2.1.

Theorem 5.2.1 (Single inhomogeneity case) *Assume that the total number of applied frequencies P is large enough. Let us denote $\mathbf{r} - \mathbf{z} = |\mathbf{r} - \mathbf{z}|(\cos\varphi, \sin\varphi)$. Then, for a fixed incident direction $\hat{\mathbf{d}}$, the $\mathcal{I}^{\infty}_{\mathrm{MDSM}}(\mathbf{z}; \hat{\mathbf{d}})$ can be represented as follows.*

$$\mathcal{I}^{\infty}_{\mathrm{MDSM}}(\mathbf{z}; \hat{\mathbf{d}}) \approx \frac{|\mathcal{M}_1(\mathbf{z}; \hat{\mathbf{d}})|}{\max\limits_{\mathbf{z} \in \Omega} |\mathcal{M}_1(\mathbf{z}; \hat{\mathbf{d}})|}, \tag{5.3}$$

where

$$\mathcal{M}_1(\mathbf{z}; \hat{\mathbf{d}}) := \frac{1}{k_P - k_1} \Big(\mathcal{S}(k_P, |\mathbf{r} - \mathbf{z}|) - \mathcal{S}(k_1, |\mathbf{r} - \mathbf{z}|) \Big) + \Lambda^1_M(k_1, k_P, \theta_1, \theta_N, |\mathbf{r} - \mathbf{z}|). \tag{5.4}$$

Here,

$$\mathcal{S}(k, |\mathbf{r} - \mathbf{z}|) = k \mathrm{J}_0(k|\mathbf{r} - \mathbf{z}|) + \frac{k\pi}{2} \Big(\mathrm{J}_1(k|\mathbf{r} - \mathbf{z}|)\, \mathbf{H}_0(k|\mathbf{r} - \mathbf{z}|) - \mathrm{J}_0(k|\mathbf{r} - \mathbf{z}|)\, \mathbf{H}_1(k|\mathbf{r} - \mathbf{z}|) \Big), \tag{5.5}$$

where $\mathbf{H}_n$ is the Struve function of n integer order and

$$\Lambda^1_M(k_1, k_P, \theta_1, \theta_N, |\mathbf{r} - \mathbf{z}|) = \frac{1}{k_P - k_1} \int_{k_1}^{k_P} \Lambda_S^{\theta_1, \theta_N}(k, |\mathbf{r} - \mathbf{z}|) \mathrm{d}k = \mathcal{O}\left(\frac{1}{\theta_N - \theta_1} \right). \tag{5.6}$$

Proof Let us recall the single frequency result from Theorem 4.3.2,

$$\begin{aligned}\langle u_\infty(\hat{\mathbf{x}}_n,\hat{\mathbf{d}},k_p),\mathrm{e}^{-\mathrm{i}k_p\hat{\mathbf{x}}_n\cdot\mathbf{z}}\rangle_{L^2(\mathbb{S}^1_{\text{obs}})}\\ =(\theta_N-\theta_1)\frac{k_p^2(1+\mathrm{i})\pi}{4\sqrt{k_p\pi}}\alpha^2\left(\frac{\varepsilon-\varepsilon_0}{\sqrt{\varepsilon_0\mu_0}}\right)\mathrm{e}^{\mathrm{i}k_p\hat{\mathbf{d}}\cdot\mathbf{r}}|\mathbf{D}|\left[\mathrm{J}_0(k_p|\mathbf{r}-\mathbf{z}|)+\Lambda_S^{\theta_1,\theta_N}(k,|\mathbf{r}_m-\mathbf{z}|)\right],\end{aligned}\tag{5.7}$$

where $\Lambda_S^{\theta_1,\theta_N}(k,|\mathbf{r}_m-\mathbf{z}|)$ is given by (4.18). This leads us to

$$\frac{\langle u_\infty(\hat{\mathbf{x}}_n,\hat{\mathbf{d}},k_p),\mathrm{e}^{-\mathrm{i}k_p\hat{\mathbf{x}}_n\cdot\mathbf{z}}\rangle_{L^2(\mathbb{S}^1_{\text{obs}})}}{||u_\infty(\hat{\mathbf{x}}_n,\hat{\mathbf{d}},k_p)||_{L^2(\mathbb{S}^1_{\text{obs}})}||\mathrm{e}^{-\mathrm{i}k_p\hat{\mathbf{x}}_n\cdot\mathbf{z}}||_{L^2(\mathbb{S}^1_{\text{obs}})}}\propto \mathrm{J}_0(k_p|\mathbf{r}-\mathbf{z}|)+\Lambda_S^{\theta_1,\theta_N}(k,|\mathbf{r}_m-\mathbf{z}|).$$

Thus, the multi-frequency extension is given by

$$\frac{1}{P}\sum_{p=1}^{P}\frac{\langle u_\infty(\hat{\mathbf{x}}_n,\hat{\mathbf{d}},k_p),\mathrm{e}^{-\mathrm{i}k_p\hat{\mathbf{x}}_n\cdot\mathbf{z}}\rangle_{L^2(\mathbb{S}^1_{\text{obs}})}}{||u_\infty(\hat{\mathbf{x}}_n,\hat{\mathbf{d}},k_p)||_{L^2(\mathbb{S}^1_{\text{obs}})}||\mathrm{e}^{-\mathrm{i}k_p\hat{\mathbf{x}}_n\cdot\mathbf{z}}||_{L^2(\mathbb{S}^1_{\text{obs}})}}\propto\Phi_1+\Phi_2,$$

where Φ_1 and Φ_2 are defined as

$$\Phi_1=\frac{1}{P}\sum_{p=1}^{S}\mathrm{J}_0(k_p|\mathbf{r}-\mathbf{z}|)\quad\text{and}\quad\Phi_2=\frac{1}{P}\sum_{p=1}^{P}\Lambda_S^{\theta_1,\theta_N}(k,|\mathbf{r}_m-\mathbf{z}|),\tag{5.8}$$

respectively.

First, Φ_1 can be expressed as

$$\begin{aligned}\Phi_1=\frac{1}{P}\sum_{p=1}^{P}\mathrm{J}_0(k_p|\mathbf{r}-\mathbf{z}|)&\approx\frac{1}{k_P-k_1}\int_{k_1}^{k_P}\mathrm{J}_0(k|\mathbf{r}-\mathbf{z}|)\mathrm{d}k\\ &=\frac{1}{k_P-k_1}\Big(\mathcal{S}(k_P,|\mathbf{r}-\mathbf{z}|)-\mathcal{S}(k_1,|\mathbf{r}-\mathbf{z}|)\Big),\end{aligned}\tag{5.9}$$

where $\mathcal{S}(k,|\mathbf{r}-\mathbf{z}|)$ is given by (5.5). The latter is obtained thanks to the hypothesis that the total number of frequencies P is large enough, and considering the following indefinite integral of the Bessel function (see (Rosenheinrich 2019, p.7))

$$\int\mathrm{J}_0(x)dx=x\mathrm{J}_0(x)+\frac{x\pi}{2}\Big(\mathrm{J}_1(x)\,\mathbf{H}_0(x)-\mathrm{J}_0(x)\,\mathbf{H}_1(x)\Big).$$

Based on the uniform convergence of the Jacobi-Anger expansion, it is clear that Φ_2 is convergent uniformly, so for every positive real number ϵ, there exists a sufficiently large $\mathcal{N}_1\in\mathbb{N}$ such that

$$\left|\Phi_2-\frac{4}{\theta_N-\theta_1}\sum_{s=1}^{\mathcal{N}_1}\frac{i^s}{s}\sin\left(\frac{s(\theta_N-\theta_1)}{2}\right)\cos\left(\frac{s(\theta_N+\theta_1-2\varphi)}{2}\right)\left(\frac{1}{P}\sum_{p=1}^{P}\mathrm{J}_s(k_p|\mathbf{r}-\mathbf{z}|)\right)\right|<\epsilon.\tag{5.10}$$

This means that

$$\begin{aligned}\Phi_2&\approx\frac{4}{\theta_N-\theta_1}\sum_{s=1}^{\mathcal{N}_1}\frac{i^s}{s}\sin\left(\frac{s(\theta_N-\theta_1)}{2}\right)\cos\left(\frac{s(\theta_N+\theta_1-2\varphi)}{2}\right)\left(\frac{1}{P}\sum_{p=1}^{P}\mathrm{J}_s(k_p|\mathbf{r}-\mathbf{z}|)\right)\\ &\approx\frac{4}{(\theta_N-\theta_1)(k_P-k_1)}\sum_{s=1}^{\mathcal{N}_1}\frac{\mathrm{i}^s}{s}\sin\left(\frac{s(\theta_N-\theta_1)}{2}\right)\cos\left(\frac{s(\theta_N+\theta_1-2\varphi)}{2}\right)\int_{k_1}^{k_P}\mathrm{J}_s(k|\mathbf{r}-\mathbf{z}|)\mathrm{d}k.\end{aligned}$$

Now, assume that $\mathbf{z}$ is close to $\mathbf{r}$. Then since $\mathrm{J}_s(k|\mathbf{r}-\mathbf{z}|) \longrightarrow 0$ for all $s = 1, 2, \cdots, \mathcal{N}_1$, the term Φ_2 becomes negligible. Assume that $\mathbf{z}$ is located away from $\mathbf{r}$ such that $k_1|\mathbf{r}-\mathbf{z}| \gg \mathcal{N}_1^2 - 0.25$. Then, since the following asymptotic form holds for $s = 1, 2, \cdots, \mathcal{N}_1$,

$$\mathrm{J}_s(k|\mathbf{r}-\mathbf{z}|) \approx \sqrt{\frac{2}{k\pi|\mathbf{r}-\mathbf{z}|}} \cos\left(k\pi|\mathbf{r}-\mathbf{z}| - \frac{s\pi}{2} - \frac{\pi}{4}\right),$$

we can observe that

$$\begin{aligned} |\Phi_2| &\leq \frac{4}{(\theta_N-\theta_1)(k_P-k_1)} \sum_{s=1}^{\mathcal{N}_1} \frac{1}{s} \int_{k_1}^{k_P} |\mathrm{J}_s(k|\mathbf{r}-\mathbf{z}|)| \mathrm{d}k \leq \frac{4\sqrt{2}\mathcal{N}_1}{(\theta_N-\theta_1)\sqrt{k_1\pi|\mathbf{r}-\mathbf{z}|}} \\ &\ll \frac{4\sqrt{2}\mathcal{N}_1}{(\theta_N-\theta_1)\sqrt{(\mathcal{N}_1^2-0.25)\pi}} \leq \frac{4\sqrt{2}}{\mathcal{N}_1(\theta_N-\theta_1)\sqrt{\pi}} \ll \mathcal{O}\left(\frac{1}{\theta_N-\theta_1}\right). \end{aligned} \tag{5.11}$$

Applying the structures Φ_1 and Φ_2, we can obtain (5.3), which completes the proof. □

Remark 5.2.2 (Properties of indicator function) *Now, we discuss some properties of the multi-frequency indicator function $\mathcal{I}^{\infty}_{\mathrm{MDSM}}(\mathbf{z};\hat{\mathbf{d}})$ and compare the imaging performance with the single-frequency one $\mathcal{I}^{\infty}_{\mathrm{DSM}}(\mathbf{z};\hat{\mathbf{d}},k_0)$ based on the results in Theorem 4.3.2 and 5.2.1.*

1. *From the observations such as $\left(\mathcal{S}(k_P,|\mathbf{r}-\mathbf{z}|) - \mathcal{S}(k_1,|\mathbf{r}-\mathbf{z}|)\right)/(k_P-k_1) = 1$ (see Figure 5.1) and $\Lambda^1_M(k_1,k_P,\theta_1,\theta_N,|\mathbf{r}-\mathbf{z}|) = 0$ when $\mathbf{z} = \mathbf{r} \in \tau$, the map of $\mathcal{I}^{\infty}_{\mathrm{MDSM}}(\mathbf{z};k_0)$ will exhibit maximum amplitude at the center of τ. However, some artifacts are still existing in the map of $\mathcal{I}^{\infty}_{\mathrm{MDSM}}(\mathbf{z};k_0)$. Notice that their appearance is highly depending the range of observation directions and total number of applied frequencies. If the range of observation directions is narrow or the total number of applied frequencies P is small, artifacts should disturb the recognition of location of targets while good imaging results will be retrieved if the range is wide and the total number is large enough.*

2. *Similar with the properties of single-frequency DSM as discussed in Remark 4.3.3, the contributing term of MDSM $\left(\mathcal{S}(k_P,|\mathbf{r}-\mathbf{z}|) - \mathcal{S}(k_1,|\mathbf{r}-\mathbf{z}|)\right)/(k_P-k_1)$ is also independent of the range of observation directions while the disturbing term is not. This means that we have to reduce the effect of $\Lambda^1_M(k_1,k_P,\theta_1,\theta_N,|\mathbf{r}-\mathbf{z}|)$ in order to improve the imaging performance.*

3. *In the full-view configuration ($\theta_N - \theta_1 = 2\pi$), we can compare the imaging accuracy between DSM operated as single- and multi-frequency by focusing only on each contributing term of DSM and MDSM represented in Theorem 4.3.2, and 5.2.1, respectively. Namely, if $\mathbf{z} = \mathbf{r} \in \tau$, we have $\Lambda^{\theta_1,\theta_N}_S(k,|\mathbf{r}_m-\mathbf{z}|) = 0$ and $\Lambda^1_M(k_1,k_P,\theta_1,\theta_N,|\mathbf{r}-\mathbf{z}|) = 0$. Hence,*

$$\mathcal{I}^{\infty}_{\mathrm{DSM}}(\mathbf{z};\hat{\mathbf{d}},k_0) \propto |\mathrm{J}_0(k_0|\mathbf{r}-\mathbf{z}|)| \tag{5.12}$$

and

$$\mathcal{I}^{\infty}_{\mathrm{MDSM}}(\mathbf{z};\hat{\mathbf{d}}) \propto \left|\frac{1}{k_P-k_1}\left(\mathcal{S}(k_P,|\mathbf{r}-\mathbf{z}|) - \mathcal{S}(k_1,|\mathbf{r}-\mathbf{z}|)\right)\right|, \tag{5.13}$$

which means that MDSM exhibits better imaging performance than single-frequency DSM due to the lesser oscillations of $\left|\left(\mathcal{S}(k_P,|\mathbf{r}-\mathbf{z}|) - \mathcal{S}(k_1,|\mathbf{r}-\mathbf{z}|)\right)/(k_P-k_1)\right|$ than those of $\mathrm{J}_0(k_0|\mathbf{r}-\mathbf{z}|)$, refer to Figure 5.1.

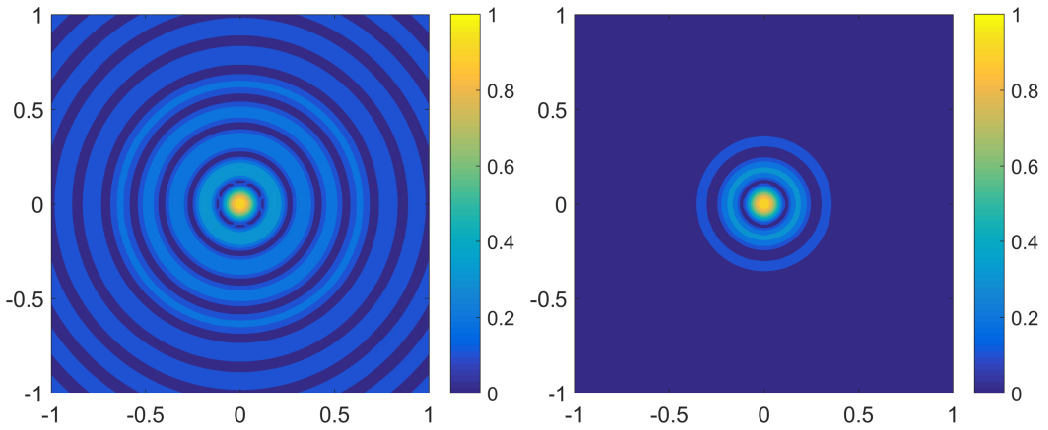

(a) $|\mathrm{J}_0(k_0|\mathbf{z}|)|$ (b) $|(\mathcal{S}(k_P,|\mathbf{z}|)-\mathcal{S}(k_1,|\mathbf{z}|))/(k_P-k_1)|$

Figure 5.1: Two-dimensional plots of $|\mathrm{J}_0(k_0|\mathbf{z}|)|$ for $f_0 = 1\,\mathrm{GHz}$ and $|(\mathcal{S}(k_P,|\mathbf{z}|)-\mathcal{S}(k_1,|\mathbf{z}|))/(k_P-k_1)|$ for $f_1 = 700\,\mathrm{MHz}$ and $f_P = 1.3\,\mathrm{GHz}$.

Unfortunately, identifying all inhomogeneities is generally impossible via $\mathcal{I}^{\infty}_{\mathrm{MDSM}}(\mathbf{z};\hat{\mathbf{d}})$ if there exist more than 2, refer to Figure 5.5. The theoretical reason is as follows.

Theorem 5.2.3 (Multiple inhomogeneities case) *Assume that the total numbers of receivers N and frequencies P is large enough. Let $\hat{\mathbf{d}}\cdot\mathbf{r}_m = |\mathbf{r}_m|\cos\psi_m$, and $\mathbf{r}_m - \mathbf{z} = |\mathbf{r}_m-\mathbf{z}|(\cos\varphi_m,\sin\varphi_m)$. Then, $\mathcal{I}^{\infty}_{\mathrm{MDSM}}(\mathbf{z};\hat{\mathbf{d}})$ can be represented as follows:*

$$\mathcal{I}^{\infty}_{\mathrm{MDSM}}(\mathbf{z};\hat{\mathbf{d}}) \approx \frac{|\mathcal{M}_2(\mathbf{z};\hat{\mathbf{d}})|}{\max|\mathcal{M}_2(\mathbf{z};\hat{\mathbf{d}})|}, \tag{5.14}$$

where

$$\mathcal{M}_2(\mathbf{z};\hat{\mathbf{d}}) := \sum_{m=1}^{M}\alpha_m^2(\varepsilon_m-\varepsilon_0)|\mathbf{D}_m|\Bigg[\frac{1}{k_P-k_1}\Big\{\mathcal{C}_1^{k_1,k_P}(|\mathbf{r}_m|,|\mathbf{r}_m-\mathbf{z}|)+\mathcal{C}_2^{k_1,k_P}(|\mathbf{r}_m|,|\mathbf{r}_m-\mathbf{z}|)\Big\} + \Lambda_M^2(k_1,k_P,\theta_1,\theta_N,|\mathbf{r}_m|,|\mathbf{r}_m-\mathbf{z}|)\Bigg]. \tag{5.15}$$

Here,

$$\mathcal{C}_1^{k_1,k_P}(|\mathbf{r}_m|,|\mathbf{r}_m-\mathbf{z}|) := \begin{cases} \mathcal{H}(k_1,k_P,|\mathbf{r}_m-\mathbf{z}|)+\int_{k_1}^{k_P}\mathrm{J}_0(k|\mathbf{r}_m-\mathbf{z}|)\mathrm{d}k & \text{if } |\mathbf{r}_m| = |\mathbf{r}_m-\mathbf{z}|,\\ \mathcal{P}(|\mathbf{r}_m|,|\mathbf{r}_m-\mathbf{z}|,k_P)-\mathcal{P}(|\mathbf{r}_m|,|\mathbf{r}_m-\mathbf{z}|,k_1) & \text{if } |\mathbf{r}_m| > |\mathbf{r}_m-\mathbf{z}|,\\ \mathcal{P}(|\mathbf{r}_m-\mathbf{z}|,|\mathbf{r}_m|,k_P)-\mathcal{P}(|\mathbf{r}_m-\mathbf{z}|,|\mathbf{r}_m|,k_1) & \text{if } |\mathbf{r}_m| < |\mathbf{r}_m-\mathbf{z}|, \end{cases} \tag{5.16}$$

$$\mathcal{C}_2^{k_1,k_P}(|\mathbf{r}_m|,|\mathbf{r}_m-\mathbf{z}|) := 2\sum_{t=1}^{\infty}\cos(t\psi_m)\int_{k_1}^{k_P}\mathrm{J}_0(k|\mathbf{r}_m-\mathbf{z}|)\mathrm{J}_t(k|\mathbf{r}_m|)\mathrm{d}k, \tag{5.17}$$

and

$$\Lambda_M^2(k_1,k_P,\theta_1,\theta_N,|\mathbf{r}_m|,|\mathbf{r}_m-\mathbf{z}|) := \frac{1}{k_P-k_1}\int_{k_1}^{k_P}\Lambda_S^{\theta_1,\theta_N}(k,|\mathbf{r}_m-\mathbf{z}|)\Big\{\mathrm{J}_0(k|\mathbf{r}_m|) + 2\sum_{t=1}^{\infty}\cos(t\psi_m)\mathrm{J}_t(k|\mathbf{r}_m|)\Big\}\mathrm{d}k, \tag{5.18}$$

where

$$\mathcal{H}(k_1,k_P,|\mathbf{r}_m-\mathbf{z}|):=k_P\left[\mathrm{J}_0(k_P|\mathbf{r}_m-\mathbf{z}|)^2+\mathrm{J}_1(k_P|\mathbf{r}_m-\mathbf{z}|)^2\right] - k_1\left[\mathrm{J}_0(k_1|\mathbf{r}_m-\mathbf{z}|)^2+\mathrm{J}_1(k_1|\mathbf{r}_m-\mathbf{z}|)^2\right] \tag{5.19}$$

and P_s is a Legendre polynomial of order s,

$$\mathcal{P}(\alpha,\beta,k):=\sum_{s=1}^{\infty}\frac{(-1)^s}{(s!)^2 4^s(2s+1)}(\alpha^2-\beta^2)P_s\left(\frac{\alpha^2+\beta^2}{\alpha^2-\beta^2}\right)k^{2s+1}\quad for\quad \beta<\alpha. \tag{5.20}$$

Furthermore,

$$\frac{1}{k_P-k_1}\int_{k_1}^{k_P}\mathrm{J}_1(k|\mathbf{r}_m-\mathbf{z}|)^2\mathrm{d}k\ll O(1) \tag{5.21}$$

and

$$\left|\Lambda_M^2(k_1,k_P,\theta_1,\theta_N,\vartheta_1,\vartheta_L,|\mathbf{r}_m-\mathbf{z}|)\right|=O\left(\frac{1}{\theta_N-\theta_1}\right). \tag{5.22}$$

Proof The combination of Theorem 4.3.2 and Jacobi-Anger expansion leads to

$$\sum_{p=1}^{P}\frac{\langle u_\infty(\hat{\mathbf{x}}_n,\hat{\mathbf{d}},k_p),\mathrm{e}^{-\mathrm{i}k_p\hat{\mathbf{x}}_n\cdot\mathbf{z}}\rangle_{L^2(\mathbb{S}^1_{\mathrm{obs}})}}{||u_\infty(\hat{\mathbf{x}}_n,\hat{\mathbf{d}},k_p)||_{L^2(\mathbb{S}^1_{\mathrm{obs}})}||\mathrm{e}^{-\mathrm{i}k_p\hat{\mathbf{x}}_n\cdot\mathbf{z}}||_{L^2(\mathbb{S}^1_{\mathrm{obs}})}}\propto\sum_{m=1}^{M}\alpha_m^2(\varepsilon_m-\varepsilon_0)|\mathbf{D}_m|\left\{\Phi_1+\Phi_2+\Phi_3+\Phi_4\right\}. \tag{5.23}$$

Here,

$$\begin{aligned}
\Phi_1&:=\frac{1}{P}\sum_{p=1}^{P}\mathrm{J}_0(k_p|\mathbf{r}_m|)\mathrm{J}_0(k_p|\mathbf{r}_m-\mathbf{z}|),\\
\Phi_2&:=2\sum_{t=1}^{\infty}\cos(t\psi_m)\left[\frac{1}{P}\sum_{p=1}^{P}\mathrm{J}_0(k_p|\mathbf{r}_m-\mathbf{z}|)\mathrm{J}_t(k_p|\mathbf{r}_m|)\right],\\
\Phi_3&:=\frac{1}{P}\sum_{p=1}^{P}\mathrm{J}_0(k_p|\mathbf{r}_m|)\Lambda_S^{\theta_1,\theta_2}(k_p,|\mathbf{r}_m-\mathbf{z}|),\\
\Phi_4&:=2\sum_{t=1}^{\infty}\cos(t\psi_m)\left[\frac{1}{P}\sum_{p=1}^{P}\Lambda_S^{\theta_1,\theta_2}(k_p,|\mathbf{r}_m-\mathbf{z}|)\mathrm{J}_t(k_p|\mathbf{r}_m|)\right],
\end{aligned} \tag{5.24}$$

where $\hat{\mathbf{d}}\cdot\mathbf{r}_m=|\mathbf{r}_m|\cos\psi_m$ and $\Lambda_S(k,\theta_1,\theta_2,|\mathbf{r}_m-\mathbf{z}|)$ is defined by (4.18). Since the total number of frequencies P is sufficiently large,

$$\Phi_1\approx\frac{1}{k_P-k_1}\int_{k_1}^{k_P}\mathrm{J}_0(k|\mathbf{r}_m|)\mathrm{J}_0(k|\mathbf{r}_m-\mathbf{z}|)\mathrm{d}k \tag{5.25}$$

and

$$\Phi_2\approx\frac{2}{k_P-k_1}\sum_{t=1}^{\infty}\cos(t\psi_m)\int_{k_1}^{k_P}\mathrm{J}_0(k|\mathbf{r}_m-\mathbf{z}|)\mathrm{J}_t(k|\mathbf{r}_m|)\mathrm{d}k. \tag{5.26}$$

According to the indefinite integrals of Bessel function of zero order in (Rosenheinrich 2019, p.214)):

$$\int\mathrm{J}_0(x)^2\mathrm{d}x=x[\mathrm{J}_0(x)^2+\mathrm{J}_1(x)^2]+\int\mathrm{J}_1(x)^2\mathrm{d}x, \tag{5.27}$$

and in (Rosenheinrich 2019, p.277):

$$\int_0^x \mathrm{J}_0(\alpha t)\mathrm{J}_0(\beta t)\mathrm{d}t = \sum_{s=1}^{\infty} \frac{(-1)^s}{(s!)^2 4^s (2s+1)} (\alpha^2-\beta^2)\mathrm{P}_s\left(\frac{\alpha^2+\beta^2}{\alpha^2-\beta^2}\right) x^{2s+1}, \quad \text{for } \beta<\alpha, \tag{5.28}$$

we have $\Phi_1 = \Phi_1^\star/(k_P-k_1)$

$$\Phi_1^\star \approx \begin{cases} \mathcal{H}(k_1,k_P,|\mathbf{r}_m-\mathbf{z}|) + \displaystyle\int_{k_1}^{k_P} \mathrm{J}_0(k|\mathbf{r}_m-\mathbf{z}|)\mathrm{d}k & \text{if } |\mathbf{r}_m| = |\mathbf{r}_m-\mathbf{z}|, \quad (5.29a) \\ \mathcal{P}(|\mathbf{r}_m|,|\mathbf{r}_m-\mathbf{z}|,k_P) - \mathcal{P}(|\mathbf{r}_m|,|\mathbf{r}_m-\mathbf{z}|,k_1) & \text{if } |\mathbf{r}_m| > |\mathbf{r}_m-\mathbf{z}|, \quad (5.29b) \\ \mathcal{P}(|\mathbf{r}_m-\mathbf{z}|,|\mathbf{r}_m|,k_P) - \mathcal{P}(|\mathbf{r}_m-\mathbf{z}|,|\mathbf{r}_m|,k_1) & \text{if } |\mathbf{r}_m| < |\mathbf{r}_m-\mathbf{z}|, \quad (5.29c) \end{cases}$$

where P_s is a Legendre polynomial of order s, and $\mathcal{P}(|\mathbf{r}_m|,|\mathbf{r}_m-\mathbf{z}|,x)$ and $\mathcal{H}(k,|\mathbf{r}_m-\mathbf{z}|)$ are defined by (5.20) and (5.19), respectively. Here,

$$\frac{1}{k_P-k_1}\int_{k_1}^{k_P} \mathrm{J}_1(k|\mathbf{r}_m-\mathbf{z}|)^2\mathrm{d}k \ll O(1). \tag{5.30}$$

Since the following relation is holding:

$$\mathrm{J}_s(x) \le \frac{|x|^s}{2^s s!}, \quad x\in\mathbb{R}, \tag{5.31}$$

by applying Hölder inequality, we can obtain

$$\int_{k_1}^{k_P} \mathrm{J}_0(k|\mathbf{r}_m|)\mathrm{J}_s(k|\mathbf{r}_m-\mathbf{z}|)\mathrm{d}k \le \frac{|\mathbf{r}_m-\mathbf{z}|^s}{2^s s!}\int_{k_1}^{k_P}|k|^s\mathrm{d}k \le \frac{(k_P^{s+1}-k_1^{s+1})|\mathbf{r}_m-\mathbf{z}|^s}{2^s(s+1)!}. \tag{5.32}$$

Now, based on (5.10), there exists a large number $\mathcal{N}_\star\in\mathbb{N}$ such that

$$\begin{aligned} &\frac{1}{k_P-k_1}\int_{k_1}^{k_P} \mathrm{J}_0(k|\mathbf{r}_m|)\Lambda_S(k,\theta_1,\theta_2,|\mathbf{r}_m-\mathbf{z}|)\mathrm{d}k \\ &\approx \frac{4}{(k_P-k_1)(\theta_N-\theta_1)}\sum_{s=1}^{\mathcal{N}_\star}\frac{\mathrm{i}^s}{s}\cos\left(\frac{s(\theta_N+\theta_1-2\varphi_m)}{2}\right)\sin\left(\frac{s(\theta_N-\theta_1)}{2}\right) \\ &\quad\times\int_{k_1}^{k_P}\mathrm{J}_0(k|\mathbf{r}_m|)\mathrm{J}_s(k|\mathbf{r}_m-\mathbf{z}|)\mathrm{d}k \end{aligned} \tag{5.33}$$

Assume that $\mathbf{z}$ is sufficiently close to $\mathbf{r}_m$ such that $k_P|\mathbf{z}-\mathbf{r}_m| \ll \sqrt{\mathcal{N}_\star+1}$. Then,

$$\int_{k_1}^{k_P} \mathrm{J}_0(k|\mathbf{r}_m|)\mathrm{J}_s(k|\mathbf{r}_m-\mathbf{z}|)\mathrm{d}k \le \frac{(k_P^{s+1}-k_1^{s+1})|\mathbf{r}_m-\mathbf{z}|^s}{2^s(s+1)!} \ll \frac{k_P\sqrt{\mathcal{N}_\star+1}}{2^s(s+1)!}. \tag{5.34}$$

If $\mathbf{z}$ is far away from $\mathbf{r}_m$ such that $k_1|\mathbf{z}-\mathbf{r}_m| \gg \mathcal{N}_\star^2-0.25$, then, the following asymptotic form holds for $s=1,2,\cdots,\mathcal{N}$,

$$\mathrm{J}_s(k|\mathbf{r}_m-\mathbf{z}|) \approx \sqrt{\frac{2}{k\pi|\mathbf{r}_m-\mathbf{z}|}}\cos\left(k|\mathbf{r}_m-\mathbf{z}| - \frac{s\pi}{2}-\frac{\pi}{4}+O\left(\frac{1}{k|\mathbf{r}_m-\mathbf{z}|}\right)\right). \tag{5.35}$$

This yields that

$$\begin{aligned} \int_{k_1}^{k_P} \mathrm{J}_0(k|\mathbf{r}_m|)\mathrm{J}_s(k|\mathbf{r}_m-\mathbf{z}|)\mathrm{d}k &\le \int_{k_1}^{k_P}\sqrt{\frac{2}{k\pi|\mathbf{r}_m-\mathbf{z}|}}\cos\left(k|\mathbf{r}_m-\mathbf{z}|-\frac{s\pi}{2}-\frac{\pi}{4}\right)\mathrm{d}k \\ &\le \sqrt{\frac{2}{\pi|\mathbf{r}_m-\mathbf{z}|}}(\sqrt{k_P}-\sqrt{k_1}) \le k_P\sqrt{\frac{2}{k_P\pi|\mathbf{r}_m-\mathbf{z}|}} \le k_P\sqrt{\frac{2}{\pi|\mathcal{N}_\star^2-0.25|}}. \end{aligned} \tag{5.36}$$

Due to the uniform convergence of the Jacobi-Anger expansion, there exists a large number $\mathcal{N}_1 \in \mathbb{N}$ such that

$$|\Phi_3| \leq O\left(\frac{1}{\theta_N - \theta_1}\right), \tag{5.37}$$

Analogously, for a large number $\mathcal{N}_2 \in \mathbb{N}$, we have

$$|\Phi_4| \leq O\left(\frac{1}{\theta_N - \theta_1}\right). \tag{5.38}$$

Then, we can choose the constant $\mathcal{N} = \min\{\mathcal{N}_1, \mathcal{N}_2\}$, and Hölder's inequality implies the conclusion (5.14)

□

Now, based on our structure analysis verified in Theorem 5.2.3, let us elucidate the reason of unexpected phenomena displayed in Figure 5.5 as follows.

Remark 5.2.4 (Reason of limitation of $\mathcal{I}^{\infty}_{\mathrm{MDSM}}(\mathbf{z}; \hat{\mathbf{d}})$ when $M \geq 2$) *On the contrary to the result of $\mathcal{I}^{\infty}_{\mathrm{MDSM}}(\mathbf{z}; \hat{\mathbf{d}})$ for imaging a single inhomogeneity, $\mathcal{I}^{\infty}_{\mathrm{MDSM}}(\mathbf{z}; \hat{\mathbf{d}})$ consists of the three terms $\mathcal{C}_1^{k_1,k_P}(|\mathbf{r}_m|, |\mathbf{r}_m - \mathbf{z}|)$, $\mathcal{C}_2^{k_1,k_P}(|\mathbf{r}_m|, |\mathbf{r}_m - \mathbf{z}|)$, and $\Lambda_M^2(k_1, k_P, \theta_1, \theta_N, |\mathbf{r}_m|, |\mathbf{r}_m - \mathbf{z}|)$. Notice that $\Lambda_M^2(k_1, k_P, \theta_1, \theta_N, |\mathbf{r}_m|, |\mathbf{r}_m - \mathbf{z}|) = 0$ if $\mathbf{z} = \mathbf{r}_m$.*

Let us focus on the behavior of $\mathcal{C}_1^{k_1,k_P}(|\mathbf{r}_m|, |\mathbf{r}_m - \mathbf{z}|)$ and $\mathcal{C}_2^{k_1,k_P}(|\mathbf{r}_m|, |\mathbf{r}_m - \mathbf{z}|)$ when $\mathbf{z} = \mathbf{r}_m$. Since $\mathbf{r}_m$ is a fixed constant, $\mathcal{C}_1^{k_1,k_P}(|\mathbf{r}_m|, 0)$ has the form of (5.16) for $|\mathbf{r}_m| > |\mathbf{r}_m - \mathbf{z}|$ and we have

$$\begin{aligned} \mathcal{C}_1^{k_1,k_P}(|\mathbf{r}_m|, 0) &= \sum_{s=0}^{\infty} \frac{(-1)^s}{(s!)^2 4^s (2s+1)} |\mathbf{r}_m|^{2s} P_s(1)(k_P^{2s+1} - k_1^{2s+1}), \\ &= {}_1\mathrm{F}_2\left(\frac{1}{2}; 1, \frac{3}{2}; \frac{|\mathbf{r}_m|^2 k_P^2}{4}\right) k_P - {}_1\mathrm{F}_2\left(\frac{1}{2}; 1, \frac{3}{2}; \frac{|\mathbf{r}_m|^2 k_1^2}{4}\right) k_1. \end{aligned} \tag{5.39}$$

The integral formula of the Bessel function in (Luke 2014, § 2.3, (1)) leads to the representation formula of $\mathcal{C}_2^{k_1,k_P}(|\mathbf{r}_m|, 0)$ as

$$\begin{aligned} \mathcal{C}_2^{k_1,k_P}(|\mathbf{r}_m|, 0) =& 2\sum_{t=1}^{\infty} \cos(t\psi_m) \int_{k_1}^{k_P} \mathrm{J}_t(k|\mathbf{r}_m|)\mathrm{d}k \\ =& \sum_{t=1}^{\infty} \frac{\cos(t\psi_m)}{2^{t-1}\Gamma(t+2)} \left\{ {}_1\mathrm{F}_2\left(\frac{t+1}{2}; t+1, \frac{t+3}{2}; -\frac{1}{4}k_P^2|\mathbf{r}_m|^2\right) k_P \right. \\ & \left. - {}_1\mathrm{F}_2\left(\frac{t+1}{2}; t+1, \frac{t+3}{2}; -\frac{1}{4}k_1^2|\mathbf{r}_m|^2\right) k_1 \right\}, \end{aligned} \tag{5.40}$$

where ${}_a\mathrm{F}_b$ is the generalized hypergeometric function of orders a and b. Hence, the combination of (5.39) and (5.40) leads to

$$\mathcal{I}^{\infty}_{\mathrm{MDSM}}(\mathbf{z} = \mathbf{r}_m; \hat{\mathbf{d}}) \neq \mathcal{I}^{\infty}_{\mathrm{MDSM}}(\mathbf{z} = \mathbf{r}_{m'}; \hat{\mathbf{d}}) \quad \text{if } m \neq m' \tag{5.41}$$

due to the properties of hypergeometric functions. In other words, the map of $\mathcal{I}^{\infty}_{\mathrm{MDSM}}(\mathbf{z}; \hat{\mathbf{d}})$ has a different amplitude at each center of the inhomogeneities even though their physical properties (e.g. permittivity, size, shape, etc.) are the same. This is the theoretical reason why we cannot identify all inhomogeneities via the map of $\mathcal{I}^{\infty}_{\mathrm{MDSM}}(\mathbf{z}; \hat{\mathbf{d}})$. Hence, we need further improvement to overcome the limitation of $\mathcal{I}^{\infty}_{\mathrm{MDSM}}(\mathbf{z}; \hat{\mathbf{d}})$.

Multiple impinging directions To improve the imaging performance, we may apply incident fields with various propagation directions. On the basis of the definition of the DSM indicator function operated at fixed frequency (4.26), we define the indicator function of MDSM with multiple impinging directions $(\hat{\mathbf{d}}_l,\ l = 1, 2, \cdots, L)$ by

$$\mathcal{I}^{\infty}_{\mathrm{MDSM}}(\mathbf{z}) := \max_{\mathbf{z}\in\Omega} \left\{ \mathcal{I}^{\infty}_{\mathrm{MDSM}}(\mathbf{z}; \hat{\mathbf{d}}_l) : l = 1, 2, \cdots, L \right\}. \tag{5.42}$$

The properties of $\mathcal{I}_{\mathrm{MDSM}}(\mathbf{z})$ (5.42) can be observed and summarized as follows. According to the results in Theorem 5.2.1 and 5.2.3,

$$\mathcal{I}^{\infty}_{\mathrm{MDSM}}(\mathbf{z}) \propto \begin{cases} \max |\mathcal{M}_1(\mathbf{z}; \hat{\mathbf{d}})| & \text{if} \quad M = 1, \\ \max |\mathcal{M}_2(\mathbf{z}; \hat{\mathbf{d}})| & \text{if} \quad M \geq 2, \end{cases} \tag{5.43}$$

where $\mathcal{M}_1(\mathbf{z}; \hat{\mathbf{d}})$ and $\mathcal{M}_2(\mathbf{z}; \hat{\mathbf{d}})$ are defined by (5.4) and (5.15), respectively. So this method does not improve the imaging performance significantly, so that the fundamental limitation discussed in Remark 5.2.4 via $\mathcal{I}^{\infty}_{\mathrm{MDSM}}(\mathbf{z})$ is still remaining even with sufficiently many incident fields. Hence, another improvement is essential to deal with it.

5.2.2 Multi-frequency alternative direct sampling method

In the previous section, we could not handle the limitation of $\mathcal{I}^{\infty}_{\mathrm{MDSM}}(\mathbf{z})$ by considering multiple impinging directions. So we suggest a multi-frequency version of DSMA (say, MDSMA) by giving weights with respect to each frequency and incident direction such that

$$\mathcal{I}^{\infty}_{\mathrm{MDSMA}}(\mathbf{z}) := \left| \frac{1}{P} \sum_{p=1}^{P} \frac{\left\langle \left\langle u_{\infty}(\hat{\mathbf{x}}_n, \hat{\mathbf{d}}_l; k_p), \mathrm{e}^{-\mathrm{i}k_p \hat{\mathbf{x}}_n \cdot \mathbf{z}} \right\rangle_{L^2(\mathbb{S}^1_{\mathrm{obs}})}, \mathrm{e}^{\mathrm{i}k_p \hat{\mathbf{d}}_l \cdot \mathbf{z}} \right\rangle_{L^2(\mathbb{S}^1_{\mathrm{inc}})}}{\max \left| \left\langle \left\langle u_{\infty}(\hat{\mathbf{x}}_n, \hat{\mathbf{d}}_l; k_0), \mathrm{e}^{-\mathrm{i}k_p \hat{\mathbf{x}}_n \cdot \mathbf{z}} \right\rangle_{L^2(\mathbb{S}^1_{\mathrm{obs}})}, \mathrm{e}^{\mathrm{i}k_p \hat{\mathbf{d}}_l \cdot \mathbf{z}} \right\rangle_{L^2(\mathbb{S}^1_{\mathrm{inc}})} \right|} \right|. \tag{5.44}$$

Note that for the single impinging direction case, the indicator function is given by

$$\mathcal{I}^{\infty}_{\mathrm{MDSMA}}(\mathbf{z}; \hat{\mathbf{d}}) := \left| \frac{1}{P} \sum_{p=1}^{P} \frac{\mathrm{e}^{-\mathrm{i}k_p \hat{\mathbf{d}} \cdot \mathbf{z}} \left\langle u_{\infty}(\hat{\mathbf{x}}_n, \hat{\mathbf{d}}; k_p), \mathrm{e}^{-\mathrm{i}k_p \hat{\mathbf{x}}_n \cdot \mathbf{z}} \right\rangle_{L^2(\mathbb{S}^1_{\mathrm{obs}})}}{\max \left| \mathrm{e}^{-\mathrm{i}k_p \hat{\mathbf{d}} \cdot \mathbf{z}} \left\langle u_{\infty}(\hat{\mathbf{x}}_n, \hat{\mathbf{d}}; k_p), \mathrm{e}^{-\mathrm{i}k_p \hat{\mathbf{x}}_n \cdot \mathbf{z}} \right\rangle_{L^2(\mathbb{S}^1_{\mathrm{obs}})} \right|} \right|. \tag{5.45}$$

According to (W.-K. Park 2018b), the structure of $\mathcal{I}^{\infty}_{\mathrm{MDSMA}}(\mathbf{z}; \hat{\mathbf{d}})$ has been verified that it is an improved version of DSM operated at fixed frequency (4.14) in full-view configuration. Here, we analyze the structure of MDSMA in limited-aperture problem. Same as in the single-frequency case, assume that the data are generated from the L multiple impinging directions which are located in $\mathbb{S}^1_{\mathrm{inc}}$ of (4.25).

Theorem 5.2.5 *Assume that the total number of observation direction N, incident directions L, and frequencies P is sufficiently large. Let $\mathbf{r}_m - \mathbf{z} = |\mathbf{r}_m - \mathbf{z}|(\cos\varphi_m, \sin\varphi_m)$. Then, the indicator function of MDSMA has the following asymptotic formula.*

$$\mathcal{I}^{\infty}_{\mathrm{MDSMA}}(\mathbf{z}) \approx \frac{|\mathcal{M}_3(\mathbf{z})|}{\max |\mathcal{M}_3(\mathbf{z})|}, \tag{5.46}$$

where

$$\mathcal{M}_3(\mathbf{z}) := \sum_{m=1}^{M} \alpha_m^2 \left(\frac{\varepsilon_m - \varepsilon_0}{\sqrt{\varepsilon_m \varepsilon_0}}\right) \left\{ \frac{1}{k_P - k_1} \left[\mathcal{H}(k_P, |\mathbf{r}_m - \mathbf{z}|) - \mathcal{H}(k_1, |\mathbf{r}_m - \mathbf{z}|) + \int_{k_1}^{k_P} \mathrm{J}_1(k|\mathbf{r}_m - \mathbf{z}|)\mathrm{d}k \right] + \Lambda_M^3(k_1, k_P, \theta_1, \theta_N, \vartheta_1, \vartheta_L, |\mathbf{r}_m - \mathbf{z}|) \right\} \quad (5.47)$$

Here,

$$\mathcal{H}(k, |\mathbf{r}_m - \mathbf{z}|) := k \left[\mathrm{J}_0(k|\mathbf{r}_m - \mathbf{z}|)^2 + \mathrm{J}_1(k|\mathbf{r}_m - \mathbf{z}|)^2 \right] \quad (5.48)$$

and

$$\Lambda_M^3(k_1, k_P, \theta_1, \theta_N, \vartheta_1, \vartheta_L, |\mathbf{r}_m - \mathbf{z}|) := \frac{1}{k_P - k_1} \int_{k_1}^{k_P} \left\{ \mathrm{J}_0(k|\mathbf{r}_m - \mathbf{z}|) \left[\Lambda_S^{\theta_1, \theta_N}(k, |\mathbf{r}_m - \mathbf{z}|) + \Lambda_S^{\vartheta_1, \vartheta_L}(k, |\mathbf{r}_m - \mathbf{z}|) \right] + \Lambda_S^{\vartheta_1, \vartheta_L}(k, |\mathbf{r}_m - \mathbf{z}|) \Lambda_S^{\theta_1, \theta_N}(k, |\mathbf{r}_m - \mathbf{z}|) \right\} \mathrm{d}k, \quad (5.49)$$

where $\Lambda_S^{\alpha,\beta}(k, |\mathbf{r}_m - \mathbf{z}|)$ *is given by* (4.18)*. Furthermore, for sufficiently large* $\mathcal{N} \in \mathbb{N}$*,*

$$\frac{1}{k_P - k_1} \int_{k_1}^{k_P} \mathrm{J}_1(k|\mathbf{r}_m - \mathbf{z}|)^2 \mathrm{d}k \ll O(1), \quad (5.50)$$

and

$$\left|\Lambda_M^3(k_1, k_P, \theta_1, \theta_N, \vartheta_1, \vartheta_L, |\mathbf{r}_m - \mathbf{z}|)\right| = O\left(\max\left\{ \frac{1}{\mathcal{N}(\theta_N - \theta_1)}, \frac{1}{\mathcal{N}(\vartheta_L - \vartheta_1)}, \frac{1}{\mathcal{N}(\theta_N - \theta_1)(\vartheta_L - \vartheta_1)} \right\} \right). \quad (5.51)$$

Proof According to (5.44), we have

$$\frac{1}{P} \sum_{p=1}^{P} \frac{\left\langle \left\langle u_\infty(\hat{\mathbf{x}}_n, \hat{\mathbf{d}}_l; k_p), \mathrm{e}^{-\mathrm{i}k_p \hat{\mathbf{x}}_n \cdot \mathbf{z}} \right\rangle_{L^2(\mathbb{S}^1_{\mathrm{obs}})}, \mathrm{e}^{\mathrm{i}k_p \hat{\mathbf{d}}_l \cdot \mathbf{z}} \right\rangle_{L^2(\mathbb{S}^1_{\mathrm{inc}})}}{\max \left| \left\langle \left\langle u_\infty(\hat{\mathbf{x}}_n, \hat{\mathbf{d}}_l; k_p), \mathrm{e}^{-\mathrm{i}k_p \hat{\mathbf{x}}_n \cdot \mathbf{z}} \right\rangle_{L^2(\mathbb{S}^1_{\mathrm{obs}})}, \mathrm{e}^{\mathrm{i}k_p \hat{\mathbf{d}}_l \cdot \mathbf{z}} \right\rangle_{L^2(\mathbb{S}^1_{\mathrm{inc}})} \right|} \propto \sum_{m=1}^{M} \alpha_m^2 |\mathbf{D}_m| \left(\frac{\varepsilon_m - \varepsilon_0}{\sqrt{\varepsilon_0 \mu_0}}\right) \frac{1}{k_P - k_1} \int_{k_1}^{k_P} (\Phi_1 + \Phi_2 + \Phi_3) \mathrm{d}k, \quad (5.52)$$

where $\Phi_s,\ s = 1, 2, 3$ are given by

$$\begin{aligned} \Phi_1 &= \mathrm{J}_0(k|\mathbf{r}_m - \mathbf{z}|)^2, \\ \Phi_2 &= \left[\Lambda_S^{\theta_1, \theta_N}(k, |\mathbf{r}_m - \mathbf{z}|) + \Lambda_S^{\vartheta_1, \vartheta_L}(k, |\mathbf{r}_m - \mathbf{z}|) \right] \mathrm{J}_0(k|\mathbf{r}_m - \mathbf{z}|), \\ \Phi_3 &= \Lambda_S^{\vartheta_1, \vartheta_L}(k, |\mathbf{r}_m - \mathbf{z}|) \Lambda_S^{\theta_1, \theta_N}(k, |\mathbf{r}_m - \mathbf{z}|), \end{aligned} \quad (5.53)$$

The indefinite integral of 1st kind Bessel function of zero order, see (Rosenheinrich 2019, p. 214)):

$$\int \mathrm{J}_0(x)^2 \mathrm{d}x = x[\mathrm{J}_0(x)^2 + \mathrm{J}_1(x)^2] + \int \mathrm{J}_1(x)^2 \mathrm{d}x, \quad (5.54)$$

leads to

$$\frac{1}{k_P-k_1}\int_{k_1}^{k_P}\Phi_1\mathrm{d}k=\frac{1}{k_P-k_1}\Big\{k_P\left[\mathrm{J}_0(k_P|\mathbf{r}_m-\mathbf{z}|)^2+\mathrm{J}_1(k_P|\mathbf{r}_m-\mathbf{z}|)^2\right]$$
$$-k_1\left[\mathrm{J}_0(k_1|\mathbf{r}_m-\mathbf{z}|)^2+\mathrm{J}_1(k_1|\mathbf{r}_m-\mathbf{z}|)^2\right]+\int_{k_1}^{k_P}\mathrm{J}_1(k|\mathbf{r}_m-\mathbf{z}|)^2\mathrm{d}k\Big\},\quad(5.55)$$

where

$$\frac{1}{k_P-k_1}\int_{k_1}^{k_P}\mathrm{J}_1(k|\mathbf{r}_m-\mathbf{z}|)^2\mathrm{d}k\ll O(1).\quad(5.56)$$

Furthermore, due to uniform convergence of Jacobi-Anger expansion, it is obvious that the remaining terms are convergent. Namely, there exist large numbers $\mathcal{N}_1$ and $\mathcal{N}_2$ such that

$$\left|\int_{k_1}^{k_P}\Lambda_S^{\theta_1,\theta_N}(k,|\mathbf{r}_m-\mathbf{z}|)\mathrm{J}_0(k|\mathbf{r}_m-\mathbf{z}|)\mathrm{d}k-\left(\int_{k_1}^{k_P}\mathrm{J}_0(k|\mathbf{r}_m-\mathbf{z}|)\mathrm{J}_s(k|\mathbf{r}_m-\mathbf{z}|)\mathrm{d}k\right)\right.$$
$$\left.\times\left(\frac{4}{\theta_N-\theta_1}\sum_{s=1}^{\mathcal{N}_1}\frac{\mathrm{i}^s}{s}\cos\left(\frac{s\left(\theta_N+\theta_1-2\varphi_m\right)}{2}\right)\sin\left(\frac{s(\theta_N-\theta_1)}{2}\right)\right)\right|\le\epsilon,\quad(5.57)$$

and

$$\left|\int_{k_1}^{k_P}\Lambda_S^{\vartheta_1,\vartheta_L}(k,|\mathbf{r}_m-\mathbf{z}|)\mathrm{J}_0(k|\mathbf{r}_m-\mathbf{z}|)\mathrm{d}k-\left(\int_{k_1}^{k_P}\mathrm{J}_0(k|\mathbf{r}_m-\mathbf{z}|)\mathrm{J}_s(k|\mathbf{r}_m-\mathbf{z}|)\mathrm{d}k\right)\right.$$
$$\left.\times\left(\frac{4}{\vartheta_L-\vartheta_1}\sum_{t=1}^{\mathcal{N}_2}\frac{\mathrm{i}^t}{t}\cos\left(\frac{t\left(\vartheta_L+\vartheta_1-2\varphi_m\right)}{2}\right)\sin\left(\frac{t(\vartheta_L-\vartheta_1)}{2}\right)\right)\right|\le\epsilon.\quad(5.58)$$

Then, there exists a large number $\mathcal{N}=\max\{\mathcal{N}_1,\mathcal{N}_2\}$ such that

$$\left|\int_{k_1}^{k_P}\Phi_2\mathrm{d}k-\sum_{s=1}^{\mathcal{N}}\frac{\mathrm{i}^s}{s}\left\{\left(\frac{4}{\theta_N-\theta_1}\right)\cos\left(\frac{s\left(\theta_N+\theta_1-2\varphi_m\right)}{2}\right)\sin\left(\frac{s(\theta_N-\theta_1)}{2}\right)\right.\right.$$
$$\left.\left.+\left(\frac{4}{\vartheta_L-\theta_1}\right)\cos\left(\frac{s\left(\vartheta_L+\vartheta_1-2\varphi_m\right)}{2}\right)\sin\left(\frac{s(\vartheta_L-\vartheta_1)}{2}\right)\right\}\right.$$
$$\left.\times\int_{k_1}^{k_P}\mathrm{J}_0(k|\mathbf{r}_m-\mathbf{z}|)\mathrm{J}_s(k|\mathbf{r}_m-\mathbf{z}|)\mathrm{d}k\right|<\epsilon,\quad(5.59)$$

According to (Abramowitz and Stegun 1964, p.362, 9.1.62), for $x\in\mathbb{R}$, the following relation is holding:

$$\mathrm{J}_s(x)\le\frac{|x|^s}{2^s s!}.\quad(5.60)$$

Then, applying Hölder inequality, we can obtain

$$\int_{k_1}^{k_P}\mathrm{J}_0(k|\mathbf{r}_m-\mathbf{z})\mathrm{J}_s(k|\mathbf{r}_m-\mathbf{z})\mathrm{d}k\le\frac{|\mathbf{r}_m-\mathbf{z}|^s}{2^s s!}\int_{k_1}^{k_P}|k|^s\mathrm{d}k\le\frac{(k_P^{s+1}-k_1^{s+1})|\mathbf{r}_m-\mathbf{z}|^s}{2^s(s+1)!}.\quad(5.61)$$

Assume that $\mathbf{z}$ is sufficiently close to $\mathbf{r}_m$ such that $k_P|\mathbf{z}-\mathbf{r}_m|\ll\sqrt{\mathcal{N}+1}$. Then,

$$\int_{k_1}^{k_P}\mathrm{J}_0(k|\mathbf{r}_m-\mathbf{z})\mathrm{J}_s(k|\mathbf{r}_m-\mathbf{z})\mathrm{d}k\le\frac{(k_P^{s+1}-k_1^{s+1})|\mathbf{r}_m-\mathbf{z}|^s}{2^s(s+1)!}\ll\frac{k_P\sqrt{\mathcal{N}+1}}{2^s(s+1)!}.\quad(5.62)$$

If $\mathbf{z}$ is far away from $\mathbf{r}_m$ such that $k_P|\mathbf{z}-\mathbf{r}_m| \gg |\mathcal{N}^2 - 0.25|$, then, for $s = 1, 2, \cdots, \mathcal{N}$, the following asymptotic form of the Bessel function of integer order is holding:

$$\mathrm{J}_s(k|\mathbf{r}_m-\mathbf{z}|) \approx \sqrt{\frac{2}{k\pi|\mathbf{r}_m-\mathbf{z}|}}\cos\left(k|\mathbf{r}_m-\mathbf{z}| - \frac{s\pi}{2} - \frac{\pi}{4} + O\left(\frac{1}{k|\mathbf{r}_m-\mathbf{z}|}\right)\right). \tag{5.63}$$

This yields that

$$\begin{aligned}\int_{k_1}^{k_P} \mathrm{J}_0(k|\mathbf{r}_m-\mathbf{z}|)\mathrm{J}_s(k|\mathbf{r}_m-\mathbf{z}|)\mathrm{d}k &\leq \int_{k_1}^{k_P}\sqrt{\frac{2}{k\pi|\mathbf{r}_m-\mathbf{z}|}}\cos\left(k|\mathbf{r}_m-\mathbf{z}| - \frac{s\pi}{2} - \frac{\pi}{4}\right)\mathrm{d}k,\\ &\leq \sqrt{\frac{2}{\pi|\mathbf{r}_m-\mathbf{z}|}}(\sqrt{k_P}-\sqrt{k_1}),\\ &< k_P\sqrt{\frac{2}{k_P\pi|\mathbf{r}_m-\mathbf{z}|}} \leq k_P\sqrt{\frac{2}{\pi|\mathcal{N}^2-0.25|}}.\end{aligned} \tag{5.64}$$

and

$$|\Phi_2| \ll O\left(\frac{1}{\theta_N-\theta_1}\right) + O\left(\frac{1}{\vartheta_L-\vartheta_1}\right). \tag{5.65}$$

Analogously, we see that

$$|\Phi_3| \ll O\left(\frac{1}{(\theta_N-\theta_1)(\vartheta_L-\vartheta_1)}\right). \tag{5.66}$$

□

Remark 5.2.6 (Properties of MDSMA) *The following properties can be examined through the result in Theorem 5.2.5.*

1. *The term* $(\mathcal{H}(k_P,|\mathbf{r}_m-\mathbf{z}|)-\mathcal{H}(k_1,|\mathbf{r}_m-\mathbf{z}|))/(k_P-k_1)$ *is independent of the range of observation and incident directions, and its value is equal to* 1 *while the term* $\Lambda_M^3(k_1,k_P,\theta_1,\theta_N,\vartheta_1,\vartheta_L,|\mathbf{r}_m-\mathbf{z}|) = 0$ *when* $\mathbf{z}=\mathbf{r}_m$. *Therefore, we can say that terms* $(\mathcal{H}(k_P,|\mathbf{r}_m-\mathbf{z}|)-\mathcal{H}(k_1,|\mathbf{r}_m-\mathbf{z}|))/(k_P-k_1)$ *and* $\Lambda_M^3(k_1,k_P,\theta_1,\theta_N,\vartheta_1,\vartheta_L,|\mathbf{r}_m-\mathbf{z}|)$ *contributes to and disturbs the imaging performance, respectively, in both single impinging and multiple impinging directions.*

2. *On the basis of the behavior of* $(\mathcal{H}(k_P,|\mathbf{r}_m-\mathbf{z}|)-\mathcal{H}(k_1,|\mathbf{r}_m-\mathbf{z}|))/(k_P-k_1)$ *displayed in Figure 5.2(b), we can observe that in contrast with* $\mathcal{I}^{\infty}_{\mathrm{MDSM}}(\mathbf{z},\hat{\mathbf{d}})$ *in Remark 5.2.4, the map of* $\mathcal{I}^{\infty}_{\mathrm{MDSMA}}(\mathbf{z},\hat{\mathbf{d}})$ *contains peaks of large magnitudes at the location of all inhomogeneities. Thus, it will be possible to recognize every locations.*

3. *To improve the imaging performance of MDSMA, the range of observation directions and incident directions should be chosen such as* $\Lambda_M^3(k_1,k_{PF},\theta_1,\theta_N,\vartheta_1,\vartheta_L,|\mathbf{r}_m-\mathbf{z}|) = 0$ *for every* $\mathbf{z}\in\Omega$. *According to (5.49), we have to choose the ranges* $[\theta_1,\theta_N]$ *and* $[\vartheta_1,\vartheta_L]$ *satisfying* $\Lambda_S^{\theta_1,\theta_N}(k,|\mathbf{r}_m-\mathbf{z}|) = 0$ *and* $\Lambda_S^{\vartheta_1,\vartheta_L}(k,|\mathbf{r}_m-\mathbf{z}|) = 0$ *as alike with the single-frequency DSMA case discussed in Remark 4.3.4, even though multiple frequencies are considered. For instance,* $\theta_N-\theta_1 \geq \pi$ *and* $\vartheta_L-\theta_1 \geq \pi$.

Remark 5.2.7 (Structure of $\mathcal{I}^{\infty}_{\mathrm{MDSMA}}(\mathbf{z},\hat{\mathbf{d}})$ with single impinging direction) *To compare the imaging performance of* $\mathcal{I}^{\infty}_{\mathrm{MDSM}}(\mathbf{z},\hat{\mathbf{d}})$ *and* $\mathcal{I}^{\infty}_{\mathrm{MDSMA}}(\mathbf{z},\hat{\mathbf{d}})$, *we consider the single impinging direction case.*

1. *If a single impinging direction is considered, i.e., $L = 1$, we have*

$$\lim_{\vartheta_L \to \vartheta_1} \Lambda_S^{\vartheta_1,\vartheta_L}(k, |\mathbf{r}-\mathbf{z}|) = 2\sum_{s=1}^{\infty} \mathrm{i}^s \mathrm{J}_s(k|\mathbf{r}_m-\mathbf{z}|)\cos(s\varphi_m), \tag{5.67}$$

and

$$\Lambda_M^3(k_1, k_P, \theta_1, \theta_N, \vartheta_1, \vartheta_1, |\mathbf{r}_m-\mathbf{z}|) = \frac{1}{k_P-k_1}\sum_{s=1}^{\infty}\int_{k_1}^{k_P}\Big\{\Big[2\mathrm{i}^s\cos(s\varphi_m)\mathrm{J}_s(k|\mathbf{r}_m-\mathbf{z}|) + \Lambda_S^{\theta_1,\theta_N}(k, |\mathbf{r}_m-\mathbf{z}|)\Big]\mathrm{J}_0(k|\mathbf{r}_m-\mathbf{z}|) + \Big[2\mathrm{i}^s\cos(s\varphi_m)\mathrm{J}_t(k|\mathbf{r}_m-\mathbf{z}|)\Big]\Lambda_S^{\theta_1,\theta_N}(k, |\mathbf{r}_m-\mathbf{z}|)\Big\}\mathrm{d}k. \tag{5.68}$$

Therefore,

$$\mathcal{M}_3(\mathbf{z};\hat{\mathbf{d}}) = \sum_{m=1}^{M}\alpha_m^2\left(\frac{\varepsilon_m-\varepsilon_0}{\sqrt{\varepsilon_m\varepsilon_0}}\right)\left\{\frac{1}{k_P-k_1}\left[\mathcal{H}(k_P, |\mathbf{r}_m-\mathbf{z}|) - \mathcal{H}(k_1, |\mathbf{r}_m-\mathbf{z}|) + \int_{k_1}^{k_P}\mathrm{J}_1(k|\mathbf{r}_m-\mathbf{z}|)\mathrm{d}k\right] + \Lambda_M^3(k_1, k_P, \theta_1, \theta_N, \vartheta_1, \vartheta_1, |\mathbf{r}_m-\mathbf{z}|)\right\}, \tag{5.69}$$

which means that the efficiency becomes worse compared to MDSMA with multiple impinging directions since

$$|\Lambda_M^3(k_1, k_P, \theta_1, \theta_N, \vartheta_1, \vartheta_L, |\mathbf{r}_m-\mathbf{z}|)| \leq |\Lambda_M^3(k_1, k_P, \theta_1, \theta_N, \vartheta_1, \vartheta_1, |\mathbf{r}_m-\mathbf{z}|)|. \tag{5.70}$$

Note that it has same structure in the single receiver case ($\theta_1 = \theta_N$), analogously.

2. *The representation formulas (5.3) and (5.69) show that*

$$\mathcal{I}_{\mathrm{MDSM}}^{\infty}(\mathbf{z};\hat{\mathbf{d}}) \propto \left|\frac{1}{k_P-k_1}\left(\mathcal{S}(k_P, |\mathbf{r}-\mathbf{z}|) - \mathcal{S}(k_1, |\mathbf{r}-\mathbf{z}|)\right)\right|, \tag{5.71}$$

and

$$\mathcal{I}_{\mathrm{MDSMA}}^{\infty}(\mathbf{z},\hat{\mathbf{d}}) \propto \left|\frac{1}{k_P-k_1}\left(\mathcal{H}(k_P, |\mathbf{r}-\mathbf{z}|) - \mathcal{H}(k_1, |\mathbf{r}-\mathbf{z}|)\right)\right|, \tag{5.72}$$

where $\mathcal{S}(k, |\mathbf{r}-\mathbf{z}|)$ and $\mathcal{H}(k, |\mathbf{r}-\mathbf{z}|)$ are given by (5.5) and (5.19), respectively. Two-dimensional plots of each function are exhibited in Figure 5.2. Based on this figure, we can observe that the map of $\mathcal{I}_{\mathrm{MDSMA}}^{\infty}(\mathbf{z},\hat{\mathbf{d}})$ has less oscillations than those of $\mathcal{I}_{\mathrm{MDSM}}^{\infty}(\mathbf{z};\hat{\mathbf{d}})$ so that MDSMA can be regarded as an improved version of MDSM. However, because of the disturbing terms, a wide range of observation directions (e.g. $\vartheta_L - \theta_1 \geq \pi$) is essential to get a better imaging efficiency via MDSMA as stated already in Remark 5.2.6.

5.3 Numerical simulations

To validate our theoretical results, we present numerical simulations where the configuration settings are exactly the same as in Examples in section 4.3.3 with multiple frequencies. The accuracy of the methods is compared again using Jaccard index A.3. For the various cases of limited-aperture problem, we recall the Table 4.1 and 4.2 for simulations with synthetic data and Table 4.3 for simulations with experimental data. Note that the red line and black line indicate the $\mathbf{x}_n$ and $-\hat{\mathbf{d}}_l$, respectively.

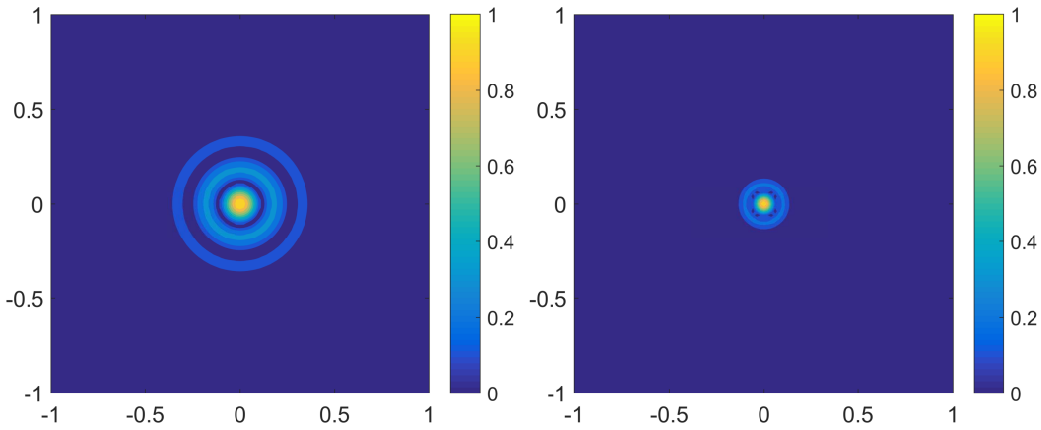

(a) $|(\mathcal{S}(k_P,|\mathbf{z}|)-\mathcal{S}(k_1,|\mathbf{z}|))/(k_P-k_1)|$ (b) $|(\mathcal{H}(k_P,|\mathbf{z}|)-\mathcal{H}(k_1,|\mathbf{z}|))/(k_P-k_1)|$

Figure 5.2: Two-dimensional plots of $|(\mathcal{S}(k_P,|\mathbf{z}|)-\mathcal{S}(k_1,|\mathbf{z}|))/(k_P-k_1)|$, and $|(\mathcal{H}(k_P,|\mathbf{z}|)-\mathcal{H}(k_1,|\mathbf{z}|))/(k_P-k_1)|$ for $f_1 = 700\,\text{MHz}$ and $f_P = 1.3\,\text{GHz}$

Synthetic data Here, the collected data are again calculated by `FEKO` with 7 frequencies from 700 MHz to 1.3 GHz, and a step size of 100 MHz.

Example 5.3.1 (Small dielectric disk) *Here, we reconstruct the small dielectric disk with radius* $\alpha \equiv 0.1\lambda_0 = 0.03\,\text{m}$ *and permittivity* $\varepsilon \equiv 5\varepsilon_0$*, where its location is* $\mathbf{r} = (-0.333\lambda_0, 0.666\lambda_0) = (-0.1\,\text{m}, 0.2\,\text{m})$

The reconstructions of the location of the inhomogeneity via $\mathcal{I}^{\infty}_{\text{MDSM}}(\mathbf{z})$ and $\mathcal{I}^{\infty}_{\text{MDSMA}}(\mathbf{z})$ are presented in Figure 5.3 and 5.4, respectively. They show that both $\mathcal{I}^{\infty}_{\text{MDSM}}(\mathbf{z})$ and $\mathcal{I}^{\infty}_{\text{MDSMA}}(\mathbf{z})$ are working well to localize the location of τ. Furthermore, the results of Jaccard index prove that they are the improved version of DSM and DSMA operated at fixed frequency (see Figure 4.5 and 4.6) as stated in Remark 5.2.2 and Remark 5.2.6. However, the result of $\mathcal{I}^{\infty}_{\text{MDSM}}(\mathbf{z})$ is not significantly improved as the total number and range of incident fields is increased. On the other hand, the imaging performance of $\mathcal{I}^{\infty}_{\text{MDSMA}}(\mathbf{z})$ is improved when a higher number and a wider rage incident fields are considered.

Example 5.3.2 (Small three dielectric disks with same size and permittivity) *We remind the information about inhomogeneities* τ_m *with* $\alpha_m \equiv 0.1\lambda_0 = 0.03\,\text{m}$ *and* $\varepsilon_m \equiv 5\varepsilon_0$*,* $m = 1,2,3$*. The locations* $\mathbf{r}_m$ *of* τ_m *are* $\mathbf{r}_1 = (-8\lambda_0/3, 0) = (-0.8\,\text{m}, 0)$*,* $\mathbf{r}_2 = (4\lambda_0/3, -2\lambda_0) = (0.4\,\text{m}, -0.6\,\text{m})$*, and* $\mathbf{r}_2 = (\lambda_0/3, 2\lambda_0) = (0.1\,\text{m}, 0.6\,\text{m})$*.*

According to Figures 5.5 and 5.6, we observe that $\mathcal{I}^{\infty}_{\text{MDSM}}(\mathbf{z})$ cannot be applied in multiple inhomogeneities imaging even with a wide range of incident directions as already stated in Remark 5.2.4, but $\mathcal{I}^{\infty}_{\text{MDSMA}}(\mathbf{z}, \hat{\mathbf{d}})$ can be as already stated in Remark 5.2.6. The τ_m are not easy to be identified in Case A1 and A2 with Case B1, but can be with more incident directions (Case B2, B3, and B4) contrarily to the result of single frequency DSM (see Figure 4.7 and 4.8). Furthermore, $\mathcal{I}^{\infty}_{\text{MDSMA}}(\mathbf{z})$ has less oscillations and better results than $\mathcal{I}^{\infty}_{\text{DSM}}(\mathbf{z}, \hat{\mathbf{d}}; k_0)$ and $\mathcal{I}^{\infty}_{\text{DSMA}}(\mathbf{z}; k_0)$. Namely, our proposal is an improved version of traditional DSM and DSMA as demonstrated in Remark 5.2.6.

Example 5.3.3 (Large dielectric disk) *The location and size of a large inhomogeneity are* $\mathbf{r} = (-\lambda_0, -\lambda_0) = (-0.3\,\mathrm{m}, -0.3\,\mathrm{m})$ *and* $\alpha_m \equiv \lambda_0 = 0.3\,\mathrm{m}$*, respectively. The dielectric permittivity is given by* $\varepsilon \equiv 5\varepsilon_0$.

Even though a single small target can be visualized in the map of $\mathcal{I}^{\infty}_{\mathrm{MDSM}}(\mathbf{z})$, a large target cannot, even with a wide range of incident directions, see Figure 5.7. On the other hand, we can identify the location and shape of the target by $\mathcal{I}^{\infty}_{\mathrm{MDSM}}(\mathbf{z})$ with wide ranges of incident and observation directions (e.g. $\theta_N - \theta_1 \geq \pi$ and $\vartheta_L - \vartheta_1 \geq \pi$). However, similarly with the single-frequency numerical simulations in Example 4.3.11, the exact location and/or shape is hard to be reconstructed via $\mathcal{I}^{\infty}_{\mathrm{MDSMA}}(\mathbf{z})$ with a single incident direction and wide ranges of observation directions (analogously with single observation direction and wide incident directions range) even though multi-frequencies are used. Nevertheless, our proposal $\mathcal{I}^{\infty}_{\mathrm{MDSMA}}(\mathbf{z})$ has better accuracy than with the single-frequency approach according to the Jaccard index.

Experimental data Now, our theoretical results are validated by numerical simulations with experimental data. Here, the MDSMA is only considered because MDSM cannot be applied in general cases (e.g. multiple targets in Example 5.3.2 and large target in Example 5.3.3). Furthermore, the single impinging direction cases are only available due to the limitation of experimental setup stated in section 4.3.3.

We consider the 8 frequencies ranged from 1 GHz to 8 GHz with a step size of 1 GHz for Example 5.3.4, and from 2 GHz to 16 GHz with a step size of 2 GHz for Example 5.3.5, Example 5.3.6.

Example 5.3.4 (Small two dielectric disks with same size and permittivity) *Two disks are located at* $(-0.012\,\mathrm{m}, -0.045\,\mathrm{m})$ *and* $(0\,\mathrm{m}, 0.045\,\mathrm{m})$*. Their radius and electrical permittivity are* $0.015\,\mathrm{m}$ *and* $\varepsilon \propto 3\varepsilon_0$.

According to Figure 5.9, the results seem to be similar to Example 5.3.2, i.e, the inhomogeneities can be visualized by $\mathcal{I}^{\infty}_{\mathrm{MDSMA}}(\mathbf{z}, \hat{\mathbf{d}})$ if $\theta_N - \theta_1 \geq \pi$. Hence, our proposal $\mathcal{I}^{\infty}_{\mathrm{MDSMA}}(\mathbf{z}, \hat{\mathbf{d}})$ is an improved version of $\mathcal{I}^{\infty}_{\mathrm{DSMA}}(\mathbf{z}, \hat{\mathbf{d}}; k_0)$ and our theoretical results still hold with experimental data.

Example 5.3.5 (Small metallic square) *Now, we consider metallic and quadrangular target which is non-circular. It is located at* $\mathbf{r} \approx (0\,\mathrm{m}, 0.04\,\mathrm{m})$ *and has the side lengths* $0.0127\,\mathrm{m}$ *and* $0.0245\,\mathrm{m}$.

The results are presented in Figures 5.10. It shows that the location of the target is identified on the right side of the exact center which is similar with the single frequency case displayed in Figure 4.12 even though the oscillations are decreased by using multiple frequencies.

Example 5.3.6 (Metallic U-shape) *A more complex U-shaped metal is considered here. Its size is* $0.05\,\mathrm{m} \times 0.08\,\mathrm{m}$ *with thickness* $0.005\,\mathrm{m}$.

Figure 5.11 means that the target cannot be properly reconstructed by MDSMA with a single source even though multiple frequencies are considered. Hence, the wide range of incident directions is necessary to image the U-shape target.

5.4 Conclusions

In this chapter, the representation formulas for DSM and DSMA using multi-frequency in limited-aperture problem are identified thanks to the asymptotic formula of far-field pattern. The indicator function of multi-frequency DSM is suggested and analyzed when only a single small homogeneity exists in the medium and theoretically proves that it can be represented by infinite series of Bessel functions of first kind with integer order and Struve function. However, the indicator function cannot be applied in the case of several well-separated inhomogeneities so that an alternative multi-frequency is proposed to overcome this limitation. Various numerical simulations with synthetic and experimental data are presented to support our theoretical results.

In the next chapter, the direct sampling method in 3D inverse electromagnetic scattering problem will be considered with the similar approach using the asymptotic formula of the scattered field.

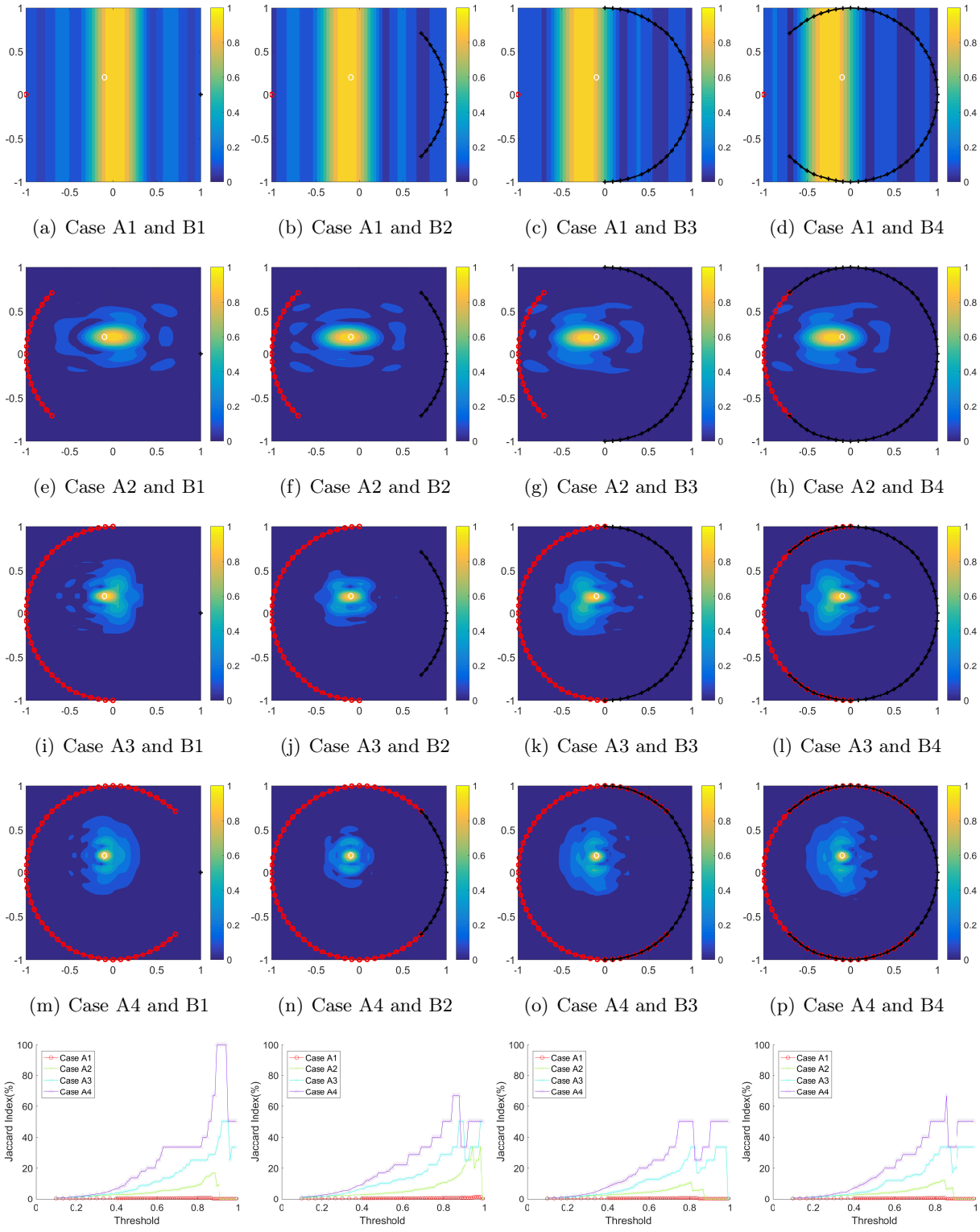

(a) Case A1 and B1 (b) Case A1 and B2 (c) Case A1 and B3 (d) Case A1 and B4

(e) Case A2 and B1 (f) Case A2 and B2 (g) Case A2 and B3 (h) Case A2 and B4

(i) Case A3 and B1 (j) Case A3 and B2 (k) Case A3 and B3 (l) Case A3 and B4

(m) Case A4 and B1 (n) Case A4 and B2 (o) Case A4 and B3 (p) Case A4 and B4

(q) Jaccard index (B1 case) (r) Jaccard index (B2 case) (s) Jaccard index (B3 case) (t) Jaccard index (B4 case)

Figure 5.3: (Example 5.3.1) Maps of $\mathcal{Z}_{\mathrm{MDSM}}(\mathbf{z})$ and Jaccard index

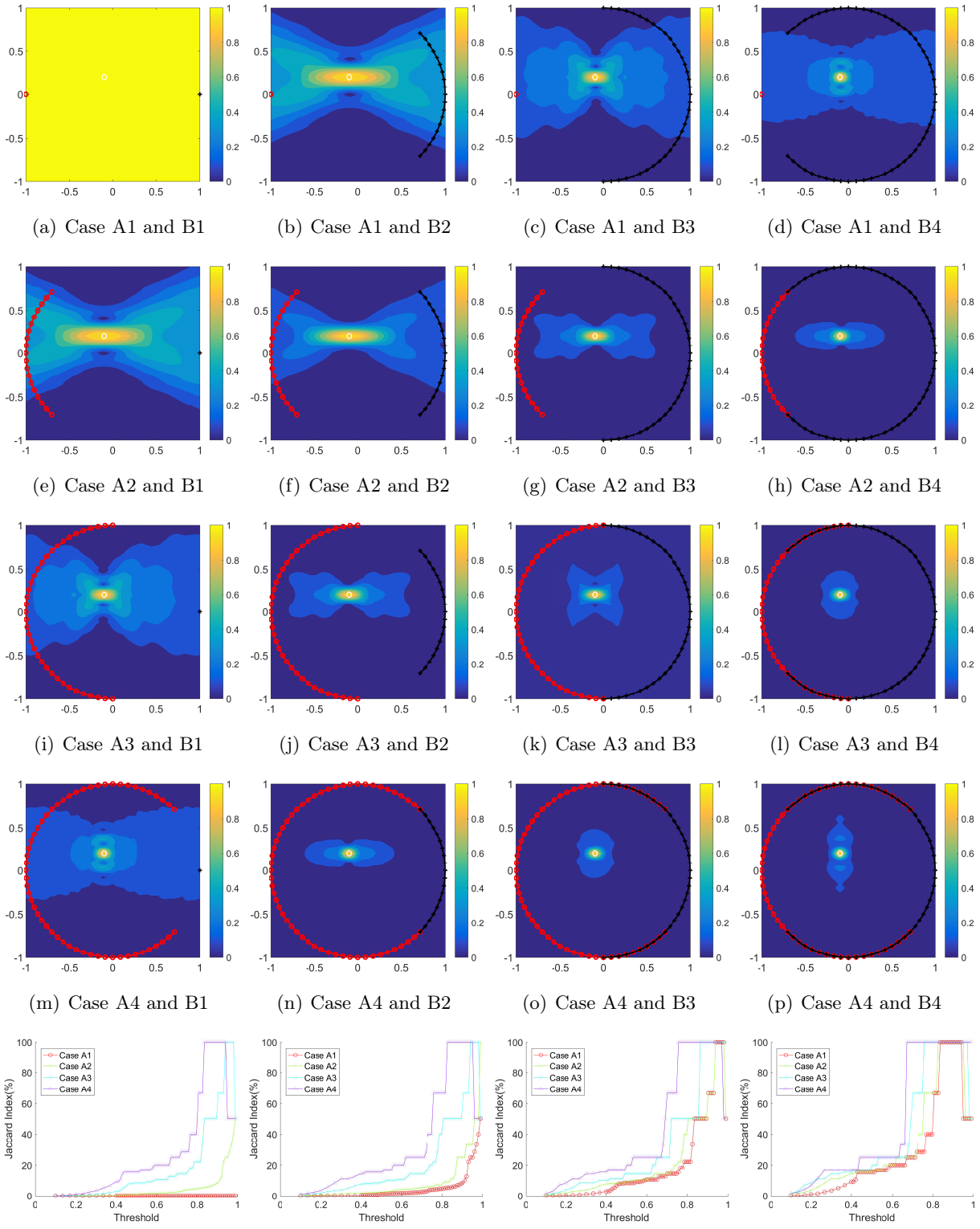

(a) Case A1 and B1 (b) Case A1 and B2 (c) Case A1 and B3 (d) Case A1 and B4

(e) Case A2 and B1 (f) Case A2 and B2 (g) Case A2 and B3 (h) Case A2 and B4

(i) Case A3 and B1 (j) Case A3 and B2 (k) Case A3 and B3 (l) Case A3 and B4

(m) Case A4 and B1 (n) Case A4 and B2 (o) Case A4 and B3 (p) Case A4 and B4

(q) Jaccard index (B1 case) (r) Jaccard index (B2 case) (s) Jaccard index (B3 case) (t) Jaccard index (B4 case)

Figure 5.4: (Example 5.3.1) Maps of $\mathcal{I}_{\mathrm{MDSMA}}(\mathbf{z})$ and Jaccard index

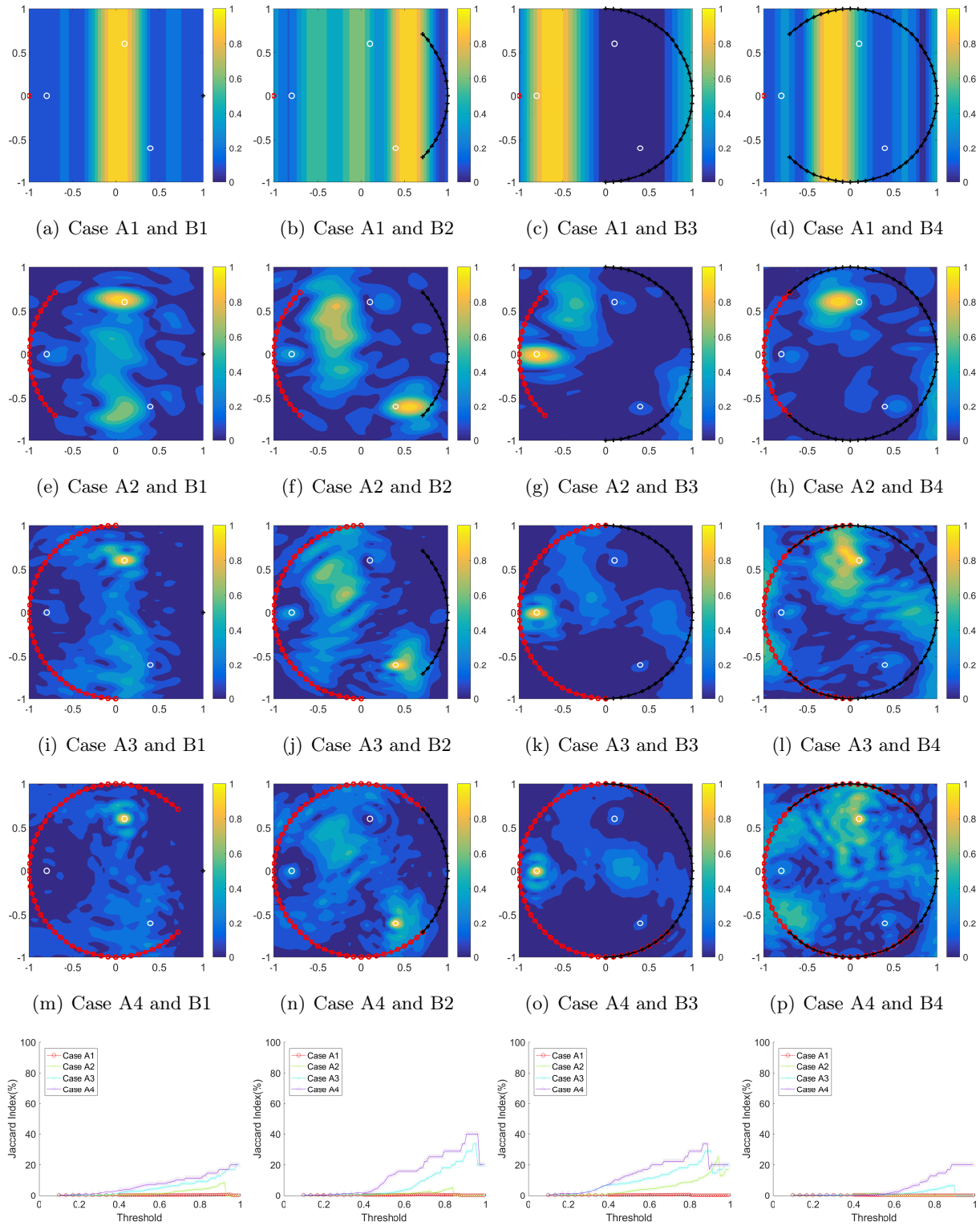

(a) Case A1 and B1 (b) Case A1 and B2 (c) Case A1 and B3 (d) Case A1 and B4

(e) Case A2 and B1 (f) Case A2 and B2 (g) Case A2 and B3 (h) Case A2 and B4

(i) Case A3 and B1 (j) Case A3 and B2 (k) Case A3 and B3 (l) Case A3 and B4

(m) Case A4 and B1 (n) Case A4 and B2 (o) Case A4 and B3 (p) Case A4 and B4

(q) Jaccard index when B1 case (r) Jaccard index when B1 case (s) Jaccard index when B1 case (t) Jaccard index when B1 case

Figure 5.5: (Example 5.3.2) Maps of $\mathcal{I}^{\infty}_{\mathrm{MDSM}}(\mathbf{z})$ and Jaccard index

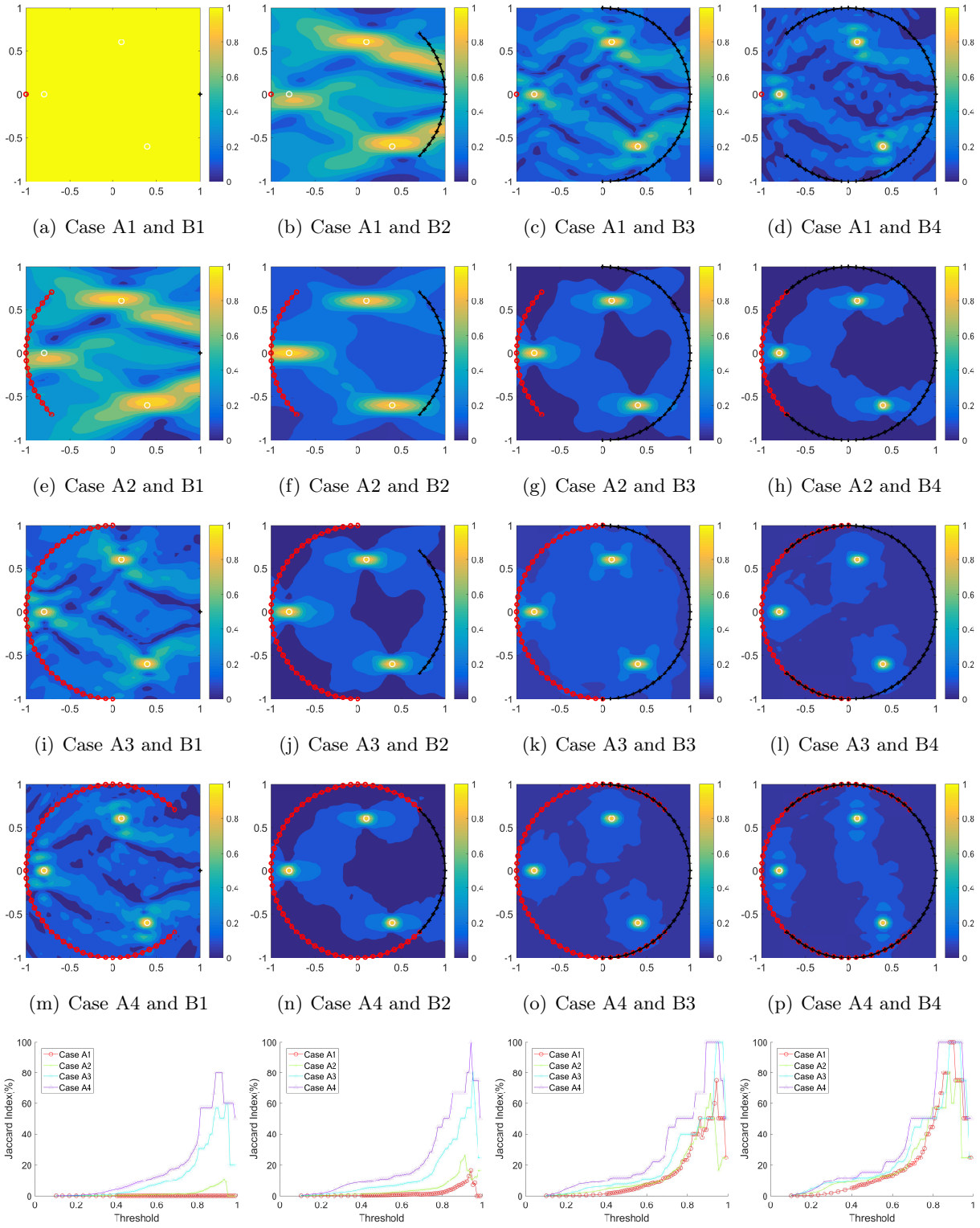

(a) Case A1 and B1 (b) Case A1 and B2 (c) Case A1 and B3 (d) Case A1 and B4

(e) Case A2 and B1 (f) Case A2 and B2 (g) Case A2 and B3 (h) Case A2 and B4

(i) Case A3 and B1 (j) Case A3 and B2 (k) Case A3 and B3 (l) Case A3 and B4

(m) Case A4 and B1 (n) Case A4 and B2 (o) Case A4 and B3 (p) Case A4 and B4

(q) Jaccard index when B1 case (r) Jaccard index when B1 case (s) Jaccard index when B1 case (t) Jaccard index when B1 case

Figure 5.6: (Example 5.3.2) Maps of $\mathcal{I}^{\infty}_{\mathrm{MDSMA}}(\mathbf{z})$ and Jaccard index

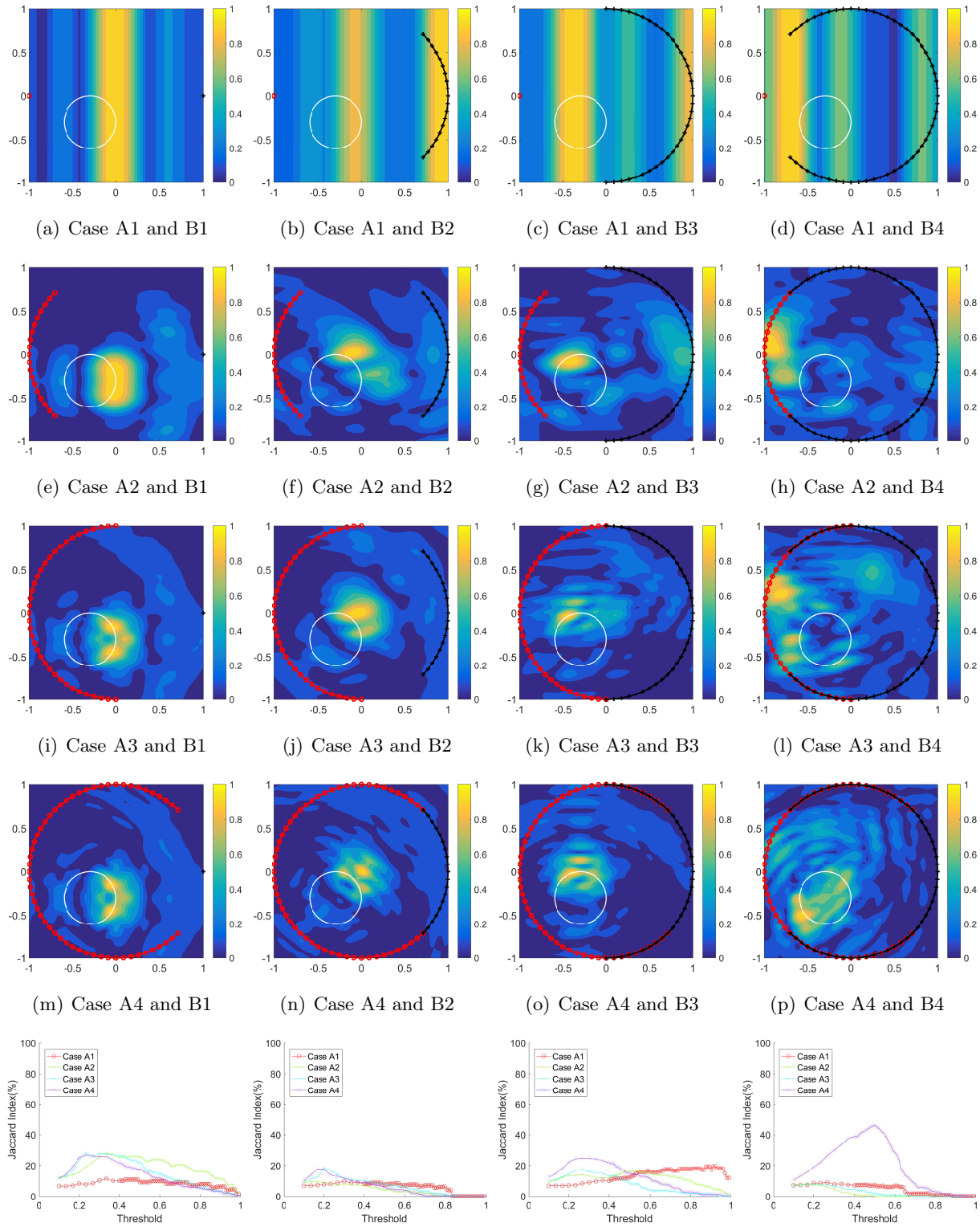

(a) Case A1 and B1 (b) Case A1 and B2 (c) Case A1 and B3 (d) Case A1 and B4

(e) Case A2 and B1 (f) Case A2 and B2 (g) Case A2 and B3 (h) Case A2 and B4

(i) Case A3 and B1 (j) Case A3 and B2 (k) Case A3 and B3 (l) Case A3 and B4

(m) Case A4 and B1 (n) Case A4 and B2 (o) Case A4 and B3 (p) Case A4 and B4

(q) Jaccard index when B1 case (r) Jaccard index when B1 case (s) Jaccard index when B1 case (t) Jaccard index when B1 case

Figure 5.7: (Example 5.3.2) Maps of $\mathcal{I}^{\infty}_{\mathrm{MDSM}}(\mathbf{z})$ and Jaccard index

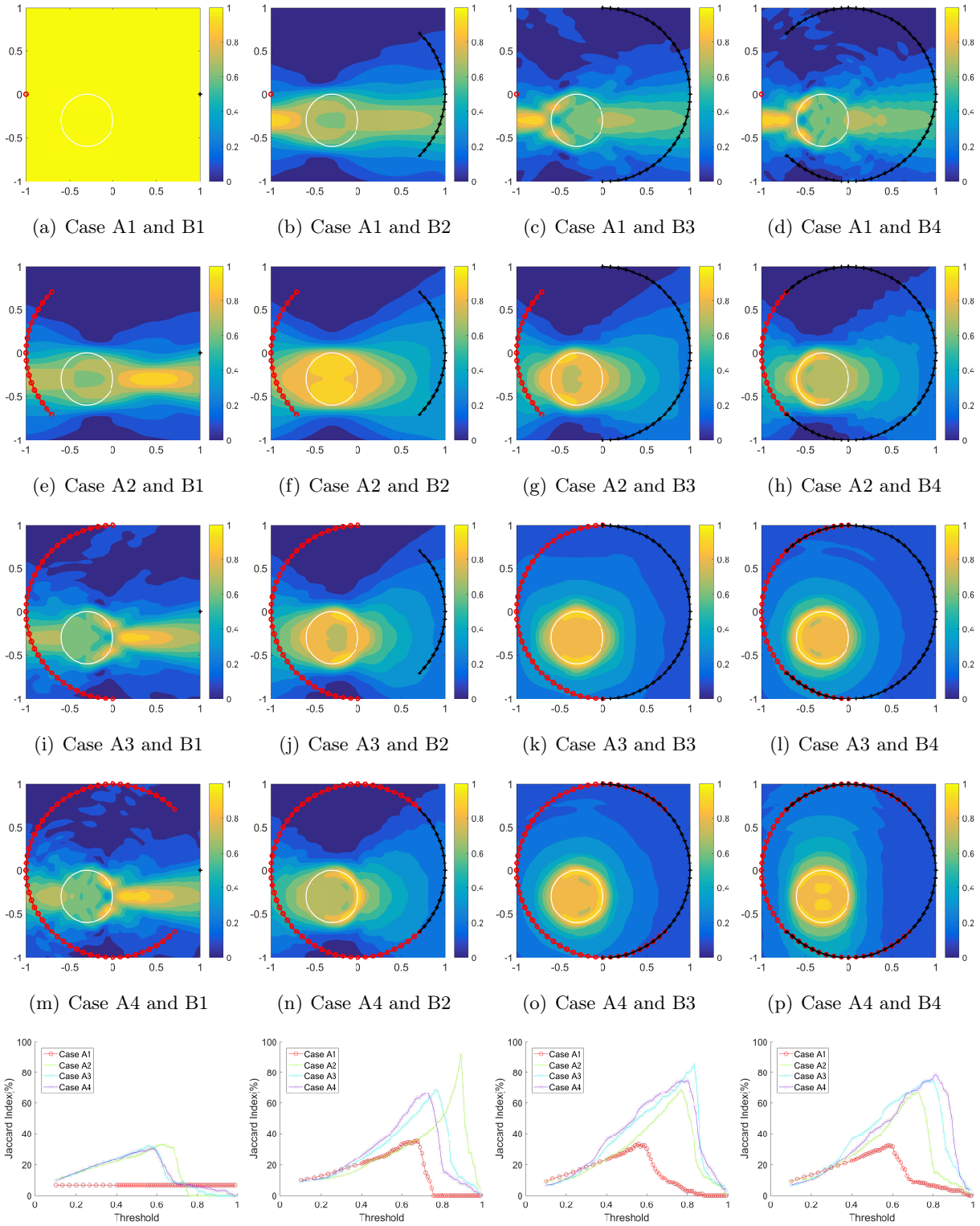

(a) Case A1 and B1 (b) Case A1 and B2 (c) Case A1 and B3 (d) Case A1 and B4

(e) Case A2 and B1 (f) Case A2 and B2 (g) Case A2 and B3 (h) Case A2 and B4

(i) Case A3 and B1 (j) Case A3 and B2 (k) Case A3 and B3 (l) Case A3 and B4

(m) Case A4 and B1 (n) Case A4 and B2 (o) Case A4 and B3 (p) Case A4 and B4

(q) Jaccard index when B1 case (r) Jaccard index when B1 case (s) Jaccard index when B1 case (t) Jaccard index when B1 case

Figure 5.8: (Example 5.3.3) Maps of $\mathcal{I}^{\infty}_{\mathrm{MDSMA}}(\mathbf{z})$ and Jaccard index

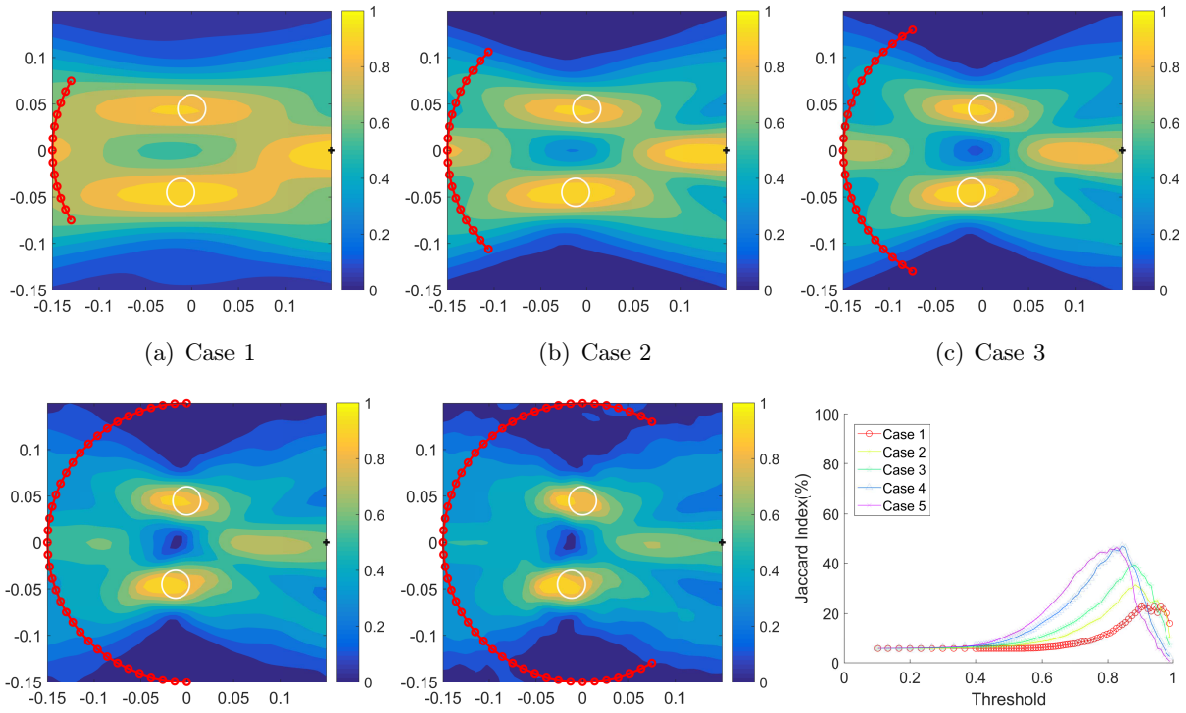

(a) Case 1 (b) Case 2 (c) Case 3

(d) Case 4 (e) Case 5 (f) Jaccard Index

Figure 5.9: (Example 5.3.4) Maps of $\mathcal{I}^{\infty}_{\mathrm{MDSMA}}(\mathbf{z}, \hat{\mathbf{d}})$ and Jaccard index

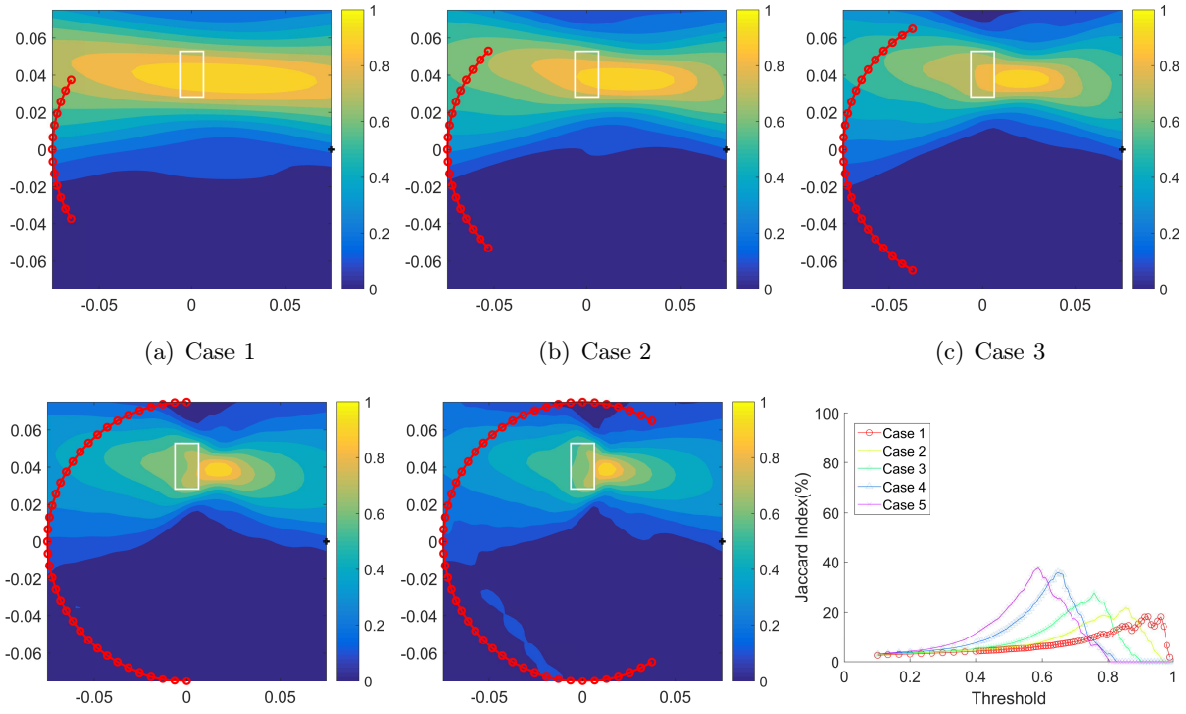

(a) Case 1 (b) Case 2 (c) Case 3

(d) Case 4 (e) Case 5 (f) Jaccard Index

Figure 5.10: (Example 5.3.5) Maps of $\mathcal{I}_{\mathrm{MDSMA}}(\mathbf{z}, \hat{\mathbf{d}})$ and Jaccard index

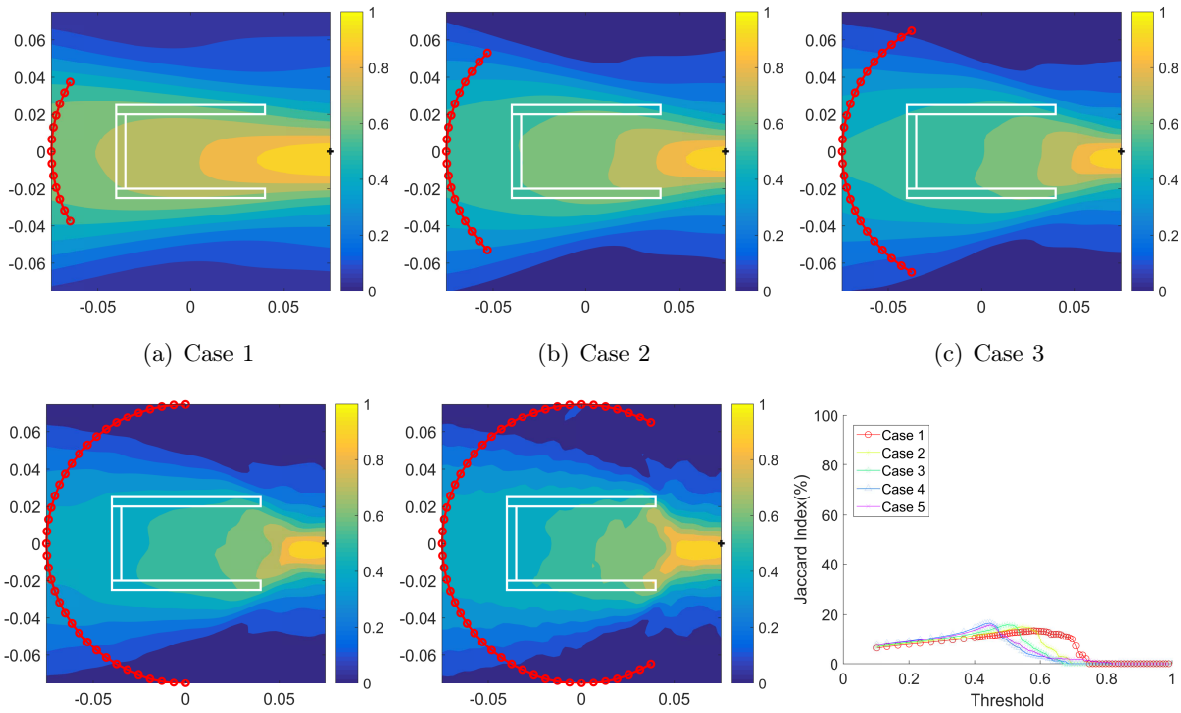

(a) Case 1 (b) Case 2 (c) Case 3

(d) Case 4 (e) Case 5 (f) Jaccard Index

Figure 5.11: (Example 5.3.6) Maps of $\mathcal{I}_{\text{MDSMA}}(\mathbf{z}, \hat{\mathbf{d}})$ and Jaccard index

6

3D imaging of dielectric inhomogeneities

Contents

6.1 Introduction

In this chapter, we extend our approach to the 3D inverse electromagnetic scattering problem. The DSM has been extended to two- and three-dimensional inverse electromagnetic scattering problem in (Ito, Jin, and J. Zou 2013) with the same conclusions: DSM is fast, robust and efficient technique for imaging the targets with only a few incident fields. The main difference between 2D and 3D DSM is the choice of the polarization of the test function. However, the result in (Ito, Jin, and J. Zou 2013) is not sufficient to explain the effect of the choice of test function for imaging the target. So the full analysis of the structure of the DSM indicator function for the 3D vectorial case is presented here. In the following, the analytical formulation of the DSM indicator is established within the framework of the asymptotic formula of scattered field for small targets in near- and far-field configuration. This analytical solution is expressed as a function of spherical Bessel functions of integer order and polarization tensor of the targets which carry the information about targets (e.g. location, size, shape, permittivity, etc.). Following (X. Chen and Zhong 2008) which dealt with the improvement of the accuracy of the MUSIC

imaging algorithm via a proper selection of the polarization test vector, the direct sampling method with proper test dipole (DSMP) is proposed to handle the choice of the polarization of the test function in near-field and far-field configurations.

The remainder of the study is structured as follows. The structure analysis of the direct sampling method, and corresponding numerical simulations are dealt with near-field and far-field data in section 6.2 and section 6.3, respectively. Additional numerical simulations using Fresnel experimental data are presented in section 6.4. Finally, section 6.6 provides conclusions and perspectives.

6.2 Direct sampling method with near-field data

6.2.1 Introduction of direct sampling method and its structure analysis

The direct sampling method has been introduced in (Ito, Jin, and J. Zou 2013) and only the main equations with our notation will be re-called. On the basis of the relation ((15) in (Ito, Jin, and J. Zou 2013))

$$\langle \mathbf{E}^s(\mathbf{x},\mathbf{y};k_0), \underline{\mathbf{G}}(\mathbf{x},\mathbf{z})\hat{\mathbf{q}}\rangle_{L^2(\Gamma_{\text{obs}})} \approx \frac{1}{k_0}\sum_{m=1}^{M} W_m \mathbf{J}(\mathbf{r}_m,\mathbf{y})\cdot\left(\text{Im}\left(\underline{\mathbf{G}}(\mathbf{z},\mathbf{r}_m)\right)\cdot\hat{\mathbf{q}}\right), \tag{6.1}$$

the indicator function of DSM ((16) in (Ito, Jin, and J. Zou 2013)) in the case of a single source located at $\mathbf{y}$ with $\hat{\mathbf{p}}^t$ as polarization direction is defined by

$$\mathcal{I}_{\text{DSM3D}}(\mathbf{z};\mathbf{y},\hat{\mathbf{q}}) := \frac{\left|\langle \mathbf{E}^s(\mathbf{x},\mathbf{y};k_0), \underline{\mathbf{G}}(\mathbf{x},\mathbf{z})\cdot\hat{\mathbf{q}}\rangle_{L^2(\Gamma_{\text{obs}})}\right|}{\|\mathbf{E}^s(\mathbf{x},\mathbf{y};k_0)\|_{L^2(\Gamma_{\text{obs}})}\,\|\underline{\mathbf{G}}(\mathbf{x},\mathbf{z})\hat{\mathbf{q}}\|_{L^2(\Gamma_{\text{obs}})}}, \tag{6.2}$$

and for L dipoles, it is given by

$$\mathcal{I}_{\text{DSM3D}}(\mathbf{z}) := \frac{1}{L}\sum_{l=1}^{L}\mathcal{I}_{\text{DSM3D}}(\mathbf{z};\mathbf{y}_l,\hat{\mathbf{q}}_l) \tag{6.3}$$

by taking into account each incident field. Here, $\underline{\mathbf{G}}(\mathbf{x},\mathbf{z})\cdot\hat{\mathbf{q}}$ is a test dipole polarized by $\hat{\mathbf{q}}$ and related to receivers. In (6.1), W_m can be seen as the strength of the induced current $\mathbf{J}(\mathbf{r}_m,\mathbf{y})$. The latter depends upon the geometric and electrical parameters of the targets and of the incident field, but its analytical expression is not available in the general case. So further analysis is needed to verify the full structure of the DSM indicator function.

Equation (6.1) shows that $\mathcal{I}_{\text{DSM3D}}(\mathbf{z};\mathbf{y},\hat{\mathbf{q}}) \approx 1$ if $\mathbf{z}=\mathbf{r}_m \in \tau_m$, otherwise $\mathcal{I}_{\text{DSM3D}}(\mathbf{z};\mathbf{y},\hat{\mathbf{q}}) \not\approx 1$ thanks to the oscillation property of the dyadic Green function. However, in the 3D vectorial case, the choice of the test polarization vector $\hat{\mathbf{q}}$ is a key parameter to proper retrieve the targets. Note that the authors of (Ito, Jin, and J. Zou 2013) proposed a guideline for choosing $\hat{\mathbf{q}}$ such that $\hat{\mathbf{q}}=\hat{\mathbf{p}}^t$, but no theoretical reason was provided.

Thanks to the use of the asymptotic formula of the scattered field introduced in Lemma 2.3.2, an analytical expression of $\mathbf{J}(\mathbf{y},\mathbf{r}_m)$ can be obtained which leads to the representation formula of the DSM indicator function $\mathcal{I}_{\text{DSM3D}}(\mathbf{z};\mathbf{y},\hat{\mathbf{q}})$ in the case of an incident field due to a dipole placed in $\mathbf{y}$ and polarized along $\hat{\mathbf{p}}^t$. Its derivation is as follows.

Theorem 6.2.1 *Assume that the total number of receiver directions N is sufficiently large and each inhomogeneity is small enough ($\alpha_m\sqrt{\varepsilon_m/\varepsilon_9} \ll \lambda$). Then, the DSM indicator function has the following representation formula.*

$$\mathcal{I}_{\mathrm{DSM3D}}(\mathbf{z};\mathbf{y},\hat{\mathbf{q}}) = \frac{|\mathcal{L}_1(\mathbf{z};\mathbf{y},\hat{\mathbf{q}})|}{\max\limits_{\mathbf{z}\in\Omega}|\mathcal{L}_1(\mathbf{z};\mathbf{y},\hat{\mathbf{q}})|}, \tag{6.4}$$

where

$$\mathcal{L}_1(\mathbf{z};\mathbf{y},\hat{\mathbf{q}}) = \sum_{m=1}^{M} A_m \left[C_1 \left(\mathrm{j}_0(k_0|\mathbf{r}_m-\mathbf{z}|) - \frac{\mathrm{j}_1(k_0|\mathbf{r}_m-\mathbf{z}|)}{k_0|\mathbf{r}_m-\mathbf{z}|} \right) + C_2 \frac{\mathrm{j}_2(k_0|\mathbf{r}_m-\mathbf{z}|)}{|\mathbf{r}_m-\mathbf{z}|^2} \right]. \tag{6.5}$$

where j_s is a spherical Bessel function of integer order s and A_m is defined in (2.25), and C_1 and C_2 are given by

$$C_1 = \left[\hat{\mathbf{p}}^t \cdot \hat{\mathbf{q}}\right] Q_1(\mathbf{y},\mathbf{r}_m) - \frac{\left[\hat{\mathbf{p}}^t \cdot (\mathbf{r}_m-\mathbf{y})\right]\left[\hat{\mathbf{q}} \cdot (\mathbf{r}_m-\mathbf{y})\right]}{|\mathbf{r}_m-\mathbf{y}|^2} Q_2(\mathbf{y},\mathbf{r}_m) \tag{6.6}$$

and

$$\begin{aligned} C_2 = {} & \frac{[\hat{\mathbf{q}} \cdot (\mathbf{r}_m-\mathbf{z})]\left[\hat{\mathbf{p}}^t \cdot (\mathbf{r}_m-\mathbf{y})\right][(\mathbf{r}_m-\mathbf{y}) \cdot (\mathbf{r}_m-\mathbf{z})]}{|\mathbf{r}_m-\mathbf{y}|^2} Q_2(\mathbf{y},\mathbf{r}_m) \\ & - \frac{\left[\hat{\mathbf{p}}^t \cdot (\mathbf{r}_m-\mathbf{z})\right]\left[\hat{\mathbf{q}} \cdot (\mathbf{r}_m-\mathbf{z})\right]}{|\mathbf{r}_m-\mathbf{y}|^2} Q_1(\mathbf{y},\mathbf{r}_m), \end{aligned} \tag{6.7}$$

respectively. Here, $Q_1(\mathbf{y},\mathbf{r}_m)$ and $Q_2(\mathbf{y},\mathbf{r}_m)$ are defined by

$$Q_1(\mathbf{y},\mathbf{r}_m) = g(\mathbf{y},\mathbf{r}_m) - \frac{g(\mathbf{y},\mathbf{r}_m)}{k_0^2|\mathbf{r}_m-\mathbf{y}|^2} + \frac{\mathrm{i}g(\mathbf{y},\mathbf{r}_m)}{k_0|\mathbf{r}_m-\mathbf{y}|}, \tag{6.8}$$

and

$$Q_2(\mathbf{y},\mathbf{r}_m) = g(\mathbf{y},\mathbf{r}_m) - \frac{3g(\mathbf{y},\mathbf{r}_m)}{k_0^2|\mathbf{r}_m-\mathbf{y}|^2} + \frac{3\mathrm{i}g(\mathbf{y},\mathbf{r}_m)}{k_0|\mathbf{r}_m-\mathbf{y}|}. \tag{6.9}$$

Proof Using the asymptotic formula of the scattered field (2.25) within the denominator of (6.2) leads to

$$\langle \mathbf{E}^s(\mathbf{x},\mathbf{y};k_0), \underline{\mathbf{G}}(\mathbf{x},\mathbf{z}) \cdot \hat{\mathbf{q}} \rangle_{L^2(\Gamma_{\mathrm{obs}})} = \mathrm{i}\omega_0\mu_0 k_0^2 Il \sum_{m=1}^{M} A_m \left\langle \underline{\mathbf{G}}(\mathbf{x},\mathbf{r}_m) \cdot (\underline{\mathbf{G}}(\mathbf{r}_m,\mathbf{y}) \cdot \hat{\mathbf{p}}^t), \underline{\mathbf{G}}(\mathbf{x},\mathbf{z}) \cdot \hat{\mathbf{q}} \right\rangle_{L^2(\Gamma_{\mathrm{obs}})} \tag{6.10}$$

$$\approx \mathrm{i}\omega_0\mu_0 k_0 Il \sum_{m=1}^{M} A_m (\underline{\mathbf{G}}(\mathbf{r}_m,\mathbf{y}) \cdot \hat{\mathbf{p}}^t) \cdot (\mathrm{Im}(\underline{\mathbf{G}}(\mathbf{z},\mathbf{r}_m)) \cdot \hat{\mathbf{q}}). \tag{6.11}$$

To go from (6.10) to (6.11), the corollary of the Helmholtz–Kirchhoff identity (see (Ito, Jin, and J. Zou 2013, (7)) and (J. Chen, Z. Chen, and Huang 2013b, Lemma 3.2) for the demonstration)

$$\langle \underline{\mathbf{G}}(\mathbf{x},\mathbf{z}_1) \cdot \mathbf{p}, \underline{\mathbf{G}}(\mathbf{x},\mathbf{z}_2) \cdot \mathbf{q} \rangle_{L^2(\Gamma_{\mathrm{obs}})} = \int_{\Gamma_{\mathrm{obs}}} (\underline{\mathbf{G}}(\mathbf{x},\mathbf{z}_1)\cdot\mathbf{p})\cdot(\overline{\underline{\mathbf{G}}(\mathbf{x},\mathbf{z}_2)}\cdot\mathbf{q})\mathrm{d}S(\mathbf{x}) \approx \frac{1}{k_0}\left\{\mathbf{p} \cdot \mathrm{Im}\left(\underline{\mathbf{G}}(\mathbf{z}_1,\mathbf{z}_2)\cdot\mathbf{q}\right)\right\} \tag{6.12}$$

is used, where $\mathbf{p} \in \mathbb{C}^3$, $\mathbf{q} \in \mathbb{S}^2$ where $\mathbb{S}^2$ is a unit sphere in $\mathbb{R}^3$.

The explicit form of $\underline{\mathbf{G}}(\mathbf{r}_m, \mathbf{y}) \cdot \hat{\mathbf{p}}^t$ can be represented by

$$\begin{aligned}(\underline{\mathbf{G}}(\mathbf{r}_m, \mathbf{y}) \cdot \hat{\mathbf{p}}^t)_s = p_s^t &\left[g(\mathbf{y}, \mathbf{r}_m) - \frac{g(\mathbf{y}, \mathbf{r}_m)}{k_0^2 |\mathbf{r}_m - \mathbf{y}|^2} + \frac{\mathrm{i} g(\mathbf{y}, \mathbf{r}_m)}{k_0 |\mathbf{r}_m - \mathbf{y}|} \right] \\ &- (\mathbf{r}_m - \mathbf{y})_s \frac{\hat{\mathbf{p}}^t \cdot (\mathbf{r}_m - \mathbf{y})}{|\mathbf{r}_m - \mathbf{y}|^2} \left[g(\mathbf{y}, \mathbf{r}_m) - \frac{3 g(\mathbf{y}, \mathbf{r}_m)}{k_0^2 |\mathbf{r}_m - \mathbf{y}|^2} + \frac{3\mathrm{i} g(\mathbf{y}, \mathbf{r}_m)}{k_0 |\mathbf{r}_m - \mathbf{y}|} \right], \end{aligned} \tag{6.13}$$

$$= p_s^t Q_1(\mathbf{y}, \mathbf{r}_m) - (\mathbf{r}_m - \mathbf{y})_s \frac{\hat{\mathbf{p}}^t \cdot (\mathbf{r}_m - \mathbf{y})}{|\mathbf{r}_m - \mathbf{y}|^2} Q_2(\mathbf{y}, \mathbf{r}_m), \ s = 1, 2, 3, \tag{6.14}$$

where $Q_1(\mathbf{y}, \mathbf{r}_m)$ and $Q_2(\mathbf{y}, \mathbf{r}_m)$ are defined in (6.8) and (6.9), respectively. Similarly, the form of $\mathrm{Im}(\underline{\mathbf{G}}(\mathbf{z}, \mathbf{r}_m))\hat{\mathbf{q}}$ is as follows

$$\begin{aligned}\left(\mathrm{Im}\left(\underline{\mathbf{G}}(\mathbf{z}, \mathbf{r}_m)\right) \hat{\mathbf{q}}\right)_s =& \frac{\hat{q}_s}{4\pi |\mathbf{r}_m - \mathbf{z}|} \left[\sin(k_0 |\mathbf{r}_m - \mathbf{z}|) - \frac{\sin(k_0 |\mathbf{r}_m - \mathbf{z}|)}{k_0^2 |\mathbf{r}_m - \mathbf{z}|^2} + \frac{\cos(k_0 |\mathbf{r}_m - \mathbf{z}|)}{k_0 |\mathbf{r}_m - \mathbf{z}|} \right] \\ &- (\mathbf{r}_m - \mathbf{z})_s \frac{\hat{\mathbf{q}} \cdot (\mathbf{r}_m - \mathbf{z})}{4\pi |\mathbf{r}_m - \mathbf{z}|^3} \\ &\times \left[\sin(k_0 |\mathbf{r}_m - \mathbf{z}|) - \frac{3 \sin(k_0 |\mathbf{r}_m - \mathbf{z}|)}{k_0^2 |\mathbf{r}_m - \mathbf{z}|^2} + \frac{3 \cos(k_0 |\mathbf{r}_m - \mathbf{z}|)}{k_0 |\mathbf{r}_m - \mathbf{z}|} \right], \end{aligned} \tag{6.15}$$

$$= \hat{q}_s f_1(\mathbf{r}_m, \mathbf{z}) - (\mathbf{r}_m - \mathbf{z})_s \left(\hat{\mathbf{q}} \cdot (\mathbf{r}_m - \mathbf{z})\right) f_2(\mathbf{r}_m, \mathbf{z}) \tag{6.16}$$

where

$$f_1(\mathbf{r}_m, \mathbf{z}) = \left[\sin(k_0 |\mathbf{r}_m - \mathbf{z}|) - \frac{\sin(k_0 |\mathbf{r}_m - \mathbf{z}|)}{k_0^2 |\mathbf{r}_m - \mathbf{z}|^2} + \frac{\cos(k_0 |\mathbf{r}_m - \mathbf{z}|)}{k_0 |\mathbf{r}_m - \mathbf{z}|} \right] \frac{1}{4\pi |\mathbf{r}_m - \mathbf{z}|}, \tag{6.17}$$

$$= \frac{k_0}{4\pi} \left[\mathrm{j}_0(k_0 |\mathbf{r}_m - \mathbf{z}|) - \frac{\mathrm{j}_1(k_0 |\mathbf{r}_m - \mathbf{z}|)}{k_0 |\mathbf{r}_m - \mathbf{z}|} \right], \tag{6.18}$$

$$f_2(\mathbf{r}_m, \mathbf{z}) = \left[\sin(k_0 |\mathbf{r}_m - \mathbf{z}|) - \frac{3 \sin(k_0 |\mathbf{r}_m - \mathbf{z}|)}{k_0^2 |\mathbf{r}_m - \mathbf{z}|^2} + \frac{3 \cos(k_0 |\mathbf{r}_m - \mathbf{z}|)}{k_0 |\mathbf{r}_m - \mathbf{z}|} \right] \frac{1}{4\pi |\mathbf{r}_m - \mathbf{z}|^3} \tag{6.19}$$

$$= -\frac{k_0}{4\pi} \frac{\mathrm{j}_2(k_0 |\mathbf{r}_m - \mathbf{z}|)}{|\mathbf{r}_m - \mathbf{z}|^2}. \tag{6.20}$$

Here, the definitions of the spherical Bessel functions of first kind are used to go from (6.17) to (6.18) and from (6.19) to (6.20), respectively.

The combination of (6.14) and (6.16) for $s = 1, 2, 3$, leads to

$$\begin{aligned}(\underline{\mathbf{G}}(\mathbf{r}_m, \mathbf{y}) \cdot \hat{\mathbf{p}}^t) \cdot (\mathrm{Im}(\underline{\mathbf{G}}(\mathbf{z}, \mathbf{r}_m)) \cdot \hat{\mathbf{q}}) &= \sum_{s=1}^{3} (\underline{\mathbf{G}}(\mathbf{r}_m, \mathbf{y}) \hat{\mathbf{p}}^t)_s \left(\mathrm{Im}\left(\underline{\mathbf{G}}(\mathbf{z}, \mathbf{r}_m)\right) \hat{\mathbf{q}}\right)_s \\ = &\left\{ \left[\hat{\mathbf{p}}^t \cdot \hat{\mathbf{q}}\right] Q_1(\mathbf{y}, \mathbf{r}_m) - \frac{\left[\hat{\mathbf{p}}^t \cdot (\mathbf{r}_m - \mathbf{y})\right] \left[\hat{\mathbf{q}} \cdot (\mathbf{r}_m - \mathbf{y})\right]}{|\mathbf{r}_m - \mathbf{y}|^2} Q_2(\mathbf{y}, \mathbf{r}_m) \right\} f_1(\mathbf{r}_m, \mathbf{z}) \\ &+ \left\{ \frac{\left[\hat{\mathbf{q}} \cdot (\mathbf{r}_m - \mathbf{z})\right] \left[\hat{\mathbf{p}}^t \cdot (\mathbf{r}_m - \mathbf{y})\right] \left[(\mathbf{r}_m - \mathbf{y}) \cdot (\mathbf{r}_m - \mathbf{z})\right]}{|\mathbf{r}_m - \mathbf{y}|^2} Q_2(\mathbf{y}, \mathbf{r}_m) \right. \\ &\left. - \frac{\left[\hat{\mathbf{p}}^t \cdot (\mathbf{r}_m - \mathbf{z})\right] \left[\hat{\mathbf{q}} \cdot (\mathbf{r}_m - \mathbf{z})\right]}{|\mathbf{r}_m - \mathbf{y}|^2} Q_1(\mathbf{y}, \mathbf{r}_m) \right\} f_2(\mathbf{r}_m, \mathbf{z}). \end{aligned} \tag{6.21}$$

After some manipulations and with the expansion of $f_1(\mathbf{r}_m, \mathbf{z})$ and $f_2(\mathbf{r}_m, \mathbf{z})$ as combination of spherical

Bessel functions as defined in (6.18) and (6.20) the final expression is obtained as

$$\left|\langle \mathbf{E}^s(\mathbf{x},\mathbf{y};k_0), \underline{\mathbf{G}}(\mathbf{x},\mathbf{z})\cdot\hat{\mathbf{q}}\rangle_{L^2(\Gamma_{\text{obs}})}\right| \approx \left|\sum_{m=1}^{M} A_m \left[C_1\left(\mathrm{j}_0(k_0|\mathbf{r}_m-\mathbf{z}|) - \frac{\mathrm{j}_1(k_0|\mathbf{r}_m-\mathbf{z}|)}{k_0|\mathbf{r}_m-\mathbf{z}|}\right) + C_2\frac{\mathrm{j}_2(k_0|\mathbf{r}_m-\mathbf{z}|)}{|\mathbf{r}_m-\mathbf{z}|^2}\right]\right|, \quad (6.22)$$

where C_1 and C_2 are given by (6.6) and (6.7) and where the constant $\frac{\mathrm{i}\omega_0\mu_0 I l k_0^2}{4\pi}$ is omitted since canceled in the final expression thanks to the Hölder inequality

$$|\langle \mathbf{f},\mathbf{g}\rangle_{L^2(\Gamma_{\text{obs}})}| \leq \|\mathbf{f}\|_{L^2(\Gamma_{\text{obs}})}\|\mathbf{g}\|_{L^2(\Gamma_{\text{obs}})}, \quad (6.23)$$

which completes the proof. □

Remark 6.2.2 (Properties of DSM with near-field data) *The properties of* $\mathcal{I}_{\text{DSM3D}}(\mathbf{z};\mathbf{y},\hat{\mathbf{q}})$ *are investigated through the result in Theorem 6.2.1 as follows.*

1. *Due to the properties of spherical Bessel functions of integer orders, we have* $\mathrm{j}_0(k_0|\mathbf{r}_m-\mathbf{z}|)=1$, $\mathrm{j}_1(k_1|\mathbf{r}_m-\mathbf{z}|)=0$ *and* $\mathrm{j}_2(k_0|\mathbf{r}_m-\mathbf{z}|)=0$ *if* $\mathbf{z}=\mathbf{r}_m$, $m=1,2,\cdots,M$. *In other words, each inhomogeneity can be identified via* $\mathcal{I}_{\text{DSM3D}}(\mathbf{z};\mathbf{y},\hat{\mathbf{q}})$ *due to the term of* $\mathrm{j}_0(k_0|\mathbf{r}_m-\mathbf{z}|)$. *But artifacts will show up in the map of* $\mathcal{I}_{\text{DSM3D}}(\mathbf{z};\mathbf{y},\hat{\mathbf{q}})$ *because of the remaining terms* $\mathrm{j}_1(k_0|\mathbf{r}_m-\mathbf{z}|)$ *and* $\mathrm{j}_2(k_0|\mathbf{r}_m-\mathbf{z}|)$.

2. *The physical characteristic of the inhomogeneities, e.g., permittivity and size (which have been concatenated within the complex amplitude* A_m *for target numbered* m*), have an important role in the map of* $\mathcal{I}_{\text{DSM3D}}(\mathbf{z};\mathbf{y},\hat{\mathbf{q}})$. *More specifically, the latter has its maximum value at the location of the inhomogeneity having a highest complex amplitude* A_m *so that the one with the smallest amplitude might be difficult to be identified. It is an inherent limitation of the DSM approach as it has been shown in detail for the 2D case in chapter 3.*

According to Theorem 6.2.1, we can know that the choice of $\hat{\mathbf{q}}$ has important role for proper reconstruction of the support of the inhomogeneities. So further discussion about choosing $\hat{\mathbf{q}}$ is essential to apply the DSM.

Remark 6.2.3 (Investigation of choice of a proper $\hat{\mathbf{q}}$)

1. *The results provided by* $\mathcal{I}_{\text{DSM3D}}(\mathbf{z};\mathbf{y},\hat{\mathbf{q}})$ *are highly dependent on the choice of the test dipole polarization* $\hat{\mathbf{q}}\in\mathbb{S}^2$ *because the disturbing term could not have effect for imaging if* $C_1=0$ *where* C_1 *given by (6.6), which means that* $\mathcal{I}_{\text{DSM3D}}(\mathbf{z};\mathbf{y},\hat{\mathbf{q}})\neq 1$ *when* $\mathbf{z}=\mathbf{r}_m\in\tau_m$. *Hence, we have to choose* $\hat{\mathbf{q}}$ *at least satisfying* $C_1\neq 0$, *i.e,*

$$\left[\hat{\mathbf{p}}^t\cdot\hat{\mathbf{q}}\right]Q_1(\mathbf{y},\mathbf{r}_m) \neq \frac{\left[\hat{\mathbf{p}}^t\cdot(\mathbf{r}_m-\mathbf{y})\right]\left[\hat{\mathbf{q}}\cdot(\mathbf{r}_m-\mathbf{y})\right]}{|\mathbf{r}_m-\mathbf{y}|^2}Q_2(\mathbf{y},\mathbf{r}_m). \quad (6.24)$$

So (6.24) is a necessary condition to identify the inhomogeneities via $\mathcal{I}_{\text{DSM3D}}(\mathbf{z};\mathbf{y},\hat{\mathbf{q}})$.

2. *On the basis of our theoretical result (6.4), the best choice of* $\hat{\mathbf{q}}$ *for imaging unknown targets with good performance is to select* $\hat{\mathbf{q}}$ *making a large magnitude of* C_1 *and a small magnitude of* C_2 *at the same time. Unfortunately, it is impossible to select it analytically without information about* τ_m *because both* C_1 *and* C_2 *depend on the unknown information* $\mathbf{r}_m$.

3. *Following the pioneer work (X. Chen and Zhong 2008) leading to an enhanced MUSIC algorithm, the polarization of the test dipole* $\hat{\mathbf{q}}_{\max}$ *was chosen in order to maximize the back-propagation amplitude at a each sampling point* $\mathbf{z} \in \Omega$. *So we suggest an alternative method to choose* $\hat{\mathbf{q}}$ *without any a priori information such as follows:*

$$\hat{\mathbf{q}}_{\max} := \arg\max_{\hat{\mathbf{q}}} \left\{ \left| \langle \mathbf{E}^s(\mathbf{x}, \mathbf{y}), \underline{\mathbf{G}}(\mathbf{x}, \mathbf{z}) \cdot \hat{\mathbf{q}} \rangle_{L^2(\Gamma_{\text{obs}})} \right| \right\}. \tag{6.25}$$

even though more computational cost is required. For the sake of clarity, DSM with $\hat{\mathbf{q}}_{\max}$ *is denoted by DSMP in this contribution.*

Now, we theoretically verify the validation of the guideline for choosing $\hat{\mathbf{q}}$ proposed from the authors of (Ito, Jin, and J. Zou 2013) ($\hat{\mathbf{q}} = \mathbf{p}^t$) through our structure analysis.

Corollary 6.2.4 *Let* $\mathbf{r}_m \neq \mathbf{y}$, $m = 1, 2, \cdots, M$ *and* $\hat{\mathbf{q}} = \mathbf{p}^t \in \mathbb{S}^2$. *Then, the necessary condition (6.24) holds.*

Proof Assume that the condition (6.24) is no longer satisfied when $\hat{\mathbf{q}} = \mathbf{p}^t$, i.e.,

$$\left[\hat{\mathbf{p}}^t \cdot \hat{\mathbf{q}}\right] Q_1(\mathbf{y}, \mathbf{r}_m) = \frac{\left[\hat{\mathbf{p}}^t \cdot (\mathbf{r}_m - \mathbf{y})\right] \left[\hat{\mathbf{q}} \cdot (\mathbf{r}_m - \mathbf{y})\right]}{|\mathbf{r}_m - \mathbf{y}|^2} Q_2(\mathbf{y}, \mathbf{r}_m), \text{ where } \hat{\mathbf{q}} = \mathbf{p}^t. \tag{6.26}$$

Then, since $|\mathbf{p}^t| = 1$ and $\mathbf{p}^t \cdot \mathbf{p}^t = 1$,

$$Q_1(\mathbf{y}, \mathbf{r}_m) = (\cos^2 \vartheta) Q_2(\mathbf{y}, \mathbf{r}_m), \tag{6.27}$$

where ϑ is the angle between of two vectors $\mathbf{p}^t$ and $\mathbf{r}_m - \mathbf{y}$. The definitions of $Q_1(\mathbf{y}, \mathbf{r}_m)$ and $Q_2(\mathbf{y}, \mathbf{r}_m)$ in (6.8) and (6.9), respectively, lead to

$$g(\mathbf{y}, \mathbf{r}_m) \left[1 - \frac{1}{k_0^2 |\mathbf{r}_m - \mathbf{y}|^2} + \frac{\mathrm{i}}{k_0 |\mathbf{r}_m - \mathbf{y}|} \right] = g(\mathbf{y}, \mathbf{r}_m) \left[1 - \frac{3}{k_0^2 |\mathbf{r}_m - \mathbf{y}|^2} + \frac{3\mathrm{i}}{k_0 |\mathbf{r}_m - \mathbf{y}|} \right] \cos^2 \vartheta, \tag{6.28}$$

which is equivalent to the case that the real and imaginary parts are simultaneously null. Namely,

$$1 - \frac{1}{k_0^2 |\mathbf{r}_m - \mathbf{y}|^2} = \left[1 - \frac{3}{k_0^2 |\mathbf{r}_m - \mathbf{y}|^2} \right] \cos^2 \vartheta, \tag{6.29}$$

and

$$\frac{1}{k_0 |\mathbf{r}_m - \mathbf{y}|} = \left[\frac{3}{k_0 |\mathbf{r}_m - \mathbf{y}|} \right] \cos^2 \vartheta. \tag{6.30}$$

Since $|\mathbf{r}_m - \mathbf{y}| \neq 0$, the imaginary part (6.30) implies to $\cos^2 \vartheta = \frac{1}{3}$. By introducing the latter to (6.29),

$$1 = \frac{1}{3}, \tag{6.31}$$

which is a contradiction. Therefore, $C_1 \neq 0$ if $\hat{\mathbf{q}} = \mathbf{p}^t$ which completes the proof. □

The above observation shows that the necessary condition (6.24) is satisfied if $\hat{\mathbf{q}} = \mathbf{p}^t$, so the spherical inhomogeneities can be identified via DSM with $\hat{\mathbf{q}} = \mathbf{p}^t$ where the targets are small.

6.2.2 Numerical simulations

In this section, our theoretical result and efficiency of our method is examined through various numerical simulations. We consider a fixed frequency $f_0 = 749.481\,\text{MHz} = c_0/\lambda_0$ where $\lambda_0 = 0.4\,\text{m}$ is the wavelength and c_0 the speed of light. `FEKO` is used to compute the fields scattered by various obstacles illuminated by a single fixed dipole placed at $\mathbf{y} = (2.5\lambda_0, 90°, 0°)$ and polarized by z-axis, where (r, θ, ϕ) indicate the radial distance, polar angle, and azimuthal angle and polarized along $\hat{\theta}$. The three components x, y, z of the scattered fields are measured at the receiver location defined as $\mathbf{x} = (r^r, \theta^r, \phi^r)$, i.e., $\mathbf{E}^s(\mathbf{x}, \mathbf{y}; k_0) = [E_x^s(\mathbf{x}, \mathbf{y}; k_0), E_y^s(\mathbf{x}, \mathbf{y}; k_0), E_z^s(\mathbf{x}, \mathbf{y}; k_0)]$. Here, $r^r = 2.5\lambda_0$, $\theta_{n_\theta}^r = 10n_\theta°, n_\theta = 1, 2, \cdots, 17$, $\phi_{n_\phi}^r = 10(n_\phi - 1)°, n_\phi = 1, 2, \cdots, 36$, i.e., the total number of receivers is $N = N_\theta \times N_\phi = 612$. A 20-dB white Gaussian random noise is added using the MATLAB function `awgn`. The region of interest (ROI) is defined as a $2.5\lambda_0$-side length cube evenly discretized in $41 \times 41 \times 41$ voxels. To apply our proposal DSMP, we calculate all the results of $\left|\langle \mathbf{E}^s(\mathbf{x}, \mathbf{y}), \underline{\mathbf{G}}(\mathbf{x}, \mathbf{z}) \cdot \hat{\mathbf{q}}_t \rangle_{L^2(\Gamma_{\text{obs}})}\right|$ for each $\hat{\mathbf{q}}_t \in \mathbb{S}^2$, $t = 1, 2, \cdots, 201$ and select the $\hat{\mathbf{q}}_{\max}$ satisfying (6.25), where $\hat{\mathbf{q}}_t$ are evenly distributed by (Deserno 2004).

The reconstructions are visualized using volume slice planes and/or isosurfaces, the latter being defined as

$$\mathcal{V}_\upsilon = \{\mathbf{z} \in \Omega | \mathcal{I}(\mathbf{z}) \geq \upsilon\}, \tag{6.32}$$

where υ is an isosurface parameter and $\mathcal{I}$ is either $\mathcal{I}_{\text{DSM}}(\mathbf{z}; \mathbf{y}, \hat{\mathbf{q}})$ or $\mathcal{I}_{\text{DSMP}}(\mathbf{z}; \mathbf{y})$. According to (Bazán et al. 2015), we choose the parameter υ such as

$$\upsilon = \min_{\mathbf{z}\in\Omega} \mathcal{I}(\mathbf{z}) + \rho \left[\max_{\mathbf{z}\in\Omega} \mathcal{I}(\mathbf{z}) - \min_{\mathbf{z}\in\Omega} \mathcal{I}(\mathbf{z})\right], \quad 0 < \rho < 1, \tag{6.33}$$

and ρ is chosen based upon the quality of the reconstructions, i.e., ρ involves the accuracy of imaging performance where the performance is measured with Jaccard index.

Example 6.2.5 (Single small sphere) *A small spherical dielectric inhomogeneity of location* $\left(\frac{\lambda_0}{4}, \frac{\lambda_0}{4}, \frac{\lambda_0}{4}\right)$, *radius* $\frac{\lambda_0}{10}$ *and electric permittivity* $\varepsilon = 5\varepsilon_0$ *is considered.*

Figure 6.1 shows that the accuracy of DSM is highly dependent on the choice of the test dipole polarization as stated in Remark 6.2.3. For example when changing the test dipole polarization in the range of $\hat{\mathbf{q}}$ in $0° \leq \theta \leq 140°$ for fixed $\phi = 45°$, the DSM results evolves from a good localization to a bad one. We can identify the inhomogeneity via DSM when the polarization is chosen either $\hat{\mathbf{q}} = \mathbf{p}^t$ (by the guideline in (Ito, Jin, and J. Zou 2013)) or $\hat{\mathbf{q}} = \hat{\mathbf{q}}_{\max}$ (by our proposal in (6.25)), See Figure 6.2 and Figure 6.3, respectively. The results show that their accuracy seems to be similar by Figure 6.4. But additional information (e.g. polarization of incident dipole) is not used in our proposal with a slightly higher computational cost.

Example 6.2.6 (Two small spheres with different radii but same permittivity) *In the following, the case of two dielectric spheres with different radii* $\alpha_1 = 0.12\lambda_0$, $\alpha_2 = 0.1\lambda_0$ *but same electric permittivity* $\varepsilon_m = 5\varepsilon_0$, $m = 1, 2$, *located at* $\mathbf{r}_1 = (\frac{\lambda_0}{4}, \frac{\lambda_0}{4}, \frac{\lambda_0}{4})$ *and* $\mathbf{r}_2 = (-\frac{\lambda_0}{2}, -\frac{\lambda_0}{4}, -\frac{\lambda_0}{4},)$, *respectively is dealt with.*

According to Figure 6.5, the proper choice of the test dipole polarization is a key parameter for the efficiency of DSM also in the multiple-target case. Figures 6.6, 6.7 and 6.8 show that both selections

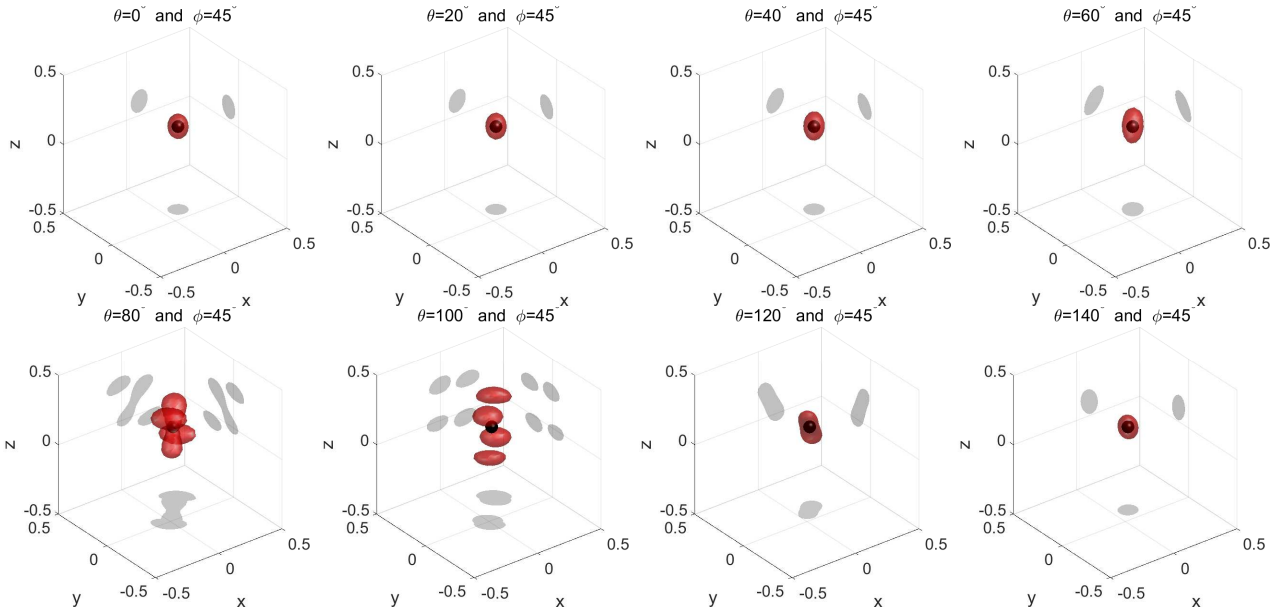

Figure 6.1: (Example 6.2.5) Maps of $\mathcal{I}_{\text{DSM3D}}(\mathbf{z};\mathbf{y},\hat{\mathbf{q}})$ using isosurface with $\rho = 0.8$, where $\hat{\mathbf{q}} = (1,\theta,\phi)$

of polarization provide a good result. Note that the isosurface representation has been drawn using $\rho = 0.4$ (instead of $\rho = 0.8$) in order to exhibit the localization of τ_2. As a matter of fact that τ_2 having a lower size and being further away from the impinging dipole, its signature has a lower value that the one of τ_2 as stated in Remark 6.2.2, which is an inherent limitation of DSM. We also note that the same phenomenon would have happened in the case of scatterers with same radii but different permittivities.

6.3 Direct sampling method analysis: far-field case

6.3.1 Introduction of direct sampling method and its structure analysis

In the following, we will treat the far field configuration in which the incident field is now a single plane wave $\mathbf{E}^i_\infty(\hat{\mathbf{x}},\hat{\mathbf{y}})$ having impinging direction $-\hat{\mathbf{y}}$ and polarization $\hat{\mathbf{p}}^t$, and the collected data are the far-field pattern $\mathbf{E}_\infty(\hat{\mathbf{x}},\hat{\mathbf{y}})$ as defined by (2.30). The DSM indicator function then is

$$\mathcal{I}^\infty_{\text{DSM3D}}(\mathbf{z};\hat{\mathbf{y}},\hat{\mathbf{q}}) := \frac{\left|\langle \mathbf{E}_\infty(\hat{\mathbf{x}},\hat{\mathbf{y}};k_0), \underline{\mathbf{G}}_\infty(\hat{\mathbf{x}},\mathbf{z})\cdot\hat{\mathbf{q}}\rangle_{L^2(\mathbb{S}^2}\right|}{\|\mathbf{E}^s(\hat{\mathbf{x}},\hat{\mathbf{y}};k_0)\|_{L^2(\mathbb{S}^2)}\,\|\underline{\mathbf{G}}_\infty(\hat{\mathbf{x}},\mathbf{z})\cdot\hat{\mathbf{q}}\|_{L^2(\mathbb{S}^2)}}. \tag{6.34}$$

As usual the DSM indicator function with L multiple impinging directions is given by

$$\mathcal{I}^\infty_{\text{DSM3D}}(\mathbf{z}) = \frac{1}{L}\sum_{l=1}^{L}\mathcal{I}^\infty_{\text{DSM3D}}(\mathbf{z};\hat{\mathbf{y}}_l,\hat{\mathbf{q}}_l), \tag{6.35}$$

where $\mathcal{I}^\infty_{\text{DSM3D}}(\mathbf{z};\hat{\mathbf{y}}_l,\hat{\mathbf{q}}_l)$ is given in (6.34) for each $\hat{\mathbf{y}}_l,\ l = 1,2,\cdots,L$ (note that (6.35) is equivalent to (6.34) if $L = 1$).

Following the same steps than for the near-field case, an analytical formulation of the DSM indicator function is proposed in Theorem 6.3.4 thanks to the use of the asymptotic formulation of the far-field

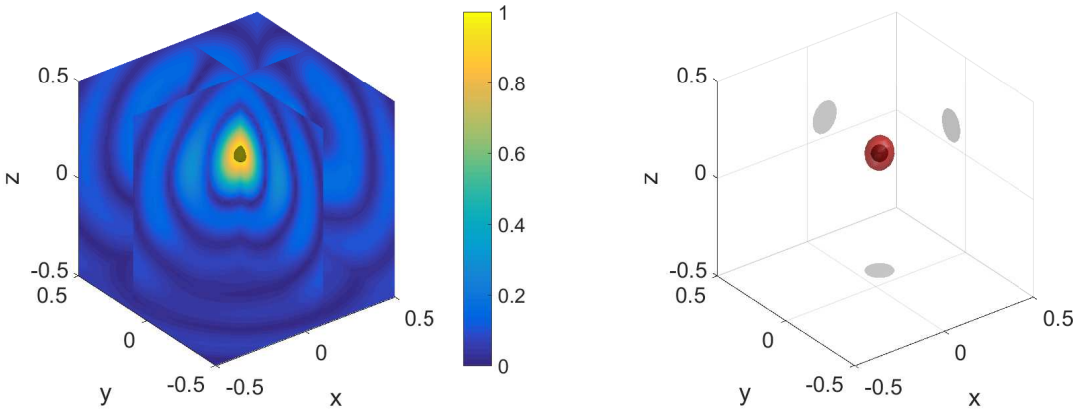

(a) Volume slice with $\mathbf{x} = 0.1$ and $\mathbf{y} = 0.1$ planes

(b) Isosurface with $\rho = 0.8$

Figure 6.2: (Example 6.2.5) Maps of $\mathcal{I}_{\text{DSM3D}}(\mathbf{z}; \mathbf{y}, \hat{\mathbf{q}})$, where $\hat{\mathbf{q}} = (1, 0°, 45°) = \hat{\mathbf{p}}^t$

.

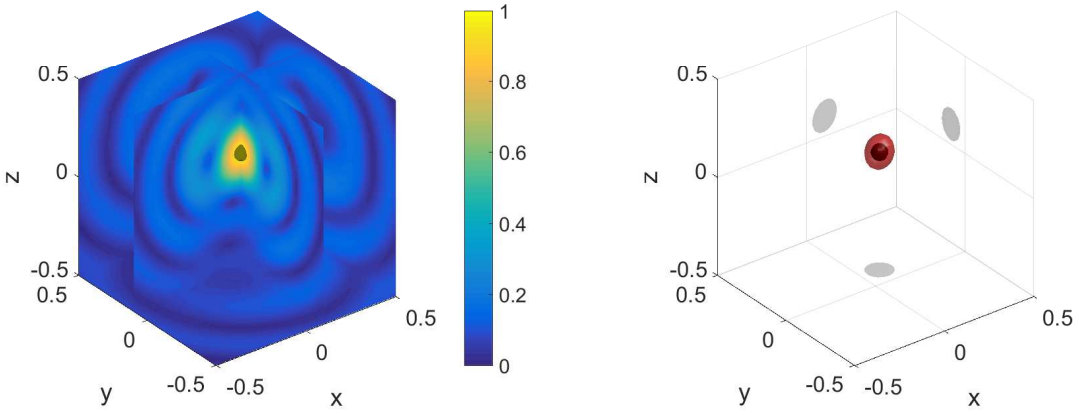

(a) Volume slice with $\mathbf{x} = 0.1$ and $\mathbf{y} = 0.1$ planes

(b) Isosurface with $\rho = 0.8$

Figure 6.3: (Example 6.2.5) Maps of $\mathcal{I}_{\text{DSMP3D}}(\mathbf{z}; \mathbf{y})$

pattern (2.30). However, some preliminary results have to be introduced first in order to deal with the following integral equation, which is a key point to establish an analytical formulation of the DSM indicator function.

$$\int_{\mathbb{S}^2} (\underline{\mathbf{G}}_\infty(\hat{\mathbf{x}}, \mathbf{z}_1) \cdot \mathbf{p}) \cdot (\overline{\underline{\mathbf{G}}_\infty(\hat{\mathbf{x}}, \mathbf{z}_2)} \cdot \mathbf{q}) \mathrm{d}S(\hat{\mathbf{x}}), \tag{6.36}$$

Let us first introduce the well-known Funk-Hecke formula (Lemma 6.3.1) involving the spherical harmonic functions. We will have to deal with a new lemma (Lemma 6.3.2) involving either the real part or the imaginary part of the spherical harmonic function (the demonstration of the latter is provided in the Appendix A.4)

Lemma 6.3.1 (Funk-Hecke formula) *For any $f \in L^2(-1, 1)$ and $\hat{\mathbf{z}}$, $\hat{\mathbf{x}} \in \mathbb{S}^2$, the following formula holds.*

$$\int_{\mathbb{S}^2} f(\hat{\mathbf{z}} \cdot \hat{\mathbf{x}}) \, \mathrm{Y}_n^m(\hat{\mathbf{x}}) \mathrm{d}S(\hat{\mathbf{x}}) = \lambda_n \, \mathrm{Y}_n^m(\hat{\mathbf{z}}) \text{ where } \lambda_n = 2\pi \int_{-1}^{1} f(t) \, \mathrm{P}_n(t) \mathrm{d}t \tag{6.37}$$

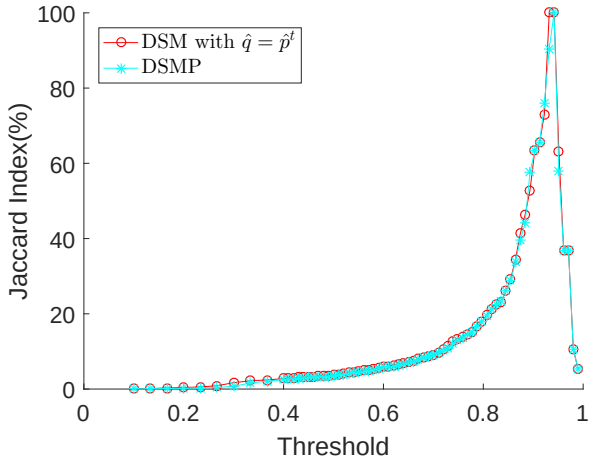

Figure 6.4: (Example 6.2.5) Jaccard index of $\mathcal{I}_{\text{DSM3D}}(\mathbf{z}; \mathbf{y}, \hat{\mathbf{q}} = \hat{\mathbf{p}}^t)$ and $\mathcal{I}_{\text{DSMP3D}}(\mathbf{z}; \mathbf{y})$

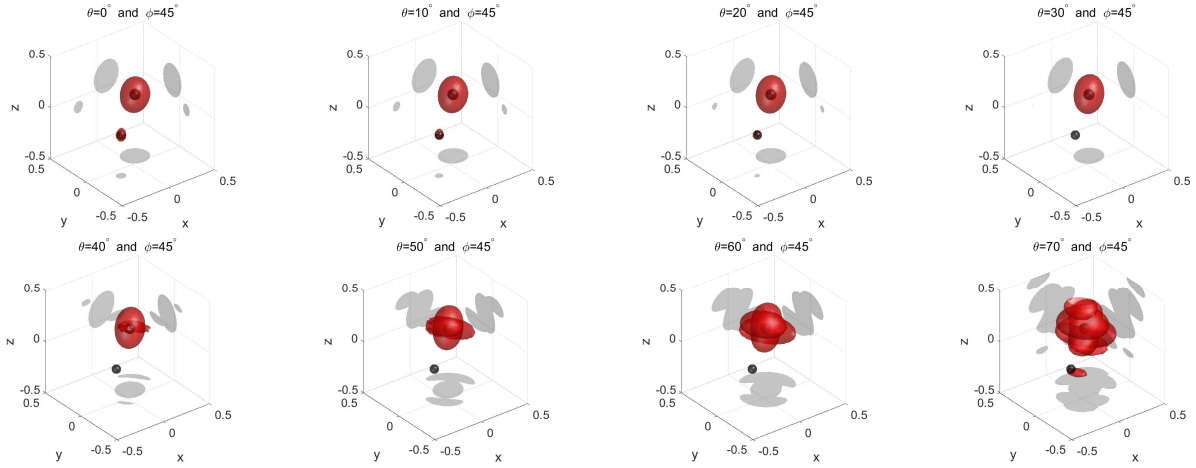

Figure 6.5: (Example 6.2.6) Maps of $\mathcal{I}_{\text{DSM3D}}(\mathbf{z}; \mathbf{y}, \hat{\mathbf{q}})$ using isosurface with $\rho = 0.4$, where $\hat{\mathbf{q}} = (1, \theta, \phi)$

for all $n \in \mathbb{N}$ *and* $m = -n, \ldots, n$. *Here,* Y_n^m *is a spherical harmonic and* P_n *is a Legendre polynomial.*

The details can be found in (Colton and Kress 1998; Kirsch and Hettlich 2009) and references therein. Following the same path as in the Funk-Hecke formula proof found in (Kirsch and Hettlich 2009, Theorem 2.16), the related results can be derived.

Lemma 6.3.2 *For any* $f \in L^2(-1, 1)$ *and* $\hat{\mathbf{z}}, \hat{\mathbf{x}} \in \mathbb{S}^2$, *the following formulas hold.*

$$\begin{aligned} \int_{\mathbb{S}^2} f(\hat{\mathbf{z}} \cdot \hat{\mathbf{x}}) \mathrm{Re}\left(\mathrm{Y}_n^m(\hat{\mathbf{x}})\right) \mathrm{d}S(\hat{\mathbf{x}}) &= \lambda_n \mathrm{Re}\left(\mathrm{Y}_n^m(\hat{\mathbf{z}})\right), \\ \int_{\mathbb{S}^2} f(\hat{\mathbf{z}} \cdot \hat{\mathbf{x}}) \mathrm{Im}\left(\mathrm{Y}_n^m(\hat{\mathbf{x}})\right) \mathrm{d}S(\hat{\mathbf{x}}) &= \lambda_n \mathrm{Im}\left(\mathrm{Y}_n^m(\hat{\mathbf{z}})\right), \end{aligned} \tag{6.38}$$

where λ_n *has been defined in* (6.37).

Proof See the Appendix. □

Let us focus on the special variant of Lemma 6.3.1 and Lemma 6.3.2 for which $f(\hat{\mathbf{z}} \cdot \hat{\mathbf{x}}) = \mathrm{e}^{-\mathrm{i}k_0|\mathbf{z}|\hat{\mathbf{z}}\cdot\hat{\mathbf{x}}} =$

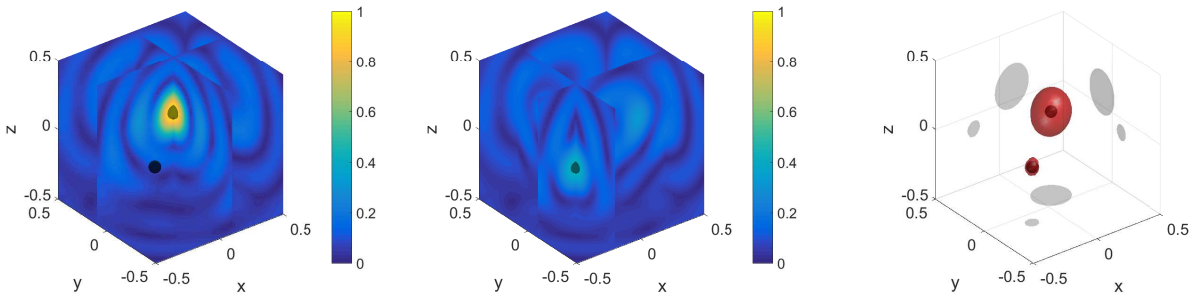

(a) Volume slice with $\mathbf{x} = 0.1$ and $\mathbf{y} = 0.1$ planes

(b) Volume slice with $\mathbf{x} = -0.2$ and $\mathbf{y} = -0.1$ planes

(c) Isosurface with $\rho = 0.5$

Figure 6.6: (Example 6.2.6) Maps of $\mathcal{I}_{\text{DSM3D}}(\mathbf{z}; \mathbf{y}, \hat{\mathbf{q}})$, where $\hat{\mathbf{q}} = (1, 0°, 45°) = \hat{\mathbf{p}}^t$

.

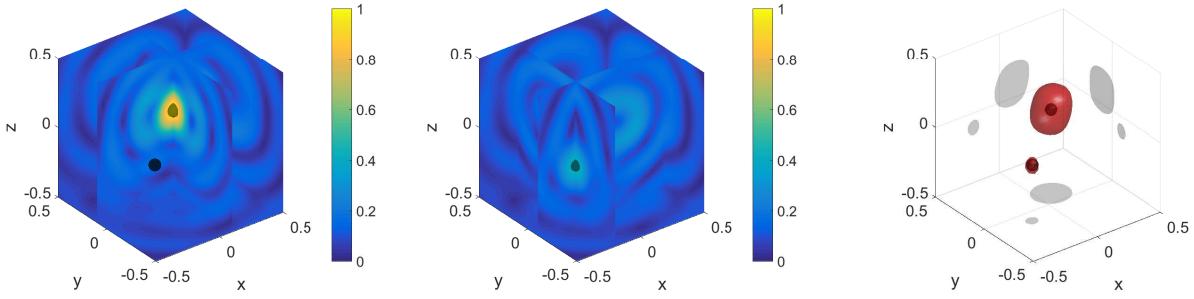

(a) Volume slice with $\mathbf{x} = 0.1$ and $\mathbf{y} = 0.1$ planes

(b) Volume slice with $\mathbf{x} = -0.2$ and $\mathbf{y} = -0.1$ planes

(c) Isosurface with $\rho = 0.5$

Figure 6.7: (Example 6.2.6) Maps of $\mathcal{I}_{\text{DSMP3D}}(\mathbf{z}; \mathbf{y})$

$\mathrm{e}^{-\mathrm{i}k_0\mathbf{z}\cdot\hat{\mathbf{x}}}$. Then λ_n is given by

$$\lambda_n = 2\pi \int_{-1}^{1} \mathrm{e}^{-\mathrm{i}k_0|\mathbf{z}|\hat{\mathbf{z}}\cdot\hat{\mathbf{x}}} \, \mathrm{P}_n(\hat{\mathbf{z}} \cdot \hat{\mathbf{x}}) \mathrm{d}(\hat{\mathbf{z}} \cdot \hat{\mathbf{x}}). \tag{6.39}$$

Since $\hat{\mathbf{z}} \cdot \hat{\mathbf{x}} = \cos\varphi$ where φ is the angle between two vectors $\hat{\mathbf{z}}$ and $\hat{\mathbf{x}}$, we have

$$\lambda_n = 2\pi \int_0^{\pi} \mathrm{e}^{-\mathrm{i}k_0|\mathbf{z}|\cos\varphi} \, \mathrm{P}_n(\cos\varphi)(-\sin\varphi)\mathrm{d}\varphi \tag{6.40}$$

$$= \frac{4\pi}{\mathrm{i}^n} \mathrm{j}_n(k_0|\mathbf{z}|) \tag{6.41}$$

thanks to the integral representation of the spherical Bessel function j_n of order $n \in \mathbb{Z}$

$$\mathrm{j}_n(\alpha) = \frac{(-\mathrm{i})^n}{2} \int_0^{\pi} \mathrm{e}^{\mathrm{i}\alpha\cos\varphi} \, \mathrm{P}_n(\cos\varphi) \sin\varphi \mathrm{d}\varphi. \tag{6.42}$$

So, in our specific case, the results provided by Lemmas 6.3.1 and 6.3.2 can be rewritten as

$$\begin{aligned}
\int_{\mathbb{S}^2} \mathrm{e}^{-\mathrm{i}k_0\mathbf{z}\cdot\hat{\mathbf{x}}} \, \mathrm{Y}_n^m(\hat{\mathbf{x}}) \mathrm{d}S(\hat{\mathbf{x}}) &= \frac{4\pi}{\mathrm{i}^n} \mathrm{j}_n(k_0|\mathbf{z}|) \, \mathrm{Y}_n^m(\hat{\mathbf{z}}), \\
\int_{\mathbb{S}^2} \mathrm{e}^{-\mathrm{i}k_0\mathbf{z}\cdot\hat{\mathbf{x}}} \mathrm{Re}\left(\mathrm{Y}_n^m(\hat{\mathbf{x}})\right) \mathrm{d}S(\hat{\mathbf{x}}) &= \frac{4\pi}{\mathrm{i}^n} \mathrm{j}_n(k_0|\mathbf{z}|) \mathrm{Re}\left(\mathrm{Y}_n^m(\hat{\mathbf{z}})\right), \\
\int_{\mathbb{S}^2} \mathrm{e}^{-\mathrm{i}k_0\mathbf{z}\cdot\hat{\mathbf{x}}} \mathrm{Im}\left(\mathrm{Y}_n^m(\hat{\mathbf{x}})\right) \mathrm{d}S(\hat{\mathbf{x}}) &= \frac{4\pi}{\mathrm{i}^n} \mathrm{j}_n(k_0|\mathbf{z}|) \mathrm{Im}\left(\mathrm{Y}_n^m(\hat{\mathbf{z}})\right),
\end{aligned} \tag{6.43}$$

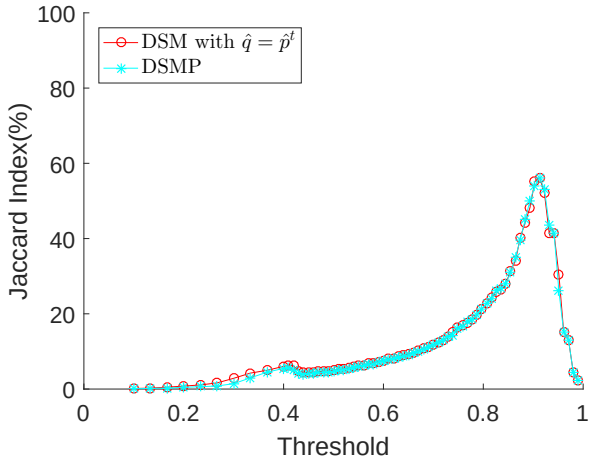

Figure 6.8: (Example 6.2.6) Jaccard index of $\mathcal{I}_{\mathrm{DSM3D}}(\mathbf{z}; \mathbf{y}, \hat{\mathbf{q}} = \hat{\mathbf{p}}^t)$ and $\mathcal{I}_{\mathrm{DSMP3D}}(\mathbf{z}; \mathbf{y})$

The next step is now to establish an analytical solution of (6.36) with the help of (6.43).

Lemma 6.3.3 *For $\mathbf{p} \in \mathbb{C}^3$ and $\mathbf{q} \in \mathbb{S}^2$, the following relation holds*

$$\int_{\mathbb{S}^2} (\underline{\mathbf{G}}_\infty(\hat{\mathbf{x}}, \mathbf{z}_1) \cdot \mathbf{p}) \cdot (\overline{\underline{\mathbf{G}}_\infty(\hat{\mathbf{x}}, \mathbf{z}_2)} \cdot \mathbf{q}) \mathrm{d}S(\hat{\mathbf{x}}) = \frac{8\pi}{3} (\mathbf{p} \cdot \mathbf{q}) \mathrm{j}_0(k_0|\mathbf{z}_1 - \mathbf{z}_2|) + (C_1 + C_2) \mathrm{j}_2(k_0|\mathbf{z}_1 - \mathbf{z}_2|), \quad (6.44)$$

where C_1 and C_2 are given by

$$C_1 = -\frac{8\pi}{3} \sqrt{\frac{\pi}{5}}\, \mathrm{Y}_2^0(\hat{\mathbf{z}})(p_1 q_1 + p_2 q_2 - 2 p_3 q_3) \quad (6.45)$$

and

$$C_2 = -8\pi \sqrt{\frac{2\pi}{15}} \Big[\mathrm{Re}\left(\mathrm{Y}_2^1(\hat{\mathbf{z}})\right)(p_1 q_3 + p_3 q_1) + \mathrm{Im}\left(\mathrm{Y}_2^1(\hat{\mathbf{z}})\right)(p_2 q_3 + p_3 q_2) - \mathrm{Re}\left(\mathrm{Y}_2^2(\hat{\mathbf{z}})\right)(p_1 q_1 - p_2 q_2) - \mathrm{Im}\left(\mathrm{Y}_2^2(\hat{\mathbf{z}})\right)(p_1 q_2 + p_2 q_1) \Big]. \quad (6.46)$$

Here, $\hat{\mathbf{z}} = (\mathbf{z}_1 - \mathbf{z}_2)/|\mathbf{z}_1 - \mathbf{z}_2|$.

Proof The introduction of the expression of the far-field approximation of the dyadic Green function (2.27) in (6.36) leads to

$$\int_{\mathbb{S}^2} (\underline{\mathbf{G}}_\infty(\hat{\mathbf{x}}, \mathbf{z}_1) \cdot \mathbf{p}) \cdot (\overline{\underline{\mathbf{G}}_\infty(\hat{\mathbf{x}}, \mathbf{z}_2)} \cdot \mathbf{q}) \mathrm{d}S(\hat{\mathbf{x}}) = \int_{\mathbb{S}^2} \mathrm{e}^{-\mathrm{i}k_0 \hat{\mathbf{x}} \cdot \mathbf{z}_1} (\Delta(\hat{\mathbf{x}}) \cdot \mathbf{p}) \cdot \mathrm{e}^{\mathrm{i}k_0 \hat{\mathbf{x}} \cdot \mathbf{z}_2} (\Delta(\hat{\mathbf{x}}) \cdot \mathbf{q}) \mathrm{d}S(\hat{\mathbf{x}}) \quad (6.47)$$

$$= \int_{\mathbb{S}^2} \mathrm{e}^{-\mathrm{i}k_0 \hat{\mathbf{x}} \cdot (\mathbf{z}_1 - \mathbf{z}_2)} \mathbf{p} \cdot (\Delta(\hat{\mathbf{x}}) \cdot \mathbf{q}) \mathrm{d}S(\hat{\mathbf{x}}) \quad (6.48)$$

$$= \mathbf{p} \cdot \int_{\mathbb{S}^2} \left(\mathrm{e}^{-\mathrm{i}k_0 \hat{\mathbf{x}} \cdot (\mathbf{z}_1 - \mathbf{z}_2)} \Delta(\hat{\mathbf{x}}) \cdot \mathbf{q} \right) \mathrm{d}S(\hat{\mathbf{x}}) \quad (6.49)$$

where the following relations $\Delta(\hat{\mathbf{x}})^T = \Delta(\hat{\mathbf{x}})$ and $\Delta(\hat{\mathbf{x}})^2 = \Delta(\hat{\mathbf{x}})$ are used to go from (6.47) to (6.48) and the fact that $\mathbf{p}$ is a complex constant vector to go from (6.48) to (6.49). The next step is to establish an explicit form of $\Delta(\hat{\mathbf{x}})\mathbf{q}$. The definition $\Delta(\hat{\mathbf{x}}) := \underline{\mathbf{I}}_3 - \hat{\mathbf{x}} \otimes \hat{\mathbf{x}}$ leads to

$$(\Delta(\hat{\mathbf{x}}) \cdot \mathbf{q})_s = q_s - \hat{x}_s (\mathbf{q} \cdot \hat{\mathbf{x}}), \ \ s = 1, 2, 3. \quad (6.50)$$

Using the expressions of the unit vector $\hat{\mathbf{x}} = (\sin\theta\cos\phi, \sin\theta\sin\phi, \cos\theta)^T$ and of the spherical harmonics Y_n^m as a function of the spherical coordinates

$$\begin{aligned}
\mathrm{Y}_2^0(\theta,\phi) &= \frac{1}{4}\sqrt{\frac{5}{\pi}}\left(3\cos^2\theta - 1\right), \\
\mathrm{Y}_2^1(\theta,\phi) &= -\frac{1}{2}\sqrt{\frac{15}{2\pi}}\sin\theta\cos\theta \mathrm{e}^{\mathrm{i}\phi}, \\
\mathrm{Y}_2^2(\theta,\phi) &= \frac{1}{4}\sqrt{\frac{15}{2\pi}}\sin^2\theta \mathrm{e}^{2\mathrm{i}\phi},
\end{aligned} \tag{6.51}$$

we can express the first component of $\Delta(\hat{\mathbf{x}})\mathbf{q}$ as

$$(\Delta(\hat{\mathbf{x}})\cdot\mathbf{q})_1 = q_1 - \sin\theta\cos\phi\,(q_1\sin\theta\cos\phi + q_2\sin\theta\sin\phi + q_3\cos\theta) \tag{6.52}$$

$$= q_1 - \frac{q_1}{2}\sin^2\theta - \frac{q_1}{2}\sin^2\theta\cos 2\phi - \frac{q_2}{2}\sin^2\theta\sin 2\phi - q_3\sin\theta\cos\theta\cos\phi \tag{6.53}$$

$$= \frac{2}{3}q_1 + \frac{2}{3}q_1\sqrt{\frac{\pi}{5}}\,\mathrm{Y}_2^0 - 2\sqrt{\frac{2\pi}{15}}\Big[q_1\mathrm{Re}\left(\mathrm{Y}_2^2(\hat{\mathbf{x}})\right) + q_2\mathrm{Im}\left(\mathrm{Y}_2^2(\hat{\mathbf{x}})\right) - q_3\mathrm{Re}\left(\mathrm{Y}_2^1(\hat{\mathbf{x}})\right)\Big]. \tag{6.54}$$

Similarly, the other components are obtained by

$$\begin{aligned}
(\Delta(\hat{\mathbf{x}})\cdot\mathbf{q})_2 &= \frac{2}{3}q_2 + \frac{2}{3}q_2\sqrt{\frac{\pi}{5}}\,\mathrm{Y}_2^0(\hat{\mathbf{x}}) - 2\sqrt{\frac{2\pi}{15}}\Big[q_1\mathrm{Im}\left(\mathrm{Y}_2^2(\hat{\mathbf{x}})\right) - q_2\mathrm{Re}\left(\mathrm{Y}_2^2(\hat{\mathbf{x}})\right) - q_3\mathrm{Im}\left(\mathrm{Y}_2^1(\hat{\mathbf{x}})\right)\Big], \\
(\Delta(\hat{\mathbf{x}})\cdot\mathbf{q})_3 &= \frac{2}{3}q_3 - \frac{4}{3}q_3\sqrt{\frac{\pi}{5}}\,\mathrm{Y}_2^0(\hat{\mathbf{x}}) + 2\sqrt{\frac{2\pi}{15}}\Big[q_1\mathrm{Re}\left(\mathrm{Y}_2^1(\hat{\mathbf{x}})\right) + q_2\mathrm{Im}\left(\mathrm{Y}_2^1(\hat{\mathbf{x}})\right)\Big].
\end{aligned} \tag{6.55}$$

The combination of (6.43) and the fact that $\mathrm{Y}_0^0(\hat{\mathbf{x}}) = \frac{1}{\sqrt{4\pi}}$ leads to

$$\int_{\mathbb{S}^2} \mathrm{e}^{-\mathrm{i}k\hat{\mathbf{x}}\cdot(\mathbf{z}_1-\mathbf{z}_2)}\mathrm{d}S(\hat{\mathbf{x}}) = 4\pi\mathrm{j}_0(k|\mathbf{z}_1-\mathbf{z}_2|). \tag{6.56}$$

Combining either (6.54) or (6.55) with (6.43), for $\hat{\mathbf{z}} = (\mathbf{z}_1-\mathbf{z}_2)/|\mathbf{z}_1-\mathbf{z}_2|$, gives the following analytical expressions

$$\begin{aligned}
\int_{\mathbb{S}^2} \mathrm{e}^{-\mathrm{i}k_0\hat{\mathbf{x}}\cdot(\mathbf{z}_1-\mathbf{z}_2)}(\Delta(\hat{\mathbf{x}})\cdot\mathbf{q})_1\mathrm{d}S(\hat{\mathbf{x}}) &= \frac{8\pi}{3}q_1\mathrm{j}_0(k_0|\mathbf{z}_1-\mathbf{z}_2|) - \frac{8\pi}{3}q_1\sqrt{\frac{\pi}{5}}\,\mathrm{Y}_2^0(\hat{\mathbf{z}})\mathrm{j}_2(k_0|\mathbf{z}_1-\mathbf{z}_2|) \\
&\quad + 8\pi\sqrt{\frac{2\pi}{15}}\mathrm{j}_2(k_0|\mathbf{z}_1-\mathbf{z}_2|)\left[q_1\mathrm{Re}\left(\mathrm{Y}_2^2(\hat{\mathbf{z}})\right) + q_2\mathrm{Im}\left(\mathrm{Y}_2^2(\hat{\mathbf{z}})\right) - q_3\mathrm{Re}\left(\mathrm{Y}_2^1(\hat{\mathbf{z}})\right)\right],
\end{aligned} \tag{6.57}$$

$$\begin{aligned}
\int_{\mathbb{S}^2} \mathrm{e}^{-\mathrm{i}k_0\hat{\mathbf{x}}\cdot(\mathbf{z}_1-\mathbf{z}_2)}(\Delta(\hat{\mathbf{x}})\cdot\mathbf{q})_2\mathrm{d}S(\hat{\mathbf{x}}) &= \frac{8\pi}{3}q_2\mathrm{j}_0(k_0|\mathbf{z}_1-\mathbf{z}_2|) - \frac{8\pi}{3}q_2\sqrt{\frac{\pi}{5}}\,\mathrm{Y}_2^0(\hat{\mathbf{z}})\mathrm{j}_2(k_0|\mathbf{z}_1-\mathbf{z}_2|) \\
&\quad + 8\pi\sqrt{\frac{2\pi}{15}}\mathrm{j}_2(k_0|\mathbf{z}_1-\mathbf{z}_2|)\left[q_1\mathrm{Im}\left(\mathrm{Y}_2^2(\hat{\mathbf{z}})\right) - q_2\mathrm{Re}\left(\mathrm{Y}_2^2(\hat{\mathbf{z}})\right) - q_3\mathrm{Im}\left(\mathrm{Y}_2^1(\hat{\mathbf{z}})\right)\right],
\end{aligned} \tag{6.58}$$

and

$$\begin{aligned}
\int_{\mathbb{S}^2} \mathrm{e}^{-\mathrm{i}k_0\hat{\mathbf{x}}\cdot(\mathbf{z}_1-\mathbf{z}_2)}(\Delta(\hat{\mathbf{x}})\cdot\mathbf{q})_3\mathrm{d}S(\hat{\mathbf{x}}) &= \frac{8\pi}{3}q_3\mathrm{j}_0(k_0|\mathbf{z}_1-\mathbf{z}_2|) + \frac{16\pi}{3}q_3\sqrt{\frac{\pi}{5}}\,\mathrm{Y}_2^0(\hat{\mathbf{z}})\mathrm{j}_2(k_0|\mathbf{z}_1-\mathbf{z}_2|) \\
&\quad - 8\pi\sqrt{\frac{2\pi}{15}}\mathrm{j}_2(k_0|\mathbf{z}_1-\mathbf{z}_2|)\left[q_1\mathrm{Re}\left(\mathrm{Y}_2^1(\hat{\mathbf{z}})\right) + q_2\mathrm{Im}\left(\mathrm{Y}_2^1(\hat{\mathbf{z}})\right)\right].
\end{aligned} \tag{6.59}$$

They lead to

$$\int_{\mathbb{S}^2} \mathbf{p}\cdot\left(\mathrm{e}^{-\mathrm{i}k_0\hat{\mathbf{x}}\cdot(\mathbf{z}_1-\mathbf{z}_2)}\Delta(\hat{\mathbf{x}})\cdot\mathbf{q}\right)\mathrm{d}S(\hat{\mathbf{x}}) = \frac{8\pi}{3}(\mathbf{p}\cdot\mathbf{q})\mathrm{j}_0(k_0|\mathbf{z}_1-\mathbf{z}_2|) + (C_1+C_2)\mathrm{j}_2(k|\mathbf{z}_1-\mathbf{z}_2|), \quad (6.60)$$

which completes the lemma. Here C_1 and C_2 are given by (6.45) and (6.46), respectively. □

Now, under the small volume and spherical shape assumptions for the inhomogeneities, the DSM indicator function (6.34) is derived thanks to the Lemma 6.3.3 and asymptotic formula (2.32).

Theorem 6.3.4 *Assume that the total number of receiver directions N is sufficiently large and each inhomogeneity is small enough ($\alpha_m\sqrt{\varepsilon_m/\varepsilon_0} \ll \lambda$). Then, the DSM indicator function has the following representation formula.*

$$\mathcal{I}^{\infty}_{\mathrm{DSM3D}}(\mathbf{z};\hat{\mathbf{y}},\hat{\mathbf{q}}) \approx \frac{|\mathcal{L}_2(\mathbf{z},\hat{\mathbf{y}},\hat{\mathbf{q}})|}{\max\limits_{\mathbf{z}\in\Omega}|\mathcal{L}_2(\mathbf{z},\hat{\mathbf{y}},\hat{\mathbf{q}})|}, \quad (6.61)$$

where

$$\mathcal{L}_2(\mathbf{z},\hat{\mathbf{y}},\hat{\mathbf{q}}) := \left|\sum_{m=1}^{M} A_m \mathrm{e}^{\mathrm{i}k_0\mathbf{r}_m\cdot\hat{\mathbf{y}}}\left[\frac{8\pi}{3}\left(\left(\Delta(\hat{\mathbf{y}})\cdot\hat{\mathbf{p}}^t\right)\cdot\hat{\mathbf{q}}\right)\mathrm{j}_0(k_0|\mathbf{r}_m-\mathbf{z}|) + (C_1+C_2)\,\mathrm{j}_2(k_0|\mathbf{r}_m-\mathbf{z}|)\right]\right|. \quad (6.62)$$

Here, for $\hat{\mathbf{z}}_m = (\mathbf{r}_m-\mathbf{z})/|\mathbf{r}_m-\mathbf{z}|$

$$C_1 = -\frac{8\pi}{3}\sqrt{\frac{\pi}{5}}\left[(\Delta(\hat{\mathbf{y}})\cdot\hat{\mathbf{p}}^t)_1\hat{q}_1 + (\Delta(\hat{\mathbf{y}})\cdot\hat{\mathbf{p}}^t)_2\hat{q}_2 - 2(\Delta(\hat{\mathbf{y}})\cdot\hat{\mathbf{p}}^t)_3\hat{q}_3\right]\mathrm{Y}_2^0(\hat{\mathbf{z}}_m) \quad (6.63)$$

and

$$\begin{aligned} C_2 = 8\pi\sqrt{\frac{2\pi}{15}}\Big[&-\mathrm{Re}\left(\mathrm{Y}_2^1(\hat{\mathbf{z}})\right)\left\{(\Delta(\hat{\mathbf{y}})\cdot\hat{\mathbf{p}}^t)_1\hat{q}_3 + (\Delta(\hat{\mathbf{y}})\cdot\hat{\mathbf{p}}^t)_3\hat{q}_1\right\} \\ &-\mathrm{Im}\left(\mathrm{Y}_2^1(\hat{\mathbf{z}})\right)\left\{(\Delta(\hat{\mathbf{y}})\cdot\hat{\mathbf{p}}^t)_2\hat{q}_3 + (\Delta(\hat{\mathbf{y}})\cdot\hat{\mathbf{p}}^t)_3\hat{q}_2\right\} + \mathrm{Re}\left(\mathrm{Y}_2^2(\hat{\mathbf{z}})\right)\left\{(\Delta(\hat{\mathbf{y}})\cdot\hat{\mathbf{p}}^t)_1\hat{q}_1 - (\Delta(\hat{\mathbf{y}})\cdot\hat{\mathbf{p}}^t)_2\hat{q}_2\right\} \\ &+\mathrm{Im}\left(\mathrm{Y}_2^2(\hat{\mathbf{z}})\right)\left\{(\Delta(\hat{\mathbf{y}})\cdot\hat{\mathbf{p}}^t)_1\hat{q}_2 + (\Delta(\hat{\mathbf{y}})\cdot\hat{\mathbf{p}}^t)_2\hat{q}_1\right\}\Big]. \end{aligned} \quad (6.64)$$

Proof According to the asymptotic formula of far-field pattern (2.31),

$$\begin{aligned} \left|\langle\mathbf{E}_\infty(\hat{\mathbf{x}},\hat{\mathbf{y}};k_0),\underline{\mathbf{G}}_\infty(\mathbf{x},\mathbf{z})\cdot\hat{\mathbf{q}}\rangle_{L^2(\mathbb{S}^2)}\right| &= \left|k_0^2\sum_{m=1}^{M}A_m\sum_{n=1}^{N}\underline{\mathbf{G}}_\infty(\mathbf{r}_m,\hat{\mathbf{x}}_n)\mathbf{E}^i(\mathbf{r}_m,\hat{\mathbf{y}})\cdot\left(\overline{\underline{\mathbf{G}}_\infty(\mathbf{z},\hat{\mathbf{x}}_n)}\cdot\hat{\mathbf{q}}\right)\right| \\ &\approx \left|k_0^2\sum_{m=1}^{M}A_m\int_{\mathbb{S}^2}\underline{\mathbf{G}}_\infty(\mathbf{r}_m,\hat{\mathbf{x}})\mathbf{E}^i(\mathbf{r}_m,\hat{\mathbf{y}})\cdot\left(\overline{\underline{\mathbf{G}}_\infty(\mathbf{z},\hat{\mathbf{x}})}\cdot\hat{\mathbf{q}}\right)\mathrm{d}S(\hat{\mathbf{x}})\right|. \end{aligned} \quad (6.65)$$

By substituting $\hat{\mathbf{p}}^t = \mathbf{E}^i_\infty(\mathbf{r}_m,\hat{\mathbf{y}}) = \mathrm{i}\omega_0\mu_0\mathrm{e}^{\mathrm{i}k_0\mathbf{r}_m\cdot\hat{\mathbf{y}}}\Delta(\hat{\mathbf{y}})\cdot\hat{\mathbf{p}}^t$ and $\mathbf{q}=\hat{\mathbf{q}}$ in Lemma 6.3.3,

$$\begin{aligned} \left|\langle\mathbf{E}_\infty(\hat{\mathbf{x}},\hat{\mathbf{y}};k_0),\underline{\mathbf{G}}_\infty(\mathbf{x},\mathbf{z})\cdot\hat{\mathbf{q}}\rangle_{L^2(\mathbb{S}^2)}\right| = \mathrm{i}\omega_0\mu_0 I l k_0^2\Bigg|&\sum_{m=1}^{M}A_m\mathrm{e}^{\mathrm{i}k_0\mathbf{r}_m\cdot\hat{\mathbf{y}}} \\ &\times\left[\frac{8\pi}{3}\left(\left(\Delta(\hat{\mathbf{y}})\cdot\hat{\mathbf{p}}^t\right)\cdot\hat{\mathbf{q}}\right)\mathrm{j}_0(k_0|\mathbf{r}_m-\mathbf{z}|) + (C_1+C_2)\,\mathrm{j}_2(k_0|\mathbf{r}_m-\mathbf{z}|)\right]\Bigg|, \end{aligned} \quad (6.66)$$

where C_1 and C_2 are given by (6.63) and (6.64), respectively. Thanks to the Hölder's inequality (6.23), the constant $\mathrm{i}\omega_0\mu_0 I l k_0^2$ is canceled and the proof is completed. □

In the following, the structure properties of the DSM indicator function are discussed. Note that due to similarity between the formulations in the near-field and in the far-field configurations some remarks will be redundant.

Remark 6.3.5 (Properties of DSM with far-field data) *According to Theorem 6.3.4, the following properties of DSM indicator function in the far-field configuration can be investigated.*

1. *As for Remark 6.2.2, $\mathcal{I}^{\infty}_{\mathrm{DSM3D}}(\mathbf{z})$ has a maximum of magnitude at $\mathbf{z} = \mathbf{r}_m \in \tau_m$ since $\mathrm{j}_0(k_0|\mathbf{r}_m - \mathbf{z}|) = 1$ and $\mathrm{j}_2(k_0|\mathbf{r}_m - \mathbf{z}|) = 0$ in that case. However, the artifacts will be show up in the maps of $\mathcal{I}^{\infty}_{\mathrm{DSM3D}}(\mathbf{z}; \hat{\mathbf{q}})$ due to $\mathrm{j}_2(k_0|\mathbf{r}_m - \mathbf{z}|) > 0$ if $\mathbf{z} \notin \tau_m$.*

2. *According to Remark 6.2.2, all targets cannot be identified through the maps of $\mathcal{I}^{\infty}_{\mathrm{DSM3D}}(\mathbf{z}; \hat{\mathbf{q}})$ when dealing with multiple targets having relative different physical properties (e.g. size and/or permittivity, etc.) in the medium .*

Now, we investigate the method to choose proper polarization of the test dipole based on Theorem 6.3.4 as following remark.

Remark 6.3.6 (Investigation of a choice of the proper $\hat{\mathbf{q}}$) *Since $\mathrm{j}_0(k_0|\mathbf{r}_m - \mathbf{z}|)$ contributes to retrieve the information of the target in the map of $\mathcal{I}^{\infty}_{\mathrm{DSM3D}}(\mathbf{z}; \hat{\mathbf{q}})$, it is necessary to choose the polarization $\hat{\mathbf{q}}$ at least satisfying the condition $\left(\Delta(\hat{\mathbf{y}}) \cdot \hat{\mathbf{p}}^t\right) \cdot \hat{\mathbf{q}} \neq 0$, i.e,*

$$\hat{\mathbf{p}}^t \cdot \hat{\mathbf{q}} \neq (\hat{\mathbf{y}} \cdot \hat{\mathbf{q}})(\hat{\mathbf{y}} \cdot \hat{\mathbf{p}}^t), \tag{6.67}$$

which is similar to Remark 6.2.3. On the contrary to (6.24), the condition (6.67) does not involve information about the localization of the target.

1. *Nevertheless, it is impossible to get an analytic solution of $\hat{\mathbf{q}}$ without a priori information about τ_m because the latter is essential to eliminate the disturbing terms $\mathrm{j}_2(k_0|\mathbf{r}_m - \mathbf{z}|)$ by making $C_1 + C_2 = 0$. Hence, we can again obtain the proper polarization of test dipole with the same process in near-field case proposed in (6.25) by*

$$\hat{\mathbf{q}}^{\infty}_{\max} = \arg\max \left\{ \left| \langle \mathbf{E}_{\infty}(\hat{\mathbf{x}}, \hat{\mathbf{y}}; k_0), \underline{\mathbf{G}}_{\infty}(\mathbf{x}, \mathbf{z}) \cdot \hat{\mathbf{q}} \rangle_{L^2(\mathbb{S}^2)} \right| ; \hat{\mathbf{q}} \in \mathbb{S}^2 \right\}. \tag{6.68}$$

   Note that the DSM indicator function with $\hat{\mathbf{q}}^{\infty}_{\max}$ will be denoted as $\mathcal{I}^{\infty}_{\mathrm{DSMP3D}}(\mathbf{z}; \hat{\mathbf{y}})$ to distinguish the indicator function of traditional DSM $\mathcal{I}^{\infty}_{\mathrm{DSM3D}}(\mathbf{z}; \hat{\mathbf{y}}, \hat{\mathbf{q}})$.

2. *Similarly with near-field case in Corollary 6.2.4, to select $\hat{\mathbf{q}}$ as $\hat{\mathbf{p}}^t$ will be a proper way to image the target via $\mathcal{I}^{\infty}_{\mathrm{DSM3D}}(\mathbf{z}; \hat{\mathbf{q}})$. Because if $\hat{\mathbf{q}} = \hat{\mathbf{p}}^t$,*

$$\hat{\mathbf{p}}^t \cdot \hat{\mathbf{q}} - (\hat{\mathbf{y}} \cdot \hat{\mathbf{q}})(\hat{\mathbf{y}} \cdot \hat{\mathbf{p}}^t) = 1 - \cos^2 \vartheta, \tag{6.69}$$

   where ϑ is the angle between $\hat{\mathbf{p}}^t$ and $\hat{\mathbf{y}}$. Since $\hat{\mathbf{y}} \nparallel \hat{\mathbf{p}}^t$ and $\cos\vartheta \neq 1$, the necessary condition (6.67) holds.

6.3.2 Numerical simulations with far-field data

Our analysis and proposal are verified through numerical simulations using synthetic far-field data obtained by `FEKO` to which a 20 dB white Gaussian random noise using the MATLAB function `awgn` is added. The configurations are the same to Example 6.2.5 and Example 6.2.6 in section 6.2.2 but in the far-field configuration.

The spherical coordinate system is again used to present the information about direction and polarization of source and observation. A single incident impinging wave of direction $(-1, 90°, 0°)$ and polarization $\hat{\mathbf{p}}^t = (1, 0°, 0°)$ $(= (0, 0, 1)$ in Cartesian coordinate system) is considered. The observation directions are evenly distributed with θ^r varying from 0° to 350° with 10°-step and ϕ^r varying from 10° to 170° with 10°-step. Since the far-field configuration is considered, only the θ^r- and ϕ^r-components of the far-field pattern are obtained. Then, a transformed far-field pattern $\widetilde{\mathbf{E}}_\infty(\mathbf{x}, \mathbf{y}) = \underline{\mathbf{P}}\mathbf{E}_\infty(\mathbf{x}, \mathbf{y})$ is used to adjust our theoretical approach (using three components of scattered field along x, y and z) where the transition matrix is defined by $\underline{\mathbf{P}} = [\hat{r}^r; \hat{\theta}^r; \hat{\phi}^r] \in \mathbb{R}^{3\times 3}$ with

$$\begin{aligned} \hat{r}^r &= (\sin\theta^r \cos\phi^r, \sin\theta^r \sin\phi^r, \cos\theta^r)^T, \\ \hat{\theta}^r &= (\cos\theta^r \cos\phi^r, \cos\theta^r \sin\phi^r, \cos\theta)^T, \\ \hat{\phi}^r &= (-\sin\phi^r, \cos\phi^r, 0)^T. \end{aligned} \tag{6.70}$$

As in the section 6.2.2, we obtain the $\hat{\mathbf{q}}_{\max}$ by considering evenly distributed $\hat{\mathbf{q}}_t \in \mathbb{S}^2$, $t = 1, 2, \cdots, 201$. Also, the results are visualized using volume slice planes and isosurfaces using isosurface parameter ν given in (6.33).

Example 6.3.7 (Single small sphere) *Let us remind the information about the inhomogeneity τ with $\mathbf{r} = (0.1\,\text{m}, 0.1\,\text{m}, 0.1\,\text{m})$, $\alpha = 0.1\lambda = 0.04\,\text{m}$, and $\varepsilon = 5\varepsilon_0$, respectively.*

As shown in Figures 6.9, 6.10 and 6.11, the results are similar with the ones obtained within the near-field configuration (Example 6.2.5). The DSM results are getting worse as the direction $\hat{\mathbf{q}}$ is changed in $0° \le \theta \le 70°$ for fixed $\phi = 45°$. But the inhomogeneity is properly identified via DSM if the polarization is selected by either $\hat{\mathbf{p}}^t$ or $\hat{\mathbf{q}}^\infty_{\max}$. Hence, we can validate that both $\hat{\mathbf{p}}^t$ and $\hat{\mathbf{q}}^\infty_{\max}$ would be good choice for imaging the target, but our proposal DSMP does not need to use the information of polarization of incident field even with more computational cost.

Example 6.3.8 (Two small spheres with same radii and different permittivity) *Similarly with example 6.2.6, two small spherical dielectric inhomogeneities with same radii $\alpha_m = 0.1\lambda = 0.04\,\text{m}$ but different permittivities $\varepsilon_1 = 3\varepsilon_0$, $\varepsilon_2 = 5\varepsilon_0$ are considered. They are located at $\mathbf{r}_1 = (0.1\,\text{m}, 0.1\,\text{m}, 0.1\,\text{m})$ and $\mathbf{r}_2 = (-0.2\,\text{m}, -0.1\,\text{m}, -0.1\,\text{m})$, respectively.*

Figure 6.13 shows that the issue of choosing proper polarization of test dipole still occurs as in the previous example. Choosing polarization as $\hat{\mathbf{p}}^t$ (Figure 6.14) or $\hat{\mathbf{q}}^\infty_{\max}$ (Figure 6.15) handles it as expected. However, as stated in Remark 6.3.5, the inhomogeneity having the smaller permittivity is difficult to identify with both DSM and DSMP, which is similar with the different radii case in Example 6.2.6.

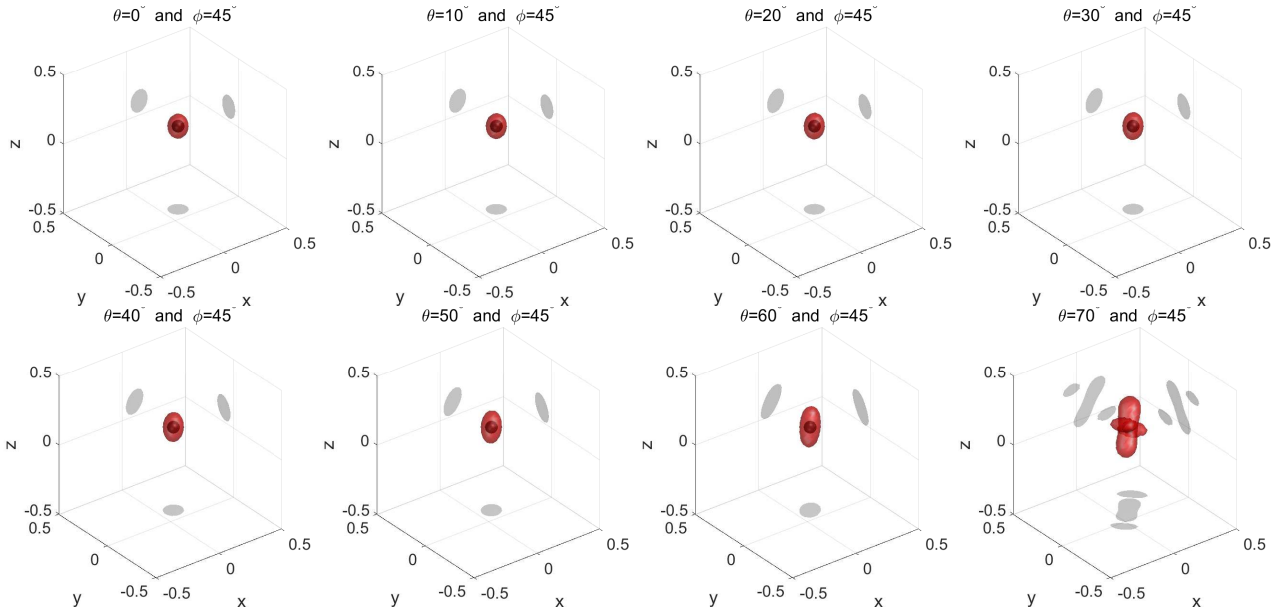

Figure 6.9: (Example 6.3.7) Maps of $\mathcal{I}^{\infty}_{\mathrm{DSM3D}}(\mathbf{z};\mathbf{y},\hat{\mathbf{q}})$ using isosurface with $\rho = 0.8$, where $\hat{\mathbf{q}} = (1,\theta,\phi)$

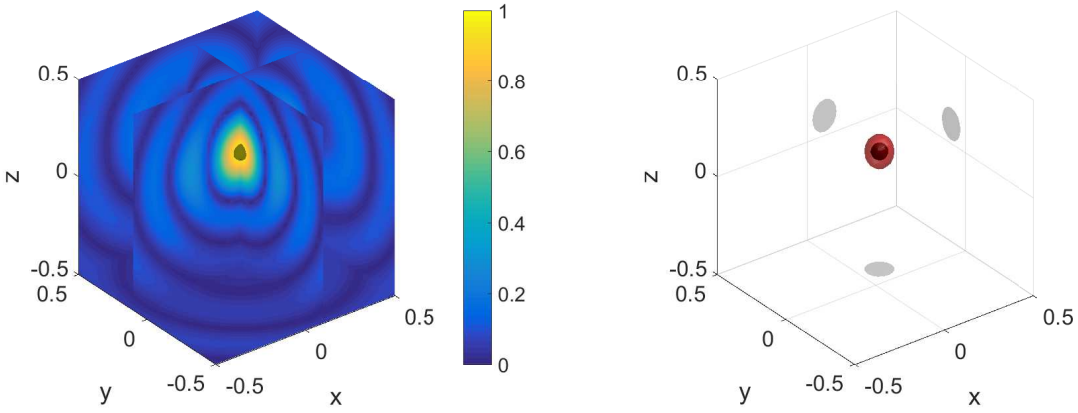

(a) Volume slice with $\mathbf{x} = 0.1$ and $\mathbf{y} = 0.1$ planes

(b) Isosurface with $\rho = 0.6$

Figure 6.10: (Example 6.3.7) Maps of $\mathcal{I}^{\infty}_{\mathrm{DSM3D}}(\mathbf{z};\mathbf{y},\hat{\mathbf{q}})$, where $\hat{\mathbf{q}} = (1, 0°, 45°) = (0,0,1) = \hat{\mathbf{p}}^t$

.

6.4 Illustration with experimental far-field data

Additional results obtained using experimental data are presented with Fresnel experimental data (`http://www.fresnel.fr/3Ddatabase/index.php`). The frequency is chosen as $f_0 = 3\,\mathrm{GHz}$ to be close to the our theoretical condition, the corresponding wavelength being $\lambda_0 = 0.099\,93\,\mathrm{m} \approx 0.1\,\mathrm{m}$. Among various types of targets, two small dielectric spheres of same radii $\alpha_m \approx 0.25\lambda_0$, permittivity $\varepsilon_m = 2.6\varepsilon_0$ with $\mathbf{r}_1 = (0.25\lambda_0, 0, 0)$ and $\mathbf{r}_2 = (-0.25\lambda_0, 0, 0)$ are selected (experimental file name are `TwoSpheres_PP.exp` and `TwoSpheres_TP.exp`). The region of interest Ω is a cube of $2.5\lambda_0$ side length evenly discretized in $41 \times 41 \times 41$ cubical voxels.

It is worth note that

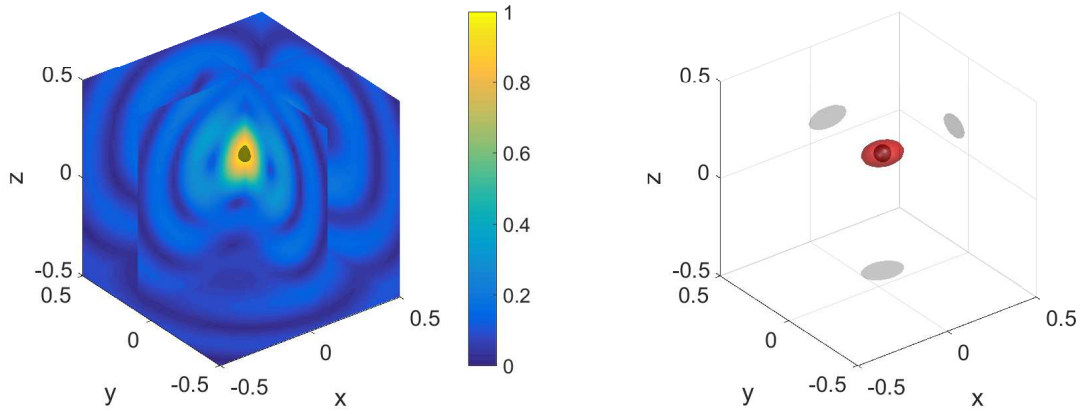

(a) Volume slice with $\mathbf{x} = 0.1$ and $\mathbf{y} = 0.1$ planes

(b) Isosurface with $\rho = 0.6$

Figure 6.11: (Example 6.3.7) Maps of $\mathcal{I}^{\infty}_{\mathrm{DSMP3D}}(\mathbf{z};\mathbf{y})$

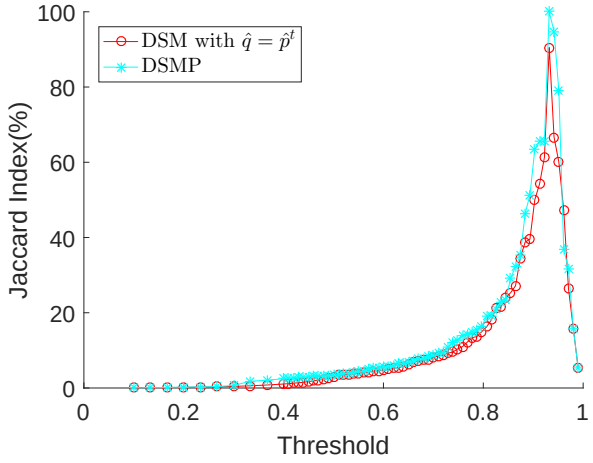

Figure 6.12: (Example 6.3.7) Jaccard index of $\mathcal{I}^{\infty}_{\mathrm{DSM3D}}(\mathbf{z};\hat{\mathbf{y}},\hat{\mathbf{q}} = \hat{\mathbf{p}}^t)$ and $\mathcal{I}^{\infty}_{\mathrm{DSMP3D}}(\mathbf{z};\hat{\mathbf{y}})$

- Since the locations of receivers and transmitters are far from the center (1.796 m) in the experimental configuration, the scattered electric field can be regarded as far-field pattern.

- Due to the limitation of experimental setup, 27 observation directions and 81 incident fields can be used. However, thanks to reciprocity, the roles of the source and the receiver can be exchanged (Geffrin et al. 2008), i.e., $N = 81$ and $L = 27$.

- to adjust our theoretical approach, the transformed scattered field $\widetilde{\mathbf{E}}_{\infty}(\mathbf{x},\mathbf{y}) = \underline{\mathbf{P}}\mathbf{E}_{\infty}(\mathbf{x},\mathbf{y})$ is used for imaging. Here $\underline{\mathbf{P}} = [\hat{r}^r;\hat{\theta}^r;\hat{\phi}^r] \in \mathbb{R}^{3\times 3}$ is the transition matrix in (6.70).

The results are presented Figures 6.17, 6.18, 6.19, and 6.20. The choice of the test dipole as $\hat{\mathbf{q}} = \hat{\mathbf{p}}^t$ or $\hat{\mathbf{q}} = \hat{\mathbf{q}}_{\max}$ provides good results. But our proposal (DSMP) has slightly better imaging performance because the artifacts are eliminated in the map of $\mathcal{I}^{\infty}_{\mathrm{DSMP}}(\mathbf{z};\mathbf{y})$.

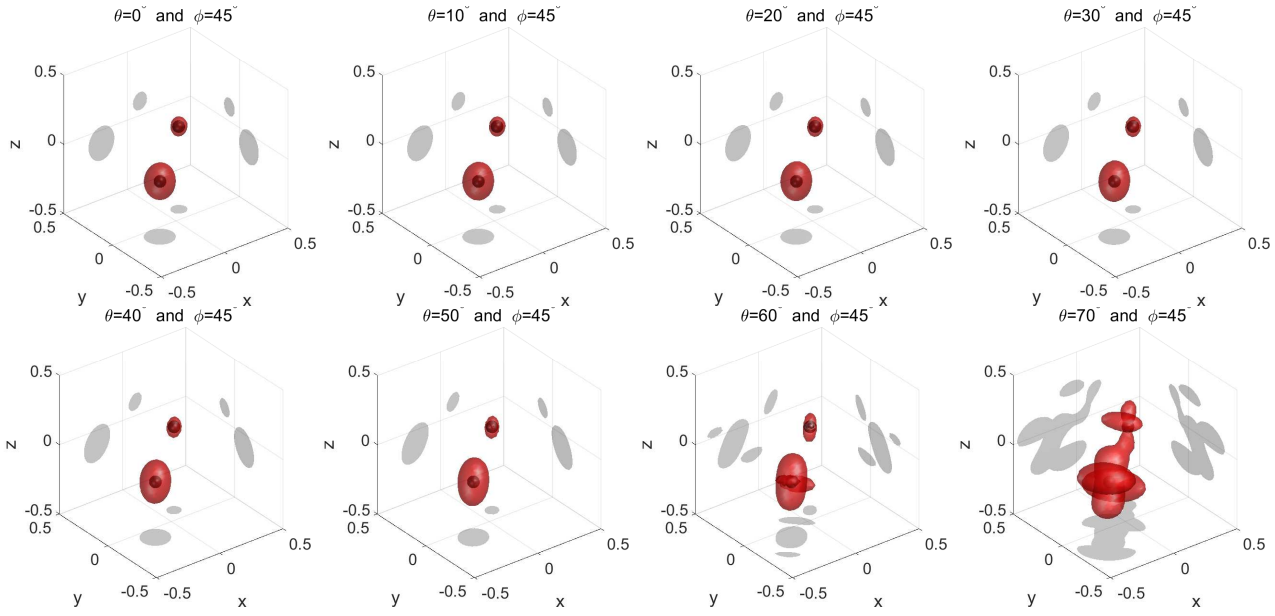

Figure 6.13: (Example 6.3.8) Maps of $\mathcal{I}^{\infty}_{\mathrm{DSM3D}}(\mathbf{z};\mathbf{y},\hat{\mathbf{q}})$ using isosurface with $\rho = 0.5$, where $\hat{\mathbf{q}} = (1,\theta,\phi)$

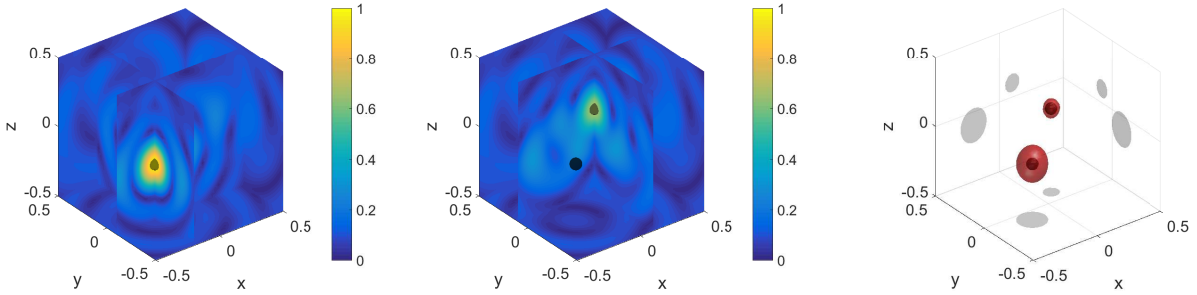

(a) Volume slice with $\mathbf{x} = 0.1$ and $\mathbf{y} = 0.1$ planes

(b) Volume slice with $\mathbf{x} = -0.2$ and $\mathbf{y} = -0.1$ planes

(c) Isosurface with $\rho = 0.6$

Figure 6.14: (Example 6.3.8) Maps of $\mathcal{I}^{\infty}_{\mathrm{DSM3D}}(\mathbf{z};\mathbf{y},\hat{\mathbf{q}})$, where $\hat{\mathbf{q}} = (1, 0°, 45°) = \hat{\mathbf{p}}^t$

.

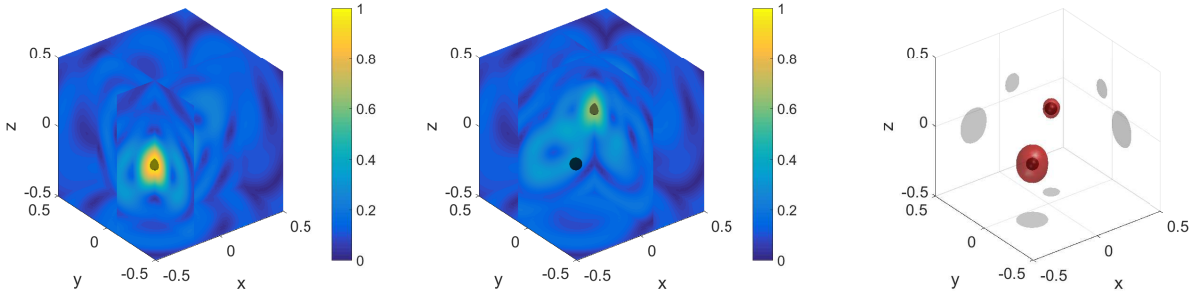

(a) Volume slice with $\mathbf{x} = 0.1$ and $\mathbf{y} = 0.1$ planes

(b) Volume slice with $\mathbf{x} = -0.2$ and $\mathbf{y} = -0.1$ planes

(c) Isosurface with $\rho = 0.6$

Figure 6.15: (Example 6.3.8) Maps of $\mathcal{I}^{\infty}_{\mathrm{DSMP3D}}(\mathbf{z};\mathbf{y})$

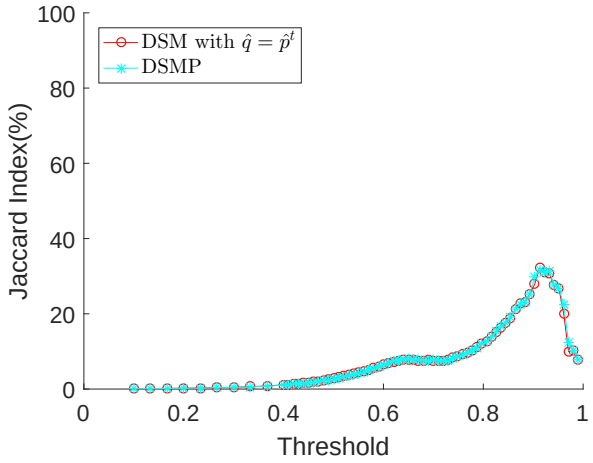

Figure 6.16: (Example 6.3.8) Jaccard index of $\mathcal{I}^{\infty}_{\text{DSM3D}}(\mathbf{z}; \hat{\mathbf{y}}, \hat{\mathbf{q}} = \hat{\mathbf{p}}^t)$ and $\mathcal{I}^{\infty}_{\text{DSMP3D}}(\mathbf{z}; \hat{\mathbf{y}})$

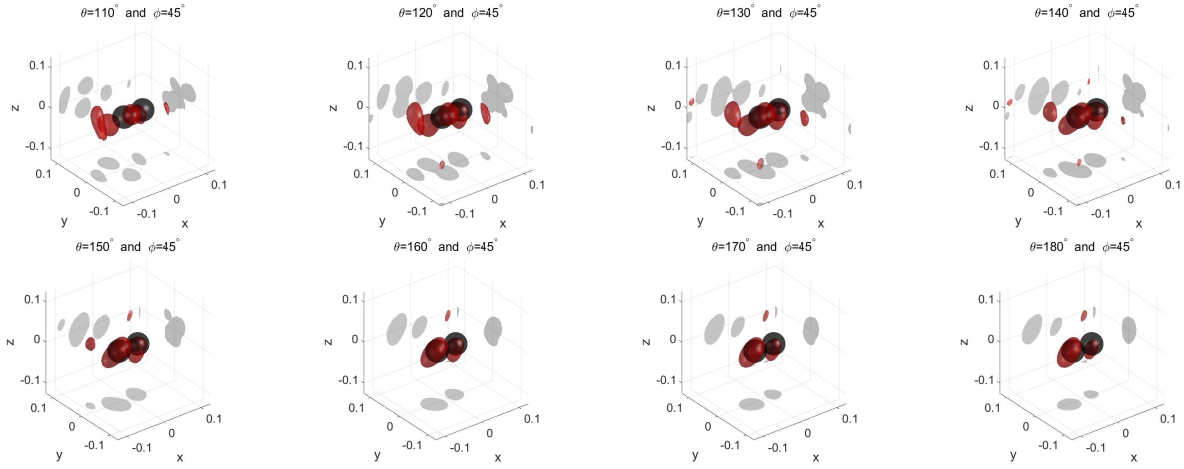

Figure 6.17: Maps of $\mathcal{I}^{\infty}_{\text{DSM3D}}(\mathbf{z}; \mathbf{y}, \hat{\mathbf{q}})$ using isosurface with $\rho = 0.8$, where $\hat{\mathbf{q}} = (1, \theta, \phi)$

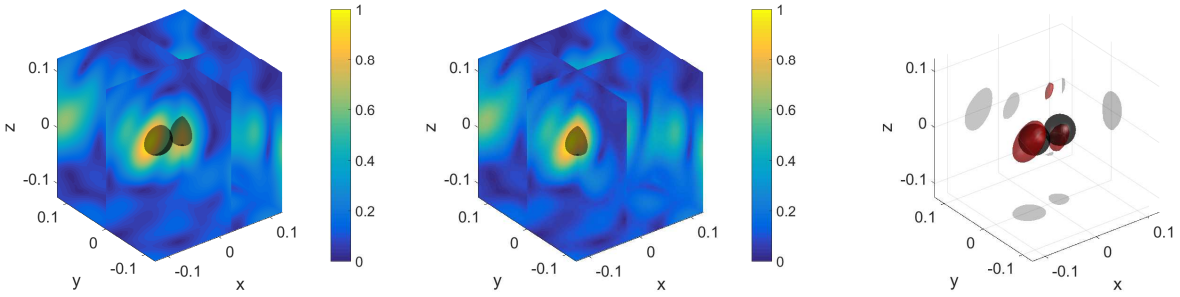

(a) Volume slice with $\mathbf{x} = 0.1$ and $\mathbf{y} = 0.1$ planes

(b) Volume slice with $\mathbf{x} = -0.2$ and $\mathbf{y} = -0.1$ planes

(c) Isosurface with $\rho = 0.8$

Figure 6.18: (Example 6.2.6) Maps of $\mathcal{I}^{\infty}_{\text{DSM3D}}(\mathbf{z}; \mathbf{y}, \hat{\mathbf{q}})$, where $\hat{\mathbf{q}} = (1, 180°, 45°) = (0, 0, -1) = \hat{\mathbf{p}}^t$

.

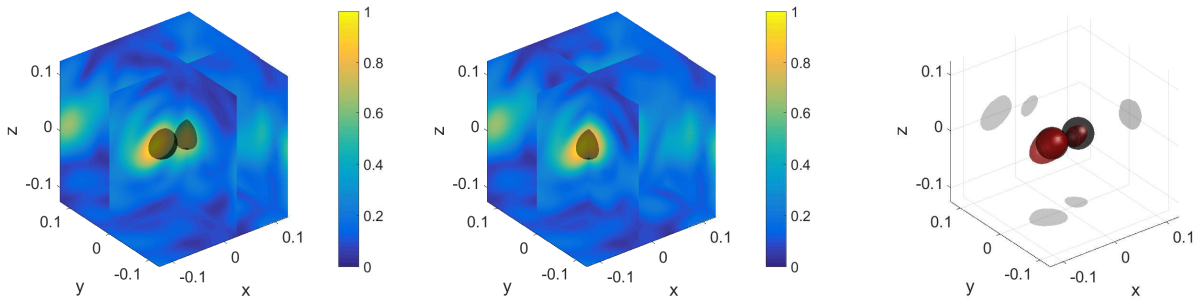

(a) Volume slice with $\mathbf{x} = 0.1$ and $\mathbf{y} = 0.1$ planes

(b) Volume slice with $\mathbf{x} = -0.2$ and $\mathbf{y} = -0.1$ planes

(c) Isosurface with $\rho = 0.8$

Figure 6.19: Maps of $\mathcal{I}^{\infty}_{\text{DSMP3D}}(\mathbf{z};\mathbf{y})$

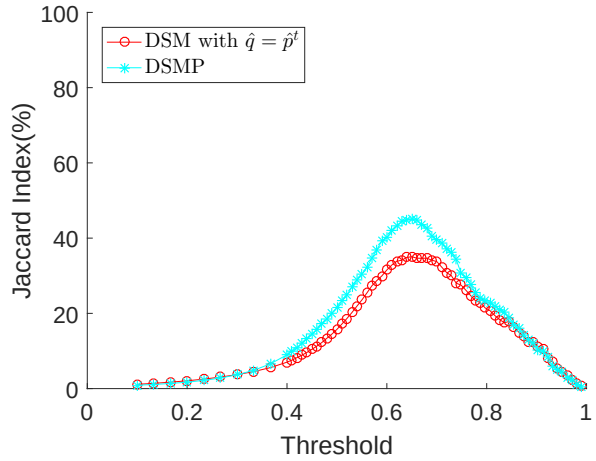

Figure 6.20: Jaccard index of DSM and DSMA

6.5 Further study about improvement imaging performance with multiple impinging directions

According to (6.3) (in near-field) and (6.35) (in far-field), the indicator function of traditional DSM for multiple impinging directions is given by an average value of the result for each impinging direction. However, it is difficult to improve the imaging performance because the definition does not consider the information about incident fields which is also generally known information like observation directions (or receivers). In 2D cases (Chapter 3, 4,and 5), we have already proposed DSMA by considering an additional test function related to each incident field and verified that DSMA has better accuracy than DSM for imaging the target with multiple sources. Hence, we extend our approach to 3D case and define the indicator function of DSMA by

$$\mathcal{I}_{\text{DSMA3D}}(\mathbf{z};k_0) := \frac{\left|\left\langle \langle \mathbf{E}^s(\mathbf{x},\mathbf{y};k_0), \underline{\mathbf{G}}(\mathbf{x},\mathbf{z})\cdot\hat{\mathbf{q}}\rangle_{L^2(\Gamma_{\text{obs}})}, (\underline{\mathbf{G}}(\mathbf{y},\mathbf{z})\cdot\mathbf{p}^t)\cdot\mathbf{a}\right\rangle_{L^2(\Gamma_{\text{inc}})}\right|}{\max\left|\left\langle \langle \mathbf{E}^s(\mathbf{x},\mathbf{y};k_0), \underline{\mathbf{G}}(\mathbf{x},\mathbf{z})\cdot\hat{\mathbf{q}}\rangle_{L^2(\Gamma_{\text{obs}})}, (\underline{\mathbf{G}}(\mathbf{y},\mathbf{z})\cdot\mathbf{p}^t)\cdot\mathbf{a}\right\rangle_{L^2(\Gamma_{\text{inc}})}\right|}, \tag{6.71}$$

and

$$\mathcal{I}^{\infty}_{\mathrm{DSMA3D}}(\mathbf{z};k_0) := \frac{\left|\left\langle \langle \mathbf{E}_{\infty}(\hat{\mathbf{x}},\hat{\mathbf{y}};k_0), \underline{\mathbf{G}}_{\infty}(\hat{\mathbf{x}},\mathbf{z})\cdot\hat{\mathbf{q}}^{\infty}\rangle_{L^2(\mathbb{S}^2)}, (\underline{\mathbf{G}}_{\infty}(\hat{\mathbf{y}},\mathbf{z})\cdot\mathbf{p}^t)\cdot\mathbf{a}\right\rangle_{L^2(\mathbb{S}^2)}\right|}{\max\left|\left\langle \langle \mathbf{E}_{\infty}(\hat{\mathbf{x}},\hat{\mathbf{y}};k_0), \underline{\mathbf{G}}_{\infty}(\hat{\mathbf{x}},\mathbf{z})\cdot\hat{\mathbf{q}}^{\infty}\rangle_{L^2(\mathbb{S}^2)}, (\underline{\mathbf{G}}_{\infty}(\hat{\mathbf{y}},\mathbf{z})\cdot\mathbf{p}^t)\cdot\mathbf{a}\right\rangle_{L^2(\mathbb{S}^2)}\right|}, \tag{6.72}$$

for near- and far-field cases, respectively. Here, $\mathbf{a} \in \mathbb{R}^3$ is constant which indicates the weight of each component of $\underline{\mathbf{G}}(\mathbf{y},\mathbf{z})$ or $\underline{\mathbf{G}}_{\infty}(\hat{\mathbf{y}},\mathbf{z})$. Simple application in Figures 6.21 and 6.22 display that our proposal might be an improved version of DSM. To theoretically verify it, the structure analysis is essential but it is not yet completed. Hence, we only present the results of numerical simulations and compare them with traditional DSM.

We recall the setting of numerical simulations with far-field data in section 6.4. But we consider the multiple incident plane waves that are evenly distributed with $\theta^t = 90°$ and ϕ^t varying from $0°$ to $350°$ with $10°$-step. In other word, $L = 36$ (the total number of incident directions). Also, we apply DSM and DSMA with $\alpha = [1,1,1]/\sqrt{3}$ and $\hat{\mathbf{q}}^{\infty} = \hat{\mathbf{p}}^t$. Figures 6.21 and 6.22 show that the artifacts can be reduced by using our proposal DSMA.

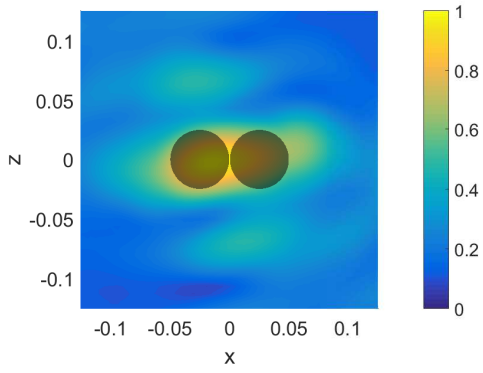

(a) DSM with xy-plane

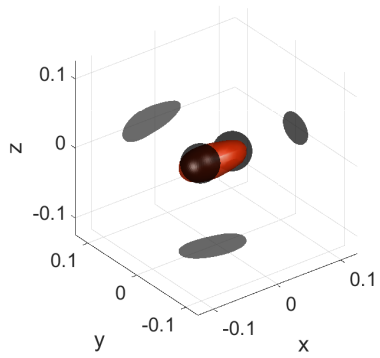

(b) Isosurface with $\rho = 0.8$

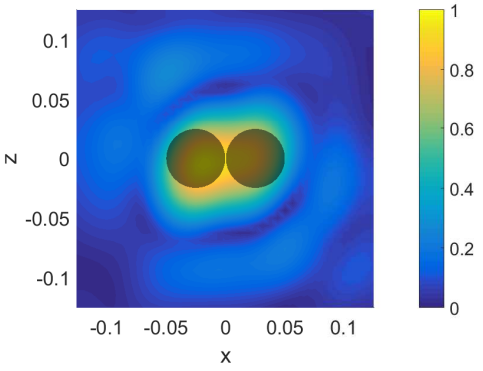

(c) DSMA with xy-plane

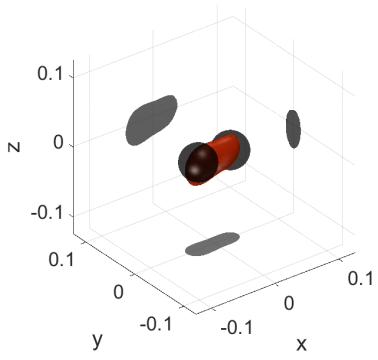

(d) Isosurface with $\rho = 0.8$

Figure 6.21: Numerical results of DSM (top) and DSMA (bottom)

.

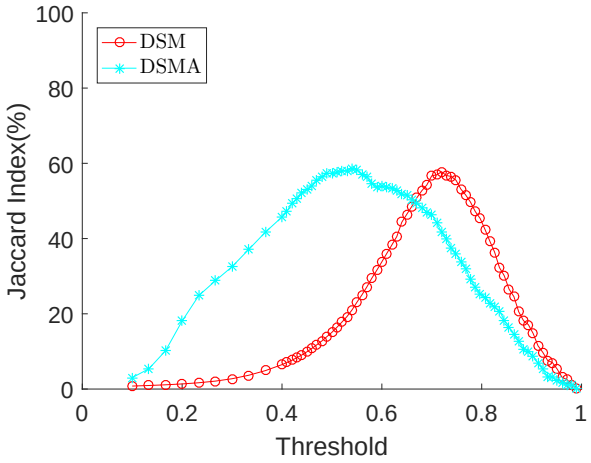

Figure 6.22: Jaccard index of DSM and DSMA

6.6 Conclusion

In this chapter, we analyze the indicator function of the DSM in the 3D inverse electromagnetic scattering problem in both near-field and far-field configurations. With such an analysis, the reasons for which DSM is able to localized the targets is explained and the reasons for which some artifacts might appear also. The key role of the choice of the test dipole polarization in the efficiency of the method is exhibited and a method to provide a better choice is proposed with a theoretical validation. The approach is validated using synthetic data and experimental data when available.

At the end of this chapter, we additionally introduce the indicator function of 3D alternative direct sampling method with some numerical simulations, but no structure analysis. It seems to be an improved version of traditional DSM like in the 2D case, so its structure analysis will be interesting future work.

7

Conclusion and perspectives

Contents

7.1 Conclusion

In this thesis, the direct sampling method (DSM) has been studied in various 2D and 3D inverse electromagnetic scattering problems. The total number of incident and observation directions must be large enough for a successful application of many existing qualitative methods. On the other hand, throughout several studies, it is well known that the DSM is a fast and effective non-iterative type method to reconstruct the support of targets with only a few incident fields. Unfortunately, most applications of DSM are heuristic. Hence, the main aim of the work was to derive the mathematical structure of indicator function of DSM for verifying the theoretical reason of observed phenomena and to design an new effective non-iterative method for imaging the target (being called DSMA in this work). The theoretical results have been validated via various numerical simulations with synthetic and experimental data.

In the first part, we analyzed the mathematical structure of traditional DSM operated at a fixed frequency. Under the 2D full-aperture configuration, the indicator function can be represented by a first-kind Bessel function of order zero and information of target (e.g./ location, size, and permittivity, etc.). This shows the intrinsic limitation of DSM such that it is difficult to identify all targets when one of them is relatively small or its permittivity is lower than others. To overcome the limitation, we considered multiple impinging directions but the imaging performance is not significantly increased. So we designed the DSMA to handle the limitation and examine that the DSMA is an improved version of traditional DSM with the similar path of derivations as in traditional DSM case. We also established the relationship of DSM, DSMA and Kirchhoff migration through our structure analysis.

Next, we studied the DSM in the restricted inverse scattering problem because a full aperture set-up is not possible in various real-world applications. More specifically, the mono-static and limited-aperture

measurement data were treated to image the target in a 2D scalar configuration. In the application of DSM in the mono-static configuration, the mathematical structure of the indicator function of the traditional DSM has been established and the reason for which it fails to image the targets was clearly identified. To overcome this miss-localization of the target, a modified DSM has been proposed and its efficiency was theoretically shown. Then, the application of DSM in the limited-aperture scattering problem was studied. We first investigated the mathematical structure of the indicator function of DSM by establishing the relationship by infinite series of Bessel functions of integer orders, the range of observation directions, and physical properties about inhomogeneities to explain unexplored intrinsic properties of DSM. The DSMA for limited-aperture problem has been designed to improve the imaging performance. Its mathematical structure has also been exhibited by showing the relationship of infinite series of Bessel functions of integer orders and the range of incident and observation and incident directions, and physical properties of targets. Unfortunately, it is still difficult to identify targets via DSM when a narrow range of incident and/or observation directions is considered.

To improve the imaging accuracy when the range of incident and/or observation directions is narrow, a multi-frequency indicator function of DSM has been introduced in the third part. On the contrary to several investigations, multi-frequency DSM is effective only for imaging a small single inhomogeneity but is not effective for several small inhomogeneities. To explain why, the mathematical structure of a multi-frequency indicator function has been derived by establishing the relationship of the Bessel functions, Struve functions, Legendre polynomials, generalized hypergeometric function, the range of incident and observation directions, and physical characteristics of targets. We then examined undiscovered properties of multi-frequency DSM, design alternative indicator function based on an exponential weight with respect to each frequency for further improvement, and analyzed its mathematical structure.

Finally, in the 3D inverse electromagnetic scattering problem, the mathematical structure of DSM has been presented in near- and far-field configurations. The main difference between 2D and 3D DSM is the choice of the polarization of the test function. We showed that the indicator function of DSM can be represented as the combination of spherical Bessel functions of integer order, polarization of test dipole, and polarization tensors of the targets which carry the information about them. Based on our analysis, we verified how the imaging from DSM is changed according the choice of polarization of test dipole, and proposed our way to choose proper the polarization for exact imaging. Moreover, we examined the adequacy of the guideline in (Ito, Jin, and J. Zou 2013) about the choice of the test polarization.

7.2 Perspectives

In this thesis, we have validated the behavior of 2D and 3D DSM through mathematical analysis in various 2D and 3D inverse electromagnetic scattering problem. However, further studies are still required.

2D inverse scattering problem

- According to section 4.2.1, the accuracy of DSM with mono-static data is lower than one with

multi-static data due to the lack of information. To improve mono-static radar imaging, the application and analysis of multi-frequency DSM and DSMA should be an interesting challenge.

- By (Joh and W.-K. Park 2014), the imaging accuracy of non-iterative reconstruction method with multi-frequency can be improved by adopting different weights with respect to each frequency. Hence, we might improve the imaging accuracy of multi-frequency DSM and DSMA if the proper weight is found.

- Throughout our analysis, DSM and DSMA is effective techniques to imaging unknown inhomogeneities. So we expect that DSM and DSMA can be extended to the reconstruction of buried inhomogeneities also.

- In (Baronian et al. 2018), LSM is applied to 2D ultrasonic Non Destructive Testing of an elastic waveguide. So, the application of DSM to this problem should be interesting since the DSM is also a sampling-type method similar with LSM.

3D inverse scattering problem

- In section 6.5, we have proposed a 3D version of alternative indicator function of DSM (DSMA) with the similar approach in 2D case demonstrated in section 3.3.2. Even though the mathematical analysis has not yet been provided, we have shown that the DSMA is an improved version of DSM through various numerical simulations. Hence, the structure analysis should be a future work.

- Section 3.4 has indicated that 2D DSMA has strong relation with Kirchhoff migration. So verification of the relation between 3D version of DSMA and migration-type technique in (J. Chen, Z. Chen, and Huang 2013b) would be interesting.

- In the present works, we only consider the 3D version of DSM in full-aperture inverse scattering problem. But, a full measurement setup is impossible in many real applications such as GPR, SAR, etc. Hence, structure analysis in limited-aperture configuration is needed.

A

Appendix

A.1 Ill-posedness and nonlinear system

Solving an inverse scattering problem can be formulated according to the following general form

$$\mathcal{F}(u) = v, \tag{A.1}$$

where u and v represent the information about the unknown inhomogeneity and the measurement data, respectively, and $\mathcal{F}$ denotes the forward operator. The problem (A.1) is called well-posed in the sense of Hadamard (Hadamard 2003) if it satisfies the following conditions.

(i) Existence: there exists a solution of the problem.

(ii) Uniqueness: there is at most one solution of the problem.

(iii) Stability: the solution depends continuously on the data.

It is called ill-posed otherwise. Note that, if the operator $\mathcal{F}$ satisfies the following two conditions, it is called a linear operator

(i) $\mathcal{F}(u_1 + u_2) = \mathcal{F}(u_1) + \mathcal{L}(u_2)$

(ii) $\mathcal{F}(cu) = c\mathcal{F}(u)$

where c is a constant. Generally, the operator $\mathcal{F}$ is ill-posed and nonlinear.

A.2 The definition of L^2 inner product and norm

For a simply connected surface (or curve) $\partial\Omega \in \mathbb{R}^d,\ d = 2, 3$, the L^2-inner product is defined by

$$\begin{aligned} \langle \mathbf{f}(\mathbf{x}_n), \mathbf{g}(\mathbf{x}_n) \rangle_{L^2(\partial\Omega)} &:= \sum_{n=1}^{N} \mathbf{f}(\mathbf{x}_n) \cdot \overline{\mathbf{g}(\mathbf{x}_n)} = \sum_{n=1}^{N} \sum_{l=1}^{L} f_i(\mathbf{x}_n) \overline{g_l(\mathbf{x}_n)} \approx \int_{\partial\Omega} \mathbf{f}(\mathbf{x}) \overline{\mathbf{g}(\mathbf{x})} \mathrm{d}S(\mathbf{x}) \\ \|f(\mathbf{x}_n)\|_{L^2(\partial\Omega)} &:= \langle \mathbf{f}(\mathbf{x}_n), \mathbf{f}(\mathbf{x}_n) \rangle_{L^2(\partial\Omega)}. \end{aligned} \tag{A.2}$$

A.3 Jaccard index

Throughout our work, we adopt the notion of Jaccard index in order to compare the accuracy of the results as objectively as possible. The Jaccard index (Jaccard 1912; Rosin and Ioannidis 2003; Gupta et al. 2014) measures the similarity between two finite samples sets A and B, and it is defined as

$$J(A,B)(\%) := \frac{|A \cap B|}{|A \cup B|} \times 100. \tag{A.3}$$

In our case the Jaccard index is calculated by comparing $\mathcal{I}^{\kappa}_{\text{exact}}(\mathbf{z}; k_0)$ with various index maps $\mathcal{I}^{\kappa}(\mathbf{z}; k_0)$ defined as

$$\mathcal{I}^{\kappa}(\mathbf{z}; k_0) = \begin{cases} \mathcal{I}(\mathbf{z}; k_0), & \forall \mathbf{z} \quad \text{such that } \mathcal{I}(\mathbf{z}; k_0) \geq \kappa \\ 0 & \forall \mathbf{z} \quad \text{such that } \mathcal{I}(\mathbf{z}; k_0) < \kappa \end{cases} \tag{A.4}$$

where κ varies from 0 to 1 and where $\mathcal{I}(\mathbf{z}; k_0)$ can be $\mathcal{I}_{\text{DSM}}(\mathbf{z}; k_0)$, $\mathcal{I}_{\text{DSMA}}(\mathbf{z}; k_0)$ or $\mathcal{I}_{\text{NKM}}(\mathbf{z}; k_0)$ and where $\mathcal{I}_{\text{exact}}(\mathbf{z})$ is defined as

$$\mathcal{I}_{\text{exact}}(\mathbf{z}; k_0) = \frac{|k(\mathbf{z}) - k_0|}{\max |k(\mathbf{z}) - k_0|}. \tag{A.5}$$

Here, $k(\mathbf{z})$ is the wavenumber at the searching point $\mathbf{z} \in \Omega$. The k_0 is analogously defined in the background medium.

A.4 Proof of Lemma 6.3.2

For fixed $\hat{\mathbf{z}}$, choose an orthogonal matrix A depending on $\hat{\mathbf{z}}$ such that $A^{-1}\hat{\mathbf{z}} = A^T\hat{\mathbf{z}} = \hat{\mathbf{z}}' = (0,0,1)^T$, i.e., $\hat{\mathbf{z}}'$ is "north pole". Then the transformation $\hat{\mathbf{x}} = A\hat{\mathbf{x}}'$ leads that

$$\int_{\mathbb{S}^2} f(\hat{\mathbf{z}} \cdot \hat{\mathbf{x}}) \, \mathrm{Y}_n^m(\hat{\mathbf{x}}) \mathrm{d}s(\hat{\mathbf{x}}) = \int_{\mathbb{S}^2} f\left(\hat{\mathbf{z}} \cdot A\hat{\mathbf{x}}'\right) \mathrm{Y}_n^m\left(A\hat{\mathbf{x}}'\right) \mathrm{d}s(\hat{\mathbf{x}}') = \int_{\mathbb{S}^2} f\left(\hat{\mathbf{z}}' \cdot \hat{\mathbf{x}}\right) \mathrm{Y}_n^m\left(A\hat{\mathbf{x}}'\right) \mathrm{d}s(\hat{\mathbf{x}}) \tag{A.6}$$

Because the orthonormal matrix A is isometry, the function $\mathrm{Y}_n^m(A\hat{\mathbf{x}})$ is again a spherical harmonic of order n and it can be expressed as

$$\mathrm{Y}_n^m(A\hat{\mathbf{x}}) = \sum_{k=-n}^{n} a_k \, \mathrm{Y}_n^k(\hat{\mathbf{x}}), \tag{A.7}$$

where $a_k = \int_{\mathbb{S}^2} \mathrm{Y}_n^m(A\hat{\mathbf{x}}) \, \mathrm{Y}_n^{-k}(\hat{\mathbf{x}}) \mathrm{d}S(\hat{\mathbf{x}})$. We know that

$$\begin{aligned} \mathrm{Re}\left(\mathrm{Y}_n^m(A\hat{\mathbf{x}})\right) &= \sum_{k=-n}^{n} \mathrm{Re}(a_k) \, \mathrm{Re}\left(\mathrm{Y}_n^k(\hat{\mathbf{x}})\right) - \mathrm{Im}(a_k) \, \mathrm{Im}\left(\mathrm{Y}_n^k(\hat{\mathbf{x}})\right), \\ \mathrm{Im}\left(\mathrm{Y}_n^m(A\hat{\mathbf{x}})\right) &= \sum_{k=-n}^{n} \mathrm{Re}(a_k) \, \mathrm{Im}\left(\mathrm{Y}_n^k(\hat{\mathbf{x}})\right) + \mathrm{Im}(a_k) \, \mathrm{Re}\left(\mathrm{Y}_n^k(\hat{\mathbf{x}})\right). \end{aligned} \tag{A.8}$$

From them and spherical coordinates $\hat{\mathbf{x}} = (\sin\theta\cos\phi, \sin\theta\sin\phi, \cos\theta)^T$ (note that $\hat{\mathbf{z}}' \cdot \hat{\mathbf{x}} = \cos\theta$),

$$\begin{aligned}
&\int_{\mathbb{S}^2} f(\hat{\mathbf{z}} \cdot \hat{\mathbf{x}}) \mathrm{Re}\left(\mathrm{Y}_n^m(\hat{\mathbf{x}})\right) \mathrm{d}S(\hat{\mathbf{x}}) \\
&= \sum_{k=-n}^{n} \int_{\mathbb{S}^2} f\left(\hat{\mathbf{z}}' \cdot \hat{\mathbf{x}}\right) \left[\mathrm{Re}\left(a_k\right) \mathrm{Re}\left(\mathrm{Y}_n^k(\hat{\mathbf{x}})\right) - \mathrm{Im}\left(a_k\right) \mathrm{Im}\left(\mathrm{Y}_n^k(\hat{\mathbf{x}})\right)\right] \mathrm{d}s(\hat{\mathbf{x}}) \\
&= \sum_{k=-n}^{n} \sqrt{\frac{(2n+1)(n-|k|)!}{4\pi(n+|k|!)}} \int_0^{\pi} \int_0^{2\pi} f(\cos\theta) P_n^{|k|}(\cos\theta) \left[\mathrm{Re}\left(a_k\right)\cos(k\phi) - \mathrm{Im}\left(a_k\right)\sin(k\phi)\right] \mathrm{d}\phi \sin\theta \mathrm{d}\theta \\
&= \mathrm{Re}\left(a_0\right) \sqrt{\frac{2n+1}{4\pi}} \left(2\pi \int_0^{\pi} f(\cos\theta) P_n(\cos\theta) \sin\theta \mathrm{d}\theta\right).
\end{aligned} \tag{A.9}$$

and

$$\begin{aligned}
&\int_{\mathbb{S}^2} f(\hat{\mathbf{z}} \cdot \hat{\mathbf{x}}) \mathrm{Im}\left(\mathrm{Y}_n^m(\hat{\mathbf{x}})\right) \mathrm{d}s(\hat{\mathbf{x}}) \\
&= \sum_{k=-n}^{n} \int_{\mathbb{S}^2} f\left(\hat{\mathbf{z}}' \cdot \hat{\mathbf{x}}\right) \left[\mathrm{Re}\left(a_k\right) \mathrm{Im}\left(\mathrm{Y}_n^k(\hat{\mathbf{x}})\right) + \mathrm{Im}\left(a_k\right) \mathrm{Re}\left(\mathrm{Y}_n^k(\hat{\mathbf{x}})\right)\right] \mathrm{d}s(\hat{\mathbf{x}}) \\
&= \sum_{k=-n}^{n} \sqrt{\frac{(2n+1)(n-|k|)!}{4\pi(n+|k|!)}} \int_0^{\pi} \int_0^{2\pi} f(\cos\theta) P_n^{|k|}(\cos\theta) \left[\mathrm{Re}\left(a_k\right)\sin(k\phi) + \mathrm{Im}\left(a_k\right)\cos(k\phi)\right] \mathrm{d}\phi \sin\theta \mathrm{d}\theta \\
&= \mathrm{Im}\left(a_0\right) \sqrt{\frac{2n+1}{4\pi}} \left(2\pi \int_0^{\pi} f(\cos\theta) P_n(\cos\theta) \sin\theta \mathrm{d}\theta\right).
\end{aligned} \tag{A.10}$$

By substituting $\hat{\mathbf{x}} = \hat{\mathbf{z}}'$ in (A.7) and from $\mathrm{Y}_n^k(\hat{\mathbf{z}}') = 0$ for $k \neq 0$,

$$\mathrm{Y}_n^m(\hat{\mathbf{z}}) = \mathrm{Y}_n^m\left(A\hat{\mathbf{z}}'\right) = \sum_{k=-n}^{n} a_k \mathrm{Y}_n^k\left(\hat{\mathbf{z}}'\right) = a_0 \sqrt{\frac{2n+1}{4\pi}} P_n(1) = a_0 \sqrt{\frac{2n+1}{4\pi}}, \tag{A.11}$$

so that

$$\mathrm{Re}\left(\mathrm{Y}_n^m(\hat{\mathbf{z}})\right) = \mathrm{Re}\left(a_0\right) \sqrt{\frac{2n+1}{4\pi}} \quad \text{and} \quad \mathrm{Im}\left(\mathrm{Y}_n^m(\hat{\mathbf{z}})\right) = \mathrm{Im}\left(a_0\right) \sqrt{\frac{2n+1}{4\pi}}. \tag{A.12}$$

Finally, (A.9), (A.10), and (A.12) imply (6.38) which is the completeness of the proof. □

B

List of my publications

B.1 Journal papers (accepted/published)

A1 S. Kang, M. Lambert, and W. Park (Nov. 2019). "Analysis and Improvement of Direct Sampling Method in the Monostatic Configuration". *IEEE Geoscience and Remote Sensing Letters* 16.11, pp. 1721–1725. DOI: 10.1109/LGRS.2019.2906366

A2 S. Kang, M. Lambert, and W.-K. Park (2018b). "Direct sampling method for imaging small dielectric inhomogeneities: analysis and improvement". *Inverse Prob.* 34. https://arxiv.org/abs/1801.05993, p. 095005. DOI: 10.1088/1361-6420/aacf1d

A3 S. Kang, M. Lambert, and W.-K. Park (2017b). "Multi-frequency direct sampling method in inverse scattering problem". *J. Phys. Conf. Ser.* 904.1, p. 012018. DOI: 10.1088/1742-6596/904/1/012018

B.2 Conference papers

C1 S. Kang and M. Lambert (Oct. 23–28, 2018a). "Alternative direct sampling method in 3D inverse electromagnetic scattering problem". *2018 International Symposium on Antennas and Propagation (ISAP 2018)*. Selected for the Best Student Paper Award. Busan, Korea, 2 pages

C2 S. Kang and M. Lambert (Aug. 20–24, 2018b). "Direct sampling method with optimal test dipole in inverse electromagnetic scattering 3D problem". *Europe-Korea Conference on Science and Technology (EKC 2018)*. Glasgow, Royaume-Unis, 1 page

C3 S. Kang, M. Lambert, and W.-K. Park (May 28–June 1, 2018a). "Analysis of Kirchhoff migration and direct sampling method within far-field approximation: from the multi-static to the mono-static configuration". *Second URSI Atlantic Radio Science Meeting (URSI-RASC 2018)*. Selected for the 6th International URSI Student Paper Prize Competition. Gran Canaria, Spain, 4 pages

C4 S. Kang, M. Lambert, and W.-K. Park (May 12, 2017a). "Multi-frequency direct sampling method in inverse scattering problem". *International Workshop on New Computational Methods for Inverse Problems (NCMIP 2017)*. Cachan, France, 6 pages

Bibliography

Abramowitz, M. and I. Stegun (1964). "Handbook of Mathematical Functions with Formulas, Graphs, and Mathematical Tables (Applied Mathematics Series 55)". *National Bureau of Standards, Washington, DC* (cit. on p. 63).

Ammari, H., J. Garnier, H. Kang, M. Lim, and K. Sølna (2012). "Multistatic imaging of extended targets". *SIAM J. Imag. Sci.* 5.2, pp. 564–600 (cit. on p. 4).

Ammari, H., J. Garnier, H. Kang, M. Lim, and S. Yu (2014). "Generalized polarization tensors for shape description". *Numer. Math.* 126.2, pp. 199–224 (cit. on p. 11).

Ammari, H., J. Garnier, H. Kang, W.-K. Park, and K. Sølna (2011). "Imaging schemes for perfectly conducting cracks". *SIAM J. Appl. Math.* 71, pp. 68–91 (cit. on pp. 4, 18).

Ammari, H., E. Iakovleva, and D. Lesselier (2005). "A MUSIC algorithm for locating small inclusions buried in a half-space from the scattering amplitude at a fixed frequency". *Multiscale Model. Simul.* 3.3, pp. 597–628 (cit. on p. 3).

Ammari, H., E. Iakovleva, D. Lesselier, and G. Perrusson (2007). "MUSIC-type electromagnetic imaging of a collection of small three-dimensional inclusions," *SIAM J. Sci. Comput.* 29.2, pp. 674–709 (cit. on pp. 3, 11).

Ammari, H. and H. Kang (2004). *Reconstruction of Small Inhomogeneities from Boundary Measurements*. Vol. 1846. Lecture Notes in Mathematics. Berlin: Springer-Verlag (cit. on pp. 9, 10).

Ammari, H., H. Kang, E. Kim, K. Louati, and M. Vogelius (2008). "A MUSIC-type algorithm for detecting internal corrosion from electrostatic boundary measurements". *Numer. Math.* 108, pp. 501–528 (cit. on p. 3).

Ammari, H. and D. Volkov (2003). "Correction of order three for the expansion of two dimensional electromagnetic fields perturbed by the presence of inhomogeneities of small diameter". *J. Comput. Phys.* 189.2, pp. 371–389 (cit. on p. 11).

Ammari., H., J. Garnier, W. Jing., H. Kang., M. Lim., K. Solna, and H. Wang. (2013). *Mathematical and Statistical Methods for Multistatic Imaging*. Vol. 2098. Lecture Notes in Mathematics. Springer (cit. on p. 14).

Aramini, R., M. Brignone, and M. Piana (2006). "The linear sampling method without sampling". *Inverse Prob.* 22.6, p. 2237 (cit. on p. 4).

Arens, T. (2003). "Why linear sampling works". *Inverse Prob.* 20.1 (cit. on p. 4).

Arens, T. and A. Lechleiter (2009). "The linear sampling method revisited". *J. Integral Equations Applications* 21.2, pp. 179–202 (cit. on p. 4).

Audibert, L. and H. Haddar (2014). "A generalized formulation of the linear sampling method with exact characterization of targets in terms of farfield measurements". *Inverse Prob.* 30.3, p. 035011 (cit. on p. 4).

Audibert, L. and H. Haddar (2017). "The generalized linear sampling method for limited aperture measurements". *SIAM J. Imag. Sci.* 10.2, pp. 845–870 (cit. on p. 4).

Bardsley, P. and F. G. Vasquez (2016). "Kirchhoff migration without phases". *Inverse Prob.* 32, p. 105006 (cit. on p. 4).

Baronian, V., L. Bourgeois, B. Chapuis, and A. Recoquillay (May 2018). "Linear sampling method applied to non destructive testing of an elastic waveguide: theory, numerics and experiments". *Inverse Problems* 34.7, p. 075006. DOI: 10.1088/1361-6420/aac21e (cit. on p. 103).

Bazán, F., J.B.Francisco, K. Leem, and G. Pelekanos (2015). "Using the linear sampling method and an improved maximum product criterion for the solution of the electromagnetic inverse medium problem". *J. Comput. Appl. Math.* 273, pp. 61–75 (cit. on p. 83).

Bektas, H. O. and O. Ozdemir (Aug. 2016). "Direct sampling method for monostatic radar imaging". *2016 URSI International Symposium on Electromagnetic Theory (EMTS), Espoo, Finland.* Pp. 152–154. DOI: 10.1109/URSI-EMTS.2016.7571338 (cit. on pp. xii, 5, 31).

Belkebir, K. and M. Saillard (2001). "Special section: Testing inversion algorithms against experimental data". *Inverse Prob.* 17, pp. 1565–1571 (cit. on pp. 22, 42, 43).

Berg, P. van den, A. V. Broekhoven, and A. Abubakar (1999). "Extended contrast source inversion". *Inverse Prob.* 15.5, p. 1325 (cit. on p. 2).

Bevacqua, M. and R. Palmeri (2019). "Qualitative Methods for the Inverse Obstacle Problem: A Comparison of Experimental Data". *J. Imaging* 5.4, p. 47 (cit. on p. 3).

Bleistein, N., J. K. Cohen, and J. W. John (2013). *Mathematics of Multidimensional Seismic Imaging, Migration, and Inversion.* Vol. 13. Springer Science & Business Media (cit. on pp. 4, 14).

Cakoni, F. and D. Colton (2003). "The linear sampling method for cracks". *Inverse Prob.* 19, pp. 279–295 (cit. on p. 4).

Cakoni, F., D. Colton, and H. Haddar (2002). "The linear sampling method for anisotropic media". *J. Comput. Appl. Math.* 146.2, pp. 285–299 (cit. on p. 4).

Caorsi, S., A. Massa, and M. Pastorino (2000). "A computational technique based on a real-coded genetic algorithm for microwave imaging purposes". *IEEE Trans. Geosci. Remote Sensing* 38.4, pp. 1697–1708 (cit. on p. 2).

Caorsi, S., A. Massa, M. Pastorino, and M. Donelli (June 2004). "Improved microwave imaging procedure for nondestructive evaluations of two-dimensional structures". *IEEE Trans. Antennas Propag.* 52.6, pp. 1386–1397. DOI: 10.1109/TAP.2004.830254 (cit. on p. 1).

Catapano, I., F. Soldovieri, and L. Crocco (June 2011). "2D GPR imaging via Linear Sampling Method: A performance assessment tool". *2011 6th International Workshop on Advanced Ground Penetrating Radar (IWAGPR),Aachen, Germany*, pp. 1–4. DOI: 10.1109/IWAGPR.2011.5963862 (cit. on pp. xii, 1, 29).

Çetin, M., I. Stojanović, N. Ö. Önhon, K. Varshney, S. Samadi, W. C. Karl, and A. S. Willsky (July 2014). "Sparsity-Driven Synthetic Aperture Radar Imaging: Reconstruction, autofocusing, moving targets, and compressed sensing". *IEEE Signal Process. Mag.* 31.4, pp. 27–40. DOI: 10.1109/MSP.2014.2312834 (cit. on pp. 1, 29).

Chandra, R., H. Zhou, I. Balasingham, and R. M. Narayanan (2015). "On the opportunities and challenges in microwave medical sensing and imaging". *IEEE Trans. Biomed. Eng.* 62, pp. 1667–1682 (cit. on pp. xi, 1).

Chen, J., Z. Chen, and G. Huang (2013a). "Reverse time migration for extended obstacles: acoustic waves". *Inverse Prob.* 29.8, p. 085005 (cit. on p. 4).

Chen, J., Z. Chen, and G. Huang (July 2013b). "Reverse time migration for extended obstacles: electromagnetic waves". *Inverse Prob.* 29.8, p. 085006. DOI: 10.1088/0266-5611/29/8/085006 (cit. on pp. 4, 79, 103).

Chen, X. (2018). *Computational Methods for Electromagnetic Inverse Scattering*. John Wiley & Sons (cit. on pp. 3, 9).

Chen, X. and Y. Zhong (2008). "MUSIC electromagnetic imaging with enhanced resolution for small inclusions". *Inverse Prob.* 25.1, p. 015008 (cit. on pp. xviii, 3, 77, 82).

Chen, Y., J. Yuan, S. Zu, S. Qu, and S. Gan (2015). "Seismic imaging of simultaneous-source data using constrained least-squares reverse time migration". *J. Appl. Geophys.* 114, pp. 32–35 (cit. on pp. 1, 29).

Cheney, M. (2001). "The linear sampling method and the MUSIC algorithm". *Inverse Prob.* 17.4, p. 591 (cit. on p. 3).

Chew, W. and Y.-M. Wang (1990). "Reconstruction of two-dimensional permittivity distribution using the distorted Born iterative method". *IEEE Trans. Med. Imag* 9.2, pp. 218–225 (cit. on p. 2).

Chow, Y., K. Ito, K. Liu, and J. Zou (2015). "Direct sampling method for diffusive optical tomography". *SIAM J. Sci. Comput.* 37, A1658–A1684 (cit. on pp. xii, 5).

Chow, Y., K. Ito, and J. Zou (2014). "A direct sampling method for electrical impedance tomography". *Inverse Prob.* 30.9, p. 095003 (cit. on pp. xii, 5).

Colton, D., H. Haddar, and P. Monk (2002). "The linear sampling method for solving the electromagnetic inverse scattering problem". *SIAM J. Sci. Comput.* 24.3, pp. 719–731 (cit. on p. 4).

Colton, D. and A. Kirsch (1996). "A simple method for solving inverse scattering problems in the resonance region". *Inverse Prob.* 12.4, p. 383 (cit. on p. 4).

Colton, D. and R. Kress (1998). *Inverse Acoustic and Electromagnetic Scattering Theory*. 2nd. Springer (cit. on pp. 9, 86).

Deserno, M. (2004). "How to generate equidistributed points on the surface of a sphere". *P.-If Polymerforshung (Ed.)* P. 99 (cit. on p. 83).

Devaney, A. (2000). "Super-resolution processing of multi-static data using time reversal and MUSIC". *preprint, Northeastern University* (cit. on p. 3).

Dorn, O. and D. Lesselier (2006). "Level set methods for inverse scattering". *Inverse Prob.* 22.4, R67–R131 (cit. on p. 2).

Dorn, O. and D. Lesselier (2009). "Level set methods for inverse scattering—some recent developments". *Inverse Prob.* 25.12, p. 125001 (cit. on p. 2).

Estatico, C., A. Fedeli, M. Pastorino, and A. Randazzo (2015). "A Multifrequency Inexact-Newton Method in L^p Banach Spaces for Buried Objects Detection". *IEEE Trans. Antennas Propag.* 63.9, pp. 4198–4204 (cit. on pp. xvi, 53).

Fear, E. C., X. Li, S. C. Hagness, and M. A. Stuchly (2002). "Confocal microwave imaging for breast cancer detection: Localization of tumors in three dimensions". *IEEE Trans. Biomed. Eng.* 49.8, pp. 812–822 (cit. on p. 1).

Geffrin, J.-M., P. Chaumet, C. Eyraud, K. Belkebir, and P. Sabouroux (2008). "Electromagnetic three-dimensional reconstruction of targets from free space experimental data". *Appl. Phys. Lett.* 92.19, p. 194103 (cit. on p. 94).

Griesmaier, R. and C. Schmiedecke (Feb. 2017). "A multifrequency MUSIC algorithm for locating small inhomogeneities in inverse scattering". *Inverse Prob.* 33.3, p. 035015. DOI: 10.1088/1361-6420/aa5bf2 (cit. on pp. 5, 54).

Griesmaier, R. (2011). "A general perturbation formula for electromagnetic fields in presence of low volume scatterers". *ESAIM-Math, Model. Num.* 45.6, pp. 1193–1218 (cit. on p. 11).

Gupta, S., R. Girshick, P. Arbeláez, and J. Malik (2014). "Learning Rich Features from RGB-D Images for Object Detection and Segmentation". *European conference on computer vision*. Ed. by D. Fleet, T. Pajdla, B. Schiele, and T. Tuytelaars. Cham: Springer International Publishing, pp. 345–360 (cit. on p. 106).

Guzina, B., F. Cakoni, and C. Bellis (2010). "On the multi-frequency obstacle reconstruction via the linear sampling method". *Inverse Prob.* 26.12, p. 125005 (cit. on pp. 5, 54).

Hadamard, J. (2003). *Lectures on Cauchy's problem in linear partial differential equations*. Courier Corporation (cit. on p. 105).

Haddar, H. and P. Monk (2002). "The linear sampling method for solving the electromagnetic inverse medium problem". *Inverse Prob.* 18.3, p. 891 (cit. on p. 4).

Haynes, M., J. Stang, and M. Moghaddam (2012). "Microwave breast imaging system prototype with integrated numerical characterization". *J. Biomed. Imag.* 2012, pp. 1–18 (cit. on p. 1).

Henriksson, T., M. Lambert, and D. Lesselier (2011). "Non-iterative MUSIC-type algorithm for eddy-current nondestructive evaluation of metal plates". *Electromagnetic Nondestructive Evaluation (XIV)*, vol. 35. Studies in Applied Electromagnetics and Mechanics. ISO Press, pp. 22–29 (cit. on p. 3).

Hou, S., K. Solna, and H. Zhao (2006). "A direct imaging algorithm for extended targets". *Inverse Prob.* 22.4, p. 1151 (cit. on p. 3).

Ireland, D., K. Bialkowski, and A. Abbosh (2013). "Microwave imaging for brain stroke detection using Born iterative method". *IET Microw. Antennas Propag.* 7.11, pp. 909–915 (cit. on p. 1).

Irishina, N., M. Moscoso, and O. Dorn (2009). "Microwave imaging for early breast cancer detection using a shape-based strategy". *IEEE Trans. Biomed. Eng.* 56, pp. 1143–1153 (cit. on p. 1).

Ito, K., B. Jin, and J. Zou (2012). "A direct sampling method to an inverse medium scattering problem". *Inverse Prob.* 28.2, p. 025003 (cit. on pp. xii, 5, 13–16, 20, 33, 38).

Ito, K., B. Jin, and J. Zou (2013). "A direct sampling method for inverse electromagnetic medium scattering". *Inverse Prob.* 29.9, p. 095018 (cit. on pp. xii, xviii, 5, 13, 77–79, 82, 83, 102).

Jaccard, P. (1912). "The distribution of the flora in the alpine zone". *New Phytol.* 11.2, pp. 37–50 (cit. on p. 106).

Joh, Y.-D., Y. M. Kwon, J. Y. Huh, and W.-K. Park (2013). "Structure analysis of single- and multi-frequency subspace migrations in inverse scattering problems". *Prog. Electromagn. Res.* 136, pp. 607–622 (cit. on pp. 5, 54).

Joh, Y.-D. and W.-K. Park (2014). "Analysis of multi-frequency subspace migration weighted by natural logarithmic function for fast imaging of two-dimensional thin, arc-like electromagnetic inhomogeneities". *Comp. Math. Appl.* 68.12, pp. 1892–1904 (cit. on pp. xvi, xix, 53, 103).

Kang, S., M. Lambert, and W. Park (Nov. 2019). "Analysis and Improvement of Direct Sampling Method in the Monostatic Configuration". *IEEE Geoscience and Remote Sensing Letters* 16.11, pp. 1721–1725. DOI: 10.1109/LGRS.2019.2906366 (cit. on p. 109).

Kang, S. and M. Lambert (Oct. 23–28, 2018a). "Alternative direct sampling method in 3D inverse electromagnetic scattering problem". *2018 International Symposium on Antennas and Propagation (ISAP 2018)*. Selected for the Best Student Paper Award. Busan, Korea, 2 pages (cit. on p. 109).

Kang, S. and M. Lambert (Aug. 20–24, 2018b). "Direct sampling method with optimal test dipole in inverse electromagnetic scattering 3D problem". *Europe-Korea Conference on Science and Technology (EKC 2018)*. Glasgow, Royaume-Unis, 1 page (cit. on p. 109).

Kang, S., M. Lambert, and W.-K. Park (May 12, 2017a). "Multi-frequency direct sampling method in inverse scattering problem". *International Workshop on New Computational Methods for Inverse Problems (NCMIP 2017)*. Cachan, France, 6 pages (cit. on p. 109).

Kang, S., M. Lambert, and W.-K. Park (2017b). "Multi-frequency direct sampling method in inverse scattering problem". *J. Phys. Conf. Ser.* 904.1, p. 012018. DOI: 10.1088/1742-6596/904/1/012018 (cit. on p. 109).

Kang, S., M. Lambert, and W.-K. Park (May 28–June 1, 2018a). "Analysis of Kirchhoff migration and direct sampling method within far-field approximation: from the multi-static to the mono-static configuration". *Second URSI Atlantic Radio Science Meeting (URSI-RASC 2018)*. Selected for the 6th International URSI Student Paper Prize Competition. Gran Canaria, Spain, 4 pages (cit. on p. 109).

Kang, S., M. Lambert, and W.-K. Park (2018b). "Direct sampling method for imaging small dielectric inhomogeneities: analysis and improvement". *Inverse Prob.* 34. https://arxiv.org/abs/1801.05993, p. 095005. DOI: 10.1088/1361-6420/aacf1d (cit. on pp. 39, 109).

Kang, S., M. Lambert, W.-K. Park, C. Y. Ahn, and T. Ha (2019). "Analysis of single- and multi-frequency direct sampling methods in limited-aperture problem within far-field approximation". *Journal of Computational Physics*. Submitted 17th July 2019.

Kirsch, A. and F. Hettlich (2009). "The mathematical theory of Maxwell's equations". *Lecture notes* (cit. on p. 86).

Li, J. and Z. Zou (2013). "A direct sampling method for inverse scattering using far-field data". *Inverse Probl. Imag.* 7.3, pp. 757–775 (cit. on pp. xii, 5, 13, 17, 30, 33, 38).

Liu, X., M. Serhir, and M. Lambert (2018). "Detectability of underground electrical cables junction with a ground penetrating radar: electromagnetic simulation and experimental measurements". *Constr. Build. Mater.* 158, pp. 1099–1110 (cit. on pp. 1, 4, 14, 29).

Luke, Y. L. (2014). *Integrals of Bessel functions*. Courier Corporation (cit. on p. 60).

Moran, M. L., R. Greenfield, S. A. Arcone, and A. J. Delaney (2000). "Multidimensional GPR array processing using Kirchhoff migration". *J. Appl. Geophys.* 43.2-4, pp. 281–295 (cit. on pp. 4, 14).

Nounouh, S., C. Eyraud, A. Litman, and H. Tortel (2014). "Quantitative imaging with incident field modeling from multistatic measurements on line segments". *IEEE Antennas Wireless Propag. Lett.* 14, pp. 253–256 (cit. on p. 2).

Odendaal, J. W., E. Barnard, and C. W. I. Pistorius (1994). "Two-dimensional superresolution radar imaging using the MUSIC algorithm". *IEEE Trans. Antennas Propag.* 42, pp. 1386–1391 (cit. on p. 3).

P.M. Van Den Berg, M. P. and R. E. Kleinman (1997). "A contrast source inversion method". *Inverse Prob.* 13.6, p. 1607 (cit. on p. 2).

Park, W.-K. (2015). "Multi-frequency subspace migration for imaging of perfectly conducting, arc-like cracks in full- and limited-view inverse scattering problems". *J. Comput. Phys.* 283, pp. 52–80 (cit. on pp. 4, 17, 30, 35).

Park, W.-K. (2016). "Detection of small electromagnetic inhomogeneities with inaccurate frequency". *J. Korean Phys. Soc.* 68, pp. 607–615 (cit. on p. 4).

Park, W.-K. (2019a). "Real-time microwave imaging of unknown anomalies via scattering matrix". *Mech. Syst. Signal Proc.* 118, pp. 658–674 (cit. on p. 4).

Park, W.-K. and D. Lesselier (2009). "Electromagnetic MUSIC-type imaging of perfectly conducting, arc-like cracks at single frequency". *J. Comput. Phys.* 228, pp. 8093–8111 (cit. on p. 3).

Park, W.-K. (2018a). "Direct sampling method for anomaly imaging from scattering parameter". *Appl. Math. Lett.* 81, pp. 63–71 (cit. on p. 33).

Park, W.-K. (2018b). "Direct sampling method for retrieving small perfectly conducting cracks". *J. Comput. Phys.* 373, pp. 648–661 (cit. on pp. xii, 5, 33, 39, 53, 54, 61).

Park, W.-K. (2019b). "Improvement of direct sampling method in transverse electric polarization". *Appl. Math. Lett.* 88, pp. 209–215 (cit. on pp. xii, 5, 53, 54).

Ploix, M.-A., V. Garnier, D. Breysse, and J. Moysan (2011). "NDE data fusion to improve the evaluation of concrete structures". *NDT & E Int.* 44, pp. 442–448 (cit. on p. 1).

Remis, R. F. and P. V. den Berg (2000). "On the equivalence of the Newton-Kantorovich and distorted Born methods". *Inverse Prob.* 16.1, p. L1 (cit. on p. 2).

Rosenheinrich, W. (2019). "Tables of some indefinite integrals of bessel functions of integer order". *Ernst - Abbe - Hochschule Jena* (cit. on pp. 55, 58, 59, 62).

Rosin, P. and E. Ioannidis (2003). "Evaluation of global image thresholding for change detection". *Pattern Recognit. Lett.* 24.14, pp. 2345–2356 (cit. on p. 106).

Rubæk, T., P. M. Meaney, P. Meincke, and K. D. Paulsen (2007). "Nonlinear microwave imaging for breast-cancer screening using Gauss–Newton's method and the CGLS inversion algorithm". *IEEE Trans. Antennas Propag.* 55.8, pp. 2320–2331 (cit. on pp. 1, 3).

Scapaticci, R., L. Di Donato, I. Catapano, and L. Crocco (2012). "A feasibility study on microwave imaging for brain stroke monitoring". *Prog. Electromagn. Res.* 40, pp. 305–324 (cit. on p. 1).

Scholz, B. (2002). "Towards virtual electrical breast biopsy: space frequency MUSIC for trans-admittance data". *IEEE Trans. Med. Imag.* 21, pp. 588–595 (cit. on p. 3).

Tilmann, F., J. Ni, and INDEPTH III Seismic Team (2003). "Seismic imaging of the downwelling Indian lithosphere beneath central Tibet". *Science* 300.5624, pp. 1424–1427 (cit. on pp. 1, 29).

Torrione, P. A., K. D. Morton, R. Sakaguchi, and L. M. Collins (2014). "Histograms of oriented gradients for landmine detection in ground-penetrating radar data". *IEEE Trans. Geosci. Remote Sens.* 52.3, pp. 1539–1550 (cit. on pp. 1, 29).

Tournier, P., M. Bonazzoli, V. Dolean, F. Rapetti, F. Hecht, F. Nataf, I. Aliferis, I. El Kanfoud, C. Migliaccio, M. de Buhan, M. Darbas, S. Semenov, and C. Pichot (Oct. 2017). "Numerical Modeling and High-Speed Parallel Computing: New Perspectives on Tomographic Microwave Imaging for Brain Stroke Detection and Monitoring." *IEEE Antennas and Propagation Magazine* 59.5, pp. 98–110. DOI: 10.1109/MAP.2017.2731199 (cit. on p. 1).

Völker, C. and P. Shokouhi (2015). "Multi sensor data fusion approach for automatic honeycomb detection in concrete". *NDT & E Int.* 71, pp. 54–60 (cit. on p. 1).

Voznyuk, I., A. Litman, and H. Tortel (2015). "Efficient combination of a 3D Quasi-Newton inversion algorithm and a vector dual-primal finite element tearing and interconnecting method". *Inverse Prob.* 31.8, p. 085005 (cit. on p. 2).

Xue, Z., Y. Chen, S. Fomel, and J. Sun (2015). "Seismic imaging of incomplete data and simultaneous-source data using least-squares reverse time migration with shaping regularization". *Geophysics* 81.1, S11–S20 (cit. on pp. xii, 1, 29).

Yaman, F., V. G. Yakhno, and R. Potthast (2013). "A survey on inverse problems for applied sciences". *Math. Probl. Eng.* 2013 (cit. on pp. xi, 1).

Yoo, J., Y. Jung, M. Lim, J. C. Ye, and A. Wahab (2017). "A joint sparse recovery framework for accurate reconstruction of inclusions in elastic media". *SIAM J. Imag. Sci.* 10.3, pp. 1104–1138 (cit. on p. 2).

Zaimaga, H., A. Fraysse, and M. Lambert (2017). "Sparse reconstruction algorithms for nonlinear microwave imaging". *2017 25th European Signal Processing Conference (EUSIPCO), Kos, Greece*. IEEE, pp. 713–717 (cit. on p. 2).

Zhang, L., M. Xing, C.-W. Qiu, J. Li, J. Sheng, Y. Li, and Z. Bao (2010). "Resolution enhancement for inversed synthetic aperture radar imaging under low SNR via improved compressive sensing". *IEEE Trans. Geosci. Remote Sens.* 48.10, pp. 3824–3838 (cit. on pp. 1, 29).

Zhang, T. and X.-G. Xia (2015). "OFDM synthetic aperture radar imaging with sufficient cyclic prefix". *IEEE Trans. Geosci. Remote Sens.* 53.1, pp. 394–404 (cit. on pp. xii, 1, 29).

Titre : Imagerie non itérative en problème inverse de diffraction des ondes : méthode DSM

Mots clés : Méthode d'échantillonnage direct, problème de diffusion électromagnétique inverse, analyse mathématique

Résumé : Le problème de l'imagerie non itérative dans le cadre de la diffraction électromagnétique inverse utilisant la méthode d'échantillonnage direct (DSM) est considéré.
Grâce à une combinaison de l'expression asymptotique du champ proche ou du champ lointain diffracté et de l'hypothèse de petits obstacles, les expressions analytiques de la fonction d'indicateur DSM sont présentées dans diverses configurations telles que des configurations 2D/3D, mono-/multi-configurations statiques, à vue limitée/complète et fréquence unique/ diversité en fréquence. Une fois l'expression analytique obtenue, sa structure est analysée et des améliorations proposées. Notre approche est validée à l'aide de données de simulation, et d'expériences le cas échéant.
Premièrement, la structure mathématique du DSM à fréquence fixe en 2D dans divers problèmes de diffusion est établie, permettant une analyse théorique de son efficacité et de ses limites. Pour surmonter les limitations connues, une méthode alternative d'échantillonnage direct (DSMA) est proposée. Puis le cas multi-fréquence est investigué en introduisant et en analysant le DSM multi-fréquence (MDSM) et le DSMA multi-fréquence (MDSMA). Enfin, notre approche est étendue aux problèmes de diffraction électromagnétique inverse 3D pour lesquels le choix de la polarisation du dipôle de test est un paramètre clé. De par notre approche analytique, ce choix peut être effectué sur la base de la polarisation du champ incident.

Title: Direct sampling method in inverse electromagnetic scattering problem

Keywords: Direct sampling method, Inverse electromagnetic scattering problem, Mathematical analysis

Abstract: The non iterative imaging problem within the inverse electromagnetic scattering framework using the direct sampling method (DSM) is considered. Thanks to the combination of the asymptotic expression of the scattered near-field or far-field and of the small obstacle hypothesis the analytical expressions of the DSM indicator function are presented in various configurations such as 2D/3D configurations and/or mono-/multi-static configurations and/or limited-/full-view case and/or mono-/multi-frequency case. Once the analytical expression obtained, its structure is analyzed and improvements proposed. Our approach is validated using synthetic data and experimental ones when available. First, the mathematical structure of DSM at fixed frequency in 2D various scattering problems is established allowing a theoretical analysis of its efficiency and limitations. To overcome the known limitations an alternative direct sampling method (DSMA) is proposed. Next, the multi-frequency case is investigated by introducing and analyzing the multi-frequency DSM (MDSM) and the multi-frequency DSMA (MDSMA). Finally, our approach is extended to 3D inverse electromagnetic scattering problems for which the choice of the polarization of the test dipole is a key parameter. Thanks to our analytical analysis it can be made based on the polarization of the incident field.

Université Paris-Saclay
Espace Technologique / Immeuble Discovery
Route de l'Orme aux Merisiers RD 128 / 91190 Saint-Aubin, France